UNIVERSITY OF CALIFORNIA, IRVINE

Interfaces in Polymer Electrolyte Membrane Water Electrolyzers

DISSERTATION

submitted in partial satisfaction of the requirements
for the degree of

DOCTOR OF PHILOSOPHY

in Materials Science and Engineering

by

Devashish Kulkarni

Dissertation Committee:
Associate Professor Iryna Zenyuk, Chair
Professor Plamen Atanassov
Assistant Professor Stacy Copp

2022

DEDICATION

To my parents Anjali and Shashi, and friends for their unwavering belief in me and in recognition of their worth

An ode to this journey...

"Unless you try to do something beyond what you have already mastered, you will never grow"

Ralph Waldo Emerson

Table of Contents

List of Figures

List of Tables

Acknowledgements

First and foremost, I would like to thank my advisor, Prof. Iryna Zenyuk for her invaluable guidance, patience, and support in my research. I have found in her, a scientist of relentless drive, an advisor who is willing to go above and beyond for her students, a dedicated educator, and a generous philanthropist. I am incredibly grateful to have had the opportunity to work under her supervision, to have spent 8+ beamtimes, have awe inspiring, intellectual conversations and learn valuable lessons that I will carry forward for the rest of my career.

I would like to thank my thesis committee members Prof. Plamen Atanassov and Prof. Stacy Copp for their valuable feedback and encouraging words that helped me in finding direction for my research and this dissertation. Special thanks to Plamen for his knowledge and humorous wit is magnetic and inspiring. I am fortunate to have had stimulating conversations and his esteemed mentorship throughout my PhD studies. I am grateful to Chris Capuano, director of research and development at Nel Hydrogen for his continued support with high quality data, research materials and stimulating collaboration on high impact research projects. His gracious hospitality made our industrial visit at Nel Hydrogen incredibly fruitful and informative. I want to thank beamline scientists Dr. Dula Parkinson and Dr. Pavel Shevchenko for their immense help during beamtimes and for sparing their weekends for us without a second thought. The text of this dissertation is in part a reprint of the material as it appears in [1]–[3], used with permission from Elsevier and Iscience. I thank them for the permission to include copyrighted figures as part of my dissertation.

I am indebted to several of my lab mates at UCI. I am thankful to Ying Huang for helping me with Tomography and XPS analysis and for her humorous energy. I am grateful to Pongsarun Satjaritanun for helping me with LBM CFD analysis and Alex Huynh for helping with Electrochemical experiments. Thanks to Yongzhen Qi and Prantik Saha for helping me integrate into the lab culture when I first joined the research group. I am thankful to Arezoo Avid, Kaustubh Khedekar and John Stansberry for their valuable friendship and encouragement throughout my Ph.D. journey. I am thankful to Hung-Ming Chang for his incredible kindness and camaraderie. His presence made the lab culture convivial and made us a family along with helping me create a winning proposal for Big Ideas Berkeley competition!

To my friends, thank you for always keeping me grounded and making me feel loved and appreciated through the thick of the pandemic and isolation. Deepest thanks to my brother Devavrat for always being encouraging and supportive of my adventures.

Finally, to my parents Anjali and Shashi, I am forever grateful for the sacrifices you made for bringing me to this stage and for always believing in me. I owe all my accomplishments and successes to you. Thank you mom, for the ridiculous amount of phone calls that kept me sane during hard times and dad, for always having by back when things seemed hopeless. Your names should be on this thesis as much as mine.

VITA

Devashish Kulkarni

2018 B.E., Mechanical Engineering, Maharashtra Institute of Technology, University of Pune

2020 MS, Materials Science and Engineering, University of California, Irvine

2022 Ph.D. Materials Science and Engineering, University of California, Irvine

FIELD OF STUDY

Materials Science and Engineering

PUBLICATIONS

1. **Devashish Kulkarni**, Stanley J Normile, Liam G Connolly and Iryna V Zenyuk "Development of low temperature fuel cell holders for Operando x-ray micro and nano computed tomography to visualize water distribution" 2020 J. Phys. Energy 2 044005
2. **Devashish Kulkarni**, Alex Huynh, Pongsarun Satjaritanun, Maeve O'Brien, Sirivatch Shimpalee, Dilworth Parkinson, Pavel Shevchenko, Francesco DeCarlo, Nemanja Danilovic, Katherine E Ayers, Christopher Capuano and Iryna V Zenyuk "Elucidating effects of catalyst loadings and porous transport layer morphologies on operation of proton exchange membrane water electrolyzers" Applied Catalysis B: Environmental 308 (2022) 121213
3. Pongsarun Satjaritanun, Maeve O'Brien, **Devashish Kulkarni**, Sirivatch Shimpalee, Cristopher Capuano, Katherine E. Ayers, Nemanja Danilovic, Dilworth Y. Parkinson, Iryna V. Zenyuk. "Observation of Preferential Pathways for Oxygen Removal through Porous Transport Layers of Polymer Electrolyte Water Electrolyzers, iScience, Volume 23, Issue 12, 2020
4. Zachary Taie, Xiong Peng, **Devashish Kulkarni**, Iryna V. Zenyuk, Adam Z. Weber, Christopher Hagen, and Nemanja Danilovic "Pathway to Complete Energy Sector Decarbonization with Available Iridium Resources using Ultralow Loaded Water Electrolyzers" ACS Applied Materials & Interfaces 2020 12 (47), 52701-52712
5. Xiong Peng, **Devashish Kulkarni**, Ying Huang, Travis J Omasta, Benjamin Ng, Yiwei Zheng, Lianqin Wang, Jacob M LaManna, Daniel S Hussey, John R Varcoe, Iryna V Zenyuk, William E Mustain "Using operando techniques to understand and design high performance and stable alkaline membrane fuel cells" Nature Communications 11, 3561 (2020)

6. Ying Huang, Yechuan Chen, Mingjie Xu, Tristan Asset, Peter Tieu, Albert Gili, **Devashish Kulkarni**, Vincent De Andrade, Francesco De Carlo, Harold S Barnard, Andrew Doran, Dilworth Y Parkinson, Xiaoqing Pan, Plamen Atanassov, Iryna V Zenyuk "Catalysts by pyrolysis: Direct observation of chemical and morphological transformations leading to transition metal-nitrogen-carbon materials" Materials Today d Volume 47 d July/August 2021

PATENTS

1. Chemical calcium hydroxide manufacturing for cement production using electrochemical separation devices. Aug 11, 2020. Patent issuer and number: US63064327

ABSTRACT OF DISSERTATION

Interfaces in Polymer Electrolyte Membrane Water Electrolyzers

By

Devashish Kulkarni

Doctor of Philosophy in Materials Science and Engineering

University of California, Irvine 2022

Associate Professor Iryna Zenyuk, Chair

The growing demand of energy and rising climate concerns call for an urgent need to decarbonize the highly polluting energy sector by adopting hydrogen economy. Polymer electrolyte membrane water electrolyzers (PEMWEs) are a promising technology to produce green hydrogen by water electrolysis at high efficiencies and low temperature. The hydrogen evolution reaction (HER) on cathode has fast kinetics hence it can happen with low precious metal loadings. However, the Oxygen Evolution Reaction (OER) occurring on iridium based (IrOx) electrocatalyst on the anode has extremely sluggish kinetics and imparts significant overpotential to the system. Hence, the widespread deployment of this technology is stifled today by the use of expensive and rare iridium and high catalyst loadings (~2 mg/cm^2). Additionally, the absence of a stable and durable catalyst support leads to underutilization of the available catalyst. The interfacial contact between the catalyst layer, the proton conducting media and the porous transport layer (PTL) morphology play a major role in influencing PEMWE performance. The nature of these microscopic interfaces and

their effect on different cell overpotentials and system durability are not well understood. Hence, understanding the factors affecting catalyst utilization by interfacial analysis and engineering better interfaces is imperative to realize GW scale deployment of these systems.

This dissertation aims to characterize the nature of interfaces and its effect of bulk transport phenomenon primarily with the use of X-ray computed tomography. We developed the method for operando X-ray characterization of PEMWEs by designing and optimizing operando cell designs. With image analysis we developed formulation for calculating the Triple Phase Contact Area (TPCA) which quantifies the electrochemically active area that otherwise cannot be calculated with electrochemical techniques in full cells. We used the developed TPCA method along with electrochemical and modeling techniques to characterize the interface for two different porous transport layers (PTLs) and catalyst layers at various loadings. We show that low porosity sintered PTLs exhibits higher TPCA that results in improved kinetics. Radiography and modeling results indicate that oxygen taking multiple transport pathways through the PTL results in slug flow through the channels that reduces mass transport overpotential. We further this study using microporous layers (MPLs) on sintered PTLs. Along with interface characterization, for the first time, we showed time averaged oxygen pathways through PTLs using X-ray tomography. We showed how MPLs shift oxygen invasion patterns through PTLs and increase catalyst utilization by suppressing bubble masking. Based on the results, we suggest optimal MPL design strategies to enable low catalyst loadings.

We developed an accelerated stress test protocol by understanding OER kinetics on IrOx catalysts and its effect on dissolution. Following the developed protocol, we concluded that most degradation is kinetically dominated resulting from loss of Ir from the cell. From XPS analysis, we saw Ir(III)-Ir(IV) redox shift during OER onset and potential cycling. Finally, we conducted

1000 hr durability tests and found that optimal MPL design can increase system lifetime and cause least voltage decay thus achieving a step forward in enabling large scale green hydrogen production.

1. Introduction

Since the industrial revolution, humans have made tremendous progress as a species to improve their life with advancements in technology. The main driver for human progress is energy. Although we have seen astonishing strides in nearly all fields of human existence in a relatively short amount of time, it came with the cost of rapid climate change due to global warming caused by unregulated and unprecedented emission of greenhouse gases (GHG) at the start of the 20th century. Governments around the world are now aggressively trying to reduce their GHG emissions when 193 countries including the United States formally took a pledge to keep global temperatures from rising 2 degrees above pre-industrial levels[4]. The major contributor to GHG emissions is the energy sector accounting for over 40% of the total emissions. To curb emissions from burning fossil fuels, there is a massive installment of renewables such as solar and wind on the energy grid. These sources have inherent issues of generation intermittency according to the time of the day or year. Although electrifying sectors seems like an easy enough solution to integrate renewables, industrial sectors such as metal refining, long haul shipping, aviation and chemical industry are still deemed ‘hard to decarbonize’ sectors. Along with that, the issue of

massive seasonal energy storage becomes more important by the day as renewable penetration increases on the grid. While technologies such as grid battery storage and pumped hydro are established routes to store excess renewable energy, their storage duration lasts from hours to days. One of the most promising concepts for cross sector energy linkage is using Hydrogen as the main energy carrier in the society. Although Hydrogen has always seemed like a prospect 10-15 years into the future, converging technologic and market conditions show tremendous momentum for the concept today. Since hydrogen is an excellent clean chemical fuel with a high energy density, its movement in the society presents a strong promise to decarbonize the previously described "hard to decarbonize" sectors. The hydrogen centric energy economy is well represented by the US department of Energy's H2@scale schematic represented in **Figure *1-1***.

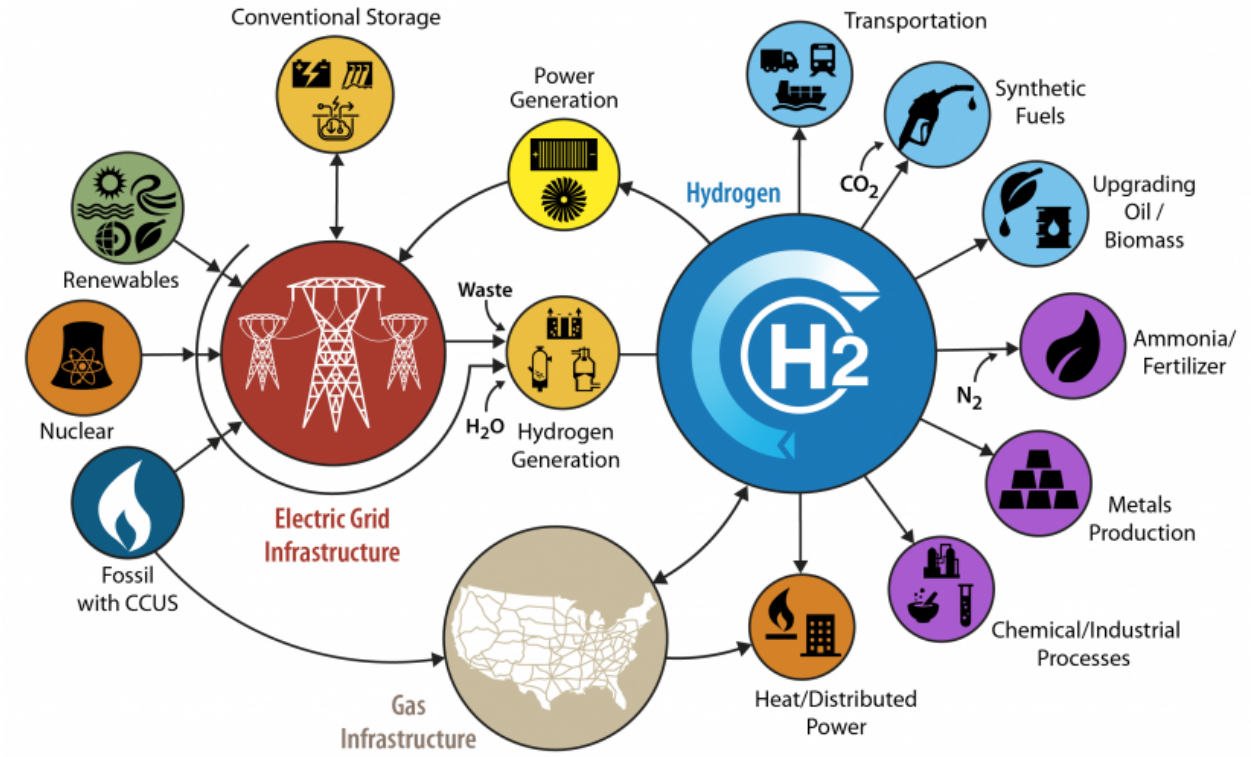

Figure 1-1 US Department of Energy's H2@Scale showing Hydrogen can be the central energy carrier for multiple hard to decarbonize industries

Producing and storing green hydrogen from the excess curtailed renewable energy by electrochemically splitting water is the cornerstone of the hydrogen economy [5]–[7]. Polymer electrolyte water electrolysis (PEMWEs) is a promising technology that is gaining widespread popularity among the available electrolysis chemistries due to its low temperature operation, dynamic start up and response times, differential pressure operation and ease of scalability [8][9]. The US and several other countries are aggressively pushing for hydrogen-based economies with the US department of energy announcing $64 million to support its H2@scale initiative [10] in 2020 alone. The European clean hydrogen alliance was launched by the EU in 2020 and estimates investments of $503 billion until 2030 [11]. Hydrogen production is targeted at a cost of $2 per kg_{H2} [12] in order to be competitive with traditional fossil fuels.

The electrochemical splitting of water by PEMWE operation involves the fast hydrogen evolution reaction (HER) on the cathode and the sluggish oxygen evolution reaction (OER) on the anode. The HER is facilitated by Pt-based electrocatalyst whereas the OER is facilitated by the current state-of-the-art IrOx based electrocatalysts [13][14]. The use of these rare metals is a substantial cost driver specifically when MW scale deployment of PEMWEs are envisaged to make the produced hydrogen cost competitive [15]. Hence, the availability of Ir is a growing concern since it is one of the rarest elements found on the earth's crust with an estimated production of only ~ 7.25 tons annually [16]. Hence in order for the meaningful adoption of this technology to completely decarbonize the energy sector, it is imperative to reduce catalyst loadings and improve the Ir-specific power which is a measure of the potentiality of the catalyst. Current commercially available PEMWE systems have an Ir-specific power of ~ 2 MW/kg_{Ir} [17] when the current density is measured at a higher heating value (HHV) based efficiency of 88%. However, this translates to a deployment of only 7.2 GW per year even if 50 % of the annual production of Ir were to be used

for PEMWEs. Considering only the energy required currently for the transportation sector, and assuming that this demand would be supplied by H_2, this would require a ~ 50-fold increase in the Ir-specific power to 100 MW/kg_{Ir} [18] . **Figure *1-2*** investigates the where the existing literature stands, relative to these targets using the Ir loading and current density to define the parameter space. The green space highlights where the 26 MW kg_{Ir}^{-1} (natural gas sector) target is met.

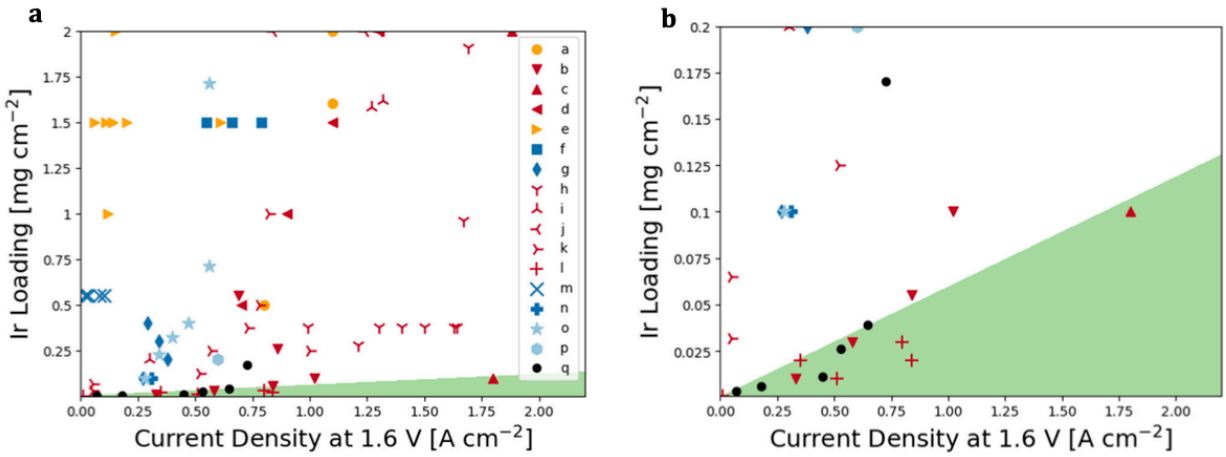

Figure 1-2 (a) Operational map showing the combinations of current density and catalyst loading necessary to achieve an Ir-specific power of 26 MW $kgIr^{-1}$ The area shaded in green achieves this target, while the white area does not. (b) Magnification of the ULL region where the target Ir-specific power is achievable. The symbol color refers to membrane thickness: dark blue, ~180 um; light blue, ~130 um; orange, ~90 um; red, ~50 um. References for the data are as follows: a [19]; b [20],; c [21],; d [22],; e [23],; f [24],; g [25],; h [26],; i [27],; j [28],; k [29],; l [30],; m [31],; n [15],; o [32],; p [33],; q [34]. Reproduced from reference [34].

The Ir-specific power can be increased by either decreasing the Ir loading or increasing the operating current density and has been widely explored in literature [21], [23], [35]. Taie et.al [16] in their recent work investigated ultra-low loaded anodes up to 0.0035 mg cm^{-2} for PEMWEs considering the available Ir resources and the target of complete decarbonization of the energy

sector by 2050. shows the performance of the low and ultralow loaded PEMWE in the green section overlayed in colored markers. Developing stable and uniform catalyst layers at such low loadings requires significant efforts, advanced manufacturing techniques like ultrasonic spray coating and optimization strategies. Moreover, the maximum current density achieved may be insufficient for practical applications. Other ways to reduce loadings are to create even dispersions of Ir on high surface area materials or thin films like TiC [23], TiO_2 [36] or nano structured thin films (NSTF) [29]. Usage of non-PGM [37] and advanced core shell catalysts [15] for OER are also being studied to reduce or eliminate the dependance on noble metals. However, these techniques are still at the experimental stage and need more technical maturity to be commercialized. While these technical strides are important for reducing the future capital cost, the need of the hour is to minimize CAPEX by reducing iridium loadings and the operating costs (OPEX) by engineering better, more durable interfaces and porous transport components

1.1 Background

1.1.1 Proton exchange membrane water electrolysis

Figure *1-3* shows the operating principle of a PEMWE. It consists of an anode and cathode separated by a proton exchange membrane. The cathode and anode are ~10 μm in thickness and are sufficiently porous to enable transport of water and protons as well as electrically conductive to enable electrochemical reactions to occur. The catalyst MEAs are sandwiched between porous media to allow reactants and products to flow in and out as well as provide mechanical support, thermal stability and electrical connection to the bipolar plates. During operation, pure liquid water

is supplied and a high potential (1.4 – 2.2 V) is applied to the anode side to split water into oxygen and protons. The protons travel through the membrane to the cathode side where they are reduced to pure hydrogen gas.

The evolved oxygen is removed through the porous transport layer (PTL) on the anode side and hydrogen is removed through the gas diffusion layer (GDL) on the cathode side. The water uptake through the membrane resulting from the electro-osmotic drag helps keep the cathode catalyst layer sufficiently humidified. Hence, there is no need for external water supply to the cathode. The half reactions occurring on the electrodes and the overall reaction is given by equations (1-1, (1-2, and (*1-3* respectively)

$$Anode\ OER: \quad H_2O \rightarrow \frac{1}{2}O_{2(g)} + 2H^+ \tag{1-1}$$

$$Cathode\ HER: \quad 2H^+ + 2e^- \rightarrow H_{2(g)} \tag{1-2}$$

$$Net\ reaction: \quad H_2O \rightarrow \frac{1}{2}O_{2(g)} + H_{2(g)} \tag{1-3}$$

Oxygen evolution reaction happens on the anode and typically an iridium oxide based electrocatalyst is used to improve reaction kinetics. On the cathode, a Pt/C electrocatalyst is used to reduce protons to hydrogen gas in Hydrogen Evolution Reaction (HER).

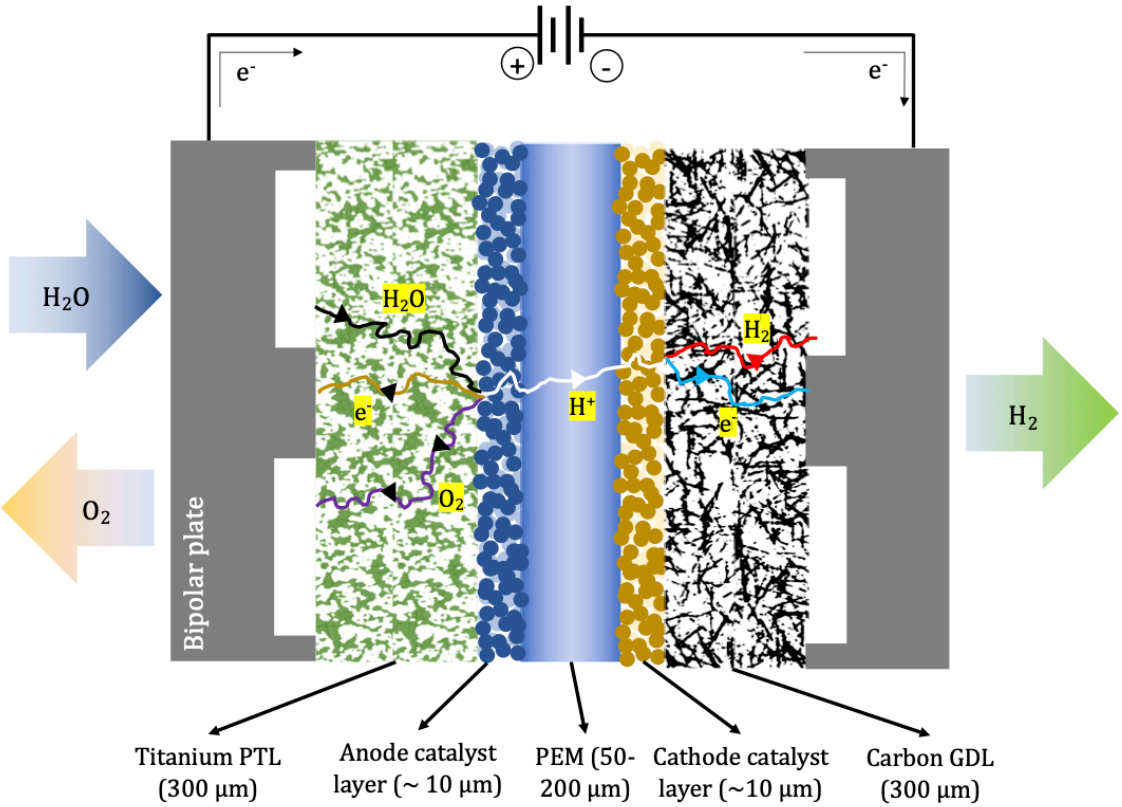

Figure 1-3 Polymer electrolyte water electrolyzer cell schematic (components not drawn to scale) showing relevant transport processes and flow paths

OER thermodynamically happens at a reversible potential of 1.23V (vs. SHE) but generally, OER is measured at a thermoneutral potential of 1.45V (vs. SHE) considering the higher heating value of hydrogen. The thermoneutral potential V_{TN} is defined as the potential at which water electrolysis can be conducted without the production or consumption of heat, i.e., where a thermally insulated electrolyzer would operate at constant temperature. HER occurs on Pt electrode at a reversible cell potential of 0.0 V. Hence, while defining absolute cell potentials, we refer only to OER. At standard conditions (298 K, 1 bar), the Gibbs free energy ΔG_0 is 237 kJ/mol for OER. This represents the minimum electrical work needed for splitting water at the corresponding reversible cell potential

$$\Delta E_{rev} = \left| -\frac{\Delta G}{nF} \right| = 1.23V$$

Where n is the number of transferred electrons in in reactions 1-1 and 1-2 (n=2 in this case) and F is the Faraday constant (96485 C mol^{-1}). The thermoneutral voltage is given by:

$$V_{TH} = \left| -\frac{\Delta H_{HHV}}{nF} \right| = 1.48V$$

where $\Delta H_{HHV} = 285.8\ Kj/mol$ is the higher heating value of hydrogen. The HHV of hydrogen considers enthalpy of vaporization (which is equal to enthalpy of condensation) of water ($\Delta H_{vap} = 44\ Kj/mol$). This is considered because hydrogen coming out of the electrolyzer is wet and total heat balance of the system considers energy to condense the water unless the produced wet H_2 is directly used energetically (for ex. a fuel cell) and the system does not benefit from condensing the water. In this case, the lower heating value (LHV) is used for voltage efficiency calculations which is rarely the case.

1.1.3 Overview of components

Porous transport layers:

The porous transport layers (PTLs) facilitate the transport of reactants and products to the reaction sites. It conducts liquid water and gases through it pore network and electrons through its solid structure to and from the bipolar plates. The PTLs at the anode side are generally made of titanium to resist the harsh corrosive environments that would typically corrode and destroy carbon-based materials. They also provide structural and mechanical stability to the membrane and catalyst layer if the PEMWE is operated at differential pressures. The PTLs on the cathode, however, can be made from carbon-based materials like the Freudenberg GDL used typically in fuel cells. We will refer to anodic layers as PTLs and the cathodic layers as GDLs throughout this work. The

morphological properties of the PTL such as the porosity, particle size and tortuosity play a significant role in influencing PEMWE performance. There are two major types of commercial used PTLs namely titanium fiber and sintered titanium. Fiber PTLs are made by evenly distributing the Ti microfibers (~ 20 µm diameter), thermally sintering and eventually roll pressing to control the thickness and smoothing the surface. Sintered PTLs are made by thermally sintering Ti powder having spherical particles either with a laser or in a furnace. The sintering conditions like the pressure and temperature can be controlled to influence properties like porosity and particle size arbitrarily. Advanced manufacturing techniques such as electron beam melting or photochemical machining of Ti foils have also been explored to obtain PTLs with tunable porosity [38].

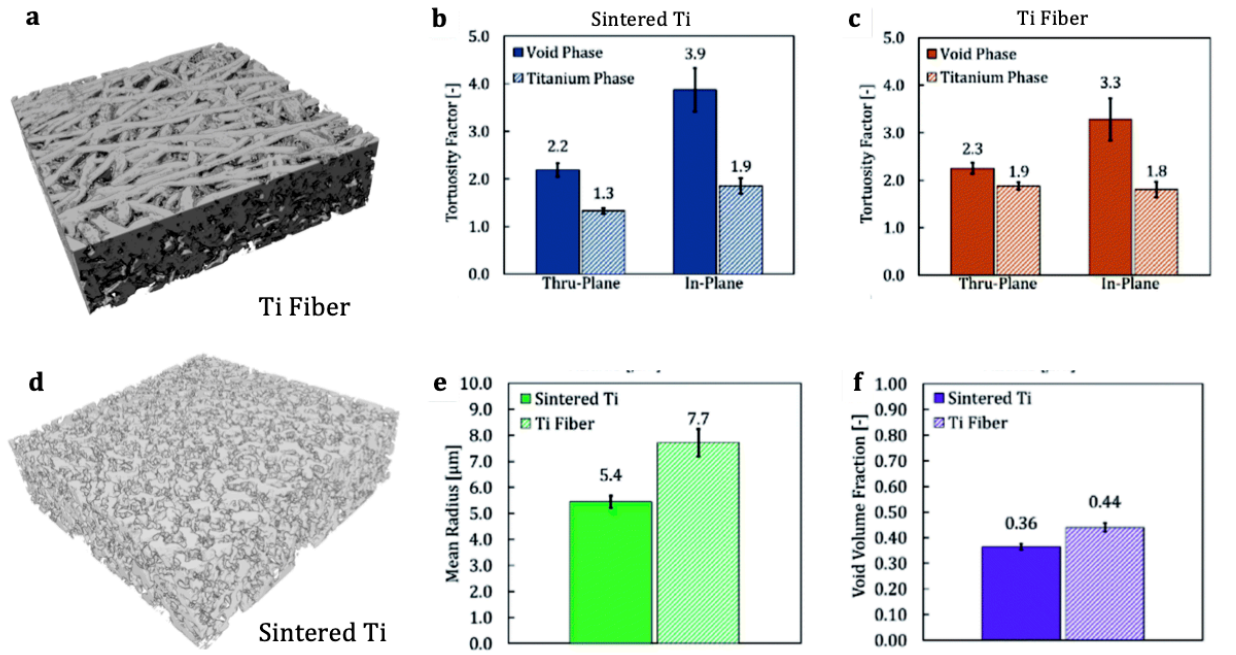

Figure 1-4 Tortuosity and pore size distribution results for the two different titanium PTL morphologies [39]. Tortuosity factor was analyzed using the TauFactor application for the solid (titanium) and void (pore) phases in the through-plane and in-plane directions. For both metrics the analyzed samples were 1 mm^2 in the through-plane perpendicular area. Results shown are for

a minimum of three samples per PTL morphology. 3D volume renderings obtained from X-ray imaging for (a) titanium fiber (d) sintered titanium. Average tortuosity factor results for (b) sintered titanium, and (c) titanium fiber PTLs. The mean pore radius of the two PTL morphologies are graphically represented in (e) and porosities of the two samples are shown in (f) by void volume fraction. Tortuosity, mean radius and porosity plots reproduced from reference [39]

Figure 1-4 shows the tortuosity and pore size distribution results for fiber and sintered Ti PTLs obtained from X-ray CT imaging. Tortuosity is the measure of how convoluted path a particle takes with respect to the shortest distance between two points when flowing through a porous medium. For both types of PTLs, the tortuosity factors through the void space are higher than the titanium phase as reported in **Figure 1-4** b and c. This can be bolstered by the fact that the void volume fractions are lesser than the solid volume fractions for both PTLs as represented in **Figure 1-4** f. Sintered Ti has a higher in-plane tortuosity factor of 3.9 as compared to Ti fiber which has a value of 3.3. The PTLs however exhibit anisotropy as the tortuosity factors in the in-plane direction vary greatly with respect to the through-plane values. Both fiber and sintered PTLs have a similar through-plane tortuosity factor of 2.2 and 2.3 respectively. While this may be attributed to sintered PTL having a lower volume fraction, the method of laser sintering can potentially induce some directionality. Looking at the volume renderings of the two PTLs in **Figure 1-4** a and d, one can notice a higher in-plane tortuosity in the fiber PTL than through-plane as there is an apparent higher quantity of void pathways in the through-plane direction. This results in fluid flow in the through plane direction since it takes the path of least resistance as opposed to fuel cell GDLs where the preferential fiber alignment forces the flow in the in-plane direction.

Figure 1-4 e shows the reports the mean pore radius for both PTLs. The fiber PTL has a larger average void radius size of 7.7 μm compared to sintered PTL of 5.4 μm, providing a less tortuous

network for water and gas to transport through.

In summary, PTL structure and morphology have a multitude of functions and play a very important role in PEMWEs. A better understanding of the transport processes and interfacial characteristics exhibited by the PTL as well as new developments in terms of materials, structure and properties could play a significant role in optimizing PEMWE performance.

1.2 Cell efficiency and voltage losses

Since all the components in the cell are electronically arranged in series with each other, the measured (total) cell voltage can be defined as the sum of the thermoneutral voltage and all associated losses.

$$E_{cell} = E_{th} + i(R_{memb} + R_{el}) + |\eta_{HER}| + \eta_{OER} + i\left(R^{eff}_{H+,cat} + R^{eff}_{H+,anode}\right) + \eta_{mt} \qquad (1\text{-}4)$$

Here E_{th} is the thermoneutral voltage obtained from the Nernst equation, η_{HER} is the kinetic overpotential for HER, η_{OER} is the kinetic overpotential for OER, R_{memb} and R_{el} are the ohmic resistance of the membrane and the electrical contact resistances (between bipolar plates and the PTL as well as other bulk PTL resistance) respectively. $R^{eff}_{H+,cat}$ is the proton transport resistance on the cathode, $R^{eff}_{H+,anode}$ is the proton transport resistance on the anode and η_{mt} is the mass transport overpotential. **Figure *1-5*** shows a typical polarization curve and identifies contributions from all associated losses.

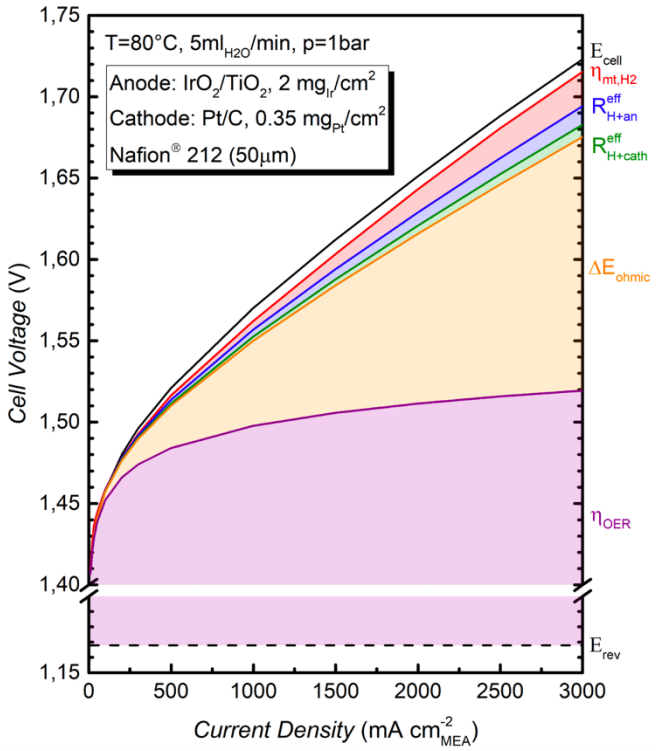

Figure 1-5 Contributions of various voltage losses to overall cell voltage. The reversible cell voltage is given by the dashed black line and the purple area represents the OER kinetic losses (y-axis is intercepted between 1.23V and 1.4V for better visualization of other losses). Ohmic losses are given by the orange area, and losses due to proton conduction resistance in the cathode and anode electrodes are shown by the green and blue areas, respectively. The red area represents the losses due to H2 mass transport and the full black line gives the cell voltage measured at ambient pressure (80°C, 5 ml_{H2O} min^{-1}). The white space between the full black line and the red line represents unaccounted voltage losses, which could originate from mass transport phenomena on the anode. Catalyst loadings are 2mg_{Ir} cm^{-2} on the anode and 0.35mg_{Pt} cm^{-2} on the cathode; ≈50 µm thick Nafion 212 membrane. Reproduced from reference [18].

Generally, for electrolytic cells where usable chemical energy is the desired output and electrical energy is the input, the ratio of the former to the latter is the energy conversion efficiency. In our case, gaseous hydrogen is the desired product. For low temperature PEMWEs, the following assumptions are made before we define its efficiency.

1. The production of hydrogen at normal pressure is regarded as the only useful output of the system and influence from production of oxygen is disregarded

2. The PEMWE is operated at a temperature below 373.15 K and electricity is the only energy input. Thermal energy cannot be incorporated from surroundings

3. The supplied water is always in liquid state and hence the enthalpy of evaporation (ΔH_{vap}^{0}) of water must come from the electrical input.

On the cell level, the voltage efficiency η_v^{HHV} can be defined as the ratio of the thermoneutral voltage V_{TN} to the actual measured voltage $V_{op}(T)$ at a specific temperature T.

$$\eta_v^{HHV} = \frac{V_{TN}}{V_{op}(T)} = \left| \frac{-\Delta H_{vap}^{0}}{2.F.V_{op}(T)} \right| \tag{1-5}$$

Equation (*1-5* is only valid assuming that the supplied current is converted completely into the electrochemical reaction of water splitting. This is practically not the case due to unmeant side reactions and stray current inside the cell. Moreover, permeation of the gases through the membrane and subsequent recombination to water and gas leakages lead to a hydrogen loss. To account for these processes, the Faradaic or current efficiency η_F is defined as the ratio of the amount of actually produced hydrogen under real conditions and the amount of theoretically produced hydrogen according to Faraday's law [9].

$$\eta_F = \frac{\dot{n}_{H2,op}}{\dot{n}_{H2,theor}} = \frac{\dot{n}_{H2,op}}{I/nF} \quad (1\text{-}6)$$

$\dot{n}_{H2,op}$ is the actual amount of produced hydrogen, $\dot{n}_{H2,theor}$ is the theoretical quantity of produced hydrogen from Faraday's law. *I* is the applied current, *n* is the number of electrons transferred and *F* is the faraday's constant.

1.3 Balance of plant and Economics at scale

Figure 1-6 shows the main balance of plant components of the PEMWE system. The five major subsystems that make up the balance of plant and their components are:

1. Power electronics subsystem: AC transformer, AC/DC rectifier, DC voltage and current transducers
2. Water management subsystem: Water purification subsystem, ion exchanger, feed and supply pumps, gas/water separators, recirculation pump, piping, valves, and instrumentation
3. Hydrogen production subsystem: Condensate traps, pressure swing adsorption (PSA) dryers, gas separators, valves and other instrumentation.
4. Heat exchange subsystem: Heat exchangers, cooling pumps, fans
5. Control subsystem: receives information from various sensors and controls valves, actuators and stack power according to control instructions for optimal operation.

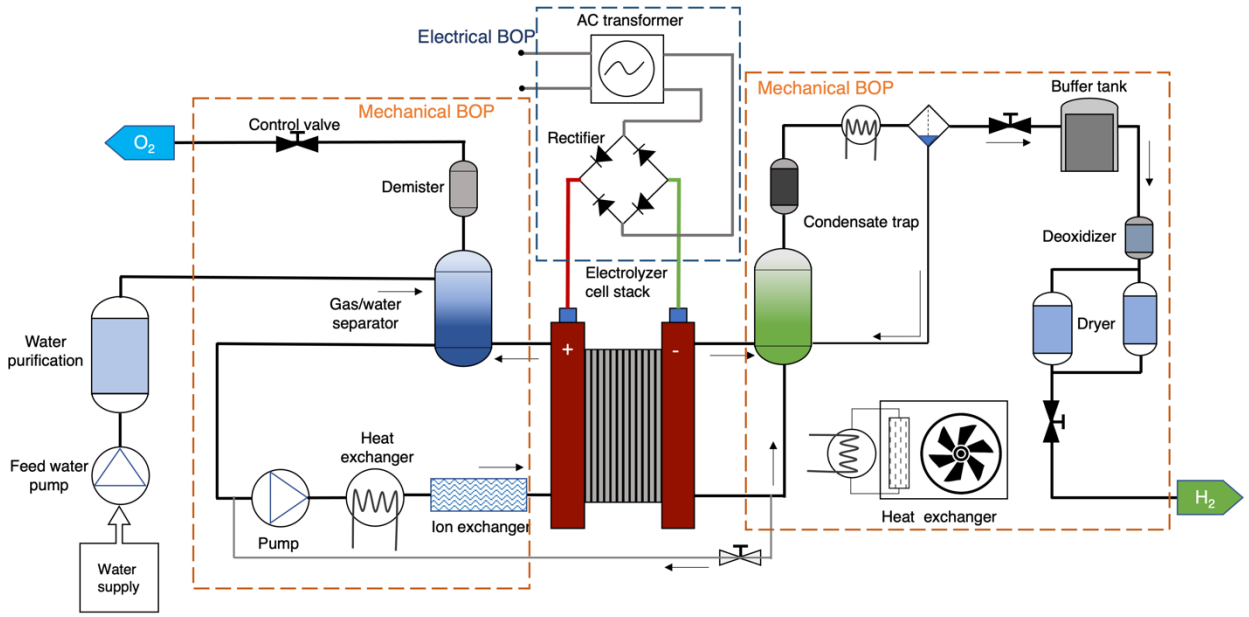

Figure 1-6 PEM electrolyzer system showing balance of plant components

During system operation, purified and deionized water (ASTM type 1, resistivity >18 MΩ cm^2) is fed to the electrolyzer stack from the water management subsystem. As oxygen is produced in the stack, it flows out into the gas water separator where oxygen is removed from the water by simple gravity-based separation. The oxygen is then passed through the demister to remove any liquid droplets and collected in a tank or let out into the atmosphere. On the hydrogen side, the condensate traps remove any large droplets of water present in the outlet gas. Hydrogen is mostly collected at a higher pressure than the water side. Hydrogen pressure should be at least 0.068 bar above the water pressure [40]. This ensures that hydrogen can be detected in the water/oxygen outlet in case the membrane is breached, and the stack needs to be shut down immediately for safe operation. The hydrogen is further dried by pressure swing adsorption (PSA) based dryers and stored in pressurized tanks for further use.

The mechanical BoP consists of the water management subsystem and hydrogen subsystem as shown in **Figure *1-6***. The electrical BoP consists of the power electronics and controls subsystem.

To date, there has been much less investment in electrolyzer manufacturing technology but its similarity to the fuel cell industry shows clear pathways of cost reduction. The estimated cost of PEM electrolyzers is currently over $1000 per kW since manufacturing capacity is limited only a few systems per year [41]. With the US department of Energy's Hydrogen Earth Shot initiative, the cost of electrolyzers must ultimately reduce to $150 per kW if the goal of hydrogen cost at $1 per kg is to be reached. **Figure *1-7*** a shows the manufacturing cost curve with annual production of electrolyzer systems. The total cost consists of over 50% in catalyst and membrane as the stack price is lowered to $150 per kW with increasing production rates [42]. Since HER has fast kinetics, PGM loadings on the cathode can be lowered to ~0.1 mg/cm^2 without imparting much overpotential to the system. However, since OER is extremely sluggish, the anode requires higher loadings of IrOx catalysts to drive the reaction. Hence, reduction in Ir loadings is critical for realizing PEM electrolysis at GW scale.

Almost 50 % of the balance of plant cost comes from the power supply as seen in **Figure *1-7*** b and c for electrolyzer systems over 1 MW. Since these systems are operated at huge currents that go over 1000 A, it requires expensive AC/DC rectifier that can supply the required amperage at relatively low voltages.

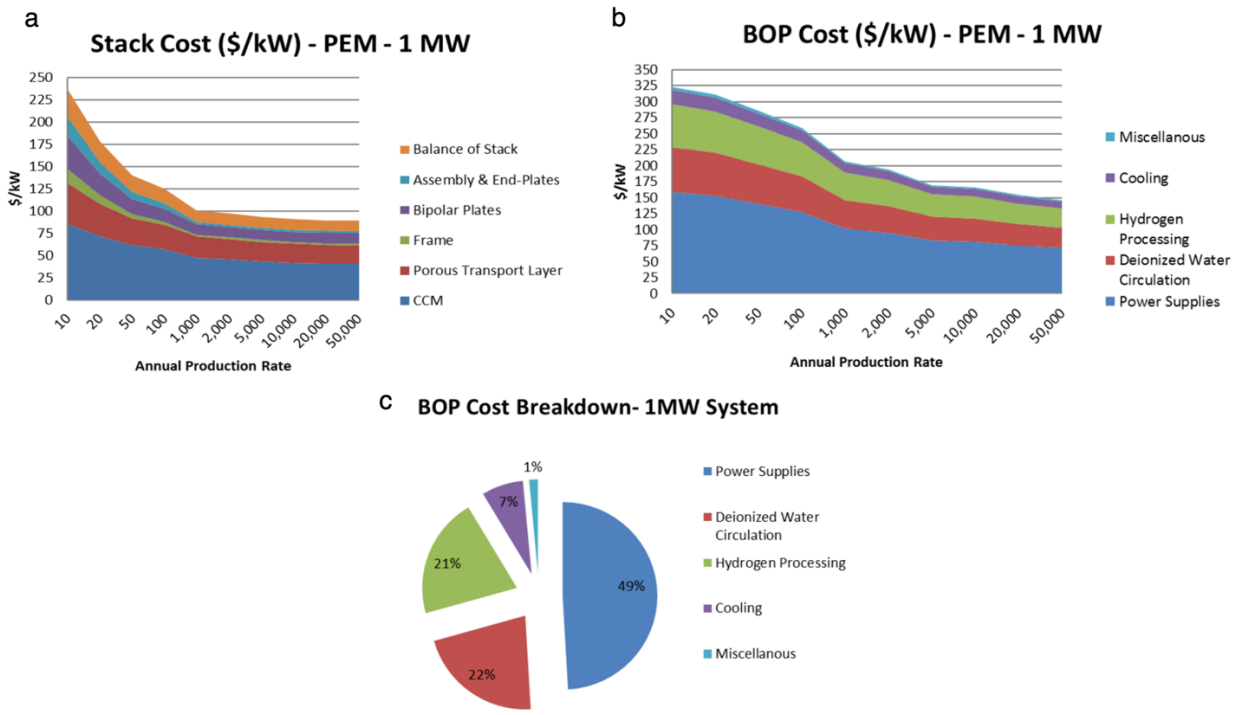

Figure 1-7 a. Manufacturing cost curve for 1-MW PEM electrolyzer stack at different scales. b. BOP cost curve as a function of the annual production rate for 1-MW system c. Cost breakdown for the BOP parts for 1-MW system. Adapted from [42]

The deionized water circulation system and hydrogen processing units contribute to about one fifth of the total BoP cost. Similar to the stack cost trend, the BoP cost comes down significantly as the production capacity is increased.

1.4 Methods

1.4.1 Electrochemical testing

A schematic of the electrolyzer test station built for the course of this thesis is shown in ***Figure 1-8***. A standard Scribner® fuel cell hardware was repurposed and used as the electrolyzer cell. The cathode bipolar plate was made with graphite and had CNC machined standard triple serpentine

channels of 1 mm x 1mm (land x channel width) dimensions. The anode bipolar plate was custom-made titanium plate with 1mm x1 mm parallel channels. The land and channel surfaces were platinized for corrosion resistance and high electrical conductivity.

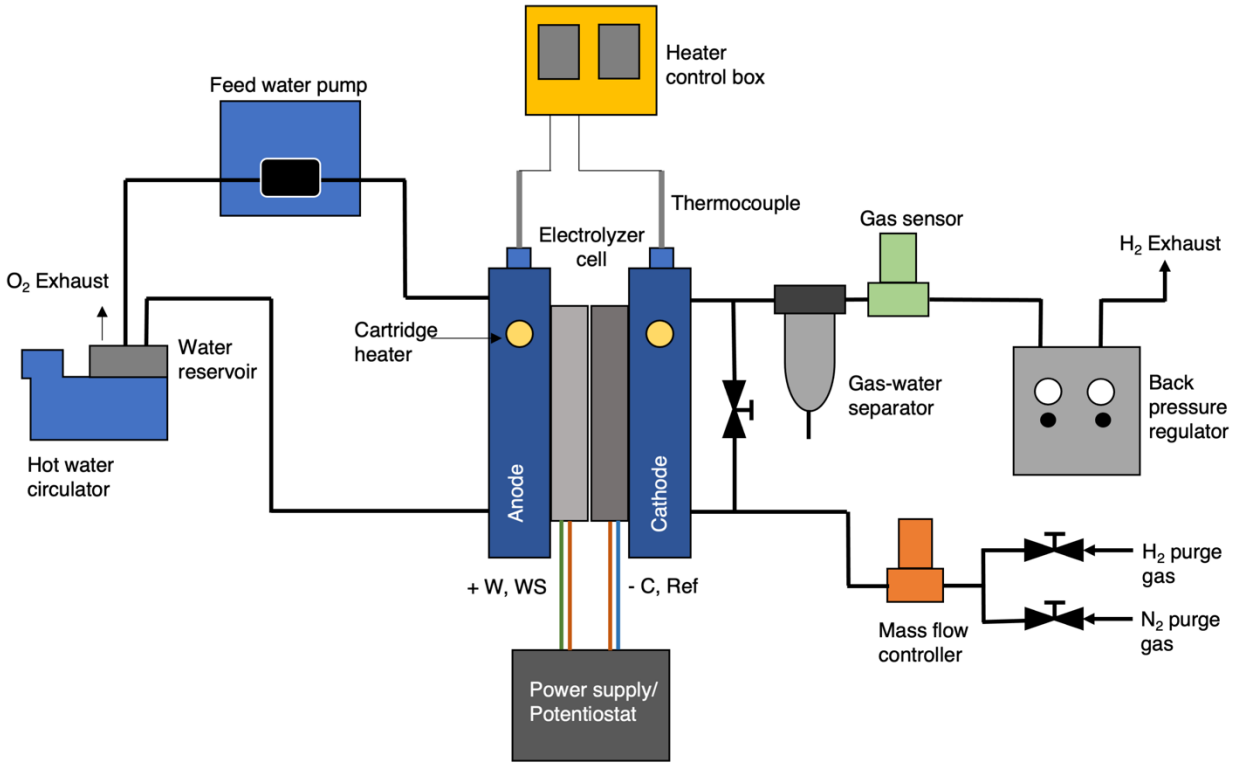

Figure 1-8 Schematic of electrolyzer test station

The cell temperature was maintained at 60-80 C by cartridge heaters and k-type thermocouples were used as temperature sensors. A two-channel heater control box was built with PID controllers to maintain the cell temperature as well as feed water temperature. The feedwater was heated in a glass beaker immersed in hot water bath. The surrounding water bath was heated with an immersion coil heater. A peristaltic pump was used to supply water to the cell and a recirculation loop allowed excess water to be reused and oxygen was exhausted into the atmosphere from the beaker.

On the cathode side, a gas water separator was used to dry the outgoing gas if differential pressure operation was required with a backpressure device. A mass flow controller was used to purge

hydrogen or nitrogen on the cathode during cyclic voltammetry experiments. Finally, a Potentiostat (Gamry 5000) or a power supply (Kiethley B-30-108, 1080W) was used to apply potential to the cell depending on the active area. Low active area (up to 2 cm^2) were operated with Gamry 5000 since EIS at high current density could be performed from the Potentiostat. The power supply was used for higher active areas as it can supply much more current than Gamry 5000 (5A max current) up to 108 A. Most recently, we have used the Gamry LPI1010 system along with the power supply that allows impedance analysis with the Potentiostat when the base current is supplied with the power supply.

1.4.2 Imaging techniques for electrolyzers

Many in-situ and operando techniques have been used to image PEMWEs, but the quality and utility of information produced is dependent on their spatial resolution and the FOVs. Spatial resolution describes how well small details can be imaged or small features can be located with respect to a point. It can be quantified in several ways, for example one way quantification is in terms of the smallest separation at which two points can be perceived as discrete entities [43]. Spatial resolution in the context of TXM depends upon not only the pixel spacing of the detector employed but also the ability to collimate the source, since source divergence leads to image blur [44]. Hence, as a general rule, the FOV is reduced when spatial resolution is increased to ensure each pixel, or volumetric pixel (voxel), is measured with a greater level of statistical significance. **Figure 1-9** plots the spatial resolution of various imaging techniques against their respective FOVs. The most powerful transmission electron microscopes (TEMs) have a spatial resolution of 0.5 Angstrom at an electron beam energy of >1 MeV [45]. The field of view of TEMs lies between 20 nm – 1 μm and measurement is limited to *in-situ* studies and does not allow observation

of water formation in fuel cell catalyst layers in *operando*. FIB-SEMs has a slightly higher FOV between 5 µm-50 µm providing a spatial resolution of 5 nm–30 nm [46]. However, FIB-SEM is a destructive imaging technique hence, it is not possible to do anything beyond *ex-situ* with this technique. Nano x-ray CT allows for 3D imaging with a voxel resolution of 10 nm- 50 nm and a FOV of 20 µm to 1 mm with acceptable x-ray attenuation losses [47]. Micro x-ray CT offers a spatial resolution of 1 µm– 50 µm for synchrotron sources with a field of view of 0.1 cm– 2 cm. This allows for visualization of water distributions in GDLs, which will be discussed in the further sections. High resolution neutron imaging has previously been used to investigate water management in fuel cells and quantify oxygen transport in electrolyzer anodes [48]–[50]. This technique measures neutron attenuation to generate images. For instruments with neutron imaging capabilities, detector systems are available with FOVs ranging from 5 mm– 400 mm with corresponding spatial resolutions ranging from 5 µm- 200 µm.

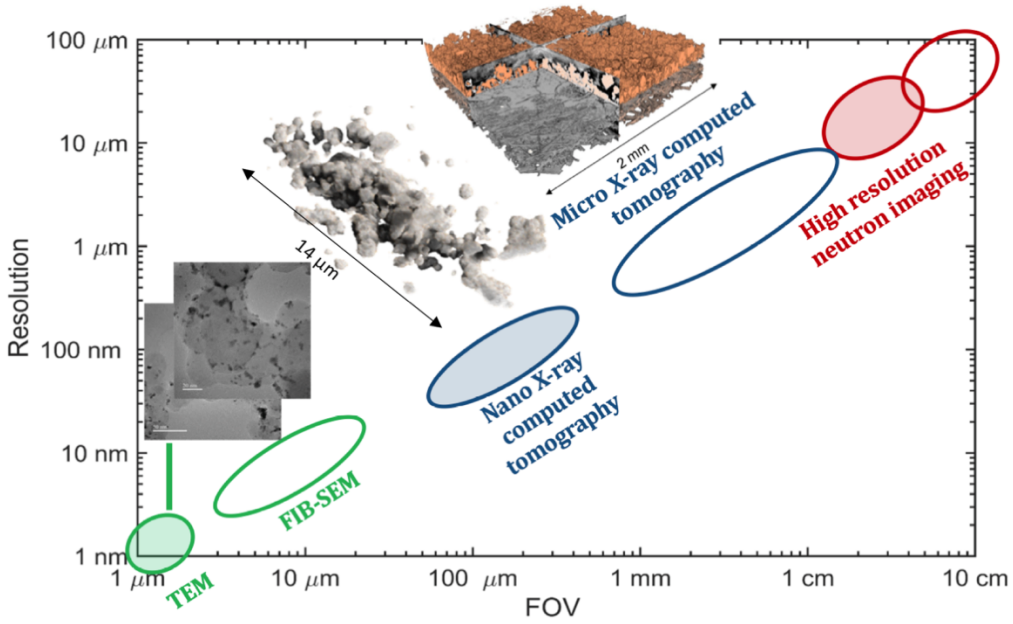

Figure 1-9 Resolution as a function of FOV for different techniques relevant for imaging electrochemical devices. (1) TEM resolution limits: 0.5 Å–1 nm, FOV: 20 nm–1 µm. (2) FIB SEM

resolution limits: 5 nm–30 nm, FOV: 5 µm–50 µm. (3) Nano x-ray CT resolution limits: 10 nm–50 nm, FOV: 20 µm–1 mm. (4) Micro x-ray CT resolution limits: 1 µm−50 µm, FOV: 0.1 cm–2 cm. (5) Neutron imaging resolution limits: 5 µm–200 µm, FOV: 5 mm–400 mm. Adapted from D. Kulkarni et.al [3]

1.4.2 X-ray computed tomography

Synchrotron X-ray computed tomography is a powerful nondestructive technique to obtain 3-D images of microscopic phenomenon with high resolution. Synchrotrons are powerful sources of X-ray radiation and the radiation flux achieved at synchrotrons is orders of magnitude higher than lab scale X-ray sources. This reduces scan time from hours for lab scale CT to minutes on the beamline. Hence, synchrotron techniques can be used to acquire large datasets for experiments in a short amount of time.

A basic schematic of synchrotron X-ray CT is shown in **Figure *1-10*** a. The synchrotron consists of a storage ring where packets of electrons are spun around a ring of ~1 km in diameter under ultra-high vacuum in a superconducting magnetic field. The beam current is maintained typically at 200-500 mA and the kinetic energy of electrons in the storage ring varies across different facilities, but state of the art synchrotron sources have electron energies of ~2 GeV. Beamlines are tangential sections to the storage ring where a packet of electrons is diverted into an insertion device which can either be an undulator or a wiggler. Both insertion devices work on the same principle of Lorentzian oscillation of electrons in an alternating magnetic field. Both wigglers and undulators have a series of electromagnets or permanent magnets placed in an alternating fashion. When electrons pass through a series of alternating magnetic fields, they oscillate due to Lorentz force and result in formation of highly brilliant and coherent X-ray radiation.

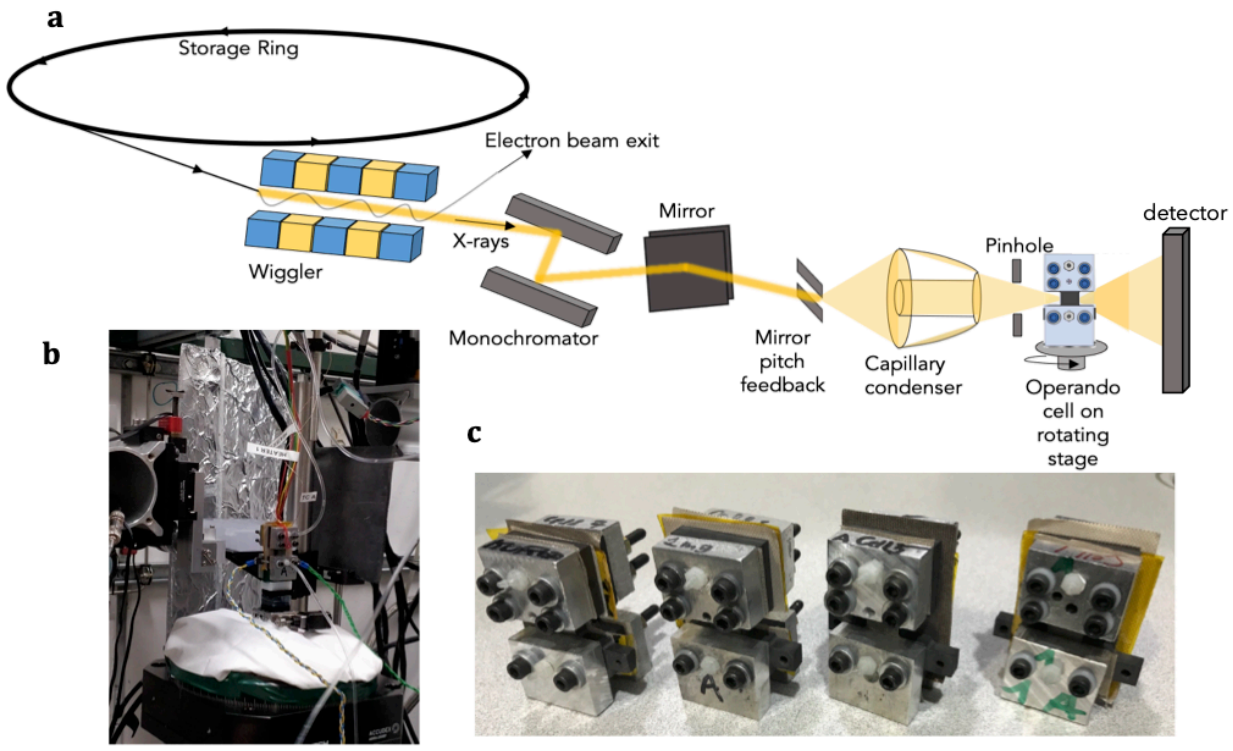

Figure 1-10 Operando PEM electrolyzer cell imaging setup (a) schematic indicating the placement of the cell on the Micro-CT beamline showing all operational components (b) actual image of cell on the beamline (c) preconditioned cells ready to be mounted on the beamline stage

The distance between the permanent magnets or current in the electromagnets can be changed to change the energy spectrum of the produced X-rays. The produced X-rays are then passed typically through a double crystal monochromator that uses Si (111) crystals to select the beam energy. The X-rays further pass through optics that are used to focus them on the sample placed on a rotating stage. X-ray images can be taken in two modes depending on the distance of the detector to the sample. When the detector is placed close to the sample, imaging is done in absorption contrast mode where the transmitted X-ray intensity is proportional to the attenuation coefficient of the material as described by the Beer-Lambert law:

$$I / I_0 = exp(-\mu l) \tag{1}$$

where I_0 and I are the incident and resultant intensity of the x-rays, μ is the attenuation coefficient, and l the thickness of the medium. In absorption contrast imaging, the intensity of the light is lowered by some of the photons being absorbed by material. X-ray attenuation is a degree of sum of all interaction between photons and matter, including scattering and absorption by a material. Phase contrast imaging relies on the shift of the x-ray wave that travels through the sample, with respect to the wave that is not perturbed by the sample. A detailed derivation of intensity of the light incident onto a detector in absorption and phase modes may be found in our previous work [51]. The attenuation coefficient is dependent on the photon energy of the incident x-rays. Once the X-rays are incident, the sample rotates 180^0 on the stage. At each angle, multiple projections are recorded, and a raw image data set called sinogram is formed. This sinogram is reconstructed into 3D image stacks using reconstruction algorithms like TomoPy. X-ray CT is a critical technique for this thesis since most of results are obtained by operando experiments done at 8+ beamtimes.

1.5 Scope of this dissertation

This dissertation discusses micro scale interfaces in PEM electrolyzers and their effect on cell performance studied primarily with X-ray computed tomography. The dissertation is divided into 7 additional chapters. The results of these sections are used as design guidelines to engineer better and more durable interfaces while reducing catalyst loadings. The second chapter is dedicated to the design of operando cells for X-ray CT analysis and discusses in depth the design process form material selection to cell geometry development. Using the optimized cell, the second chapter concludes with preliminary results of water formation and removal through gas diffusion layers in PEM fuel cells. The third chapter discusses development of experimental techniques and

formulation of interfacial analysis method to analyze nature of interfaces. The fourth chapter utilizes the interfacial analysis formulation and discusses nature of interfaces formed using two commercially available porous transport layers (PTLs) and two electrode configurations with varying catalyst loadings. The interfacial properties of 12 different cell combinations and their effect on various overpotentials are studied and the factors affecting catalyst utilization are identified. The fifth chapter discusses the effect of interfaces on gas transport in PTLs and its link to durability and mass transport overpotentials. A Lattice Boltzmann CFD model is formulated, and its results are validated by X-ray CT studies. The sixth chapter introduces MPLs and elucidates its effect on Triple Phase Contact Area and gas transport. For the first time, gas transport pathways through PTLs with MPLs have been shown and flow regimes have been experimentally demonstrated using X-ray CT. Chapter seven discusses catalyst durability and ways to engineer durable interfaces. A thorough background of OER pathways on Ir based catalysts is discussed and an AST protocol is developed to probe evolution of interfaces and catalyst degradation. With these results, Ir degradation mechanisms are identified. Additionally, the use of MPLs is demonstrated for PEMWE durability and optimal MPL design parameters are suggested based on the results. Finally, chapter 8 reviews the conclusions of this work and suggests recommendations for future work.

2. Operando cell design and development for X-ray CT

2.1 Overview and need to design Operando hardware

Recent developments in transmission x-ray microscopy (TXM) techniques such as x-ray radiography and computed tomography (CT) have enabled the acquisition of high-resolution images at both the micro and nano scales with relatively short scan times [52]–[55]. These advances in TXM, have enabled imaging of processes within electrochemical energy devices such as batteries, fuel cells and electrolyzers. Recently, *operando* studies have shown new insights into morphological changes of the various components of electrochemical devices[56]–[59]. However, these studies generally require custom test apparatuses, which have to be adapted for a use at each specific beamline, limiting broader applicability. Fuel cells, electrochemical energy conversion devices that use hydrogen as a fuel at the anode and oxygen at the cathode to produce electricity, with water as the by-product, require effective water management to have high power densities and reliability. For polymer electrolyte membrane (PEM) fuel cells, water is a by-product on the

cathode side, where the oxygen reduction reaction (ORR) takes place, as shown by Figure A1 of the Appendix A. For alkaline exchange membrane (AEM) fuel cells, water management is even a larger issue, as water is formed on the anode side and is a reactant in the ORR on the cathode side[60]. The key focus of study revolves around the stack of membrane, the catalyst layers and often the gas diffusion layers (GDLs) typically termed the membrane electrode assembly (MEA). Water is needed to hydrate the membrane, as ion conductivity depends on water content in the membrane, however, too much water can be detrimental to fuel cell performance, as it can flood the catalyst layers and block oxygen flow, effectively lowering electrochemically accessible surface area in the MEA. It is critical to understand water distribution during fuel cell operation and to observe its formation in the catalyst layer, so future MEA designs can be optimized to reduce the power density impact of unwanted flooding. While in previous work MEA components morphology was extracted with *ex-situ* and *in-situ* imaging and used as input to drive computational simulations to predict water distribution [61], *operando* studies are needed to further validate and parametrize models [62]. Current state of the art *operando* x-ray techniques are capable of visualizing water at the microscale, however microscale resolution is not sufficient to resolve the porous structure of the catalyst layer and the water contained therein. This paper presents a first of its kind *operando* fuel cell that is capable of nanoscale resolution, thus enabling the visualization of water in the porous catalyst layer.

Significant effort was dedicated to micro x-ray CT and radiography cell hardware development for visualizing water transport in PEM fuel cells. Manke et al. pioneered some of the first fuel cell for x-ray study by drilling an 8 mm hole into the metallic plate of a conventional fuel cell and imaging through it using x-ray radiography [63]. This apparatus offered a significant improvement in resolution over neutron imaging (1.5 μm vs 75 μm), however the field of view

(FOV) was limited to sub 10 mm x 10 mm and in radiography no three-dimensional information can be obtained. Schneider et al. built upon these results and developed the first *operando* cell compatible with x-ray CT [64]. Eller et al. improved on Schneider's design by changing the orientation of the flow channels to be perpendicular with the incident x-rays. This also lengthened the flow channels so that the flow of gasses would be fully developed once the flow reached the imaging FOV. Eller et al. reported that their cell could reach a current density of 1 A/cm^2 and maximum active area of 30 mm^2. Initially this cell design relied on rubber O-rings for cell compression, limiting control of cell compression important factor in fuel cell performance. Although no additional details are provided, the images in Eller et al.'s more recent work show metal bolts were added to improve the mechanical compression [65].

That said, the curved design of Eller et al.'s cell makes it difficult to machine, and thus inhibits rapid testing of the effects varying flow-channel geometry has on cell performance. White et al. developed an *operando* cell for a lab-scale x-ray CT machine, leveraging a 3D printed holder which allowed for rapid prototyping [66]. The downside of this approach is that the material that the cell was made from is not electrically conductive. While a copper current collector was added to one end of the cell, they were only able to achieve a current density of 0.1 A/cm^2 due to Ohmic limitations. It should be noted that the reported current densities of Eller et al. and White et al. were recorded using different catalyst layer materials and under different conditions. Nevertheless, the order of magnitude difference in current density underscores the effect of cell architecture on electrochemical performance. The cell designs discussed thus far were for micro x-ray CT or radiography experiments and designed to fit into a FOV of 3-5 mm in width and varied heights.

2.2 Experimental and hardware design

2.2.1 Design and material constraints

The most important quality of the operando cell is that it must be sufficiently x-ray transparent. Figure 2-1a shows the x-ray transmission (I/I_0), as a function of energy for various materials that were considered for the cell construction across typical micro x-ray CT range (20 keV – 30 keV) and nano x-ray CT energy range (4 keV- 23 keV). In addition, these materials must be electrically conductive or have a layer of electric conductor (such as gold plating). The higher the transmission, the lower the signal-to-noise ratio that we will observe in the resulting images. At least 30 % of x-ray transmission is required in single radiograph to achieve reconstructed tomography data with minimal artefacts, using current state-of-art detectors installed at the synchrotron facilities in the U.S. For low transmission samples unwanted artefacts, such as rings on the images will appear. For example, in Figure 2a we observe that ½'' graphite plate (which most of the operando cells for fuel cell imaging use) is above the 30% threshold for all energies above 20 keV. On the other hand, gold-sputtered polyether ether ketone (PEEK), another possible material for operando cells, only becomes a viable option at energies above 25 keV.

Nano x-ray CT synchrotron beamlines operate at lower energy ranges, as nano x-ray imaging requires the beam to be focused onto the sample. This is typically done with a Fresnel zone plate[67], which is a diffractive optical element (Figure 4a). From Figure 2b it is evident that 15 μm Kapton film is x-ray transparent, ¼" graphite plate can be used only at energies above 15 keV, and ¼" PEEK plate can only be used at energies close to 20 keV. Another option is to use graphite on the cathode side of the cell and Kapton on the anode. This half-graphite half-Kapton cell uses a total thickness of 1/8" of graphite and represents a compromise between the transparency of Kapton and the electrochemical advantages of graphite. The nano CT beamlines

that these experiments were performed at operate at energies of 8 keV, 15 keV or 17.5 keV. From this analysis, we can conclude that nano x-ray CT cell material selection is limited to Kapton film for 8 keV energy, however at the higher energies, graphite and PEEK become feasible provided that their thickness is minimized.

Accurately controlling the temperature of the cell is critical to its performance, as water transport is dependent on both the temperature of the cell and the local temperature gradients within the cell. Weber et al. noted that water which is evaporated in the cathode catalyst layer tends to move down the temperature gradient and condense in areas of lower temperature [68]. This temperature gradient exists through the thickness of the cell (thru-plane). The in-plane temperature gradient should be minimized, as a large variation in temperature along the length or width of the cell could result in uneven current density and water pooling in the cooler areas. This can be avoided by minimizing the spreading resistance of the bipolar plate material. Thermal spreading resistance describes the resistance of heat transfer from a small source (in this case, the cartridge heater) to a larger area (in this case, the graphite plate). Conductive thermal resistance in direction i is given by

$$R_i = \frac{l_i}{k_i A_i} \tag{2}$$

where R is the thermal resistance, l is the length along which the heat is travelling, k is the thermal conductivity and A is the cross-sectional area. If the thermal conductivity is isotropic, the thermal resistance in the two in-plane directions will be higher than that of the through plane, due to the longer length scales and smaller cross-sectional areas. The plate would therefore be defined as having a high spreading resistance, resulting in an uneven temperature distribution along the length of the channel. On the other hand, if the in-plane thermal conductivity is much higher than the

thru-plane thermal conductivity, as is the case for graphite, the thermal resistances in the three coordinate directions will be much closer to equal, allowing the heat to spread evenly in all directions. More detailed material selection for the micro x-ray CT cell design are summarized in Appendix A. We consider the same set of materials shown in **Figure *2-1***a: two ¼" PEEK plates with 300 nm gold sputtering, two 1/4'' graphite plates, as well as two ¼'' aluminum plates. The physical properties that we consider relevant are x-ray transmission, electrical resistance, thermal conductivity, maximum displacement, durability and machinability. These metrics are provided for all three materials under consideration.

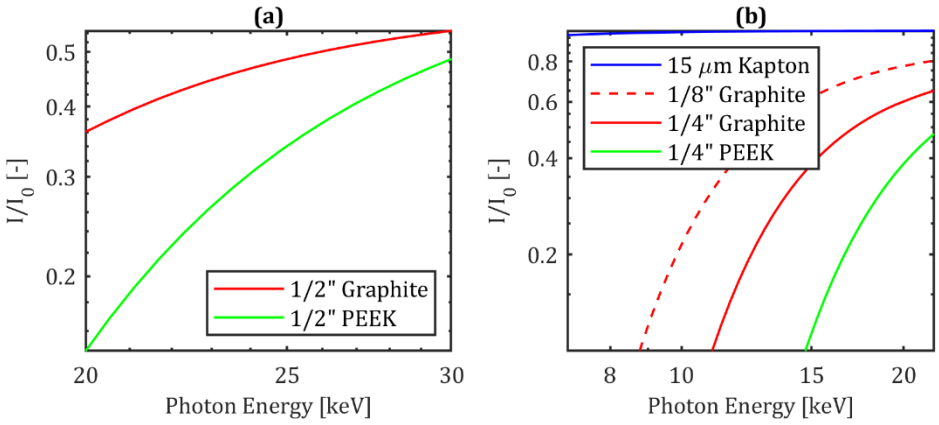

Figure 2-1. X-ray transmission for various materials across a) micro and b) nano x-ray CT beamlines energy ranges. The material thicknesses specified represent the total thickness of material on both sides of the cell (i.e. 1/4" (6.35mm) Graphite refers to two 1/8" (3.18mm) plates, one at the anode and one at the cathode). The 1/8" graphite represents the thickness of the half-graphite half-Kapton cell which features a graphite plate on the cathode and Kapton film on the anode

2.2.2 Cell geometry development

Figure 2-2 shows the generational development of the micro x-ray CT cell. All of the cells featured two gas channels. The generation (Gen) 1 cell was designed based on Eller et al.'s cell and the main cylindrical components of this cell were 3D printed by resin stereolithography for rapid prototyping. However, this cell lacked adequate compression, thermal stability, electrical conductivity and was only able to reach a steady-state current density of 0.1A/cm^2. The Gen 2 cell was made by sputtering 300 nm gold on a machined ¼'' PEEK flow field and using aluminum bolts for compression. While this improved the overall performance of the cell, it had some shortcomings. Sputtered gold has low electrical in-plane conductivity due to inter-grain or grain boundary contact resistances and moreover, poor external electrical connections further increased Ohmic resistance. Increased resistance in turn results in higher joule heating:

$$W = i^2 R \tag{3}$$

where W is the heat produced in Watts, i is current flowing through the cell, and R is resistance. Furthermore, as the cell was used repeatedly, the sputtered gold flaked off in places. This resulted in an uneven electrical resistance and caused localized temperature gradients with hot spots in areas of higher resistance. If the temperature gradient along the length of the gold sputtered plate is uneven, pockets of condensed water may form in the areas of lower temperature. The next generations of cells addressed this thermal gradient issue by using fuel cell grade graphite (properties shown in **Table A2**, Appendix A) for the bipolar plates with variations in the flow field design and compression techniques. The Gen 3 cell had a long area with a serpentine channel that could be used for imaging and was compressed with an external compression fixture, which introduced a pressure gradient and was not repeatable. To solve this issue, Gen 4 and 5 cells were

made with integrated Al compression plates, which provided even compression, heat distribution, and a capacity to hold a cartridge heater close to the active area.

The final design sought to combine the most advantageous properties of graphite and aluminum by adhering graphite plates to an aluminum backing along the entire length of the cell except for a region that is left open to allow x-rays to pass through as shown in Figure 3 (Gen 3-5). The length of the x-ray window varies between 0.5 cm – 1 cm. A smaller length provides higher compression of the MEA, but limits FOV. The active area of the cell can be as large as 1 cm^2. This design allows the aluminum plates to provide all the mechanical stiffness without cracking. The temperature fluctuations are modeled to be within 1 degree along the 3 cm of graphite modeled that include the flow channel (**Figure A2**). Typically, Teflon gaskets are used as a hard-mechanical stop to control compression of the porous materials within the fuel cell. The thickness of the gaskets is chosen in such a way that the overall porous media components within the fuel cell are compressed by 15 %– 20 %. The local pressure distribution was measured using a Fuji Prescale Low Film that registers a range of 2.5 MPa- 10 MPa and while the x-ray window was only compressed by 3 MPa of clamping pressure, the rest of the cell area measured 10 MPa of clamping pressure. An image of the compression pattern is shown in **Figure A3**. The design of Gen 5 cell also allows it to be assembled and disassembled quickly, an especially advantageous feature when the cell is used at synchrotron facilities where beamtime is limited. The use of acetal alignment pins ensures that the components are roughly aligned during reassembly.

The Gen 4 and 5 cells can also be used as either fuel cells or electrolyzers. The cells shown in Figure 3 have parallel channels, however they can be easily swapped for serpentine channel plates to understand water transport near the serpentine bends. An example of different flow

channel geometries that can be employed in this setup can be found in the Appendix A, **Figure A4**.

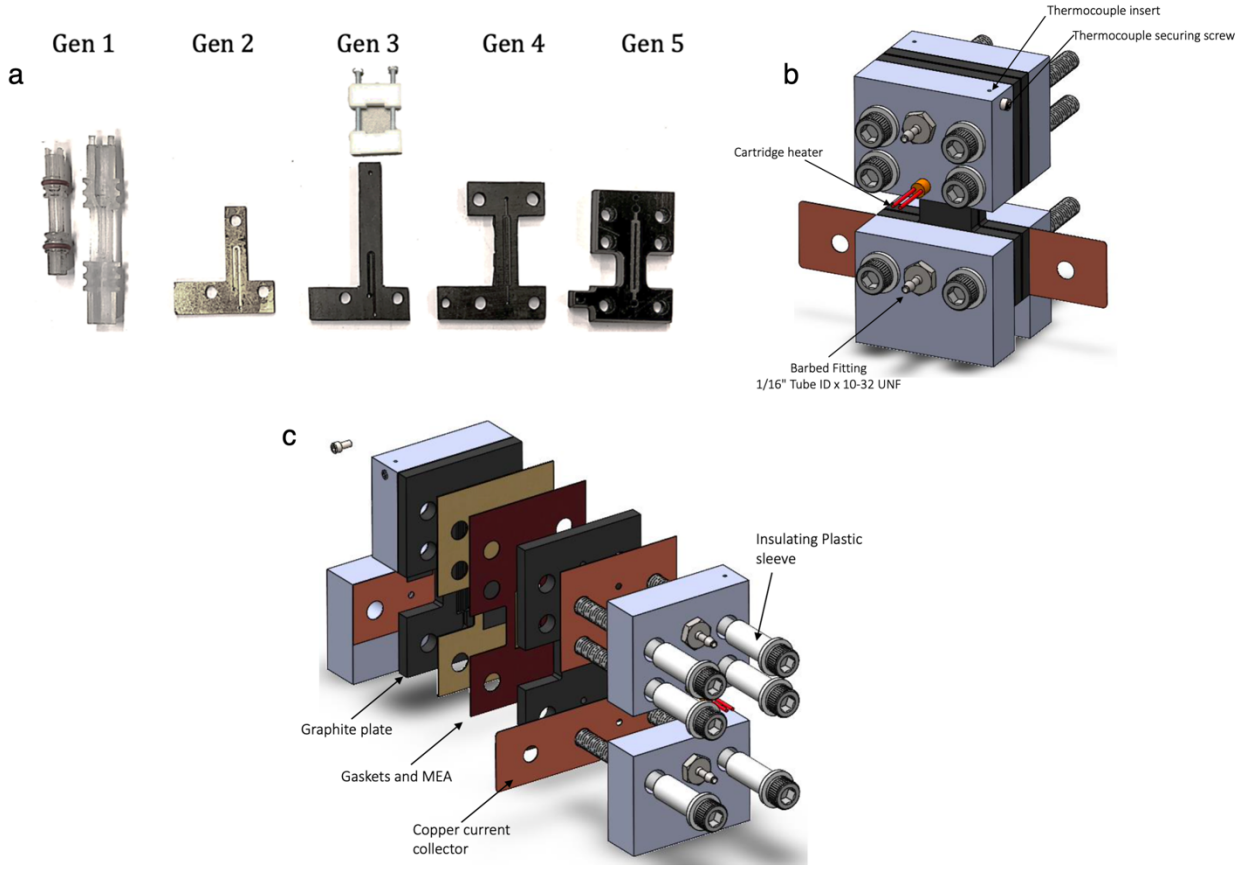

Figure 2-2. Micro x-ray CT operando Cell a) generational development of the cells. B) A photograph of the assembled cell, c) Exploded view of the Gen 5 cell showing all the components.

The mechanical compression of the cell coupled with the high electrical conductivity of the graphite led to measured electrical resistance of just 0.1 Ω when assembled without any MEA or gaskets. In order to reduce the resistance of the junction between the graphite plate and the copper wire used to connect the plate to the potentiostat, the contact region of the plate is electroplated with copper. The copper wire can then be soldered directly to the copper contact pad, creating a low-resistance bond. Graphite is an excellent heat conductor due to its very high in-plane

(275 W/mK) and high thru-plane thermal conductivity (5.0 W/mK), as shown in Table S1.

Using graphite as the gas flow-field and a hole in the aluminum plate to hold a cartridge heater enabled closed loop heating control of the cell, using a single 0.75 W cartridge heater on each side of the cell. We created a thermal model of the cell and found that the temperature varied by only 1.1 °C along the length of the channel, as shown by **Figure A2**. The complete thermal analysis is provided in the Appendix A. **Figure A5** shows the heater response to a step temperature change. The cell's electrochemical performance for fuel cells and electrolyzers reached 500 mA/cm^2 for Pt-group metal free (PGM-free) catalyst layers [69]. Comparing Gen 4 and Gen 5 micro CT cell polarization curves, as shown in **Figure A6**, they both show very similar performance. However, Gen 5 has shorter channel design, and is more mechanically robust with better thermal management and thus it is recommended to use Gen 5 cell.

2.2.3 Image analysis

Figure 2-3 shows micro x-ray CT cross-section tomographs of the Gen 2, 4 and 5 operando fuel cells fully assembled all imaged with resolution of 1.3 μm using 5x lenses. The details of the materials used for fabrication these cells are provided in Appendix A. PGM-based Pt/C or Pd/C MEAs are used in these cells. The catalyst layers are bright in all three cross-sections and are clearly visible. The membrane used in the Gen 2 cell was twice as thick as those used in the Gen 4 and Gen 5 cells. The microporous layer (MPL) next to the catalyst layer is seen in Gen 2 and 4, but was not used in Gen 5, as it was an AEM fuel cell. The GDL fiber cross-sections are seen in all three tomographs. In the case of the Gen 2 cell, the highly absorbing gold sputtering on the PEEK frame distorts the contrast on the nearby catalyst coated membrane (CCM) and GDL. Median filter of radius 2 was used to smooth the greyscale image shown for Gen 2 cell, while the

Gen 4 and Gen 5 images were not filtered. The Gen 4 and Gen 5 cell images have an even contrast throughout the cross section and the graphite bipolar plates are clearly visible. Although there is little visible difference between the Gen 4 and Gen 5 cross sections, the Gen 5 cell has better compression and heat distribution. The Gen 3 cell results have been previously published in Normile et al [69]. The Gen 5 with AEM have been published by Peng et al [70]

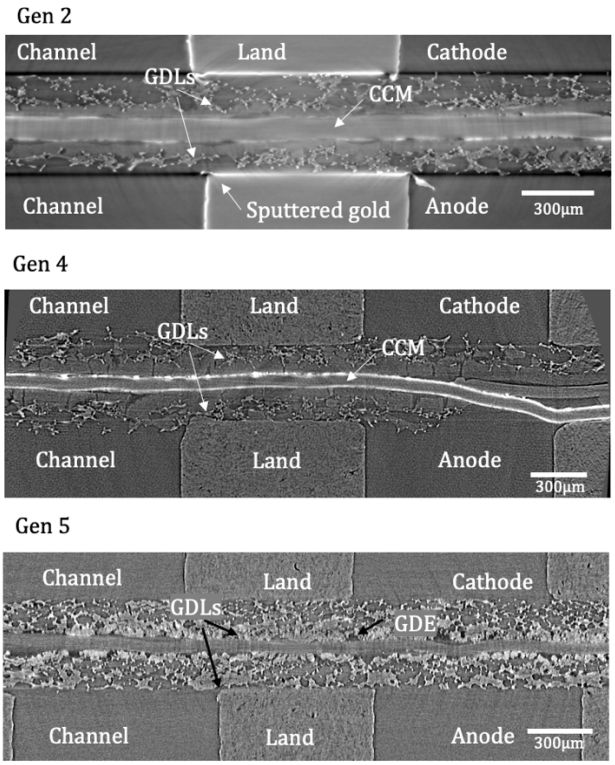

Figure 2-3. Micro CT operando x-ray CT images of a fuel cell a) Gen 2 cell cross section b) Gen 4 cell cross section c) Gen 5 cell cross section. 1.3 μm resolution. Gen 2 data collected at 2-BM APS, Gen 4 and 5 collected at 8.3.2 at ALS.

Since water attenuates x-rays weakly, studies that aim to show water content in carbon materials should theoretically be imaged in a phase contrast mode. **Figure A9** shows that the linear attenuation coefficients of water and carbon are similar across a wide energy range. That said,

phase contrast can introduce artefacts from the sample holder, so the images were therefore taken in absorption contrast mode. Image subtraction with a dry, non-active CT data set is used to visualize water location. This method of water separation was first developed by Eller et al. As shown by **Figure 2-4**a, the first scan is taken with the cell at open circuit voltage (OCV) conditions, which will not produce any water. Since the gases are humidified to 100 % RH before flowing into the cell, they will cause the MEA to swell. This is necessary for the base subtraction data set so that it will be possible to align the dry and wet images. The second scan is taken with the cell running at a specified current density. The reason the cell is maintained at constant current, and not constant voltage, is that the amount of water produced is proportional to the current density by Faraday's law of electrolysis:

$$N_{H_2O} = \frac{A}{2F}\int idt$$

where N_{H2O} represents the number of moles of water produced, A is the active area of the cell, F is Faraday's constant, and i is the current density. After 2-3 minutes, the cell reaches steady-state, where the rate of water production and removal will be equal. It is at this time when the scan is taken to identify the steady-state water content in the GDLs, channels and ideally, in the catalyst layer. The polarization curves for this cell have been previously published in Normile et al. and are reproduced in Appendix A, **Figure A10**. **Figure 2-4** shows a cross-section tomograph for the cell operating at a low 40 mA/cm^2 current density, where water can be observed. The reason for water observed at this low current density is that the cell temperature was 30^{o}C and inlet gas was fully humidified and thus water was formed as liquid, as phase-change-induced flow and evaporation is minimal at this low temperature. Cell operation was stable at this current density for close to 2 hours (Figure A10). Constant current holds are often repeated for several different current densities in order to establish a trend in water content. The dry image is then subtracted

from the wet image in order to threshold the water. This process can be done in absorption contrast mode, as the minute changes in attenuation from the water will be visible once the images are subtracted. The result of this subtraction is shown in **Figure 2-4**c. Notice that dry and wet scans cannot be aligned perfectly, for example due to membrane and ionomer swelling. Thus, some noise and error is expected in thresholded image, as can be seen in **Figure 2-4c**, where smaller specs of single voxel are most likely noise. The thresholded water domain is then overlaid with the grey-scale image with water and is shown by **Figure 2-4**d. Through the 8-bit greyscale histogram we observe the region that corresponds to water, as shown by Figure 6e. This region also overlaps with some of the carbon material. Finally, **Figure 2-4**f shows the grey-scale values distribution along the dashed line drawn in **Figure 2-4**a and b. In future work, machine learning algorithms will make it possible to automatically segment water without need for a background dry scan.

Figure A11 shows the cross-section tomographs for a conventional Pt/C catalyst fuel cell with the Gen 5 hardware. Water was observed both within the cracks of the MPL and the flow channel. For this data set the OCV scan was of marginal quality, and therefore proper thresholding was not possible. As can be seen, the image quality and grey scale of water is very similar to that reported by **Figure 2-4**. From these micro x-ray CT images, it is also evident that for conventional Pt/C catalyst layer less than 10 μm thick, it is not possible to see water within the catalyst layer due to the solution limitations of micro x-ray CT of about 1 μm.

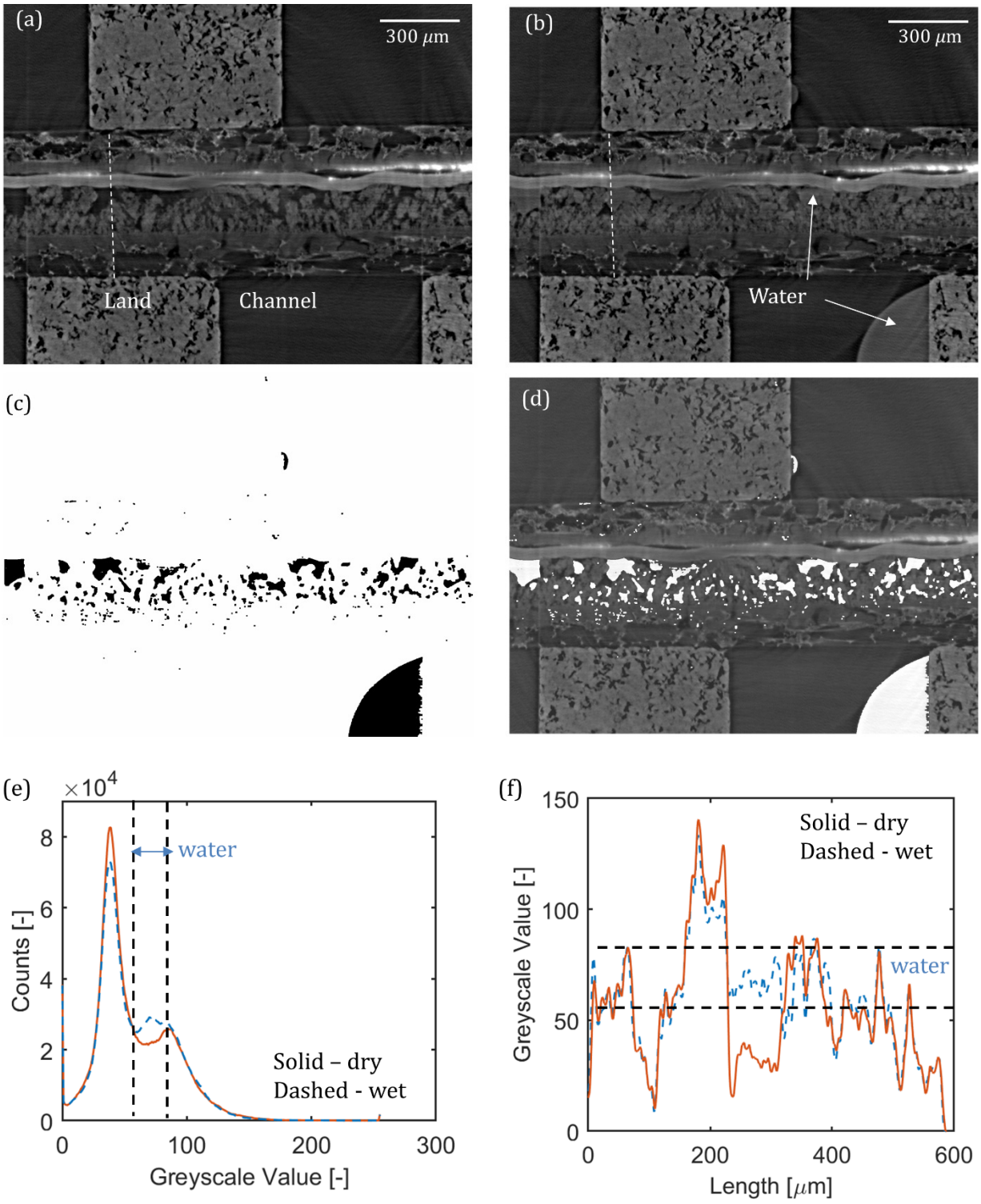

Figure 2-4. Cross-section tomographs of the assembled fuel cell having a PGM-free cathode at 30°C under a) OCV (dry), b) with a current density of 40 $mAcm^{-2}$ drawn from the cell (wet), c) thresholded water clusters and d) overlay of thresholded water and image from plot b. e) A

histogram of greyscale dry and wet images, with the region belonging to water, f) the greyscale values along the dashed line shown in a and b, where the window for greyscale values for water is shown too. Gen 3 cell. 1.3 µm resolution. Data is collected at 8.3.2 beamline at ALS.

2.3 Conclusions and summary

In this work, we presented the roadmap for the *operando* cells designed in our group for imaging water in fuel cells with x-ray CT and x-ray radiography. The *operando* cells presented here enable the visualization of water in fuel cells at micro scales as well as oxygen in electrolyzer mode. The micro x-ray CT fuel cell/electrolyzer underwent five generations of design iterations to optimize electrical conductivity, mechanical stability, thermal management and compression. This cell has been used to image fuel cells and electrolyzers with various catalyst layers with the aim to visualize water/oxygen. Water segmentation for operando fuel cells was achieved by subtracting an OCV background scan from the data measured at constant current density to reduce number of image phases from three (water, carbon and pore) to just two (water and pore/carbon). Further, the development of a novel *operando* nano CT fuel cell is detailed in further sections of reference [3] including lessons learned and the challenges in x-ray imaging on this scale. The main challenge of beam damage is difficult to overcome due to the low energy < 10 keV that many of the beamlines use. We showed that this can be overcome by using beamlines that rely on Kirkpatrick-Baez (KB) mirrors (at ESRF) instead of Fresnel zone plates (APS, NSLS II) for beam focusing, as KB x-ray optics can enable imaging at nanoscale at higher energies (such as 17.5 keV at ESRF). Despite the challenges, the nano- x-ray CT sample holder design enables multiscale 3D imaging.

3.Analyzing nature of interfaces

3.1 Overview

Currently, there are limited number of studies dedicated to understanding the complex two-phase transport phenomenon through the anodic PTL and its effect on the performance [71]–[73]. While it has been well established that the understanding and improving interfaces is the key to improving PEMWE performance, the underlying processes that limit and affect catalyst utilization are still ambiguous. Several studies use neutron imaging to study the oxygen flow in the channels [48], [50], [74] but are limited by spatial resolution. Leonard et al [39] used x-ray computed tomography (XCT) to investigate the morphology of two types of commercially used PTLs, sintered titanium and fiber titanium and analyzed their effect on oxygen transport in the channels. Fiber PTLs were found to have a higher porosity, larger pore sizes, and lower tortuosities than sintered PTLs which translated into slightly lower overpotentials at 1 A cm^{-2}. Furthermore, they studied two type of electrodes: catalyst coated membrane (CCM) and porous transport electrode (PTE) or gas diffusion electrode (GDE). Their modeling study predicted ionic conductivity limitations for GDEs which

may cause the observed performance loss. To further understand the behaviour of oxygen transport, Satjaritanun et.al [2] found evidence of oxygen taking preferential pathways through the PTL at current densities up to 4 A cm-2. However, most of the studies directed towards understanding interfaces and gas transport consider a constant anodic catalyst loading.

In the preliminary results of this work, detailed investigation of the of the effect of loadings on the performance of PEMWEs with two different electrode configurations: catalyst coated membrane (CCM) and gas diffusion electrodes (GDE) using commercial IrOx electrocatalyst are presented. X-ray computed tomography was used to quantify the interfaces and observe oxygen transport in the channels. Additionally, using electrochemical characterization, the question of how we can improve interfaces in existing devices and how PTL morphologies can be tuned to with respect to loadings in order to utilize maximum gas transport pathways is addressed. This chapter discusses the experimental and image processing techniques for characterizing interfaces.

3.2 Experimental design

To understand the effect of various PTLs and electrode combinations on interfaces, building the correct sample set is important. Electrolyzer configurations with varying loadings were prepared for x-ray imaging, as well as electrochemical characterization. **Table 3-1** lists the cell names and the type of PTL used, electrode configurations (CCM or GDE) and their respective catalyst loadings. Based on the loadings, the cells are segregated into three categories: i) high loadings of 1.75 mg cm^{-2} – 2.20 mg cm^{-2}, ii) medium loadings of 1 mg cm^{-2} – 1.26 mg cm^{-2}, iii) low loadings of 0.5 mg cm^{-2} – 0.65 mg cm^{-2}. Sintered and fiber Ti PTLs were provided by NEL (Wallingford, CT). For CCM configuration the PTLs were not coated by the catalyst, whereas for the GDE configuration the PTLs were coated by iridium based (IrOx) ink in a proprietary procedure by NEL

with the loading indicated in the table. For both anode and cathode inks Nafion ionomer solution (1100 EW, 5 wt% ionomer; D521 from Ion Power, USA) was used. The CCMs were fabricated with a single pass screen printing technique to deposit the catalyst ink directly on the membrane surface and the GDEs were coated using an ultrasonic spray coater. GDEs used an I:C weight ratio of 1.0 and CCMs used a weight ratio of 0.5. For all the GDE configurations, Toray TGP-H-120 carbon paper was used on the cathode side. Toray paper was coated by catalyst loading of 2 mg cm^{-2} of ink containing Pt/C. Nafion 117 from Fuel Cell Store (College Station, TX) was used in all the experiments as a membrane.

Table 3-1 Electrolyzer configurations for x-ray CT and electrochemical characterization

Sample #	Cell name	Fiber PTL	Sintered PTL	CCM	GDE	Loading (mg cm^{-2})
1	Fiber CCM 0.5 mg cm^{-2}	✓		✓		0.5
2	Fiber CCM 1 mg cm^{-2}	✓		✓		1
3	Fiber CCM 2 mg cm^{-2}	✓		✓		2
4	Sintered CCM 0.5 mg cm^{-2}		✓	✓		0.5
5	Sintered CCM 1 mg cm^{-2}		✓	✓		1
6	Sintered CCM 2 mg cm^{-2}		✓	✓		2
7	Fiber GDE 0.65 mg cm^{-2}	✓			✓	0.65
8	Fiber GDE 1.1 mg cm^{-2}	✓			✓	1.1
9	Fiber GDE 1.75 mg cm^{-2}	✓			✓	1.75
10	Sintered GDE 0.65 mg cm^{-2}		✓		✓	0.65
11	Sintered GDE 1.1 mg cm^{-2}		✓		✓	1.1
12	Sintered GDE 1.75 mg cm^{-2}		✓		✓	1.75

Six distinct x-ray *operando* cells with 1 cm^2 active area were built for x-ray characterization and were used at 3 different beamtimes for ease of experimentation as well as swiftness in testing. Our previous work describes the design and development of these high-performance *operando*

cells in detail [3]. All the cells were preconditioned by break-in procedure including five linear sweep voltammetries from 0 to 5 A cm^{-2} and then holding the cells at 1 A cm^{-2} for 30 minutes at 60 ^{o}C prior to imaging. The polarization curves collected at the beamline are reported in **Figure B1** in Appendix B. **Figure B2** indicates the EIS spectra of the conditioned cells as tested at the beginning of life. The HFR of the preconditioned cells was ensured to be 0.2- 0.35 Ohm cm^2 during lab testing, but additional wiring during beamtimes can induce slight electrical resistance. However, this does not affect oxygen saturation in the channels at an applied current density. Additionally, there is no beam damage during the scan time which is previously reported in literature [39] and the before and after polarization curves were the same.

3.3 Electrochemical characterization

The electrochemical characterization is performed at UCI on the test station discussed in chapter 1. At NEL Hydrogen, the characterization is performed using multi cell stacks at 50 ^{0}C temperature. Catalyst used for the fabrication of both the CCMs and GDEs were iridium oxide and platinum black for the anode and cathode electrodes, respectively. For MEAs fabricated as CCMs, the anodes were coated using an electrode transfer process after being deposited onto a Teflon substrate. GDEs were sprayed onto the PTL, using an ultrasonic coater. To isolate the changes associated with the PTL construction and loading of the anode, all cathodes were processed as GDEs and spray coated onto a single sheet of carbon paper, in which the smaller test parts were cut from. Test parts were assembled into one of Nel's commercial cell hardware containing 3 cells with a total 28 cm^2 active area (**Figure B3** in Appendix B). Loading for the cathode was 2.0 mg cm^{-2}. These were selected to leverage proven stable cell design and because of the cell stack ability to handle multi-cell testing. Using this hardware, multiple cells could be

tested at the same time, under the exact same conditions, making data more easily compared. Tests were conducted on one Nel's R&D test stands, with the same location used for all operational tests. The test stands are designed as a subscale version of Nel's commercial systems to simulate what would be expected in a fielded electrolyzer. All tests were allowed to reach the steady-state operating temperature of 50°C and 30 bar H_2 pressure before collecting data. Polarization curves were collected by multiple step chronoamperometry starting from current density of 2-3 A/cm^2 and ramping down to 10 mA/cm^2 in 15 steps each held for 300 sec for voltage to stabilize. The last point of each current hold was used to plot the polarization curves. Alternatively, for operando cells, the polarization curves were collected by linear sweep voltammetry by sweeping voltage from 0-3 V with a step size of 100 mV and ramp rate of 1 mV/sec. Polarization curves at 30 bar differential H_2 pressure were collected up to 2 A cm^{-2} for beginning and end of life. All polarization curves were measured twice to ensure repeatability of the data. All samples processed and fabricated for the before mentioned operational tests were made in duplicate, with the second set of samples sent to University of California, Irvine for further characterization

3.3.1 Tafel analysis

The Tafel equation is derived from the Butler-Volmer equation. Under high anodic overpotential conditions, the overall current is mainly attributed to the anodic end while the contribution from the cathodic part is negligible. Hence the Butler-Volmer equation can be simplified to a Tafel equation 3.1.

$$i \approx i_0 \left[exp\left(\frac{\alpha_a nF\eta}{RT}\right)\right] \quad \ldots\ldots\ldots \quad 3.1$$

$$\log(i) = \log(i_0) + \frac{\eta}{b} \quad \ldots\ldots\ldots \quad 3.2$$

$$b = \frac{\partial \eta}{\partial \log(i)} = \frac{2.303RT}{\alpha F} \quad \ldots\ldots\ldots \quad 3.3$$

Where b is the Tafel slope obtained by plotting ln |i| – or of $\log_{10}$ |i| – versus η, that yields a straight line in this region. From its slope and intercept the transfer coefficient and the exchange current density can be obtained.

The Tafel analysis and the double layer capacitance measurements were conducted using a Gamry 5000 potentiostat. The test station used was an in-house made test rig comprising of a DI water heating and water recirculation system, and a repurposed Scribner fuel cell holder. The cathode bipolar plate was a standard graphite triple serpentine flow field, and the anode bipolar plate was a custom-made parallel channel (0.5 mm land and channel dimensions) titanium flow filed with a platinized surface to reduce ohmic losses due to Ti passivation.

A 5 cm^2 active area was used for electrochemical measurements. Before any electrochemical testing, the cell was heated to 80 ^oC using cartridge heaters. DI water at 80 ^oC was circulated through the anode at 5 mlpm for 30 minutes for the cell to heat up and the membrane to

achieve adequate hydration. The cell temperature was maintained by using a k-type thermocouple and a PID temperature controller. The cell was then conditioned by applying chrono potentiometric hold of 1 A cm^{-2} for 30 minutes for the cell operation to be reproducible during the testing interval. The Tafel slopes were recorded by chronoamperometric holds from 1.3 V to 1.65 V (iR free) with an increment of 10 mV. Each hold had a duration of 5 minutes to ensure a stable current draw. The slopes were then plotted by taking the average of the points recorded in the last one minute in the potential hold interval and on a semi log current density on the x-axis.

3.3.2 Measuring double layer capacities

When an electrochemical system is subjected to a voltage ramp, a steady state capacitive current is obtained in a short time (i_C). A steady state current is only observed when there is pure charging of the electrical double layer that is, movement of ions on either side of an electrode/electrolyte interface. For ideal capacitors, iC is related to the capacitance (C) and to the scan rate (ν) as described in Equation below [75]

$$i_C = \nu . C$$

For obtaining the double layer capacitance (C_{dl}) cyclic voltammograms at various scan rates within are recorded within a potential region where no redox processes take place. Then, i_C is extracted from the anodic and cathodic scans of the recorded voltammograms, and subsequently C_{dl} is calculated from the slope of the resulting i_C vs ν plot.

To obtain double layer capacities experimentally, the cell was purged with 5 % dry H_2 on the cathode at 50 mlpm at ambient pressure to ensure a pseudo-steady reference electrode for electrolyzer operation. The cell was maintained at 80 ^oC and heated DI water at 5 mlpm was fed on the anode side. iR free cyclic voltammetry scans were performed via voltage sweep from 0.3 V

to 1.5 V. For each cell, 5 different scan rates were used between 20 $mVsec^{-1}$ and 150 $mVsec^{-1}$ (**Figure *3-1*** depicts an example of CVs with different scan rates). The current densities at 1 V – 1.2 V (potential at which the CVs have the least slope and no Faradaic reactions) were plotted vs. scan-rates and the slope of the fitted line in this plot gives us the double layer capacity (**Figure B4 – B5**).

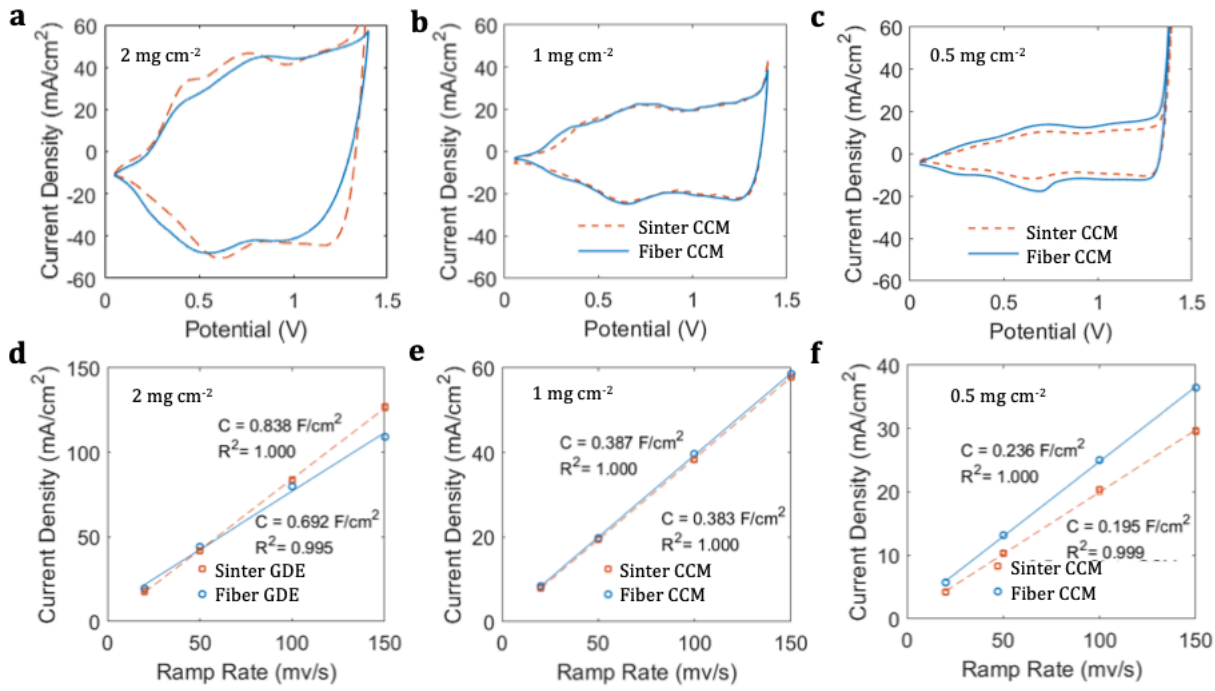

Figure 3-1 Cyclic voltammetry (CV) scans for fiber and sintered CCMs for double layer capacity calculations a-c) CV scans obtained at 50 mV sec^{-1} juxtaposed for fiber CCM (solid lines) and sinter CCM (dotted lines) at various loadings d-f) scan rates plotted against measured current density within a potential range of 0.9 V -1.1 V for various loadings. The slope of the scan rate against the current density gives the double layer capacitance.

3.3.3 Impedance analysis

Electrochemical impedance spectroscopy is an important electrochemical diagnostic for understanding the ohmic resistance and other physical process like proton and mass transport in PEM electrolyzers [76][77]. The technique involves applying a small AC perturbation (~ 1 mV) on a base DC voltage (selected according to requirements, for the sake of this thesis, the DC voltage is 1.7-2V in the mass transport dominated region of the polarization curve) and recording the system response. The response of the cell to the stimulus is measured as the AC voltage across the cell. The impedance is obtained by calculating the ratio of the AC voltage and AC current. The typical frequency for EIS analysis is 0.1 Hz- 100 kHz. **Figure *3-2*** shows the EIS spectra of two operando cells with 1 mg/cm^2 and 0.5 mg/cm^2 IrOx loading.

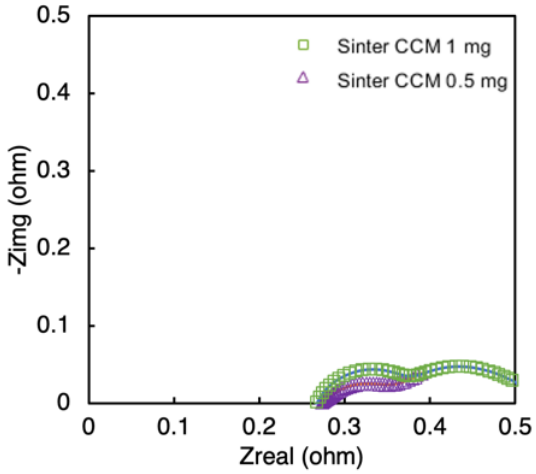

Figure 3-2 EIS spectra of 1 mg/cm^2 CCM and 0.5 mg/cm^2 CCM obtained from operando cell.

The high frequency intercept of the semicircles on the x-axis in the Nyquist plots is attributed to the ohmic resistance (sum of electronic and ionic resistances, R_{ohmic}). The difference between the low frequency intercept in the Nyquist plot and R_{ohmic} is assumed as the polarization resistance (R_{pol}). The total resistance corresponding to the low frequency intercept on the abscissa in the

Nyquist plot ($R_{ohmic} + R_{pol}$) is corresponding to the differential resistance of the polarization curves [76].

3.4 X-ray CT image processing and visualization

X-ray micro-tomography and radiography experiments were conducted at Beamline 8.3.2 at the Advanced Light Source (ALS) at Lawrence Berkeley National Laboratory and Beamline 2-BM-A at Advanced Photon Source (APS) at Argonne National Laboratory. At ALS, the image acquisition was performed at a beam energy of 25 keV selected using a double multilayer monochromator. Using a 20 μm LuAgB scintillator, an optical magnification of 4X, the images were captured by a sCMOS PCO Edge camera. This resulted in a spatial resolution of 1.16 μm $pixel^{-1}$. The tomography scans were conducted at an exposure time of 300 ms per projection. An average of 1500 projections were collected for 180 degrees of sample rotation resulting in a total scan time of 9 minutes (including bright field background acquisition and optical adjustments) for tomography.

At APS, the image acquisition was performed at a beam energy of 27 keV selected using a double multilayer monochromator. Using a 20 μm LuAgB scintillator, an optical magnification of 5X, the images were captured by a sCMOS PCO Edge camera. This resulted in a spatial resolution of 1.73 μm $pixel^{-1}$. The tomography scans were conducted at an exposure time of 150 ms per projection. An average of 1500 projections were collected for 180 degrees of sample rotation.

For X-ray radiography imaging, chronopotentiometric holds were applied for different current densities on the *operando* cell and the projections were acquired at an exposure time of 5 ms in both cell in-plane and through-plane directions. In this case, in-pane is defined when the x-

rays pass parallel to the MEA and through plane is defined, as when they pass perpendicular to the MEA. Smaller exposure time allows observation of the oxygen transport in the channel especially at high current densities when gas formation and transport is very rapid. However, smaller exposure time also resulted in low signal-to-noise ratio making it difficult to segment oxygen from water while image processing. For this experiment, 5 ms acquisition time per projection was ideal to achieve a reasonable signal-to-noise ratio, while also capturing the rapid oxygen transport.

The tomography image datasets were reconstructed using TomoPy [78] and Gridrec algorithm. Our earlier works report parameters and details of the reconstructions [79][57]. The reconstructed images were further processed using Fiji ImageJ. The images were converted to 8- bit, cropped and thresholded manually. The thresholded catalyst, PTL and other parts were visualized in 3D using ORS Dragonfly. The PTL porosity and pore size distribution were calculated by using MATLAB's TauFactor application. Subsequently, we attempted to calculate the catalyst loadings for all the cells by using the thresholded catalyst images as depicted in **Figure B6** in Appendix B. The total volume of the catalyst was calculated using the ImageJ plugin BoneJ. This volume was then multiplied with catalyst density to obtain the total mass which was then divided by the area to give the loadings in mg cm^{-2}. It is important to note that the loadings obtained by this method may not be completely accurate since catalyst particles smaller than the limit of resolution of micro x-ray CT may not be captured and human error contributes to overall thresholding error. Nevertheless, the obtained values can give us a rough estimate of the true loading and hence help validate the ensuing data.

3.5 Quantifying Triple Phase Contact Area

Our previous work details the interfacial analysis of the two types of electrolyzer configurations [39]. That is, the GDE vs CCM for sintered and fiber titanium PTL. The purpose of interfacial analysis is to quantify the triple phase contact area (%TPCA) at the anode side. Since the catalyst materials attenuate x-rays highly due to their higher atomic weight and density, they appear perceptively bright in absorption contrast x-ray imaging. For each sample, 1 mm x 1 mm representative areas were selected and the catalyst and PTL were thresholded manually. It is crucial to capture all the catalyst pixels and segment them from the remaining greyscale to report the %TPCA values accurately. Hence during the thresholding process, only the areas having greyscale values between 250-255 (255 being the brightest feature) were selected and everything else was '0'. The reason for choosing an interval over a single value was to capture all the catalyst pixels that lie within the statistical limit of imaging process and hence this scheme was kept consistent across the entire sample pool.

Once the phases were thresholded, a 2D interfacial projection was generated by summing all slices within ~ 5 μm of the interface in the through-plane direction. This ensures that the surface roughness is captured, as well as swelling of the membrane into the PTL during PEMWE operation [9]. For this investigation, we assume that the ion conduction media, that is, the membrane or the ionomer is present at all places surrounding the PTL and the catalyst. Here, we define the equation of %TPCA as:

$$\%TPCA = \frac{Area\ of\ catalyst\ phase}{Intercept\ area\ \ of\ two\ phases\ (PTL + Membrane)} \times 100\% \tag{3-1}$$

where %TPCA is the triple phase contact area. The areas of the different phases are calculated by ImageJ using the corresponding 2-D projections. The following assumptions are made during the calculations:

i) the ion exchange media (ionomer) is present everywhere at the interfacial region and is considered as a 3D entity; ii) the membrane and catalyst layer are considered as 2D entities within the interfacial region.

To study and quantify the interfaces within the PEMWE system, it is essential to first establish an understanding of the x-ray images and the representative areas. **Figure *3-3*** shows the complete 3D volume rendering of the PEMWE cell and the representative cross sections required for this study.

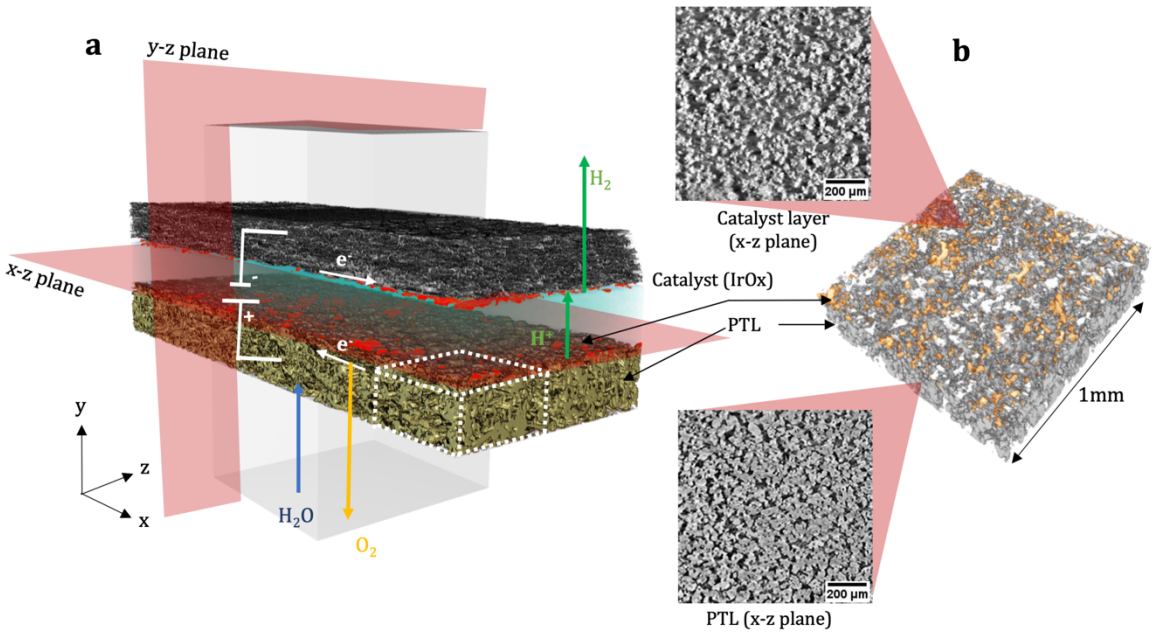

Figure 3-3. a) Complete 3D volume rendering of a PEMWE obtained from x-ray CT showing all the components and the transport processes, b) 3D rendering of the representative cross section of the anode used for the purpose of this investigation. The blown-out regions show the 2D

tomographs of the catalyst layer and the PTL as seen from the x-z plane. The catalyst shows up bright from the surrounded grayscale and hence can be segmented easily.

As shown in **Figure *3-3***, the cell consists of a proton conducting membrane (Nafion 117) sandwiched between a Ti PTL anode and a carbon based GDL. The PTL carries liquid water to the anode catalyst layer from the underlaying channels and draws out the product oxygen gas. Oxygen evolution reaction (OER) occurs at the anode catalyst layer driven by the high applied potential vs. cathode. At the same time, HER occurs at the catalyst layer and the evolved hydrogen gas is drawn out through the GDL into the gas channel. The PTL and the catalyst layer interface play a crucial role in the overall PEMWE performance and hence will be the primary focus of this work. **Figure *3-3***b shows the 3D volume rendering of the interfacial region (dotted region in **Figure *3-3***a) and the PTL as seen from the x-z plane. All analysis was conducted on these representative 1 mm x 1 mm areas. The histogram, thresholded catalyst image and overlay between the thresholded and original image is shown in **Figure B8** in Appendix B. The yellow portions in **Figure *3-3*b** represent the catalyst layer, and the grey areas represent the adjacent PTL. As discussed earlier, the catalyst shows up brighter than the PTL in the x-ray CT images as shown in the blown out 2D tomographs. The x-z plane was used for interfacial analysis and the y-z plane was used for radiography imaging to quantify the oxygen content in the water channels.

3.6 Conclusions and summary

The electrochemical and X-ray imaging methods for analyzing nature of interfaces are summarized in detail. The experimental sample set for operando X-ray CT experiments is identified based on research objectives. The electrochemical methods to measure polarization curves, Electrochemical Impedance Spectroscopy, Double layer capacity and Tafel slopes are discussed in detail. From X-ray CT imaging, the method to calculate the Triple Phase Contact Area (TPCA) is formulated.

4.Influence of PTL morphology and electrode configurations on interfacial contact and cell performance

4.1 Visualizing Electrodes with various catalyst loadings

The 2D reconstructed tomography slices at the interfacial region and the corresponding 3D volume rendering of the total catalyst were compared to better understand the effect of loadings and electrode configurations as shown in **Figure *4-1***. The in-plane images (x-y plane) highlighting the selected representative areas are shown in **Figure B9** in Appendix B. The overlay between the thresholded catalyst outlines and the original grayscale images for all representative cross sections is shown in **Figure B10** in Appendix B. For the fiber CCM configuration (**Figure *4-1***a), the catalyst distribution is sparse for the low loaded 0.5 mg cm^{-2} sample and gets denser as the loading is increased. For medium and high loaded samples, the degree of clustering and agglomeration is seen to increase with loading. Similar behavior was observed for sintered CCM samples (**Figure**

4-1c). Although x-ray micro CT cannot capture catalyst particles under 1 μm, which is the limit of resolution [3], it can map localized particle agglomeration and portions of sparse loading. These heterogeneities limit geometric area and cause discontinuities in electrical percolation networks especially in loadings at or below 0.5 mg cm^{-2}.

These heterogeneities on the anode have a greater detrimental consequence as compared to the cathode because of two concurrent reasons: the fast kinetics of HER on Pt/C and the possibility to use high surface area carbon as a support, leading to well-dispersed and electrically stable electrodes. Hence it is important to tune the interface and improve the anode catalyst layer homogeneity to ensure maximum utilization of the available catalyst. Although ball milling, sonicating and other chemo-mechanical processes can reduce particle size and improve the stability and dispersion of ink, the coating and drying process can greatly influence the catalyst layer homogeneity for CCMs.

For GDEs, the catalyst was directly coated on the PTL. As shown in the **Figure *4-1***b, the catalyst conformed to the fiber PTL surface morphology and the packing density increased with loading. For low loaded samples, discrete patches of catalyst were observed to accumulate on the top portion of the ~ 20 μm fiber strands and the catalyst coating within the remaining curved surface area of the fibers was minimum. These discontinuities were reduced for the medium loaded samples as the catalyst occupied almost the entire top area and some of the curved surface area of the fibers. For high loaded samples, dense catalyst was seen throughout the surface area of the fibers and the catalyst also deposits coarsely on the adjacent layer of fibers. Similarly, for sintered GDEs, (**Figure *4-1*** e) the catalyst packing density increased with loading. However, as opposed to fiber PTL, sintered PTLs were made of interconnected Ti particles and the end surfaces were flat for smooth connectivity with the membrane and current collector. Hence, most of the catalyst

was deposited on the flat surfaces during coating process and there was less catalyst penetration within the PTL.

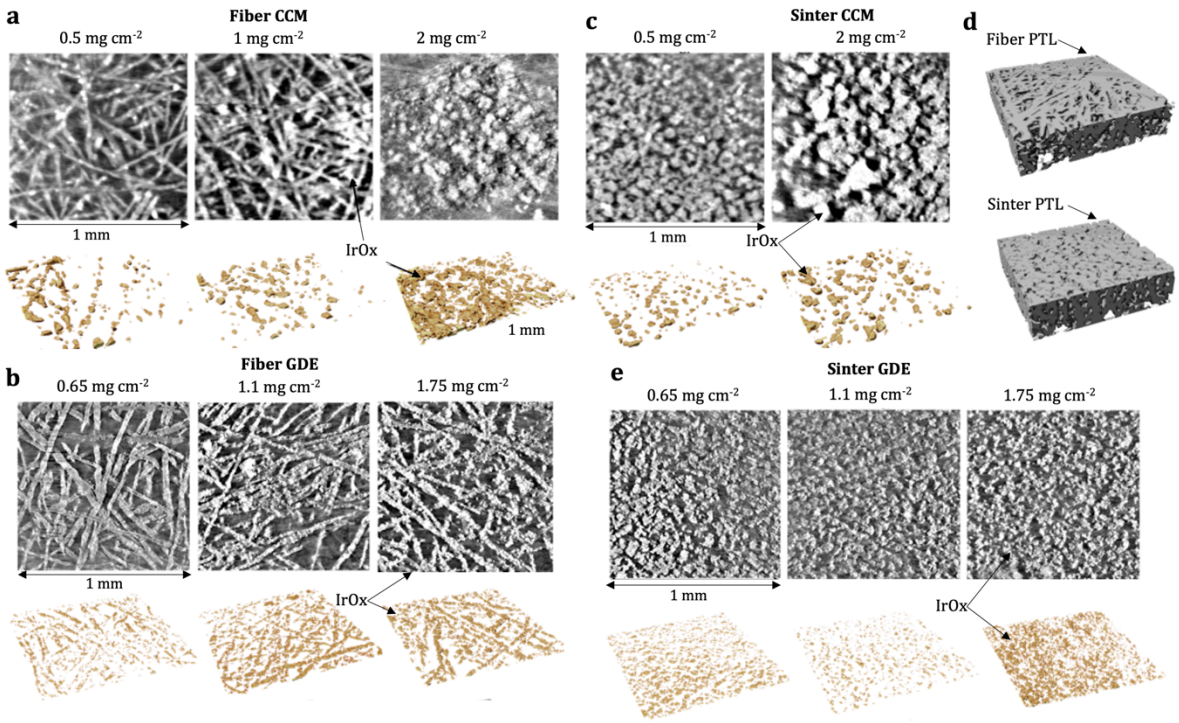

Figure 4-1. 2D reconstruction and 3D renderings of catalyst and PTLs in different cells obtained from x-ray tomography a) Fiber CCM 0.5 mg cm^{-2}, 1 mg cm^{-2} and 2 mg cm^{-2} b) Fiber GDE 0.65 mg cm^{-2} and 1.1 mg cm^{-2} and 1.75 mg cm^{-2} c) sintered CCM 0.5 mg cm^{-2} and 2 mg cm^{-2} d) sintered GDE 0.65 mg cm^{-2} and 1.1 mg cm^{-2} and 1.75 mg cm^{-2} e) 3D renderings of fiber and sintered PTLs.

Although it is apparent that CCMs showed a higher degree of catalyst clustering than GDEs, the catalyst layer homogeneity can be tuned by improving the water to solvents ratio in the ink, ink drying properties, or the coating process of the ink [80]. This degree of freedom cannot be as well achieved when fabricating GDEs since the catalyst layer properties are also dictated by the

surface morphology of the PTL. The catalyst layer homogeneity becomes increasingly important for reduced catalyst loadings for the following reasons: i) higher loadings can circumvent poor in-plane electrical percolation networks [81]–[83], ii) higher catalyst contact area with PTL and membrane leads to better % TPCA and reduces interfacial contact and catalyst layer electron transport resistances.

4.2 Validating Electrochemical performance

While the electrochemically active surface area (ECSA) can be easily calculated for Pt-based electrodes because of the hydrogen underpotential deposition fingerprint [84], [85], it is ineffective for IrOx based electrodes. Hence, ECSA for IrOx based electrodes is determined either from known specifications or experimentally using mercury underpotential deposition [86] or zinc adsorption [87]. These techniques present challenges in application for working PEMWE cells. ECSA is measured at low current densities, whereas many of the sites calculated to be active under ECSA measurements can become inactive under higher current densities, where transport cannot be neglected. The % TPCA in PEMWE is dictated by the localized hydration-based swelling of the membrane into the PTL and the irregularities in compression due to surface roughness of the PTL-catalyst layer interface. X-ray CT provides unfettered access into the operating PEMWE cell interfaces and provides an alternative measure of the ECSA, relying on geometry. The values of the %TPCA obtained for all the cell configurations from Table 1 were reported in **Figure B11**. The nature of the interfaces in different electrode configurations can be better understood by calculating the anodic double layer capacities.

Figure *4-2* shows the double layer capacities (C_{dl}) obtained for all four electrode configurations with varying loadings. It also correlates the double layer capacitance with the

%TPCA. Primarily, C_{dl} represents interface between IrOx and water and is an indirect measure of electrocatalyst surface area. Generally, for CCMs (**Figure *4-2*** a) one observes the trend of specific double layer capacity decrease with decrease in IrOx loading. This is expected, as with lower loading lower surface area of catalyst translates into lower double layer capacitance. We also report mass-normalized double layer capacitances in Appendix B, **Figure B12.** For the high loaded CCMs (**Figure *4-2*** a), sintered CCMs show about 0.3 F cm^{-2} higher average C_{dl} value than their fiber counterpart. This is substantiated by the fact that high loaded sintered CCM showed almost 20 % higher TPCA. Fiber CCMs showed large standard deviation in double layer capacity values. The difference between C_{dl} of sinter and fiber CCM is due to porosity of PTLs near the interface with the catalyst layer but also catalyst agglomeration observed for fiber PTL. In contrast, we observed a 20 % higher TPCA for sintered PTL owing to its low porosity (47 %) (**Figure B16** in Appendix B) and good contact with the catalyst layer. The values for C_{dl} are almost identical between the sintered and fiber PTLs for medium and low loaded CCMs. At 1 mg cm^{-2}, sintered CCMs still show about 10 % higher TPCA than their fiber counterpart. However, at low loadings, sintered CCMs show only ~ 3% higher TPCA. The C_{dl} as a function of %TPCA for CCMs was plotted in **Figure *4-2*** c. Generally, a linear trend was observed between the %TPCA and double layer capacitance, indicating that both methods show similar type of information.

Figure *4-2* b shows the C_{dl} values for GDEs. Again, generally, with the decrease in loading the double layer capacity values also decrease, except for 1.75 mg cm^{-2} having lower average C_{dl} compared to 1.1 mg cm^{-2} for sinter GDE. For high loaded 1.75 mg cm^{-2} samples, fiber GDE shows about 12 mF/cm^2 higher C_{dl} value than its sintered counterpart. This can again be explained by the fact that fiber GDE shows about 20 % higher TPCA than its sintered counterpart. For medium and low loaded GDEs, the difference in C_{dl} between fiber and sinter GDEs is within the 2 mF cm^{-2}

range as shown in **Figure *4-2*** d. The substantially higher %TPCA and C_{dl} for fiber GDE at high loadings can be due to the increased coverage of the catalyst over the curved surface area of the fibers as opposed to only the flat surfaces in sintered GDE. However, as the loading reduces to 1.1 mg cm^{-2} we observed a slight increase in C_{dl} for sintered GDE. Although this could be due to a nucleating oxygen bubble or residual gas in the PTL masking the catalytic site, the local heterogeneities in the catalyst layer could also affect the measurements. GDEs at low loadings of 0.65 mg cm^{-2} show almost identical C_{dl}, although sintered GDE shows a 2 % higher TPCA, it is inadequate to affect the C_{dl} substantially. Again, almost linear trend is observed for double layer capacitance vs. %TPCA for fiber and sintered GDEs, with 1.1 mg cm^{-2} sample being outlier.

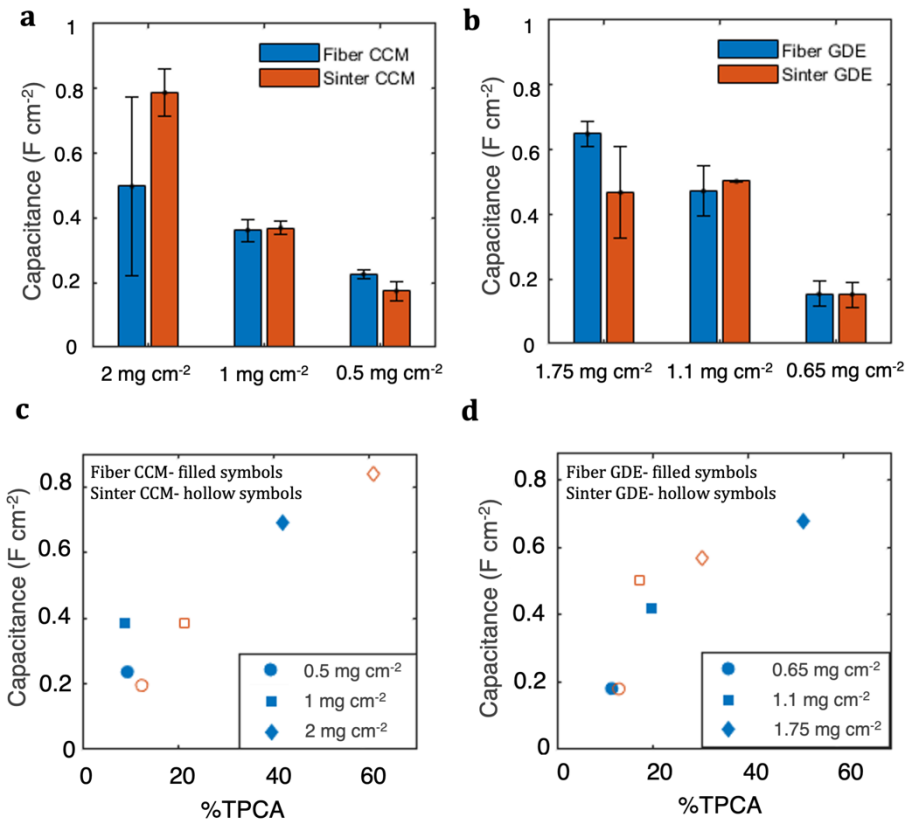

Figure 4-2 a) Double layer capacities of fiber and sintered CCMs for high, medium and low loadings, b) double layer capacities of fiber and sintered GDEs for high, medium and low loadings Average double layer capacitance plotted against % TPCA for c) CCMs and d) GDEs, respectively.

Comparing the high loaded fiber CCMs and GDEs, fiber GDE show over 10 mF cm^{-2} higher C_{dl} and concomitantly ~ 10 % higher TPCA than fiber CCM. A reasonable explanation for these observations could be that in fiber GDE compared to fiber CCM, the catalyst has a greater surface area due to the surface roughness of the PTL. Another reason could be that imaging results is an underestimation of the TPCA especially for high loadings due to resolution limits. However, in case of high loaded sintered electrodes, sintered CCM show a substantial 30 mF cm^{-2} higher C_{dl} and concomitantly ~ 30% higher TPCA than sintered GDE. In this case, because of the low porosity of the PTL, the catalyst is deposited mostly on the surface of the sintered PTL causing agglomeration. Hence, the exposed area of the catalyst was lower as compared to CCM resulting in smaller C_{dl}.

Figure *4-3* shows the measured beginning of life (BOL) polarization curves for all the samples. Cell performance for fiber and sintered CCM at low, medium, and high loadings are shown (**Figure *4-3*** a). Similarly, cell performance for fiber and sintered GDE at low, medium, and high loadings is plotted (**Figure *4-3*** b). There is a slight difference in loadings that were used for x-ray characterization and electrochemical testing since the experiments were conducted separately by UCI and Nel Hydrogen.

The polarization performance at current densities up to 1.5 A cm^{-2} can be related to the C_{dl} vs TPCA parameter space. The most notable detail of the CCM polarization curves is the better performance because of high TPCA and C_{dl} for high loaded sintered electrodes followed by medium loaded sintered electrodes. In comparison, high loaded fiber CCM show over 100 mV higher overpotential compared to sintered CCM at current densities below 0.5 A cm^{-2} suggesting limitations in OER kinetics stemming from anodic interfacial area. No significant performance drop was observed for medium loaded sintered CCM although there is significant decrease in

%TPCA and C_{dl} compared to high loaded CCM configuration. At low loadings, fiber CCM shows an 800 mV improvement compared to its sintered CCM counterpart which is surprising, since there is no significant difference in TPCA and C_{dl} between these two configurations. The poor performance of these sintered CCMs can arise from low %TPCA, but we cannot rule out the possibility of some other factors at play here. One of them can be the inhomogeneity of the catalyst layer revealed by XRF mapping pictured in **Figure B19** in Appendix B. Another reason could be the hydrogen crossover because of 30 bar differential operation. The crossed over hydrogen renders some catalytic sites inactive and possibly PTL cohesion issues that may be overcome with the use of an MPL.

The performance of all sintered GDEs was apparently similar until 1.5 A cm^{-2}, which is surprising, since we expected performance loss in lower loaded samples due to lower available double layer capacity of about 30 mF cm^{-2} than medium and high loaded samples. However, there was only 5-10 % difference in the TPCA between the medium and low loaded samples, which suggests that contact areas between PTL, catalyst layer and membrane were similar. The performance of fiber GDEs was also similar to sintered GDEs for high and medium loadings as seen in **Figure *4-3*** b. However, low loaded fiber GDEs show a 100 mV increase in overpotential than high and medium loadings due to increasing contribution of mass transport overpotential at 2 A cm^{-2}.

We found that GDEs typically have a poorer performance than their CCM counterparts at similar loadings, which is consistent with our earlier work [39]. At low current densities of 10 mA cm^{-2}, where the overpotential is described by kinetics, higher loaded sintered CCMs show approximately 200 mV improvement than their corresponding GDEs. This is a substantial potential

difference since kinetic overpotential contributes significant two thirds to the total overpotential until 2 A cm^{-2} [88]. This suggests possible proton or electron transport limitations at the interface.

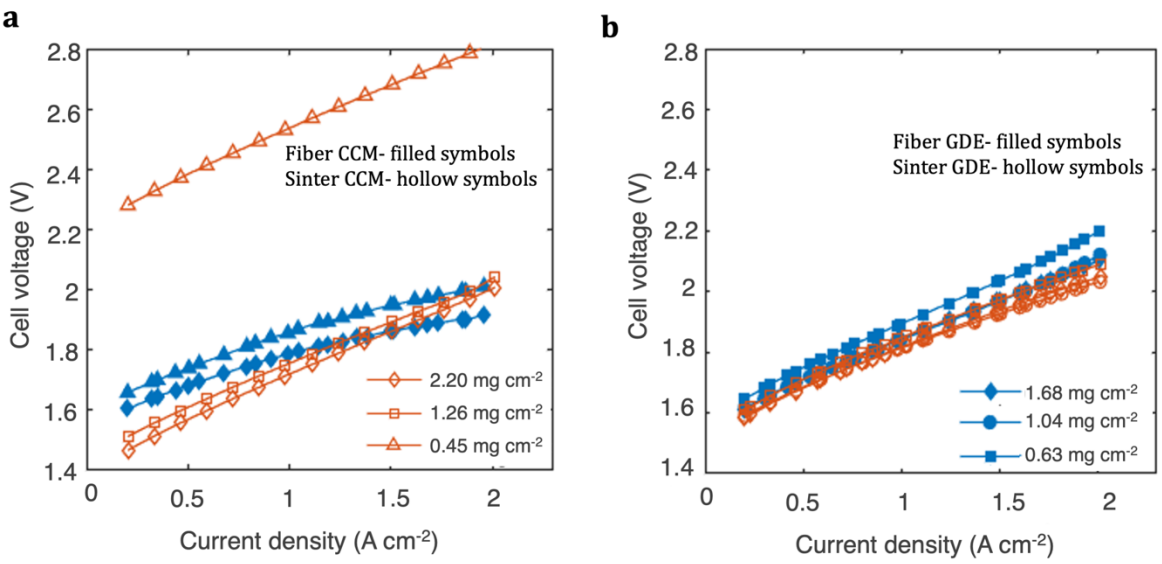

Figure 4-3 BOL polarization curves for a) fiber and sintered CCMs, b) fiber and sintered GDEs. The tests were conducted at 50 °C in a 28 cm^2 active area cell using a Nafion 117 membrane. Cathode Pt loadings were kept at 0.2 mg cm^{-2} for all tests. The filled symbols represent fiber PTLs, and hollow symbols represent sintered PTLs.

4.3 Investigating Kinetic and mass transport losses

To better understand the reaction mechanisms at low current densities, the Tafel plots for fiber CCM and GDE (**Figure *4-4*** a,c), sintered CCM and GDE (**Figure *4-4*** b,d) are presented and slopes were displayed (**Figure *4-4*** e). The associated CVs and slopes are reported in **Figure B4** and **Figure B5** in Appendix B for GDEs and CCMs, respectively. The Tafel slopes were obtained by a linear regression on the semi-logarithmic plot of iR-free cell voltage. The regression lines were plotted for points below 100 mA cm^{-2} assuming this as the kinetically dominated region for all

cells. The Tafel slopes obtained for CCMs are within the range of 57.6 mV dec^{-1} to 64.3 mV dec^{-1}, which are in good agreement with the values reported in literature for unsupported IrOx based catalysts in acidic medium up to 70 °C [19], [83], [88], [89]. The Tafel slope b is empirically defined as $2.303\ RT/\alpha F$ and the total kinetic overpotential η_k as a function of the Tafel slope is given by $\eta_k = b\log(j/j_0)$. Here R is the universal gas constant, T is the absolute temperature, α is the electron transfer coefficient, F is the Faraday's constant, j is the current density and j_0 represents the exchange current density. Hence the Tafel slope was directly proportional to the absolute temperature, and the total kinetic overpotential is dependent on the exchange current density. However, this is a simplified theoretical derivation of the Tafel slope, which assumes the coverage of the intermittent species in the reaction progress as constant at either $\theta \approx 1\ or\ \theta \approx 0$. When the actual surface kinetics are considered, the Tafel slope also depends on the surface oxides coverage [90], the nature of the electrode and the interface leading to dynamic utilization of the catalyst, which has been previously reported and substantiated in literature [72].

For fiber GDEs the Tafel slope show a decreasing trend with increase in loading. The recorded Tafel slope for low loaded sample was 76.8 mV dec^{-1} and it steadily decreased to 74.7 mV dec^{-1} for medium loaded sample and finally the high loaded sample show the lowest slope of 62.9 mVdec^{-1} as reported in **Figure *4-4*** c and e. This trend is consistent with that reported in literature [72], [73] since higher loadings facilitate better kinetics. However, this trend was not followed by the CCMs, since we observed a dip in the in Tafel slope from 61.5 mV dec^{-1} for low loaded sintered CCM to 57.6 mV dec^{-1} for medium loading and an apparent rise to 63 mV dec^{-1} for high loaded sample. The same trend was observed for fiber CCMs. Sintered GDEs show an increase in Tafel slope from 63.6 mV dec^{-1} to a fairly constant 73 mV dec^{-1} for medium and high loaded samples. While the TPCA shows a consistent rise with loading for all CCMs and GDEs,

the discrepancy in Tafel slopes between different loadings is unlikely to be due change in the reaction mechanisms, but likely due to factors like nature of the electrode, the catalyst layer homogeneity, catalyst layer utilization and increased mass transport resistance [27][91]

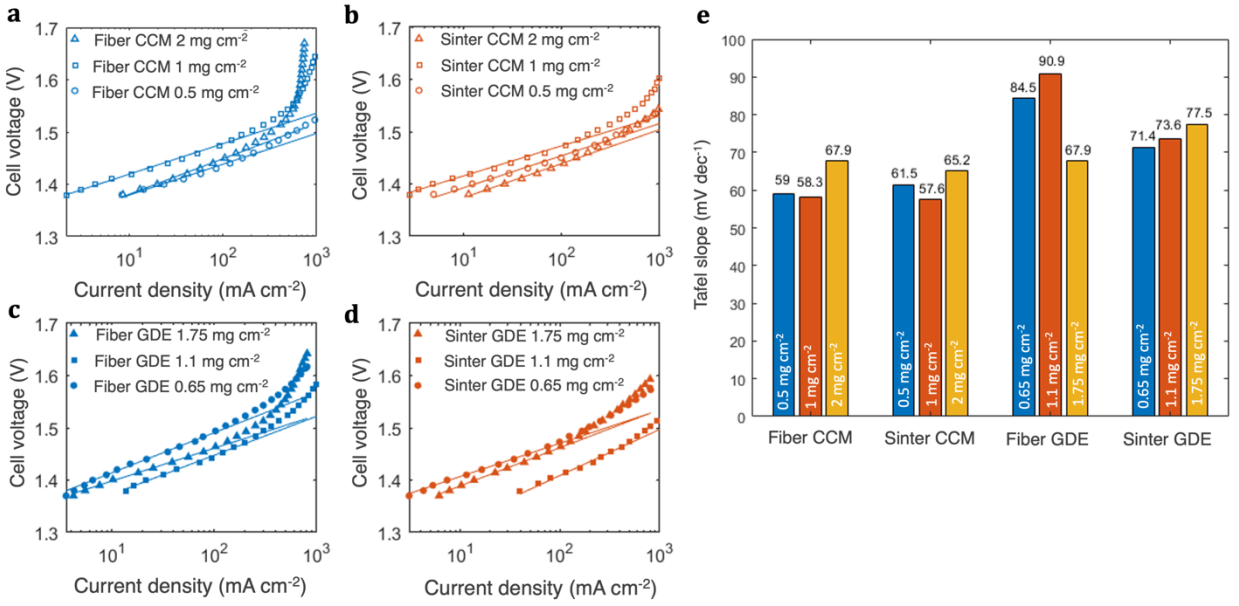

Figure 4-4 Experimentally obtained Tafel plots for a, b) fiber and sintered CCMs respectively c, d) fiber and sintered GDEs respectively e) tabulated Tafel slopes for all configurations and loadings. All Tafel slopes were collected at 80 ºC in a 5 cm^2 active area cell.

It is important to note that for similar loadings, GDEs consistently show a higher Tafel slope than their CCMs counterpart. Low loaded fiber CCM and fiber GDE have a Tafel slope difference of nearly 18 mV dec^{-1}. However, this difference reduces as the loadings increase suggesting that the underlying mass transport losses or conductivity limitations negatively affect the reaction kinetics, as the loadings are reduced below 0.5 mg cm^{-2}. Between similar loaded CCMs, the Tafel slope difference remained within ± 2 mV dec^{-1} even though the TPCA difference between high loaded

fiber and sintered CCM was ~20 %. For GDEs, we observed Tafel slope difference of nearly 13 mV dec^{-1} between the lowest loaded samples but a TPCA difference of only ~3 %.

Mass transport losses are the major contributor to the PEMWE overpotential at high current densities, especially at low IrOx loadings and are greatly influenced by the interfacial characteristics and the PTL morphology. High and medium loaded CCMs show an average 100 mV lower overpotential than their GDE counterparts at 1.5 A cm^{-2}. In general, we saw substantial mass transport limitations for low loaded samples especially at the EOL, as will be discussed later. Hence interfaces and the PTL morphology have a greater significance at reduced loadings. **Figure B14** in Appendix B represents mass transport and kinetic overpotentials as a function of TPCA at 1.5 A cm^{-2} for CCMs and GDEs. The TPCA calculated earlier (**Figure *4-4***) is in direct relation to the mass transport characteristics since a higher TPCA relates to larger number of reaction sites and concomitantly higher number of bubble nucleation sites for oxygen. This also results in reduced kinetic overpotentials. For sintered CCMs, the kinetic overpotential reduces by over 50 mV when the TPCA increases from 12% to 60%. Similar trends are observed for GDEs. At higher TPCAs both CCM configurations showed reduction in mass transport overpotential, whereas no clear correlation was observed between the TPCA and mass transport overpotential for GDE configurations (**Figure B14** in Appendix B). The nature of the electrode structure and its hydrophobicity also influences the gas transport [92]. Kadyk et al. [93] developed a structure based model to optimize gas evolution in electrolyzers and concluded that having preferential nucleation sites on the surface of the electrode leads to easier gas removal into the surrounding electrolyte (water) and reduces the mechanical stress leading to catalyst degradation or destruction.

In terms of the PTL morphologies, sintered PTL had a lower porosity (44.7 %) than fiber PTL (56.5 %). The porosity profiles of both samples were shown in **Figure B15** in Appendix B.

The pore-size distribution of these samples were reported in **Figure B16** showing significantly lower average pore size for sintered PTL of 8.1 μm compared to fiber PTL of 13.3 μm. The in-plane and through plane tortuosity factors for both PTLs can be found in the SM **Figure B17**. The in-plane tortuosity factors were higher in general than through plane values and the void pathways were more tortuous than the solid pathways for both PTLs as reported earlier [39]. For fiber PTLs, the in-plane tortuosity was found to be higher (2.7) than sintered PTLs (2.56). However, the through plane tortuosity for sintered PTLs was slightly higher than fiber PTL but still within the statistical limit of measurement. The through-plane tortuosity is a critical morphological parameter as it dictates oxygen removal from the catalyst layer into the flow channel.

To quantify the gas transport in these configurations and understand its impact on PEMWE performance, we analyzed x-ray radiography images at different current densities at several locations at the anode channel. **Figure *4-5*** indicates the oxygen content in the channels at various current densities for all samples at constant water flow rate of 3 mlpm. **Figure B18** in Appendix B shows the effect of different water flow rates on the oxygen residence in channel, as well as cell performance. The image processing for extracting oxygen content considers the average grayscale values that pass through the ROI. The correction factor *f* quantifies the extent to which the removal of oxygen occurs as discrete bubbles or slugs. A higher *f* signifies a higher slug flow regime and vice versa as shown in c and **Figure *4-5*** f, respectively. Oxygen content x *f* was measured through x-ray radiography and *f* cannot be decoupled from oxygen content. When the channel is fully filled by oxygen then oxygen content x *f* will be equal to 1, however, when the channel is filled by water this value will be 0. For CCMs generally oxygen percentage in the channel increased with increase in current density. This is expected, as with more oxygen generated and the same water flow-rate oxygen content in the channel should increase. For fiber CCMs, we observed a slower increase in

oxygen percentage in the channel compared to the sinter CCMs, as seen in **Figure *4-5*** a and b. Slower increase in oxygen content in the channel suggests that either oxygen accumulates within the PTL, the catalyst layer, or the *f* factor is smaller, indicating removal of oxygen as bubbles and not slugs. The last explanation is very likely, as with fiber PTL the fibers are smooth and there is lower number of sites for bubble nucleation compared to sintered PTL. With higher number of nucleation sites, the bubbles coalesce and are removed in the slug form. In case of sintered CCMs, a clear trend was evident, for the same current density a CCM with higher loading show higher content of oxygen in the channel (**Figure *4-5*** b). This is indicative that at higher loadings oxygen travels through more pathways within the PTL and then nucleates on more sites after which bubbles coalesce into slugs, showing higher f factor. For high loadings, the oxygen content plateaus as the current density nears 4 A cm^{-2}. As the oxygen content in the channel nears 80 %, we observed a sharp increase in the potential since most of the transport pathways were occupied leading to insufficient flow of water to the active sites. Hence, we can safely assume 80 % as the upper oxygen saturation limit in the channels beyond which unstable PEMWE performance at high current densities will occur.

For high loaded GDEs, the oxygen content increased to about 80 % and plateaued at 2 A cm^{-2}. As the current density increased further to 3 A cm^{-2}, there was an apparent drop in the oxygen content as seen in **Figure *4-5*** d, e. This may be due to variation in the correction factor *f* due to varying flow regimes. The low loaded GDEs also show a drop in oxygen content as current density nears 2 A cm^{-2}. During x-ray CT beamtime GDEs were not able to support current densities higher than 2 A cm^{-2}, hence the radiography data is missing for higher current densities. Generally, well-functioning PTLs and CCMs or GDEs should show increase in oxygen content in the channel with

increase in current density, as shown by **Figure *4-5*** b. However, above 80 % oxygen content in the channel will result in mass transport limitations.

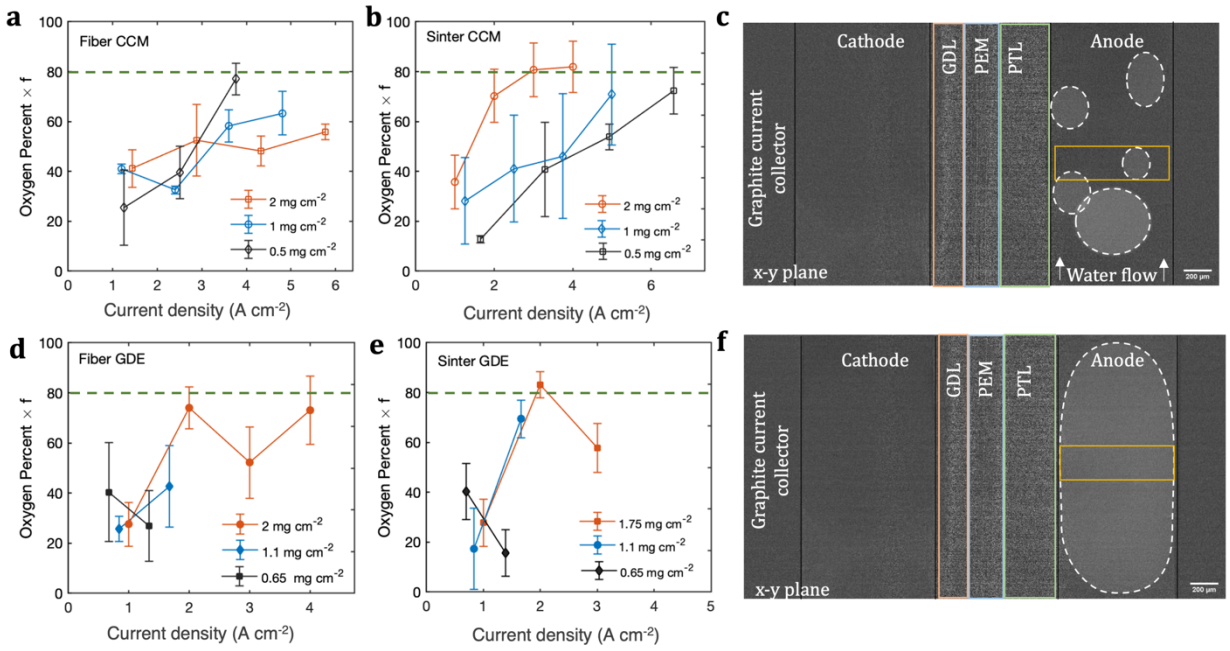

Figure 4-5 Oxygen content in channels as a function of current density for a, b) fiber and sintered CCMs d, e) fiber and sintered GDEs obtained from X-ray radiography c, f) through-plane radiography images of two cells showing the ROI (yellow rectangle) and oxygen bubbles (dotted circles). The oxygen content detected is a function of current density as well as the correction factor *f*. The correction factor *f* depends on the size of the bubble flowing through the ROI. The magnitude of *f* is considered large for a slug flow regime as indicated in f and small for discretized bubble flow as indicated in c.

4.4 0-D model for overpotential breakdown

To further understand the contributions of different overpotentials to the total cell potential, the BOL polarization curves were fitted using a 0D model. The parameters and equations used to fit the curves can be found in the **Table B1** in Appendix B. The total cell voltage, E_{cell} is the sum of the thermoneutral voltage and associated voltage losses:

$$E_{cell} = E_{rev} + \eta_{kin} + \eta_{\Omega} + \eta_{MT} \tag{4-1}$$

where E_{rev} is the thermoneutral voltage, η_{kin} is the kinetic overpotential for OER, η_{Ω} is the Ohmic overpotential and η_{mt} is the mass transport overpotential. Equations S1-S5 show the calculations to obtain each of these potentials. The mass transport overpotential is the remainder. The cathode kinetic overpotential is neglected in this analysis. **Figure 4-6** presents the overpotential breakdown for high and low loaded electrode configurations. The kinetic overpotential was calculated by using the Tafel slopes and the TPCA values obtained from electrochemical characterization and imaging, respectively (Equation S5). **Figure B13** in Appendix B depicts the bar plot of overpotentials breakdown at 1.5 A cm^{-2} for all the cells. The kinetic overpotential is the major contributor especially at current densities below 1 A cm^{-2} and its total share was observed to increase monotonically across the full current density range with decrease in catalyst loading. An increase in the TPCA and decrease in Tafel slope was inversely proportional to the kinetic overpotential. Peng et al [94] show the variation of kinetic overpotential with interfacial contact area for low loaded electrodes and attribute the trends to two main limiting factors: in-plane electron transport and catalyst accessibility.

It is worth mentioning that the ohmic share in this set of computations was obtained by using the membrane conductivity since the HFR values were unavailable. However, it is safe to assume that the electrical contribution to the HFR was constant since all the tests were conducted in similar cell hardware on the same test stand. Since mass transport overpotential was the remining overpotential, after calculating kinetic and ohmic transport overpotentials it also might include additional overpotentials that are not accounted by ohmic and kinetic losses.

For fiber CCMs (**Figure 4-6** a-b) kinetics occupied over 40% of the total overpotential at 1.5 A cm^{-2}, however, mass transport starts to dominate as the IrOx loading decreased, and we see an apparent decrease in the percentage of kinetic share with decrease in loading. Low loaded sintered CCMs had a significant increase in mass transport, as compared to their high and medium loaded counterparts (**Figure 4-6** c-d). This is rooted in the gas transport through the PTL and the channel discussed in the following sections. Low loaded GDEs had a higher kinetic overpotential at any given current density than their CCM counterparts. For example, at 1.5 A cm^{-2} and low loadings, fiber GDE had a 45 mV higher kinetic overpotential than its CCM counterpart, whereas sintered GDE had a ~5 mV higher kinetic overpotential than its CCM counterpart. In terms of the mass transport and additional overpotentials, the values depend on several factors, but we will be confining ourselves to their dependance on TPCA and PTL morphology, since we believe that these are the most significant contributors. The mass transport and other overpotentials increased with decrease in catalyst loading. In terms of the absolute potentials, we observed a higher mass transport loss in GDEs compared to their CCM counterparts (**Figure 4-6** e-h), except for low loaded sintered electrodes.

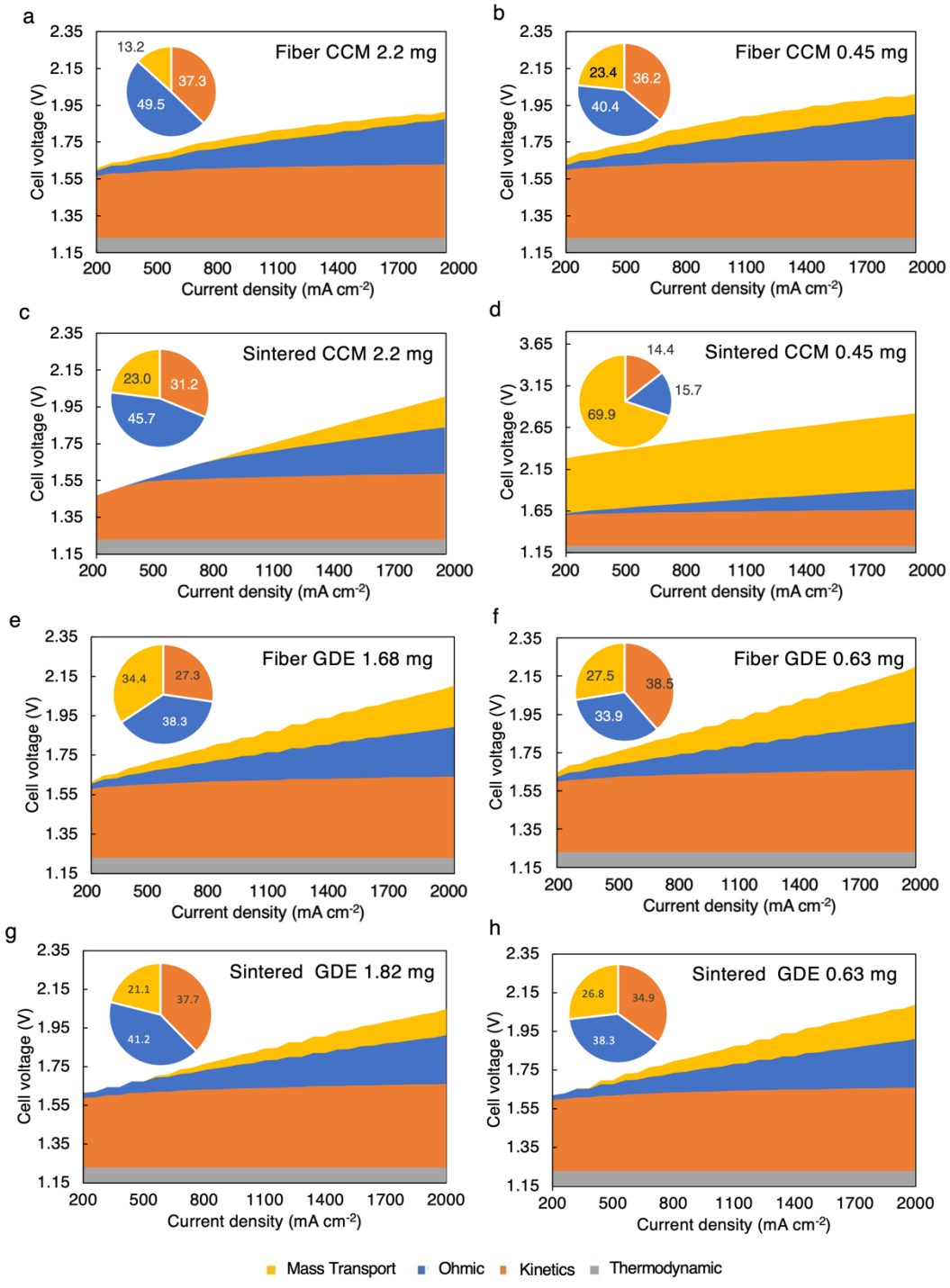

Figure 4-6. Overpotential breakdown of polarization curves into thermodynamic, kinetic, ohmic and mass transport and other contributions for a) fiber CCM 2.2 mg cm^{-2}, b) fiber CCM 0.45 mg cm^{-2}, c) sintered CCM 2.2 mg cm^{-2}, d) sintered CCM 0.45 mg cm^{-2}, e) fiber GDE 1.68 mg cm^{-2},

f) fiber GDE 0.63 mg cm^{-2}, g) sintered GDE 1.82 mg cm^{-2}, h) sintered GDE 0.63 mg cm^{-2}. Inset pie charts show the percentage overpotential share at 1.5 A cm^{-2}.

4.5 Durability analysis

The cell durability was probed after steady state electrolyzer operation for 90 hours. The cells were allowed to reach a steady state at 50 ^{0}C temperature and 30 bar H_2 pressure before collecting BOL polarization curves. The cells were then held at a constant current density of 1.8 A cm^{-2} for 90 hours (**Figure B24**) at a constant water flow rate on the anode, and the same operating conditions of temperature and pressure. Subsequently, the EOL polarization curves were collected. The testing focused on the influence of interfaces and PTLs on the steady operation, while the other cell components, such as the membrane, current collectors, back pressure etc. were kept constant. The steady-state analysis was conducted as opposed to the established triangle and square wave potential perturbation as accelerated stress tests [95], [96] to maintain focus on the effect of electrode configurations on the potential response and establish a baseline in the interface engineering efforts for existing systems.

The measured BOL and EOL polarization curves (Error! Reference source not found. a-d) and the corresponding potentials at 1.5 A cm^{-2} (**Figure *4-7*** e) are shown for all samples. High loaded fiber CCMs show a similar activation potential at low current densities of 0.1 A cm^{-2} but show about 100 mV increase in overpotential at 1.5 A cm^{-2} at the EOL, as shown in **Figure *4-7*** a. However, for low loadings, fiber CCMs showed a substantial 570 mV rise at 1.5 A cm^{-2} and over 200 mV rise in activation potential at low current densities at the EOL. As can be seen from **Figure *4-7*** b, for high and medium loaded sintered CCMs, the EOL voltage followed approximately a

constant 100 mV rise in overpotential until 2 A cm^{-2}. For low loaded sintered CCM, the EOL polarization curves showed a 100 mV decrease in overpotential at 1.5 A cm^{-2}. Although the BOL polarization curve stood at a substantially higher 800 mV than the high and medium loaded sample, a decrease in overpotential suggests possible conditioning even after 90 hours of steady state operation.

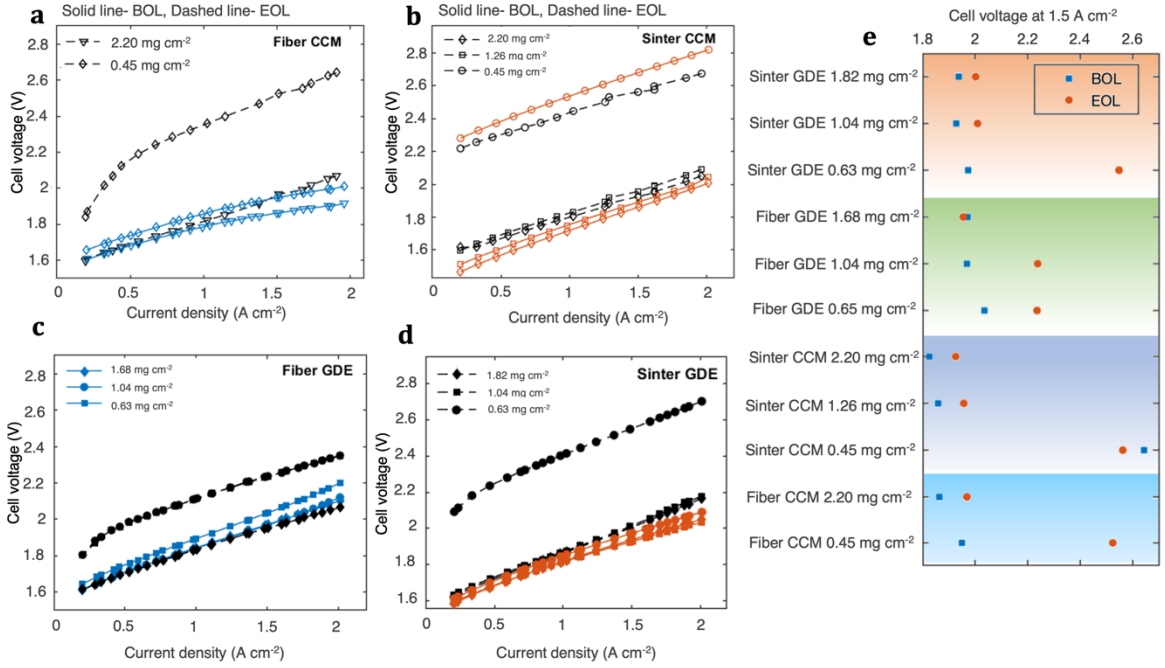

Figure 4-7 BOL and EOL polarization curves for a, b) fiber and sintered CCMs respectively c, d) fiber and sintered GDEs respectively e) Initial and final potential for all configurations at 1.5 A cm^{-2}. The tests were conducted at 50 ºC in a 28 cm^2 active area cell. The final polarization curves were obtained after holding each cell at a current density of 1 A cm^{-2} for 90 hours. The filled symbols represent fiber PTLs, and hollow symbols represent sintered PTLs.

4.6 Conclusions and summary

A systematic matrix of twelve PEMWE configurations with two different types of PTLs, two types of electrode configurations namely CCM and GDE and three levels of catalyst loadings were characterized using x-ray micro-CT to quantify the interfaces and elucidate its effect on electrochemical performance and gas transport in flow-field channels. Moreover, steady-state durability testing of all the samples was conducted and a Lattice Boltzmann Method model was constructed based on the tomography results to simulate gas transport in the two types of PTLs for varied catalyst loadings. From the tomography images, it was clear that the catalyst agglomeration and clustering increases with loadings for the CCMs and the catalyst conforms to the PTL surface during coating for the GDEs. The calculated TPCA was correlated with the double layer capacities obtained by electrochemical testing. In general, the TPCA increases with increase in catalyst loadings and C_{dl} scales proportionally. The conjunction of the TPCA along with C_{dl} gives us a measure of the electrochemically active surface area. The PTL surface morphology plays a vital role in affecting the TPCA. High loaded sintered CCM showed the highest TPCA and concomitantly highest C_{dl} among all other samples. **Figure 4-8** summarizes our understanding of the micro scale transport processes for CCMs and GDEs and proposes the idea of TPCA activity. Although TPCA signifies the electrochemically active area, its activity may be dependent on the form factor of PTL contact and type of electrode. For example, in GDEs, the catalyst deposited on the inner PTL surface is catalytically active, however, it may not have the same magnitude of activity as compared to a region that touches the membrane because protons must take a larger path to migrate into the membrane. We propose modeling approaches to calculate overpotentials associated with proton transport and quantify the activity of the TPCA.

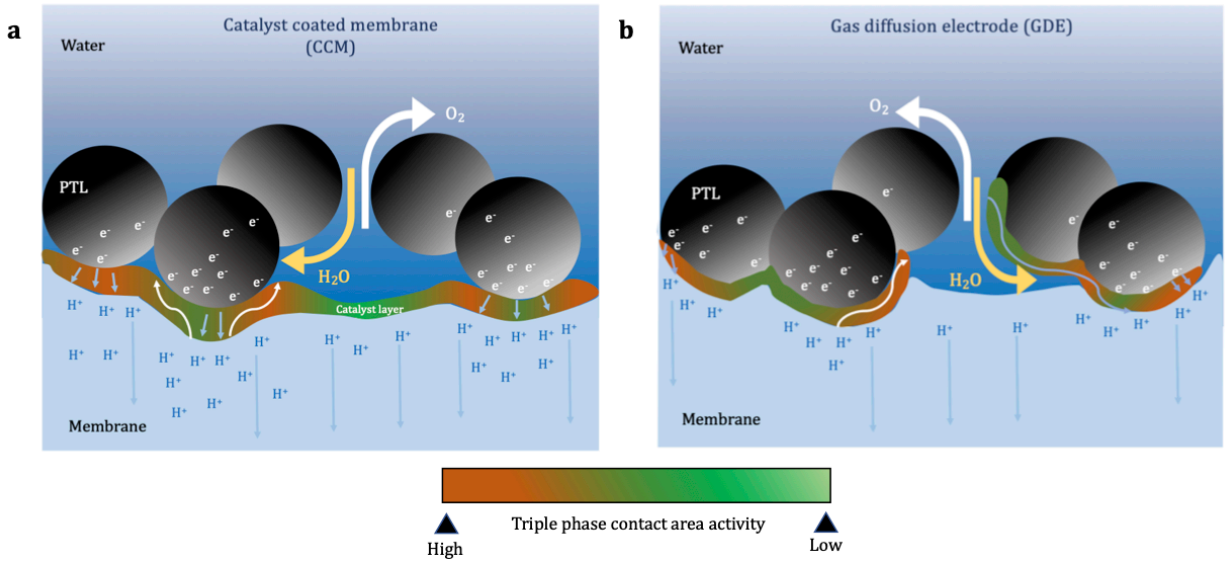

Figure 4-8 Visualizing microscopic effect of electrode configurations on transport processes at the anodic interface (a) CCM configuration, (b) GDE configuration. Blue arrows indicate the path of proton transport in the catalyst layer and white arrows represent the diffused oxygen transport through the catalyst layer and through the bulk electrolyte at the triple phase region. The red regions in the catalyst layer represent high level of TPCA activity and the gradual color change to green represents reducing activity

The general order of C_{dl} vs TPCA on the parameter space for CCMs is sintered CCM 0.5 mg cm^{-2} < fiber CCM 0.5 mg cm^{-2} < fiber CCM 1 mg cm^{-2} < sintered CCM 1 mg cm^{-2} < fiber CCM 2 mg cm^{-2} < sintered CCM 2 mg cm^{-2}. This directly relates to the BOL potential measured at 1.5 A cm^{-2}, where the cell overpotentials follow the same exact trend. Similarly, the general order of C_{dl} vs TPCA on the parameter space for GDEs is sintered GDE 0.65 $mgcm^{-2}$ < fiber GDE 0.65 $mgcm^{-2}$ < fiber GDE 1.1 $mgcm^{-2}$ < sintered GDE 1.1 $mgcm^{-2}$ < fiber GDE 1.75 $mgcm^{-2}$ < sintered GDE 1.75 $mgcm^{-2}$. This trend relates directly with the measured improvement in overpotential

until medium loadings, but high loaded fiber GDE shows a ~ 30 mV rise than sintered GDE. The discrepancies associated with such performance loss especially in GDEs is attributed to influence of undesirable overpotentials that affect the kinetics as shown by the Tafel analysis. The Tafel analysis shows that on average GDE configurations had higher Tafel slopes compared to CCM configurations, indicating that there are some other non-kinetic losses are present. Low loaded GDEs show the most performance loss after steady state current density holds possibly due to mechanical degradation of the catalyst. The investigation of oxygen content in the channels sheds light on the mass transport overpotentials. We determine 80 % oxygen in the channel to be the maximum to avoid water depletion in the catalyst layer. CCM configurations showed increase in oxygen content in the channel with increase in current density, as at higher current density more oxygen is produced and removed in the channel. The 3-D modeling suggests that for low-loaded catalyst layers the pathways for oxygen transport through the PTLs are limited, as oxygen is transported through a few preferential pathways. Fiber PTL has larger pores and more inhomogeneous pore size distribution leading to preferential oxygen transport pathways even at high catalyst loading. Sintered PTLs have more uniform and smaller pores, resulting in more uniform oxygen distribution in the PTL.

These findings add in-depth experimental and modeling insight into the nature of the PTL-catalyst layer interface and contribute to the understanding of impact of PTL bulk properties on gas and water transport. From these findings the following design guidelines for PEMWE can be proposed:

- Sintered CCMs with 44.7 % porosity can be used to obtain a high triple phase contact area between the catalyst layer and PTL and better gas removal at loadings above 0.5 mg cm^{-2}.

- Uniform gas removal through the PTL results in the slug flow regime and the optimal oxygen saturation in the channels should be 80 % or below to ensure stable performance at high current densities.
- The catalyst utilization is affected by the nature of the catalyst layer and morphology of the PTL, since GDEs can be limited by proton transport and CCMs can be limited by electron transport. To have highly active TPCA the PTL surface can be tailored to have larger area of deposited catalyst contacting the membrane.
- For commercial electrolyzers with immediate demand, we recommend using sintered CCMs with 0.5- 1 mg cm^{-2} loadings of unsupported IrOx for reasonable overpotentials at high current densities and since any higher loading does not result in significant durability or overpotential improvement. Although, for low loaded CCMs to be operated with differential pressure operation, we suggest using MPLs in to retain catalyst layer cohesion and maintain high interfacial contact. We suggest investigating interface behaviour during differential pressure operation as a future direction of research.

5.Investigating 2-phase flow through PTLs

5.1 Overview

Several studies have been conducted to understand the two-phase transport behavior in the PTLs [49], [93], [97]–[100] and have focused on using imaging techniques to investigate the evolution and transport of oxygen in electrolyzers, including optical, neutron, or X-ray imaging, as well as computational studies. Optical microscopy was utilized by Dedigama et al. [98] in order to study two-phase flow in an operating electrolyzer. With a 7,000-fps camera, as well as a transparent sheet and specific backlighting, they were able to capture anodic two-phase behavior with high temporal accuracy. Following this study, Lee et al. [101] employed a microfluidic platform, termed PTL-on-Chip, to study the effect of microstructure on the growth of oxygen bubbles, using an optical microscope. It was concluded that the morphology of the PTL has a significant impact on the governing force of the oxygen gas cluster growth and dictates the flow regime during PEMWE operation.

Neutron radiography has been utilized by Seweryn et al. [49] to visualize steady-state oxygen distribution in the PTLs. They were able to observe oxygen residence time in a PTL, specifically porous titanium (Ti), and show an equilibrium in the two-phase flow in the PTL. Their observations surprising at a time, suggested that the PTL would always be saturated with water,

regardless of the current density, and that oxygen saturation did not change with current density in the regime of 0.1–2.5 A/cm^2. Lee et al. [102] have investigated the dynamic gas transport behavior in the anode PTL by using *operando* synchrotron X-ray imaging. When they applied the current with a steep ramp-up and a shallow ramp-down, they concluded that the oxygen responds more rapidly, which means that the gas saturation in the PTL reached a steady state quickly. Zlobinski et al. [103] have studied the effect of the two-phase flow behavior within the PTLs under steady state and dynamic load of the electrolyzer by using a neutron imaging with high spatial resolution (6 μm) and relatively high temporal resolution (1 s exposure time). They concluded that the two-phase flow in the PTLs is purely capillary driven for a wide range of operating conditions and that viscous forces are negligible. They further confirmed the findings of Seweryn et al. that water and gas distribution is not affected by current density (from 10 to 2000 mA/cm^2). Leonard et al. [100] were able to observe oxygen bubble formation and transport with X-ray computed tomography (CT) and radiography using *operando* hardware. This work demonstrated that as the current density increased, the residence time of oxygen bubbles in the channel decreased; this was expected, as higher current density would result in more oxygen being formed, enabling faster oxygen bubbles detachment. With Ti PTLs currently, it is experimentally not possible to differentiate between water and oxygen in the PTL, as Ti is highly X-ray attenuating material. Therefore, limited information is known on microscale distribution of oxygen in the PTL and how PTL morphology can be tailored to remove oxygen more effectively, as the in-plane vs through-plane transport properties can be rationally designed.

The aim of this chapter is to investigate oxygen content in the PTLs and its relation to both PEMWE current density and water flow rate, as well as understand whether oxygen takes preferential pathways when transporting through the PTL. So, a PEMWE was set up with model

Ecarbon fiber PTLs (with similar morphological properties to Ti PTL) in order to directly observe and quantify both the oxygen content and preferential pathways oxygen could take as it exits PTL using *operando* X-ray CT. Using carbon fiber PTLs and short experimental imaging time enables direct observation of the steady-state pathways for oxygen transport within the carbon PTL. This is unprecedented, as no previous study has seen the pore-scale observation of oxygen content within the PTL with *operando* techniques. The direct three-dimensional model-based lattice Boltzmann method (LBM) was used to better understand the physics behind the two-phase transport in the PTL under different cell operating conditions.

5.2 Unraveling preferential pathways for oxygen removal from PTLs

To better understand oxygen transport in the PTL, oxygen content within the three through-thickness portions of the PTL was investigated. ***Figure 5-1*** shows the comparison of oxygen content distribution within the PTL at 1 A/cm^2 with the flow rate of 2 mlpm. The PTL was separated into three portions: near the catalyst layer interface (CL/PTL), middle of the PTL (mid PTL), and near the land/channel interface (PTL/channel), as shown at the top of ***Figure 5-1***a. The through-plane view of oxygen content generated with the z-project (averaged from 3D volume and projected onto a single slice) is depicted in ***Figure 5-1***a, where the volumetric information of oxygen content in the PTL was combined into a single image.

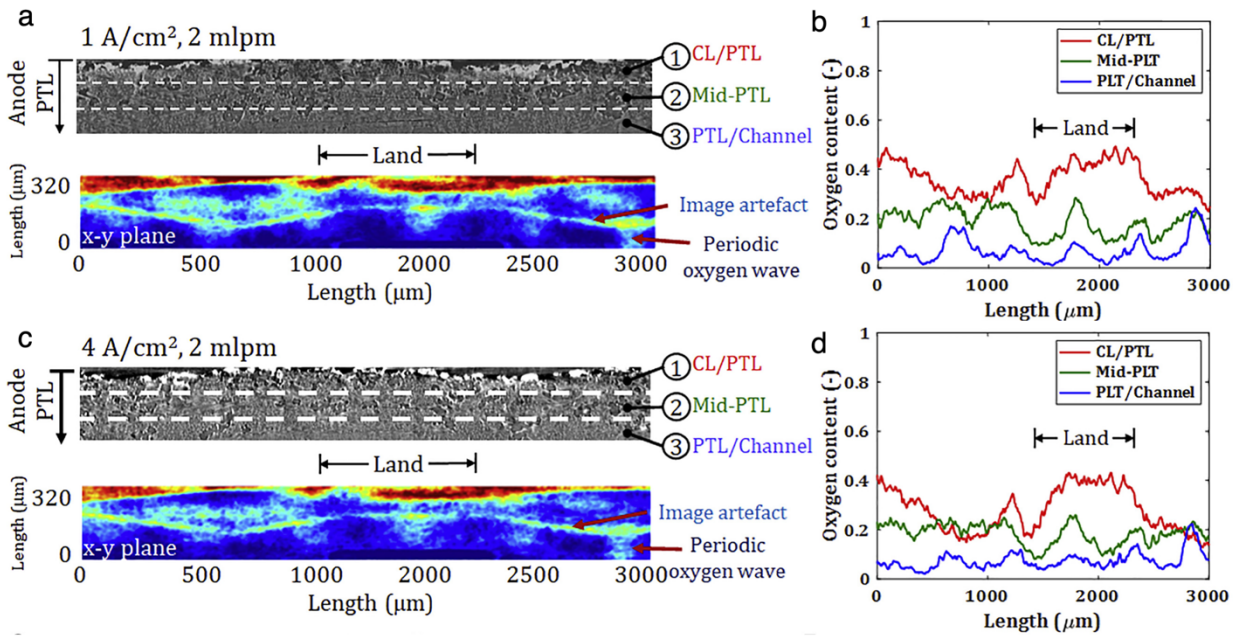

Figure 5-1 (a,b) The Comparison of Oxygen Content within the Different Portions of the PTL at the Operating Condition of 1 A/cm^2, and 2 mlpm (a) (Top) 1-3 portions of the PTL that located CL/PTL interface, middle of PTL, and PTL/channel interface. (Bottom) 2D oxygen content of the PTL at x-y plane by using the Z-project method. (b) Oxygen content comparison within the different PTL portions as a function of distance. (c,d) The Comparison of Oxygen Content within the Different Portions of the PTL at the Operating Condition of 4 A/cm2, 2 mlpm (c) (Top) 1-3 portions of the PTL that located CL/PTL interface, middle of PTL, and PTL/channel interface. (Bottom) 2D oxygen content of the PTL at x-y plane by using the Z-project method. (d) Oxygen content comparison within different PTL portions as a function of distance.

The location near the catalyst layer shows that the local oxygen content can be as high as 70 % in certain locations, mainly under the land; however, it is below 40 %. The oxygen content gradually decreases when transporting through the mid PTL and PTL/channel, respectively. The oxygen content of each portion was measured along the length of the sample and plotted, as shown in ***Figure 5-1***b. The average oxygen content in each PTL portion from catalyst layer/PTL to

PTL/channel was 35.7 %, 18.8 %, and 7.1 %, respectively. Thus, it roughly halved as oxygen transported through each of the 1/3 sections of the PTL. The results show that the distribution of oxygen content seems to be a "spatially periodic front", especially at the mid PTL and PTL/channel portions. The spatial pattern is parallel to the land channel location and is in the same direction of water flow. The oxygen peaks appear every 400 μm, where the oxygen peaks vary from 12 to 25 %, whereas the oxygen content valleys (water-rich locations) vary from 2.5 to 7 %.

Figure 5-1 c and d presents the oxygen content comparison in the three portions of the PTL for the PEMWE operating at 4 A/cm^2 with the water flow rate of 2 mlpm. The result shows that the average oxygen content in each PTL portion from CL/PTL to PTL/channel is 27.5 %, 18.4 %, and 7.5 %, respectively, as shown in ***Figure 5-1***d. These values are slightly lower than the ones observed for operation at 1 A/cm^2. As explained before, at 1 A/cm^2, the CCM was most likely not fully conditioned well, not reaching its full steady state. Peaks in the oxygen content are observed below the land regions, similar to the case of 1 A/cm^2, indicating that some oxygen was trapped under the land.

The spatially periodic oxygen front observed here for all the current densities has not been reported before. We provide several hypotheses to explain its physics, which we will attempt to prove or disprove: (1) oxygen periodic front is due to catalyst layer inhomogeneous distribution, (2) electrochemical decoupling of catalyst sites due to local oxygen flooding at the catalyst sites, (3) interplay between in-plane/through-plane PTL morphology, wettability and resulting bubble coalescence and transport. Regarding hypothesis 1, we plotted catalyst layer distribution and correlated it to the oxygen waveform. There was little to no correlation found between the catalyst distribution and the oxygen content, as correlation coefficients are below 0.1. Hypothesis 2 attempts to explain the periodicity in oxygen front with electrochemical decoupling of the catalyst

sites. As when the oxygen locally saturates the catalyst layer, catalyst will not be active toward splitting water due to either proton limitations or unavailability of water vapor; however, after oxygen diffuses away, the catalyst becomes active again. In general, within the catalyst layer, the IrOx is hydrophilic and it is likely that liquid water is present either within the ionomer or directly on the surface of the catalyst; if that is not the case, water can react in the vapor phase, as well [104]. There are no literature studies investigating the length scale of these decoupling phenomena. In this study, the periodic oxygen front was found to be pronounced in the location of 160 μm, away from the catalyst layer, which is a half of the PTL thickness, as shown in ***Figure 5-1*** a and c. Therefore, this hypothesis is unlikely; however, we did perform additional model simulations with this options And these model simulations did not predict the experimentally observed oxygen wave front. Therefore, we believe it is transport and not kinetics that is responsible for the periodic oxygen front observation.

This periodicity is perhaps due to oxygen taking preferential pathways as it exits the PTL, which would account for the apparent periodicity, hypothesis 3. Zlobinski et al.[103] suggest that the pore network inherent to a porous media – in their case it was sintered Ti PTL – could account for the gas traps. Gas traps are areas of either high hydrophobicity or hydrophilicity inherent to a porous media. Since the PTL was well treated and OCV data show no hydrophobic locations within the PTL, it is difficult to explain the periodicity with the gas traps. Instead, we believe that the observed oxygen removal is due to different PTL in-plane vs through-plane tortuosities, 1.3 vs. 1.7, its wettability (completely aerophobic), and pore-size distribution. We explore the third hypothesis in more detail in the next section using a multi-physic model.

5.3 Lattice Boltzmann modeling of oxygen flow

Figure *5-2* shows the comparison of oxygen content in the PTL between the computational fluid dynamics (CFD) simulation and the experimental data at 1 and 4 A/cm^2 having water flow rate of 2 mlpm. The CFD simulations were able to adequately predict oxygen content in the PTL having aerophobic pores (water contact angle of 10°), especially in the middle and at the interface with the flow field, as evidenced by the agreement of average oxygen content with experimental data (**Figure *5-2*** C and 6D). The model overpredicts oxygen content near the catalyst layer by 10 %. Oxygen content in the PTL for 1 A/cm^2 and 4 A/cm^2 predicted by the model is very similar, and oxygen pathways do not change when current density is increased. The shape of the oxygen front is somewhat different, also periodic but with the period of 200 μm, which is half of that observed experimentally. Furthermore, the simulations reveal that more oxygen was trapped in the PTL under the land area, compared to the experimental observations.

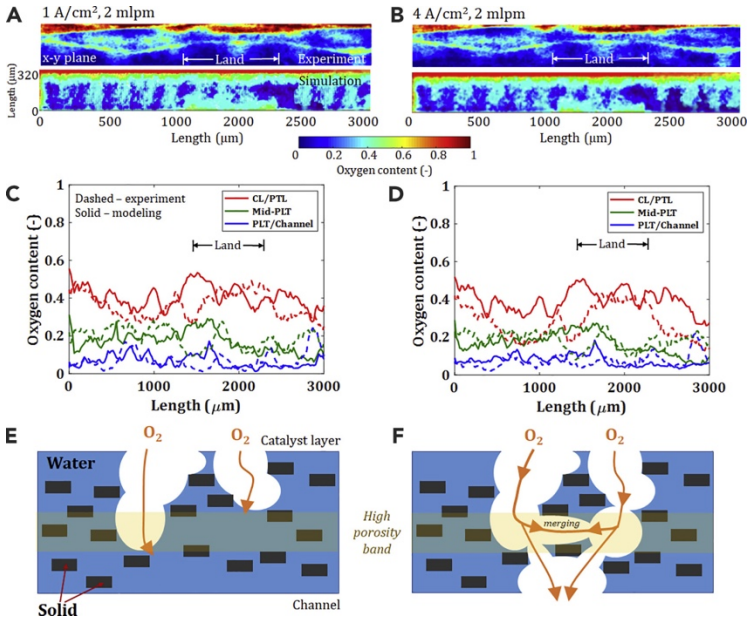

Figure 5-2 The Comparison of Oxygen Content in the PTL between the CFD Simulation and the Experimental Data at 1 and 4 A/cm2 with Water Flow Rate of 2 mlpm (A) CFD simulation

comparison with experimental results at the operating condition of 1 A/cm2, 2 mlpm. (B) CFD simulation comparison with experimental results at the operating condition of 4 A/cm2, 2 mlpm. (C) Average oxygen content for the three domains selected comparing CFD and experiment results for 1 A/cm2. (D) Average oxygen content for the three domains selected comparing CFD and experiment results for 4 A/cm2 current densities. (E and F) A conceptual schematic showing transport of oxygen in the PTL.

To understand the differences between experimental and CFD data, we need to better understand model assumptions, physics incorporated, and its current limitations. These are listed in the SI, but we will focus on the most relevant assumptions here. Within the model, oxygen bubbles nucleate within the catalyst layer with the nucleation radius of 1 μm and nucleation site density of 1 site/μm. The exact location and density of the nucleation sites and bubble nucleation radius are not well known, although other studies have assumed 1 nm nucleation radius [93]. Generally, oxygen is formed in dissolved form and nucleates over the hydrophobic defects, when the dissolved oxygen critical saturation concentration is reached. We cannot determine here from the experimental data whether oxygen bubble nucleation is uniform over the catalyst layer area due to the resolution limitation. Once the bubble nucleates, its radius will grow to a critical size and it will detach from the nucleation site and the next bubble will nucleate and grow and the process will repeat. The radius of a bubble upon detachment depends on mechanical balance of forces, such as buoyancy, pressure, capillary, drag, and lift. The shape and size of the bubble can be characterized by the Eotvos (Eo) number, which is correlated to gravity, g, density difference between fluids, $\Delta\rho$, and surface tension,

$$E_O = \frac{\Delta\rho g b^2}{\sigma}$$

where *b* is characteristic length scale taken to be the mean size of the pores of the PTL of 10.3 μm in this work. The calculated Eo number was 1.36×10^{-4}, and the parameters used for calculation are reported in Table S1. Eo << 1 indicates that the bubble transport is dominated by the surface tension and hence capillary forces are dominant, whereas gravity and buoyancy are minor driving forces. [105] From here, it is evident that bubble shape and path of transport will be determined by PTL wettability and pore size distribution, as well as current density (oxygen gas pressure).

The wettability of the PTL in this study is the following: it is hydrophilic and aerophobic. Oxygen first will displace water from the large hydrophilic pores and then from the small hydrophilic pores. If any hydrophobic pores are present, then oxygen will first fill those before advancing into the hydrophilic domains; however, here we do not observe hydrophobic pores. The shape of the oxygen bubbles will always be concave, as water has convex menisci in the hydrophilic porous media. Thus, the bubble transport will be guided by the pore size distribution of the PTL, as shown by **Figure *5-2*** E and 6F. Oxygen will nucleate and grow as bubbles at the surface of the catalyst layer, transport through the large pores of the PTL displacing water. The PTL selected here has good in-plane transport properties and also large porosity in the middle of the PTL, therefore, oxygen gas will merge and coalesce in plane, as these are the pores of low resistance before finally transporting into the channel. The high-porosity band in the middle of the PTL is mainly due to two PTL layers stacked together in this study, and it allows oxygen to merge and to form a periodic waveform. Note that the PTL does not have porosity that replicates oxygen pattern here. Once the pathway is established for oxygen removal, the energy it takes for oxygen to form a new pathway is much higher than that for it to take the established pathway. The flux of oxygen will be higher at higher current densities, but the oxygen pathways remain the same. Therefore, the morphology of the PTL determines the expulsion pathways through which oxygen travels. As discussed above,

the model physics do not currently capture the nucleation and growth of bubbles at the catalyst layer surface effectively, and we believe this causes the deviation between the modeling and experimental results. This study is also performed with a CFD simulation with a uniform flux of oxygen and a PTL that is aerophilic (water contact angle of 170°), as shown in **Figure B25** and **B26** The simulations show that the oxygen transport pathways did not change from 1 to 4 A/cm^2 and no periodicity in oxygen removal was observed. Additionally, we explored the PTL contact angle of 10 and 50° as shown by **Figure B27**, indicating that oxygen content in the PTL does not change significantly when contact angle increased to 50°.

Existing commercial PTLs, such as sintered or fiber PTLs, have uniform morphology and pore size distribution through the thickness of the PTL . These PTLs also have lower through-thickness vs. in-plane tortuosities, essentially eliminating the possibility of oxygen front merging in plane in the middle of the PTL. The periodic waveform in this study also enables effective water delivery to the catalyst sites. Good in-plane transport properties, as shown in this study, can eliminate oxygen accumulation under the lands. It is possible to tailor the Ti-based PTL morphology to enable better in-plane transport by introducing gradient in particle sizes through the thickness of the PTL or using the fiber-based Ti PTLs and stacking two thinner layers instead of one thicker, although PTL-PTL contact resistances have to be accounted for.

We applied the same CFD modeling framework to fiber and sintered PTLs at varying catalyst loadings. **Figure 5-3** shows the model prediction and comparison of oxygen content and velocity distributions in the different PTLs with varied catalyst loading. **Figure 5-3** a shows the oxygen content (left) and velocity distribution (right) for the fiber PTL at high catalyst loading. **Figures B20** – **B22** in Appendix B show the 3D volume rendering of the oxygen concentration for high, medium, and low loaded fiber PTL, sintered PTL and associated velocity profiles, respectively.

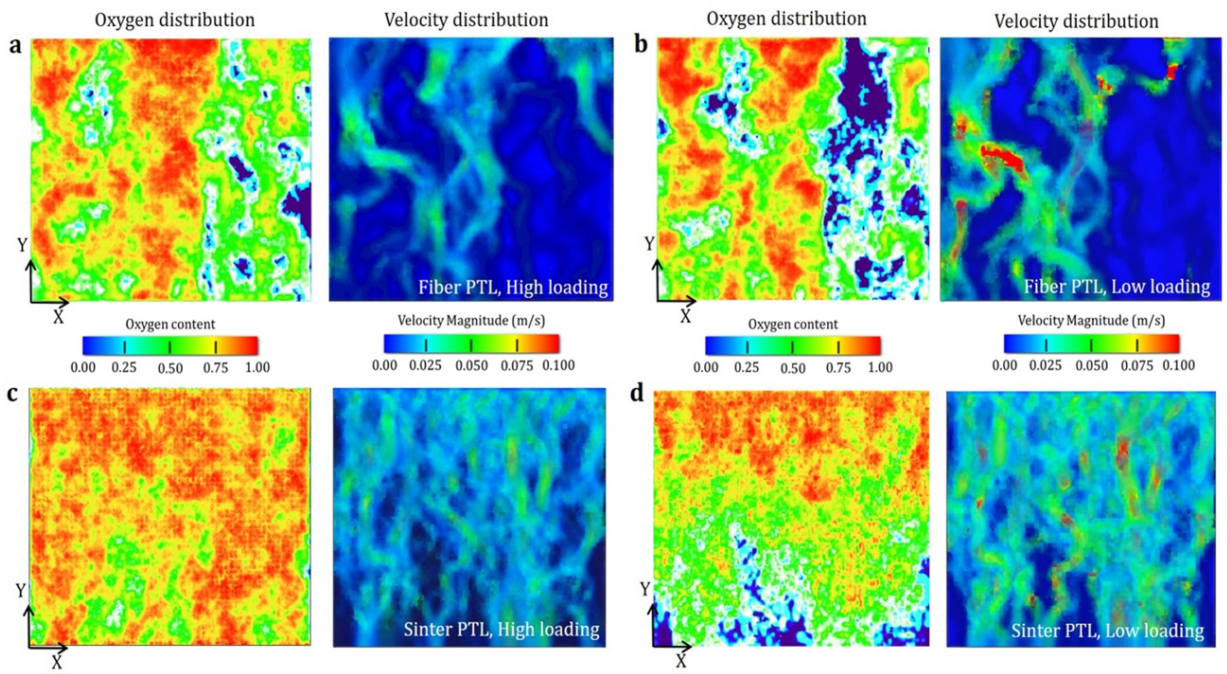

Figure 5-3 Modeling prediction of oxygen flow and corresponding velocity profiles in a) High loaded fiber PTL, b) Low loaded fiber PTL, c) high loaded sintered PTL, and d) low loaded sintered PTL. Left of each figure show the volume profiles and right of each figure show the corresponding velocity profiles. The top part of each image is the catalyst layer. The model assumes uniform distribution of catalyst for high loaded samples and non-uniform distribution for low loaded sample. The model was operated at the current density of 1 A cm^{-2} with the flow rate of 2 mlpm.

The oxygen bubbles were generated at the top of the PTL at the catalyst layer and they transported through the PTL via preferential pathways. The oxygen tended to merge at the PTL mid portion where the higher porosity band is located. The average oxygen velocity in the PTL was about 0.056 m s^{-1} for current density of 1 A cm^{-2} At low catalyst loading for fiber PTL, there was lower oxygen content existing in the PTL because oxygen did not take some of the possible transport

pathways, as shown in **Figure 5-3** b. This is because of a smaller inlet area for oxygen corresponding to less homogeneous catalyst distribution based on our assumptions, which resulted in a low active number of catalytic sites. The average velocity in this case was about 0.068 m s^{-1}, which was higher than the high catalyst loading case because of lower number of pathways that oxygen was taking (lower cross-section area that the flux crosses). Importantly, for low loaded sample (**Figure 5-3** b) there were locations where velocity magnitude was as high as 0.1 m s^{-1}. It is undesirable to have local high flux locations within the PTL, as if these pathways were to be blocked, significant mass-transport losses are expected.

Figure 5-3 c and **Figure 5-3** d show oxygen transport through the sintered PTL with the high and low catalyst loading, respectively. At high catalyst loading, oxygen was taking all the possible transport pathways with a high amount of oxygen content within the PTL. Oxygen concentration in sintered PTL was very different than in fiber PTL. This is mainly due to pore sizes of the PTLs. Sintered PTLs have very uniform pore-size distribution with a mean radius of 8.1 μm, as shown in **Figure B16**. The cumulative oxygen content in the PTLs is reported in **Figure B23.** Oxygen will be transported as a front within the first 100 μm, as shown by **Figure 5-3** c and **Figure B23** for high catalyst loading. After that, the oxygen saturation gradients through the rest of the PTL until it reaches the channel. These results are consistent with experimental findings from De Angelis et al [106]. Since most of the pores were of the same size there were no preferential pathways for oxygen to take, and there was no higher porosity in the middle of the PTL, as shown for fiber PTLs. There are more pathways for transport existing in this case, which shows a large amount of oxygen content distribution in the PTL. The velocity vectors were very uniform, showing that all the pores within the PTL were utilized for oxygen transport. At low catalyst loading, oxygen front was suppressed, and velocity profile show several bottlenecks with 0.1 m s^{-}

[1] maximum velocities. The LBM suggests that preferential transport through the PTL occurred when PSD was non-uniform, such as for fiber PTLs (**Figure B16**). The advantage of fiber PTLs is that water delivery can be efficient, as oxygen does not occupy all the pores, however, it can also result in blockage of oxygen transport pathways. For the sintered PTLs very uniform oxygen transport through the PTLs was observed, even for low loaded PTLs, which is desirable.

5.4 Conclusions and summary

In this chapter, X-ray CT and CFD were used to investigate oxygen transport in the PTLs of PEWMEs. This study aimed to explain the preferential pathways of oxygen transport through the PTL. X-ray CT was performed using the in-house designed electrolyzer at different water feed rates (1-3 mlpm) and current densities (1 - 4 A/cm^2). Here, an acid-treated Freudenberg GDL was used as a model PTL on the anode because its pore size distribution most closely resembles conventional Ti-based sintered or fiber PTLs.

The results show that more oxygen was present in the PTL near the catalyst layer (~27.5 %), compared to near the flow field (~7.5 %). Oxygen content in the PTL varied very little with either flow rate or current density, within the studied range. In addition, the oxygen content exhibited spatial periodicity, with peaks appearing at approximately 400 μm. These peaks range from 12 % oxygen content to a height of 25 % oxygen content. These findings are novel, as this is the first-time oxygen content has been directly observed and quantified on a pore scale with direct observations.

The CFD model was able to correctly elucidate the oxygen content in the PTL as a waveform. However, the model predicted a period of 200 μm instead of experimentally observed 400 μm. The

difference between the experimental and the modeling results, we believe, is due to the limitations in the implementation of bubble nucleation and growth in the CFD model. Overall, oxygen transport in this hydrophilic/aerophobic PTL is guided by pore size distribution of the PTL. Oxygen will transport through the large voids first before filling smaller voids. Thus, once the pathway through the thickness of the PTL is established, oxygen bubbles will preferentially follow the pathway and no new pathways will be introduced within the current densities range studied here. The high in-plane transport properties of the PTL (tortuosity of 1.3) compared to the through-plane (tortuosity of 1.8) enable oxygen to merge in the middle of the PTL and form the waveform. This periodic waveform has not been previously observed, and we believe this is due to the fact that commercial Ti PTLs have better through-plane than in-plane transport properties and thus merging of the oxygen pathways will not occur.

Since oxygen tends to take preferential pathways through the PTL, one can rationally design PTLs for selective water transport in and oxygen removal out. This can be achieved by either tailoring pore sizes or wettability. Hydrophobic PTL patterning will enable oxygen transport from the PTL at low resistance; however, water transport will be impeded. Gradient in porosity [107] in a hydrophilic PTL can direct oxygen transport, as oxygen will transport along the large voids. If MPLs are to be designed [83], we believe introduction of cracks into the MPL can help with oxygen removal. Similar to this study, providing a high-porosity band in the middle of the PTL can help merge oxygen bubbles into a single channel, minimizing the area of the PTL for oxygen removal and providing more area within the PTL for water transport. The solutions suggested here can be expensive and will improve mass transport at high current densities (>2 A/cm^2). The voltage gains due to improved PTL transport properties have to be assessed with respect to the cost of production of advanced PTLs.

6.Elucidating use of MPLs for interfacial contact enhancement and effect on oxygen distribution

6.1 Overview

In the previous chapters, we discussed the importance of PTL microstructure and the resulting interfacial contact between PTL and catalyst layer on kinetic, ohmic and mass transport overpotentials. The morphological properties of PTLs such as porosity, tortuosity and pore radii are key factors that influence oxygen removal and water delivery to and from the catalyst layer [2]. However, the nature of interfacial contact also depends on the form factor of the PTL. This implies that two PTLs having the same nominal porosity and pore sizes, but different geometries result in different triple phase contact, different oxygen removal patterns and hence differences in

electrolyzer performance [108][109]. Several parametric and pore network modeling studies have shown that small powder based sintered PTLs outperform large powder based PTLs and having a microporous layer has been postulated to increase interfacial contact and subsequently, the electrochemical performance [110]. However, the effect of MPLs on oxygen removal and its effect on catalyst and cell durability are still unknown.

Several attempts at understanding oxygen transport have been done until now including neutron imaging, optical imaging in 2-D model PTLs, as well as X-ray CT using carbon GDLs for electrolyzer anodes [111]. Neutron imaging is less sensitive to metals than water and gas and can allow for visualizing oxygen transport but has inherent drawbacks of low resolution, non-3-D imaging being a 2D technique, and low time resolution. Most recently, De Angelis et. Al [106] used X-ray CT for the first time to resolve oxygen transport in Ti-based PTLs with operando studies. The use of staining agents to enhance oxygen contrast was a novel approach. However, a scan time of 2.5 seconds is not sufficient to capture fully developed transport pathways since Lee et al. [101] observed initiation of oxygen breakthrough at least 18 sec into gas formation. Hence, capturing time averaged oxygen transport renders a better understanding of flow regimes and PTL transport pathways utilization. Although oxygen transport becomes fast at high current densities, it also establishes fully developed transport pathways that can be captured with time averaged oxygen saturation measurement. Oxygen saturation here is defined as volume of oxygen divided by the pore volume. To date, no studies have been published that elucidate the effect of different MPLs on oxygen transport and their correlation to the catalyst and cell durability. Understanding these key parameters and their interrelation will greatly help enhance our understanding of PTL design and answer the question whether the presence of MPLs can improve catalyst utilization and enable lower IrOx loadings in commercial systems.

In this study, we used operando X-ray CT to observe time averaged oxygen distribution at different current densities and conducted durability studies on three different PTLs with and without MPL. **Figure *6-1*** shows the 3-D renderings and through plane porosity of three different PTL samples obtained using X-ray CT. The first sample is a baseline sintered PTL without an MPL with a nominal thickness of 250 µm, and an average porosity of 38%. The second sample named MPL 1 has a total nominal thickness of 270 µm and has a thin MPL 20 µm in thickness. The third sample named MPL 3 has a nominal total thickness of 315 µm and has a relatively thick MPL of 58 µm thickness. All the PTL samples were obtained from DeNora Inc. and were manufactured by selective laser sintering of Ti powders of various particle sizes. The MPLs were manufactured separately using fine Ti powder and the macro and micro porous layers were fused together by additional heat treatment. **Table *6-1*** details all the morphological information for the three samples obtained using X-ray microtomography.

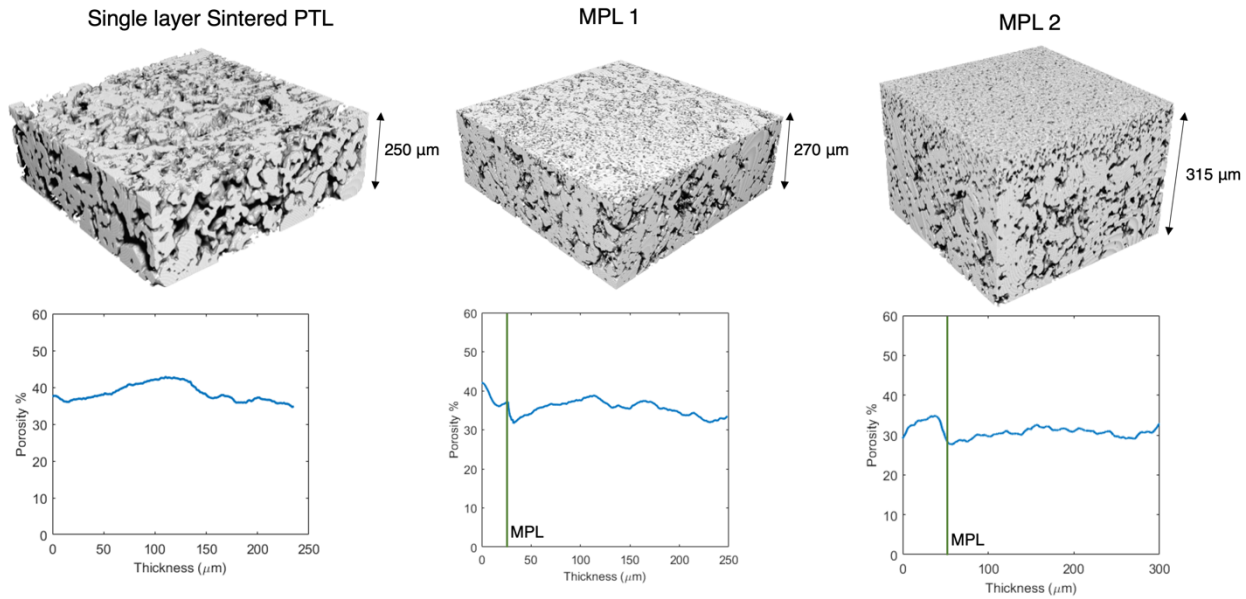

Figure 6-1 3-D renderings and porosity of three different selected PTL samples obtained using X-ray micro tomography. The baseline single layer PTL has a nominal thickness of 250 µm with an

average porosity of 38%. MPL 1 has a total nominal thickness of 270 μm and has a thin microporous layer of 20 μm thickness. Average porosity of MPL1 is 38% and corresponding macro porous layer is 35 % porous. MPL 2 has a total nominal thickness of 312 μm and a relatively thick microporous layer of 58 μm. Average porosity of MPL 2 is 35 % and corresponding macro porous layer is 30% porous.

The porosity values were calculated using an ImageJ macro that calculates the % area occupied by pores through the entire thresholded image stack. The total tortuosity factors were calculated using Tau factor application in MATLAB through the pore volume as detailed in the earlier chapters. The pore size distribution was calculated using BoneJ plugin in ImageJ that uses inscribed sphere method to define local "thickness" in void spaces as pore radii. The pore size distribution is represented as a histogram with a probability density function (PDF) fit to calculate statistical values of significance such as average pore radius as reported in **Table 6-1**. The details and PDF fits along with 2-D tomography cross sections are detailed in Appendix C. Operando X-ray CT experiments were done at beamline 8.3.2 of the Advanced Light Source at Lawrence Berkeley National Laboratory and at beamline 2-BM at Advanced Photon Source in Argonne National Laboratory using a white X-ray beam. The details of the beamline can be found in Appendix A. Three distinct operando cells (detailed in Chapter 2) were built with the above mentioned PTLs and preconditioned at UCI prior to beamtime. The MEA used in the operando cells had an anode IrOx loading of 1 mg/cm^2 and a cathode Pt/C loading of 1 mg/cm^2.

Table 6-1 Morphological characteristics of the three different PTL samples with and without microporous layer calculated from X-ray micro tomography imaging. The total tortuosity factors combine the MPL and the macro porous layer and are calculated in the through plane (along thickness) direction.

Sample	Overall Thickness (µm)	Total Tortuosity factor	Macro porous layer			Microporous layer (MPL)		
			Thickness (µm)	Porosity % (through plane)	Average pore radius (µm)	Thickness (µm)	Porosity % (through plane)	Average pore radius (µm)
Baseline	250	1.68	250	38	6.57	--	--	--
MPL 1	270±5	2.82	250±6	35.5	6.25	20 ±4	38	2.02
MPL 2	312±4	2.61	254±7	30.4	3.52	58 ±6	34	2.89

6.2 Interfacial analysis of PTLs with various MPL thicknesses

The presence of MPL was found to have significant impact on the nature of interface formed, specifically the triple phase contact area and number of contact points that the PTL makes with the catalyst layer. The details of interfacial analysis have been discussed in detail in Chapter 3. ***Figure 6-2*** shows the catalyst distribution and triple phase contact distribution in a 1 mm^2 ROI at the interface. For the baseline single layer PTL, the average triple phase contact was found to be 56%, it increased to 71.7% for MPL 1 and 74.3% for MPL 2. The density of contact points of the PTL with the catalyst layer was also calculated using ImageJ. The density of contact points was found to be 0.809-1.02 per μm^2 for baseline sintered PTL, 0.865-1.5 per μm^2 for MPL 1 and 1.23-1.6 per μm^2 for MPL 2. This means that the presence of MPL significantly improves interfacial contact, as well as the number of contact points with the catalyst layer increases by an order of magnitude.

The triple phase contact distribution is independent of MPL thickness since only the topmost several microns of the PTL constitute the interface. Increased triple phase contact implies reduction in kinetic and ohmic overpotential as discussed in Chapter 3. MPLs also reduce the heterogeneity of contact with the catalyst layer since the contact points are significantly closer to each other, which leads to a more uniform contact. This reduces the need of catalyst layer to be highly in-plane electronically conductivity and hence reduces the high frequency resistance as seen in **Figure** ***7-12***.

In addition to increasing catalyst utilization, in terms of thermal properties, MPLs have been shown to have superior heat transfer from the catalyst layer. The through plane thermal conductivity plays a dominant role in PTLs and the samples with MPLs show higher values because of better contact with the catalyst layer.

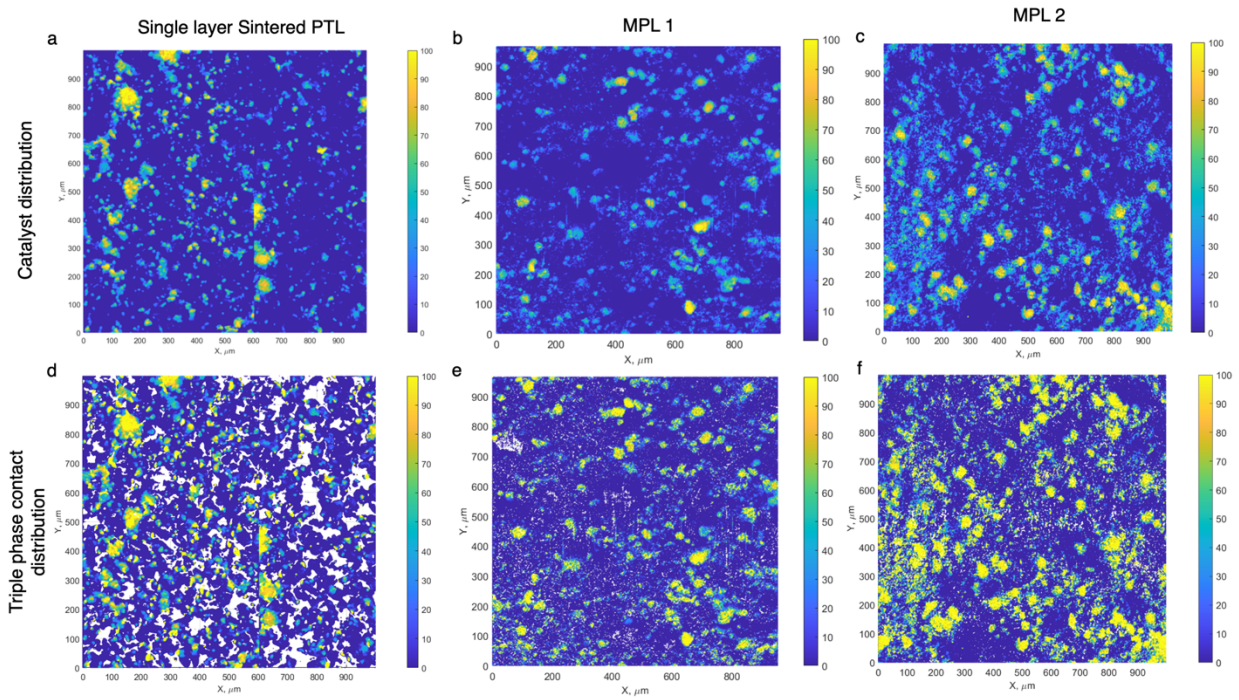

Figure 6-2 Catalyst distribution and Triple Phase contact distribution in 1mm^2 section of the ROI for all PTL samples. The MEA used for all cells has an Ir loading of 1 mg/cm^2 and a membrane thickness of 50 μm. The color bar for catalyst distribution represents the percentage of catalyst as

measured through the entire thickness of the catalyst layer. The color bar for the Triple Phase contact distribution represents the percentage of contact of the entire catalyst layer with the PTL. The average TPCAs were 56%, 71.7% and 74. 3% for baseline, MPL 1 and MPL 2 respectively.

It has also been shown that the nature of contact between the PTL and the catalyst layer induces mechanical stresses and strains in the catalyst layer causing morphological changes that leads to formation of cracks [71]. Crack formation can lead to distortions in the electronic percolation networks which may induce further ohmic overpotentials. The mechanical distortions of the catalyst layer post testing with highly porous fiber PTLs have been studied previously in literature and the dominant regions of cracks were found to be in between two adjacent fibers which has been proposed to inhibit catalyst utilization [112]. The presence of MPLs can reduce these mechanical deflections since the pressure distribution becomes much more even as the contact points are close to each other. Although this does not prove that mechanical deflections are completely mitigated, the dominant factor in mechanical deflections for PTLs with MPLs is the bulk surface roughness which are present at size scales of cm and not inter-particle micro scale level which has negligible effect on catalyst utilization.

6.3 Micro X-ray CT challenges for oxygen phase segmentation from Ti

The principle of absorption contrast X-ray imaging is based on Beer Lambert's law as discussed at length in Chapter 2. The intensity of transmitted X-rays through matter depends on thickness through which X-rays must travel and the attenuation coefficient. The attenuation coefficient mainly depends on the atomic number of the element. Heavier the element, greater is the X-ray attenuation and brighter is the formed X-ray image. In PEM electrolyzer anodes, Ti PTLs are

highly attenuating than surrounding water phase and hence appear bright. This makes segmenting oxygen phase from water and Ti nearly impossible. Hence, to improve contrast of oxygen, the surrounding water should appear bright along with Ti.

6.3.1 Use of staining agents for contrast enhancement

Several studies have been conducted to observe water formation and removal from fuel cell cathodes using X-ray micro tomography [113]. The GDLs in fuel cells are made of carbon-based materials which have a relatively low attenuation coefficient and can be differentiated easily with water. **Figure *6-3*** illustrates the basic differences in segmenting water and oxygen phases in PEM fuel cells and electrolyzers.

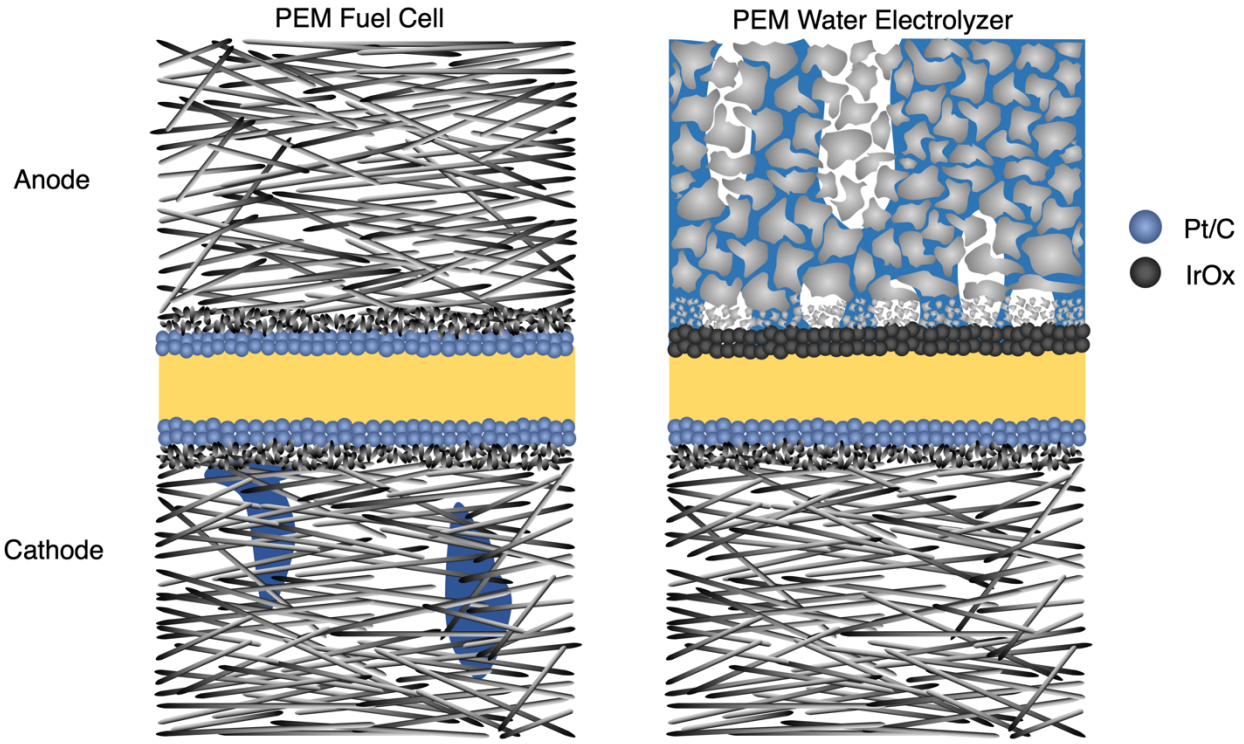

Figure 6-3 6-4 Illustration representing basic differences in segmenting water and oxygen phases in PEM fuel cells and electrolyzers. For a PEM fuel cell, water can be segmented easily from the

cathode as the surrounding carbon based GDL does not attenuate X-rays as strongly as titanium resulting in a relatively lesser contrast. To segment oxygen from the bright titanium phase in electrolyzers, the surrounding water needs to be stained with a heavier element (Iodine) so oxygen appears relatively dark and can be segmented.

The process of segmenting water from operando fuel cell cathodes has been discussed in detail in Chapter 2. For PEM electrolyzer anodes, we used 20 % NaI as a staining agent for water to produce a sufficient contrast for oxygen phase segmentation. ***Figure 6-5*** shows the X-ray transmission through the above discussed materials at micro–CT X-ray energy ranges of 20 keV- 30 keV. For a 20 % NaI solution, the X-ray attenuation increases by 11 % as compared to water at low X-ray energies. Since the imaging is conducted in a white beam, the produced contrast is the sum of attenuation produced at all energies which further improves image analysis procedures.

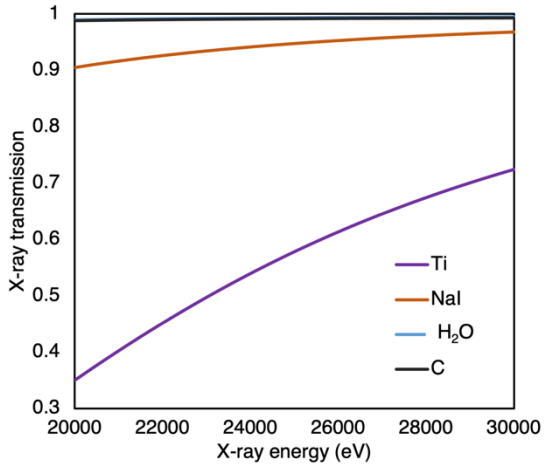

Figure 6-5 X-ray transmission through various materials at Micro CT energy ranges from 20 keV-30 keV. The thicknesses considered here are for 40 % porous Ti of 250 µm thickness, 20 % solution of NaI within the 250 µm thickness into PTL, 80 % water within PTL thickness and 40 % porous

carbon GDL. Carbon and water are almost fully transparent to X-rays at these energies however, an attenuation of even 1-2 % is enough for producing a clear image, thanks to sophisticated reconstruction algorithms and noise filters.

Before imaging, the operando cells are preconditioned with DI water according to the protocol detailed in appendix B. While imaging, the stained water is introduced in the cell and allowed to circulate for 10 minutes until all the DI water is replaced. A small back pressure is also applied on the cell by constricting the water outlet tube to ensure that the stained water is forced into the PTL, and all pores are wetted. Tomography scans are then done at OCV and then 0.2-2 A/cm^2. Since the exposure at each frame is 200 ms and total projections are ~2100, each scan takes about 8 min to complete, and the images obtained represent time averaged oxygen distribution.

The addition of stained water increases the cell voltage since a part of it goes into NaI decomposition reaction. However, the oxygen produced is purely from the OER from water since NaI reaction does not produce any gaseous products. Hence gas production under chronopotentiometric control is purely water derived making it possible to observe oxygen flow in real time in operando cells giving us valuable insights into the complex two-phase flow regime and subsequent PTL design strategies.

6.3.2 Image processing for oxygen phase segmentation

We developed an innovative image processing procedure to segment oxygen since the images obtained from tomography scans require significant amount of post processing to enhance oxygen contrast that can be reliably thresholded. **Figure *6-6*** shows the image processing steps for oxygen phase segmentation. The first step is to align the all the image stacks from OCV to 2 A/cm^2 so that

each slice in every stack corresponds to the same location in the cell. The image stacks are aligned using Dragonfly software.

The aligned image stacks are rotated, cropped, and smoothed at the same location using an ImageJ macro. The OCV images are then subtracted from images at applied current densities by applying a statistical minimum function between the two images since oxygen has lower grayscale values than surrounding water and Ti PTL. This results in an image with better contrast for oxygen than the raw images. The resulting 32-bit image is converted back to 8-bit and the OCV image is subtracted again using the statistical minimum function. This process is repeated until a sufficient oxygen contrast is reached. A custom bandpass filter can then be used to filter out any noise and increase contrast further to make image segmentation even more reliable and true to the actual form.

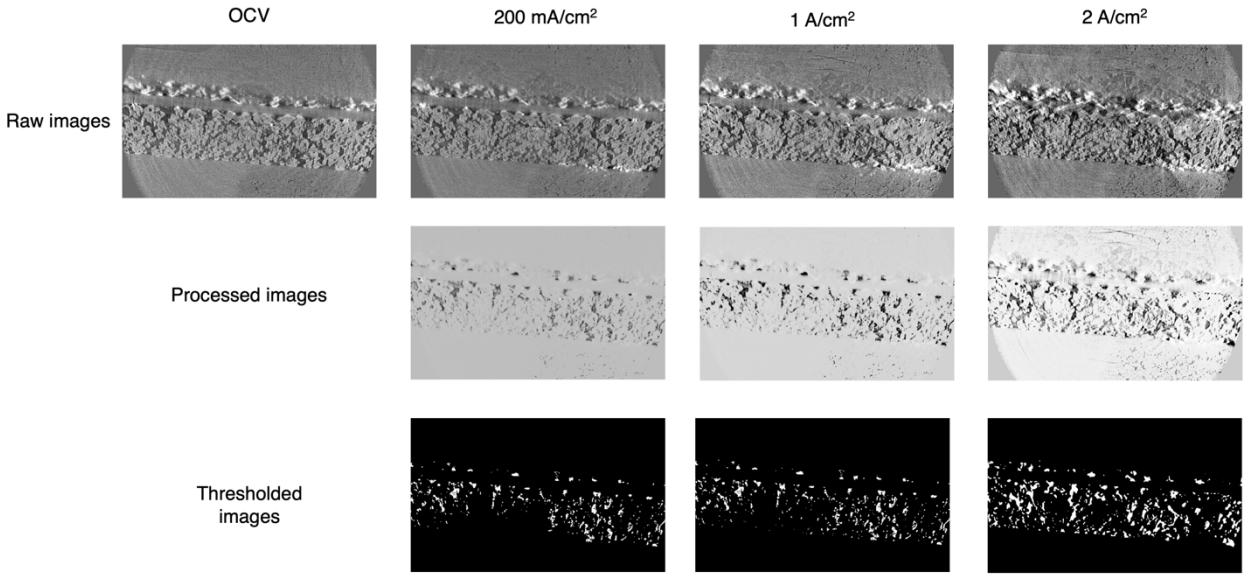

Figure 6-6 Image processing procedure for segmenting oxygen phase. For each current density image, the OCV images are aligned, and the statistical min is obtained against grayscale values of both images and the process is repeated with the resulting image. The final product image has a better contrast for oxygen phase and can be easily segmented in the following step.

The thresholded images can be further processed by applying a median filter with suitable pixel radius. Applying a median filter on thresholded images essentially eliminates features smaller than the specified pixel radius and is a good method of reducing further unwanted noise.

6.4 Visualizing oxygen phase distribution with varying current densities

During PEM electrolyzer operation, oxygen is produced at the catalyst layer and transported in a gas phase via PTL into the channel. Through-plane transport is the dominant direction for oxygen removal through the PTLs. To date, real time visualization of oxygen distribution in sintered PTLs has not been reported and flow predictions have relied solely on CFD models. **Figure *6-7*** a and b show the 3-D time averaged oxygen saturation in the baseline sintered PTL pore volume at different current densities obtained with X-ray CT. The 3-D volume rendering shows areas of the PTL surface with blocks being the bipolar plate land and open regions being the channel. The raw images can be found in Appendix C.

Figure *6-7* c and d show the corresponding Z-projects of the 3D images and the color bar represents the oxygen saturation, which is volume of oxygen normalized to the PTL pore volume. Although the term 'saturation' is used, it does not mean that the oxygen is stagnant at those locations. It corresponds to the amount of pore volume that is utilized for oxygen transport and those locations are established pathways in a time averaged measurement discourse. For an applied current density of 200 mA/cm^2, the oxygen saturation in pores is relatively low and oxygen takes preferential pathways for removal. The regions under the channel have significantly lower oxygen saturation as compared to saturation under the lands. This provides evidence that oxygen gets trapped under the land and in-plane transport becomes important in this case for its efficient removal. As the current density is increased to 1 A/cm^2, the pore volume utilization increases

significantly, and the preferential pathways appear much more pronounced. This provides firsthand experimental evidence of viscous fingering as the dominating fluid displacement phenomenon in sintered Ti based PTLs. Bulk of the oxygen transport occurs through established pathways that appear better connected with increasing current density. Although pore volume utilization is seen to increase monotonically, the evidence of formation of newly developed pathways is low.

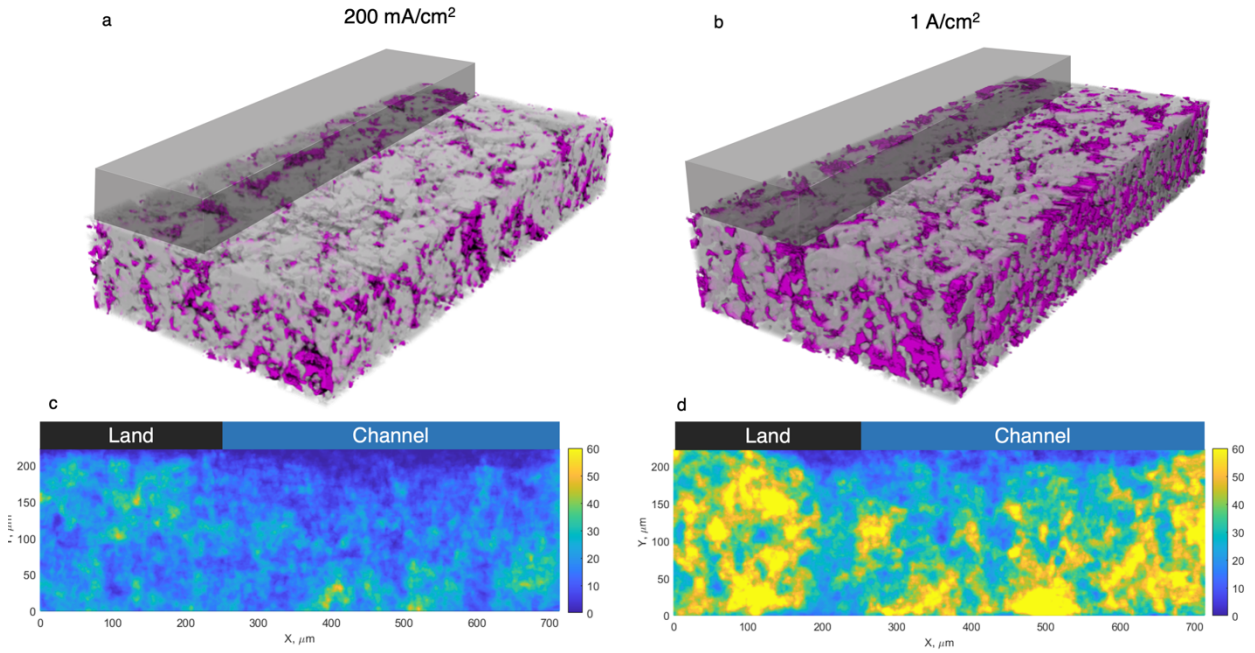

Figure 6-7 3-D volume renderings and corresponding Z-projects of time averaged oxygen saturation in single layer baseline sintered PTL at 200 mA/cm^2 and 1 A/cm^2. The color bar for Z-projects represents the % of oxygen normalized to pore volume. The oxygen is seen to take preferential pathways for removal and gets trapped under the lands.

With the addition of a MPL, the flow profiles show a significant change. **Figure *6-8*** shows the 3-D volume renderings and corresponding Z-projects of MPL 1 at current densities of 200 mA/cm^2 to 2 A/cm^2. Although oxygen in the MPL could not be resolved with X-ray CT, its

general effect on oxygen distribution in the macro porous layer is clearly evident. At low current densities of 200 mA/cm^2, the number of pathways that oxygen takes is significantly higher than the baseline sintered PTL. The presence of MPL increases the injection points for oxygen into the macro porous layer hence the oxygen front appears more evenly distributed along its length. As the current density is increased to 1 A/cm^2, the pore volume utilization is seen to increase, and pathways seem to be better developed similar. However, some oxygen still appears to be trapped under the land.

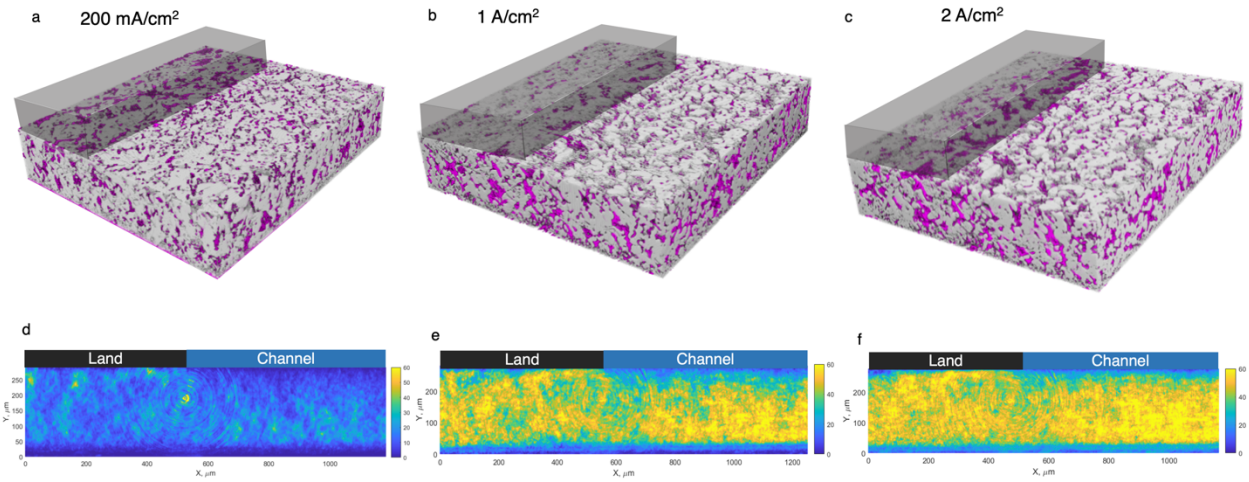

Figure 6-8 3-D volume renderings and corresponding Z-projects of time averaged oxygen saturation in MPL1 at 200 mA/cm^2, 1 A/cm^2 and 2 A/cm^2. The color bar for Z-projects represents the % of oxygen normalized to pore volume. Oxygen could not be resolved within the MPL; however, it allows formation of better and more well-connected pathways for oxygen removal through the macro porous layer.

Interestingly, towards the PTL surface under the lands, the oxygen paths seem to coalesce into in-plane transport directed towards the channel. This is likely because of the proximity of transport pathways creating localized regions of low capillary pressure that can merge into a bigger

section that drains into the channel. Similar observations can be made for MPL 2 which is thicker than MPL 1. **Figure *6-9*** depicts the 3-D volume renderings and corresponding Z-projects for oxygen flow in MPL 2 at current densities of 200 mA/cm^2 and 1 A/cm^2. The microporous layer in MPL 2 is ~40 µm thicker than MPL 1 and the macro porous layer is the same thickness as the other two samples. Hence the oxygen has to travel a much longer path in order to exit into the channels. Similar to MPL 1, the oxygen could not be resolved in the micro porous layer but the transport pathways in the macro porous layer are quantified.

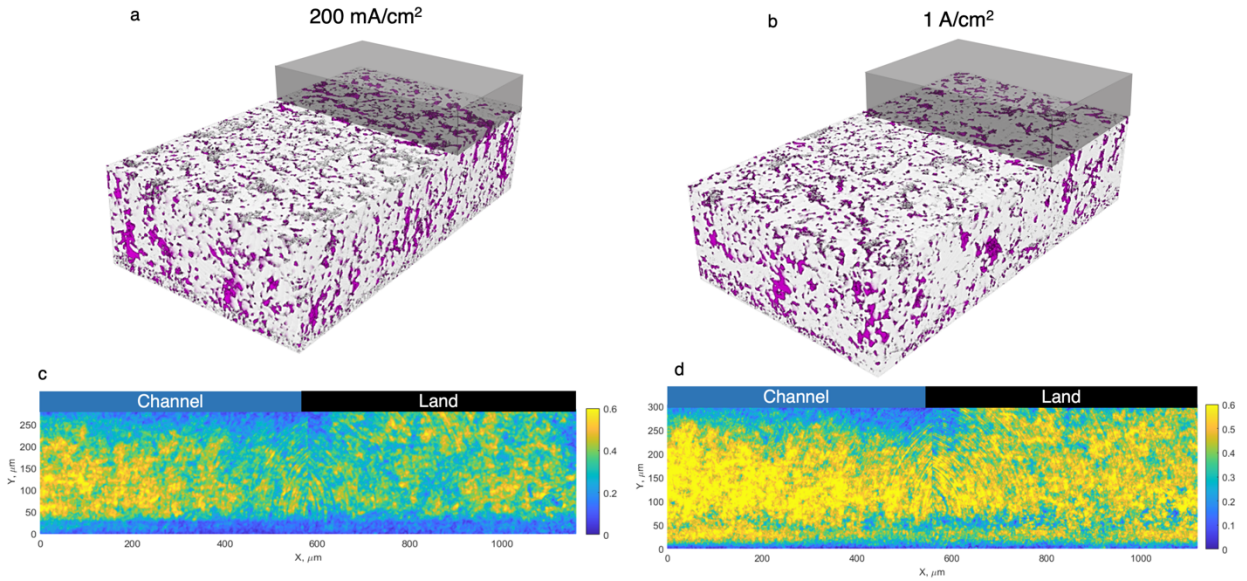

Figure 6-9 3-D volume renderings and corresponding Z-projects of time averaged oxygen saturation in MPL 2 at 200 mA/cm^2 and 1 A/cm^2. The color bar for Z-projects represents the % of oxygen normalized to pore volume.

The gas breakthrough characteristics of PTLs can also be quantified by bubble point tests as referenced in Appendix C. The bubble point is the critical pressure at which oxygen first passes through a fully wet PTL. The applied pressure must exceed the capillary pressure of the fluid in the largest pore throat. Increase in bubble point implies that a higher pressure buildup is required

at the catalyst layer to break the surface tension of water and start oxygen transport. For baseline PTL, the initial bubble point is at 0.46 psi while for MPL 1, it is 0.52 psi and for MPL 2, it rises to 1 psi. From our measurements, we conclude that the bubble point is directly proportional to the MPL thickness and inversely proportional to mass transport resistance.

6.5 Identifying flow regimes in porous transport layers for PEM electrolyzers

The flow through porous media is influenced by viscous forces, capillary forces, gravity, and surface tension of wetting fluids. The two major dimensionless numbers used for flow characterization are the capillary number and viscosity ratio of fluids. The capillary number Ca is defined by ***Equation 6.1***

$$C_a = \frac{\mu_d \nu}{\sigma \cos\theta} = \nu \times \frac{\mu_{oxygen}}{\sigma \cos\theta} \quad \ldots\ldots\ldots\ldots \text{ Eq 6.1}$$

Where μ_d is the viscosity of defending fluid (in this case, oxygen), ν is the injection velocity (***Equation 3***), σ is the interfacial tension and θ is the contact angle. The viscosity ratio of fluids is defined by ***Equation 6.2***

$$M = \frac{\mu_{non-wetting}}{\mu_{wetting}} = \frac{\mu_{oxygen}}{\mu_{water}} \quad \ldots\ldots\ldots\ldots \text{ Eq 6.2}$$

Where μ_{oxygen} and μ_{water} are the dynamic viscosities of oxygen and water respectively.

The effective gas speed is calculated by ***Equation 6.3*** (reproduced from [103] Zlobinski et al)

$$\nu(n) = \frac{\dot{V}_{O_2}(n)}{(t_{H_2O}(i=0) - t_{H_2O}(i=n)) \times l_{PTL}} \ (m/s) \quad \ldots\ldots\ldots \text{ Eq 6.3}$$

Where $\dot{V}_{O_2}(n)$ is the volumetric flux of oxygen calculated according to Faraday's law, t_{H_2O} is the thickness of water at *i=0* mA/cm^2 and at operating current density *i=n* and l_{PTL} is the thickness of the PTL.

By calculating the values of *Ca* and *M*, we can identify flow regimes for oxygen in PTLs. In this case, there are three different flow regimes, namely viscous fingering, capillary fingering, and compact displacement that have been widely identified in literature [114]. Viscous fingering happens when a less viscous fluid displaces a more viscous fluid leading to formation of finger-like protrusions due to an unstable interface. Viscous fingering occurs when viscous forces dominate over the capillary forces and result in a high capillary number (*M*<1, *Ca*>>1) [115]. Capillary fingering occurs when capillary forces dominate over viscous forces (*M*<<1, *Ca* <1) when a non-wetting fluid displaces a wetting fluid in porous media. In this case the non-wetting fluid cannot enter the pore volume until the fluid pressure reaches a certain threshold (~σ/pore diameter, bubble point). Hence the non-wetting fluid displaces the wetting fluid one pore at a time. At each time, the fluid invades regions of low capillary pressure characterized by large pore sizes. The flow behavior thus follows pathways of least resistance leading to capillary fingering that is characterized by a ramified and disordered pathway [116]. Capillary fingering has been widely identified as the dominant transport regime in PTLs [103]. The plot showing various flow regimes as a function of *M* and *Ca* are shown in Appendix C.

Calculating the logarithmic viscosity ratio of oxygen to water at 60^0 C using equation 6.2,

$$\log(M_{60C}) = \log\left(\frac{2.244 \times 10^{-5}}{4.656 \times 10^{-4}}\right) = -1.32$$

We calculated local velocity of oxygen gas from LBM CFD which gave average local velocity for baseline sintered PTL at $v_{PTL} = 0.068\, m/s$ and $v_{MPL} = 0.585\, m/s$ at 1 A/cm^2 current density and 1 mg/cm^2 IrOx loading. Plugging these values in Equation 6.1, the logarithmic capillary

numbers for baseline PTL is *log* (C_a)= -4.32 and for MPL 1, *log* (C_a)= -3.4. Although C_a <<1, its increase for MPLs is indicative of suppression of capillary fingering. According to *log (Ca)* vs *M* phase diagram for oxygen flow by Chen et. Al [117], an increase of *log (Ca)* from -4.32 to -3.4 at above calculated *M* value shifts flow regime from capillary fingering to viscous fingering [118][119]. **Figure *6-7*** that shows oxygen flow through baseline sintered PTL, clearly shows a capillary fingering regime whereas **Figure *6-8*** and **Figure *6-9*** that show flow with MPL 1 and MPL 2, show a suppression in capillary fingering and transition to viscous fingering. This is an important observation as MPLs can change the flow regimes leading to better reactant transport and oxygen removal.

The physical interpretation of these shift in flow regimes is illustrated in **Figure *6-10***. The regions marked in green represent the primary oxygen fingers that advance from the interface and moves in the through plane direction towards the channel. For baseline sintered PTLs, these oxygen fingers bifurcate into secondary fingers shown by red circles that advance laterally due to low capillary pressures in neighboring pore throats and invade interface sites thus inhibiting water flow and cause site masking.

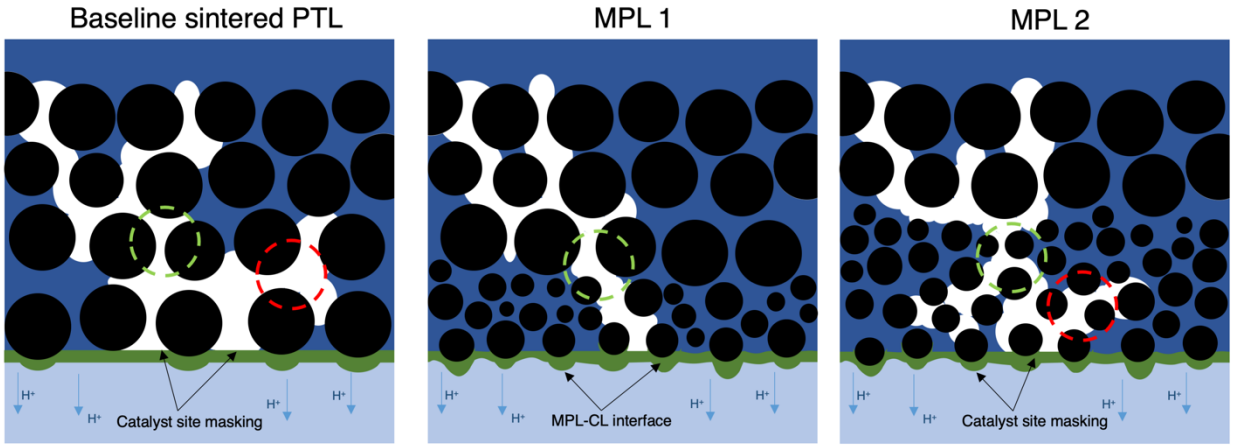

Figure 6-10 Oxygen gas invasion patterns through MPLs and macro porous layers. Green dotted circles represent primary advancing oxygen finger and red dotted circles represent lateral displacement of oxygen fingers

In the presence of a thin MPL, the primary gas finger cannot invade laterally since local capillary pressure is high and pore gradient in a near vicinity forces oxygen to move in a through plane direction. In case of thicker MPLs, lateral transport is more likely due to higher thickness and high bubble point pressure. If local capillary pressure is lower than the breakthrough pressure, oxygen will travel in the lateral direction and mask interface catalytic sites [101].

For the baseline PTL, the oxygen preferential pathways (capillary fingering) are partly dominated by the triple phase contact distribution since they are the oxygen injection points into the PTL. A heterogeneous TPCA distribution will cause underutilization of catalyst and consequently of transport pathways leading to increased kinetic and mass transport overpotentials. MPL addition reduces the dependance of oxygen pathways on TPCA distribution but rather on PTL morphology. For the baseline sintered PTL, the triple phase contact points are farther away from each other, so the bubble growth and detachment frequency is low as compared to MPLs where the contact points are much closer resulting in a higher frequency of bubble growth and detachment. Hence, the time

of catalyst inactivity because of suppression in capillary fingering leading to bubble masking is much lower for MPLs resulting in a higher utilization.

Figure *6-11* shows the average oxygen saturation throughout the thickness of the PTL at various current densities starting from the catalyst layer to the channel. For all three PTLs, the oxygen saturation is maximum near the catalyst layer and drops to a minimum value at the PTL channel interface. These results are consistent with the modeling and experimental results previously reported in literature [111][120][121]. The average oxygen saturation increases monotonically with increase in current density for all PTLs. The initial dips in oxygen saturation observed for MPL samples is because oxygen could not be resolved within the MPLs. For the baseline PTL at 200 mA/cm^2, the maximum saturation of oxygen in the pores near the catalyst layer is 23 %. As the current density is increased to 1 A/cm^2, the oxygen saturation near the catalyst layer increases to 40 %. For MPL 1 the maximum oxygen saturation near the catalyst layer is 34 % at 200 mA/cm^2, which increases to 47 % at 1 A/cm^2, and 53 % at 2 A/cm^2. For MPL 2, an instability region exists where the MPL merges into the macro porous layer. The localized dips in the oxygen near the MPL 2-macro porous phase is due to this instability region generated either by sudden transition into a different pore morphology leading to water saturation or staining agent accumulation. Although the latter explanation is less likely since crystallized NaI appears bright and we did not find any evidence of crystallization near the MPL-macro porous layer boundary.

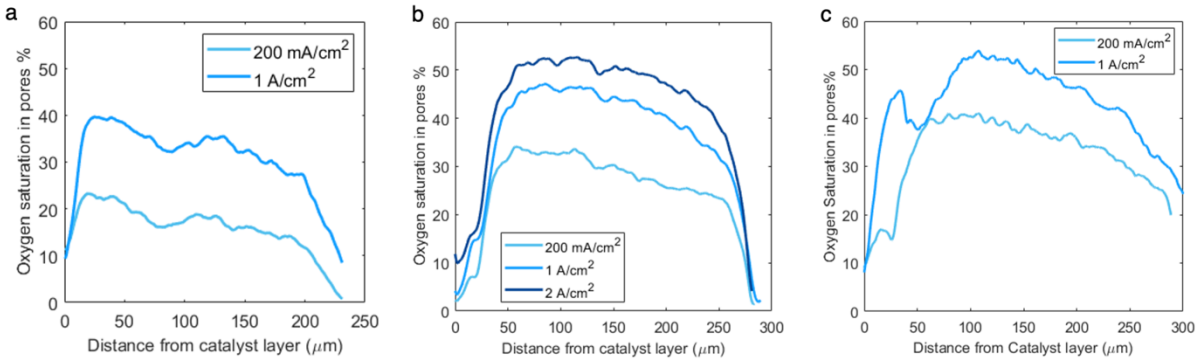

Figure 6-11 Average oxygen saturation in pores as measured from the catalyst layer through the PTL thickness at different current densities for a. baseline PTL, b. MPL1, c. MPL 2

The average oxygen saturation throughout the PTL for MPLs generally show a higher value at a given current density than the baseline PTL as shown in **Figure *6-12*** a. Oxygen saturations have been averaged starting at 50 µm from the catalyst layer into the macro porous layer till the channel such that the MPLs are excluded. Although there appears to be a direct relation between the thickness of the MPL and average oxygen in the PTL, the underlying physics is unclear and needs to be investigated with CFD models.

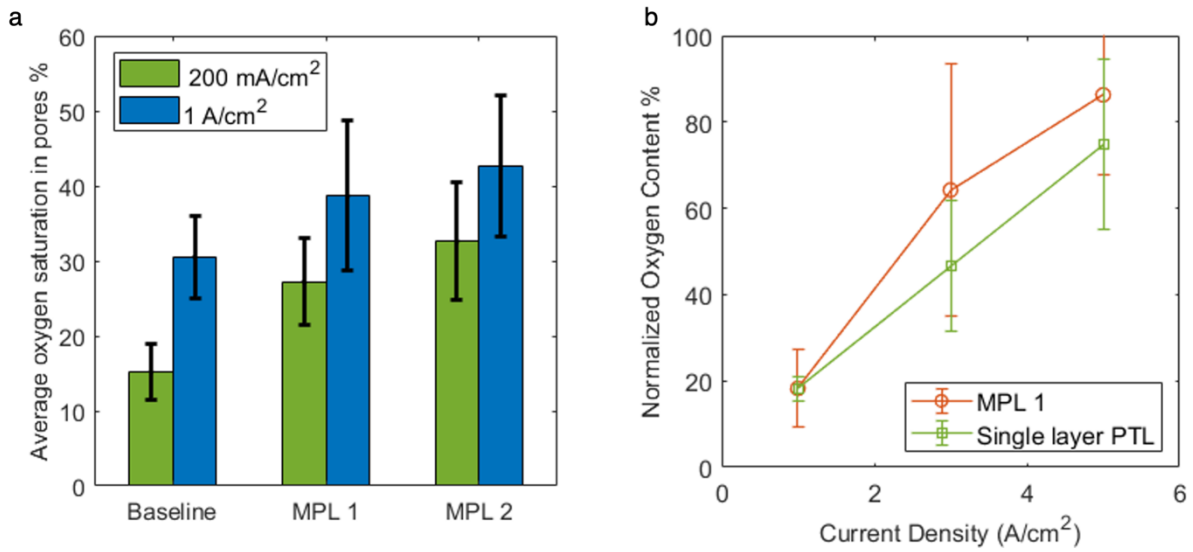

Figure 6-12 Average oxygen saturation in PTLs and corresponding oxygen removed in channels as measured using Micro X-ray tomography and radiography respectively. The average oxygen in pores is measured starting at a distance of 50 µm from the interface since oxygen could not be resolved in the MPLs. Radiography was conducted with DI water circulated into the cell at 20 ml per minute and 1500 radiographs were collected at intervals of 5 ms.

The effect of MPLs on oxygen removal into the channels can be studied with high-speed X-ray radiography as shown in **Figure *6-12*** b. The radiography images were collected at applied current densities of 1 A/cm^2, 3 A/cm^2 and 5 A/cm^2 with DI water circulated into the operando cells at a flow rate of 20 ml per minute. The exposure time was set to 5 ms and ~1500-2000 radiographs were collected at each applied current density. The radiography image processing procedure has been discussed in detail in Chapter 3. At 1 A/cm2, the average oxygen content in the channels was found to be 20 % for both baseline PTL and MPL 1. As the current density is increased to 3 A/cm^2, the oxygen content increased to 42 % for baseline PTL and 62 % for MPL 1 with a higher error margin. Similarly, with increase in current density to 5 A/cm^2, the oxygen saturation in baseline PTL increased to 70 % whereas for MPL 1, the oxygen content starts to level out around 80 %

which is consistent with our previous observations in Chapter 4. The oxygen content in the channel at a given time is an indication of the ability of the PTL to remove oxygen from the catalyst layer. Higher the oxygen content in the channels, higher is the efficiency of the PTL to remove oxygen. Since MPL samples show a higher pore volume utilization for oxygen flow, the trends in oxygen content within PTLs correlate directly to the trends in oxygen removal into the channels. At 1 A/cm^2, MPL 1 has over 10 % higher average oxygen saturation than baseline as seen in **Figure *6-12*** a. This is exactly within the error of oxygen content seen in radiography analysis at 1A/cm^2 in **Figure *6-12*** b further reinforcing the direct correlation as stated above. Hence, the increase in utilization of transport pathways and suppression of viscous fingering due to MPL make oxygen removal much efficient with the presence of an MPL.

6.7 Design considerations for PTL morphological optimization

Based on the operando time averaged oxygen saturation studies and electrochemical data, the following major factors influence overall cell performance and durability when MPLs are present:

1. Triple Phase contact: The triple phase contact can be enhanced with MPLs but the form factor of MPLs is essential to determine electrocatalytic activity of the interface which influences catalyst utilization.
2. MPL thickness and morphology: Although TPCA is improved with MPLs, the two-phase transport is affected by the thickness of MPL since higher thicknesses and small pore sizes constrict pore throat sizes and impose higher capillary pressure which has been found to be the governing factor for gas movement in porous media. Higher thickness can also affect

heat transfer from the catalyst layer and can generate localized hot spots that can dehydrate the membrane.

3. Hydrophobicity: The degree of hydrophobicity and wettability of the MPL can alter the contact angle of water thus affecting its transport to the catalyst layer and cause discrepancies in bubble nucleation and detachment dynamics.

With these three factors in consideration, the MPL morphology should be tuned according to catalyst loading such that:

- Lower loadings should be used with finer MPL particle sizes to maximize interfacial contact. We recommend using Ti powders with 2-4 μm particle diameter and ~40 % porosity to make MPLs with a thickness of 20 μm for CCM loadings below 1 mg/cm^2.
- The MPL contact point density should be 1.3-2 per μm^2 of CCM for maximum utilization of catalyst and increased durability.
- Overall PTL thickness should be under 300 μm to optimize gas flow while imparting sufficient mechanical support to the catalyst layer. Thicker PTLs can induce mass transport overpotentials, poor heat transfer and higher electrical resistance.
- MPL hydrophobicity should be tuned according to its morphology to maximize bubble detachment and water delivery to the catalyst layer.

6.8 Conclusions and summary

In this study, for the first time, we demonstrated the use of stained water to quantify time averaged oxygen saturation in sintered PTLs without MPL and with MPLs of varying thicknesses using X-ray microtomography. The first sample was a baseline sintered PTL with no MPL, the second sample was MPL 1 with a thin MPL of 20 μm and the third sample studied was MPL 2 with a

thicker MPL of 58 μm. We quantified the effect of MPLs on triple phase contact at the interface and found that MPLs result in over 20 % higher TPCA and increase the PTL contact point density by twice as compared to sintered PTLs with no MPL. We developed novel image processing techniques to segment oxygen from total pore volume and calculated pore volume utilization. Baseline sintered PTLs were found to have lower average pore volume utilization than MPL samples. MPL samples were found to have over 20 % higher pore volume utilization at any given current density. Higher pore volume utilization in PTL was also found to proportionately increase oxygen content in channels implying improved oxygen removal efficiencies. Our bubble point measurements showed increased bubble point pressures for increasing MPL thicknesses. Hence bubble points show direct relation to MPL thickness and inverse relation to mass transport overpotentials.

Based on the 3D data as well as calculations of *Ca* and *M*, baseline sintered PTL was found to have capillary fingering as the dominant transport regime. Capillary fingering occurs when capillary forces dominate in a porous media and oxygen takes preferential pathways of removal based on following pore-to pore transition following pathways of least capillary pressure. MPLs are seen to suppress capillary fingering and transition oxygen flow to viscous fingering which is a very important result.

7. Engineering interfaces for durability

The previous chapters focused on understanding the nature of interfaces formed with different electrode combinations and PTLs. Specifically, we down selected sintered PTLs with MPLs and optimized their morphology for enabling maximum catalyst utilization at low catalyst loadings. This topic covers the effect of interfacial properties on system durability by systematically reviewing state of the art understanding of OER mechanisms and its interrelation to Ir dissolution. Based on understanding of Ir transformation above OER potentials, an accelerated stress test protocol is developed and tested. Finally, durability testes are conducted with PTLs mentioned in chapter 6 and methods to engineer durable interfaces are proposed.

7.1 Kinetics of oxygen evolution on IrOx based catalysts

OER imparts significant overpotential to the system operation since it is kinetically sluggish than HER as shown in ***Figure 7-1***. OER is a four electron-proton coupled reaction while HER is only

a two electron-transfer reaction, and hence it is expected that OER requires higher energy (higher overpotential) to overcome the kinetic barrier of OER to occur[122].

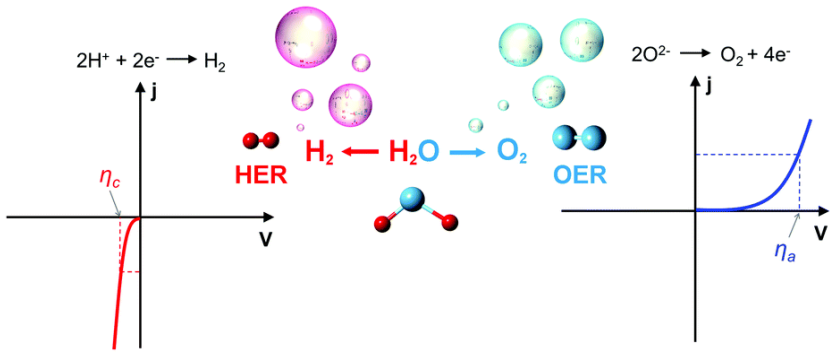

Figure 7-1 Polarization curves for HER (left) and OER (right). The *ηc* and *ηa* are the overpotentials for cathode and anode at the same current (j), respectively (adapted from reference [122]) .

To date, several studies have been conducted to propose reaction pathways for OER on heterogeneous catalysts based on kinetic studies, or density functional theory (DFT) calculations. ***Figure 7-2*** shows some of those pathways. However, none of the proposed OER mechanisms have been experimentally validated. In a seminal work, Matsumoto and Sato [123] proposed kinetic models for a variety of different conceivable OER mechanisms, some of which are shown in **Figure 7-2** a I-III. For most of these pathways, the forming and cleaving of M-OH bond to form intermediate metal oxides or hydroxides has been considered the rate determining step of the reaction. For metals that bind too strongly to oxygen, the activity is limited by proton-electron transfer to O* or OH*. On the other hand, for metals that bind oxygen too weakly, the activity is limited by proton-electron transfer to O_2* (associative mechanism) or splitting of the O-O bond in O_2 (dissociative mechanism), depending on the applied potential[124]. Because catalyst materials for the OER are generally metal oxides, volcano plots for the OER have been constructed for a wide variety of metal oxide surfaces using $\Delta G_O - \Delta G_{OH}$ as the descriptor as shown in **Figure 7-2**b.

a

I) Oxide Path		II) Electrochemical Oxide Path	
1)	$H_2O + M \rightarrow M\text{-}OH + H^+ + e^-$	1)	$H_2O + M \rightarrow M\text{-}OH + H^+ + e^-$
2)	$2\,M\text{-}OH \rightarrow M\text{-}O + M + H_2O$	2)	$M\text{-}OH \rightarrow M\text{-}O + H^+ + e^-$
3)	$2\,M\text{-}O \rightarrow 2\,M + O_2$	3)	$2\,M\text{-}O \rightarrow 2\,M + O_2$
III) Electrochemical Metal Peroxide Path		**IV) DFT-predicted Peroxide Path**	
1)	$H_2O + M \rightarrow M\text{-}OH + H^+ + e^-$	1)	$H_2O + M \rightarrow M\text{-}OH + H^+ + e^-$
2)	$2\,M\text{-}OH \rightarrow M\text{-}O + M + H_2O$	2)	$M\text{-}OH \rightarrow M\text{-}O + H^+ + e^-$
3)	$M\text{-}O + H_2O \rightarrow M\text{-}OOH + H^+ + e^-$	3)	$M\text{-}O + H_2O \rightarrow M\text{-}OOH + H^+ + e^-$
4)	$2\,M\text{-}OOH \rightarrow M\text{-}O + H_2O + O_2 + M$	4)	$M\text{-}OOH \rightarrow M + O_2 + H^+ + e^-$

b

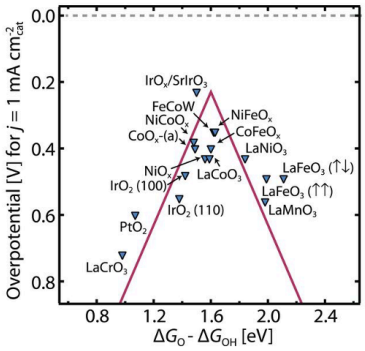

Figure 7-2 a. Proposed reaction mechanisms for the oxygen evolution reaction b. Volcano plot for OER activity on various metal oxides (adapted from references [13],[125])

For OER catalysis in acid, IrO_2 and RuO_2 are considered among the highly active catalysts because of their stability in binding to reaction intermediates [126]. For instance, rutile-type RuO_2 exhibits excellent OER catalytic activity in both acidic and alkaline electrolytes. However, RuO_2 is highly unstable in both electrolytes under high anodic potential, in which it will be oxidized to form RuO_4 and dissolved in solution. The advantage of IrO_2 is that it is more stable than RuO_2, and it can sustain at higher anodic potential in both acidic and alkaline electrolytes. Although IrO_2 has indeed been shown experimentally to be among the better OER catalysts today, based on activity and stability under reaction conditions, it is far from an ideal OER catalyst in terms of activity and is not completely stable under high oxidative potentials. Due to their high cost and low earth abundance, it is important to deeply understand the interfaces they form and nature of their active sites to control and tailor their properties in the appropriate manner to improve catalyst utilization and increase mass activity. Combining theory, computational studies, and sophisticated in situ and operando characterization techniques will help understand and address these critical issues.

7.1.1 Theoretical modeling of OER

The interdependence of overpotential on current density is one of the most important relationships in electrochemistry and is modeled by the Butler-Volmer equation (7-1).

$$i = i_0 \left[exp\left(\frac{\alpha_a nF\eta}{RT}\right) + exp\frac{\alpha_c nF\eta}{RT} \right] \quad \ldots\ldots. \text{ Eq7-1}$$

Where i is the current density, i_0 is the exchange current density, α_a and α_c are the anodic and cathodic charge transfer coefficients respectively, n is the number of electrons transferred, F is the faraday's constant η is the overpotential and T is the absolute temperature. In practical systems, a significant overpotential is required to drive the required amount of current density. In general, a faster increase in current density with smaller overpotential is desired. Under high anodic overpotential conditions, the overall current is mainly attributed to the anodic end while the contribution from the cathodic part is negligible as seen in ***Figure 7-3***a. Hence the Butler-Volmer equation can be simplified to a Tafel equation (2).

$$i \approx i_0 \left[exp\left(\frac{\alpha_a nF\eta}{RT}\right) \right] \quad \ldots\ldots\ldots \text{ Eq 2}$$

$$\log(i) = \log(i_0) + \frac{\eta}{b} \quad \ldots\ldots\ldots \text{ Eq 3}$$

$$b = \frac{\partial \eta}{\partial \log(i)} = \frac{2.303RT}{\alpha F} \quad \ldots\ldots\ldots \text{ Eq 4}$$

Where b is the Tafel slope obtained by plotting ln |i| – or of $\log_{10}$ |i| – versus η, that yields a straight line in this region. From its slope and intercept the transfer coefficient and the exchange current density can be obtained. The experimentally obtained Tafel plots and its temperature dependance

is shown in ***Figure 7-3***b. The linearity of the Tafel plot starts to deviate after a certain current density when the mass transport and other losses start to play a significant role. Hence, for practical purposes, the Tafel slope is obtained by the linear fitting of points within the current density ranges of 10-100 mA/cm^2 of an iR free polarization curve where the current is almost entirely dictated by reaction kinetics.

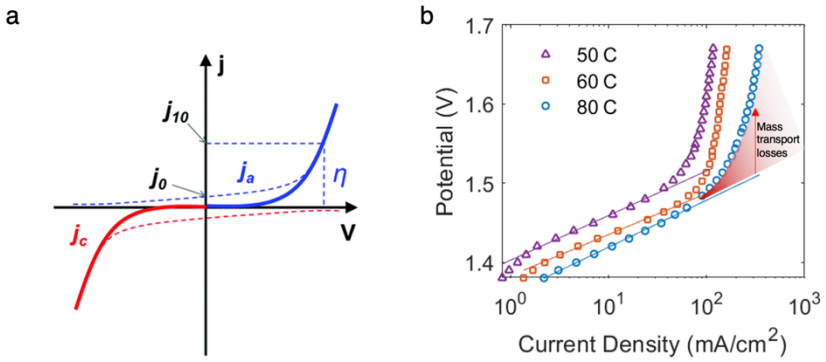

Figure 7-3 a. Polarization curves for cathode (red) and anode (blue) electrode. j_0 is the exchange current when $j_a = -j_c$. j_{10} is a commonly agreed value for one to report overpotential (η) at this current (assuming the area is 1 cm^2) value b. Experimentally obtained Tafel slopes showing temperature dependance and onset of mass transport losses.

A smaller Tafel slope means that a lesser overpotential is required to drive the same current density implying good electrocatalytic kinetics and a higher voltage efficiency. Furthermore, the Tafel slope give insight into the mechanism of the reaction especially for elucidating the rate determining step. The aforementioned Tafel analysis has some phenomenological considerations as based on works by Schmickler and Santos [127]. However, equation 4 is a simplified derivation of the Tafel slope, which assumes the coverage of the reaction intermediate species in the reaction progress as constants. When the actual surface kinetics are considered, the Tafel slope also depends on the

surface oxides coverage [90], the nature of the electrode and the interface leading to dynamic utilization of the catalyst, which has been previously reported and substantiated in literature [112][1].

In a single-electron transfer reaction, the transfer coefficient (α) usually refers to symmetry factor (β) and can be seen in equation 5.

$$\alpha = \beta = \frac{1}{2} + \frac{\eta}{\lambda} \qquad \text{……. Eq 5}$$

Commonly, the symmetry factor β is equal to 0.5 since the overpotential (η) is usually much smaller than the re-organization energy (λ). Considering this assumption, we can calculate the Tafel slope of 120 mV dec^{-1} from equation 4. This suggests that the rate-determining step in the reaction is controlled by the single-electron transfer step. In practical electrochemical systems, the situation is much more complex, and reactions may proceed via multiple steps. For these multiple electron reactions, the transfer coefficient has been derived by Bockris and Reddy [128] as represented in equation 6.

$$\alpha_a = \frac{n_b}{\nu} + n_r\beta \qquad \text{…… Eq 6}$$

where n_b is the number of electrons that transfer back to the electrode before the rate-determining step, ν is the number of rate-determining steps that have taken place in the overall reaction and n_r is the number of electrons that participate in the rate-determining step. According to Schmickler and Santos [127], it is improbable to have more than one electron transferred simultaneously and

hence n_b is either 1 or 0. Once the rate-determining step is an electron transfer reaction, n_b is equal to 1 while the value of n_b is 0 in the case of chemical reaction. Equation 6 is of vital importance for predicting the rate-determining step. For a 4-electron transfer reaction like OER, if the rate-determining step is the third electron transfer step, n_b and ν are equal to 2 and 1 (n_r and β are 0), respectively. This yields a transfer coefficient of 2 and a Tafel slope of 30 mV dec^{-1}.

Hence, it is evident that different Tafel slopes suggest different rate-determining steps. In each system, the transfer coefficient and the corresponding Tafel slopes are closely correlated to the electrons involved in the reaction. In a consecutive reaction, a smaller Tafel slope implies that the rate-determining step is at the ending part of the multiple-electron transfer reaction, which is a characteristic of a good electrocatalyst[122].

7.1.2 Mechanisms of OER

The OER is a complex electrochemical reaction involving four electron and proton transfers and at least two reaction intermediates. The initial studies conducted by Brockis et al [129] using Tafel analysis showed that the reaction proceeds via the electrochemical oxide pathway illustrated in **Figure *7-2***a. Since then, several studies have been done to elucidate OER pathways each taking a different approach. Most of the proposed mechanisms include the same intermediates such as M-OH and M-O, while the major difference is probably featured around the reaction that forms oxygen. There are two different approaches to form O_2 from M-O intermediate as shown in ***Figure 7-4***a. The first pathway is direct combination of 2M-O to form oxygen (green route) and the other is through the formation of M-OOH which subsequently decomposes to O_2 (black route). Despite this difference, the common consensus is that the electrocatalysis of OER is a heterogeneous

reaction, in which the bonding interactions (M–O) within the intermediates (MOH, MO and MOOH) are crucial for the overall electrocatalytic ability.

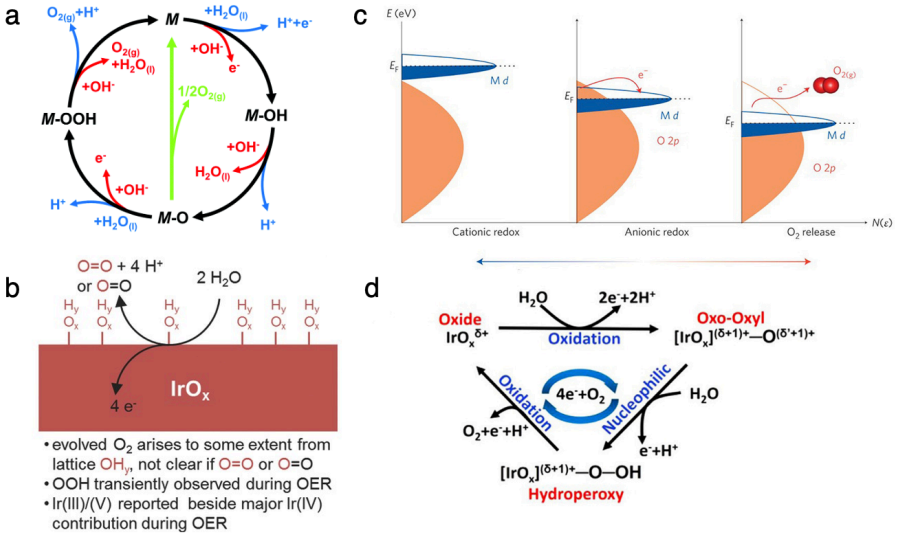

Figure 7-4 a. The OER mechanism for acidic (blue line) and alkaline (red line) conditions. The black line indicates that the oxygen evolution involves the formation of a peroxide (M–OOH) intermediate (black line) while another route for direct reaction of two adjacent oxo (M–O) intermediates (green) to produce oxygen is possible as well (adapted from [122]) b. Graphical representation of the experimental in-situ insights into the OER mechanism on IrOx (adapted from [13]) c. Schematic representation of O 2p bands penetrating into Ir d orbitals and triggering an anionic redox process (adapted from [130]) d. OER scheme showing the formation of oxyl species, as a result of hybridization of Ir and O orbitals, which are prone to nucleophilic attack by water and the formation of an O−O bond (adapted from [131])

In a Differential Electrochemical Mass Spectrometry (DEMS) with isotope-labeled electrolyte ($H_2{}^{18}O$ enriched) study on thermally prepared IrO_2 [132] a OER study showed the amount of lattice

oxygen, which is involved in the oxygen exchange reaction, is in the order of 1% of the total IrO_2 loading. They also showed that in acidic media, only several outer monolayers of IrO_2 participate in the OER. However, this DEMS study did not address the issue whether O_2 was formed from two oxide lattice-related oxygen atoms or if an oxygen atom from the oxide reacts with water to form O_2. Based on these in-situ insights, neither the acid-base nor the direct coupling mechanism can be conclusively confirmed or dismissed for IrOx [13] (***Figure 7-4***b). Hence, more in-depth DEMS investigations might be able to provide additional mechanistic insights.

To date, many ex-situ X-ray photoemission spectroscopy (XPS) studies of IrO_2 synthesized as thin films, hydrous oxides, or other forms (keeping Ir and O ratio constant) have proposed a cationic catalytic cycle involving an electrochemical oxide pathway, where iridium is oxidized to an Ir^{VI} intermediate which is reduced back to Ir^{IV} in the next step with a simultaneous release of an oxygen molecule. While other in-situ XPS and XAS studies have, in contrast, suggested a Ir^{V}–Ir^{III} transition, with the presence of both oxidation states under the OER conditions [133]. This mechanism was experimentally validated by Sivasankar et al., who successfully detected Ir-OOH intermediate by probing iridium oxide nanoclusters using rapid scan FT-IR spectroscopy [134]. These studies were based on cationic redox processes which have been conventionally proposed mechanism of charge storage.

Tarascon et al [135] first proposed the idea of an anionic redox mechanism and how it led to the discovery of anion-driven capacity storage in Li-ion battery and its relation to oxygen evolution electrocatalysis. They confirmed that shifting the p-band of the oxygen atom closer to the Fermi level in metal oxides with a highly covalent network can trigger the redox activity of the lattice

oxygen atoms (***Figure 7-4***c). J. Velasco-Vélez et al [131] studied the electronic structure of a free standing graphene electrode decorated with Ir NPs for OER in acidic environment. Their In-situ X-ray spectroscopy revealed that OER is driven by the formation of shared electron-holes in the O 2p and Ir 5d which activate oxygen by making it electron-deficient. Thus, the oxidation of water into dioxygen involves the formation of an oxo-oxyl-metal-complex and the oxygen in this complex is susceptible to nucleophilic attack by water or OH, which results in hydroperoxy bond formation. The hydroperoxy species is then finally transformed into molecular dioxygen (***Figure 7-4***d).

Understanding the changes in oxidation state of Ir with OER is of major significance since these changes are directly related to the charge storage mechanism which has been shown to be the driving force of the reaction. Recent in-situ and ex-situ spectroscopic techniques reveal that OER may be explained as having contributions of both cationic and anionic mechanisms. It has been shown that, as a result of a strong hybridization of the iridium and oxygen orbitals, the positive charge is shared between cations and anions [131]. Specifically, the oxidation state of Ir influences the formation of the reactive oxyl species. With application of high anodic potentials on the catalyst, the electron-deficient oxygen species accumulates a positive charge thereby decreasing the activation energy for the nucleophilic attack of water molecules and the formation of an O−O bond, which is currently understood to be the rate-determining step of the OER.

7.1.3 Interdependence of OER and iridium dissolution mechanisms

Achieving a balance of activity and stability of Ir catalysts is the perquisite of making efficient and durable PEMWE systems. From recent works, there is a consensus that dissolution of iridium is

the dominant degradation mechanism at industrially relevant current densities and potentials. The detection and elucidation of dissolution kinetics of iridium has been made possible with techniques such as in-line ICPMS [136][133]. The dissolution kinetics are affected by both the operational parameters and physicochemical properties of the catalyst. In the case of iridium, the less active rutile (IrO_2) form is known to be stable under the OER conditions, whereas its amorphous analogues exhibit higher activity for oxygen evolution, but also lower stability. The Ir dissolution studies suggest that the OER mechanism and dissolution are linked by a common reaction intermediate. Additionally, the participation of lattice oxygen in OER can lead to destabilization of the Ir-oxide structure and result in dissolution.

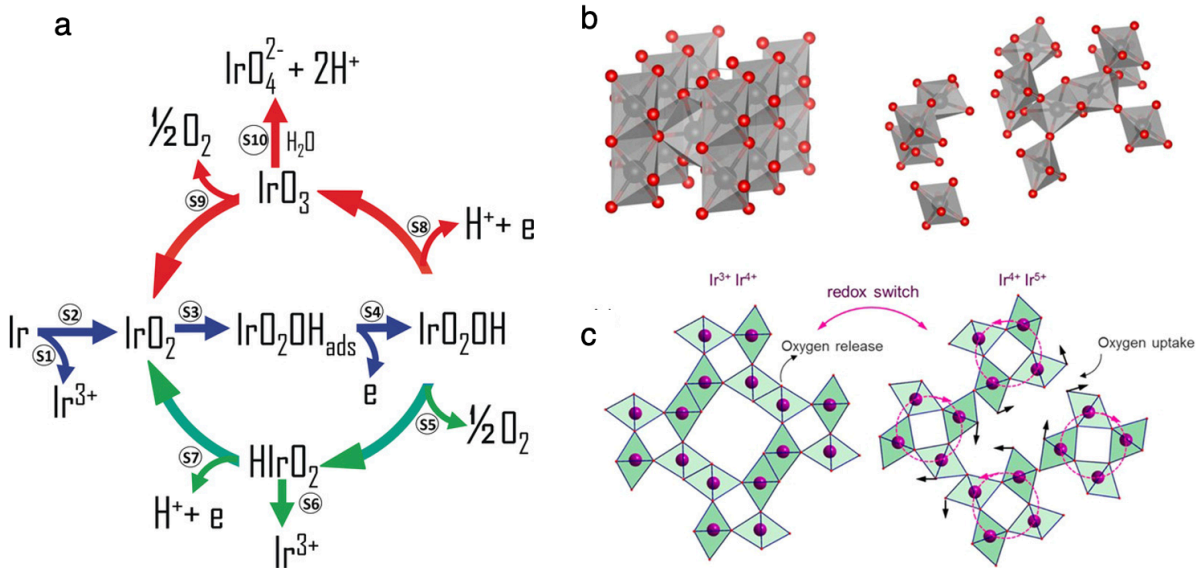

Figure 7-5 a. Universal mechanism correlating both the OER and dissolution pathways proposed by Kasian et al [137] b. Ordered rutile structure with edge-sharing octahedra and hydrated amorphous structure with activated corner-sharing oxygen atoms (adapted from[138]) c. "Paddle wheel" reaction scheme, proposed by Willinger et al [139]

The potential dependent association of OER mechanism and Ir dissolution was proposed by Kaisan et al (***Figure 7-5***a). The blue arrows indicate the first step of the OER onset which is the elimination of water and adsorption of an OH radical on the surface of the catalyst which is material independent. This is followed by the oxidation of the iridium center and leads to the formation of the $Ir^{V}O_2(OH)$ intermediate. The following steps are potential dependent with green arrows indicating low potentials (<1.23V) and red arrows indicating high anodic potentials (>1.23V). If the OER is catalyzed by thermal oxide, the required potential is high enough for further oxidation of iridium to $Ir^{VI}O_3$. This intermediate can then either decompose to O_2 and IrO_2 and close the catalytic cycle or react with water and dissolve as IrO_4^{2-}. At low potentials, however, the $Ir^{V}O_2(OH)$ complex can decompose to O_2 and $HIr^{III}O_2$ after which it can dissolve as Ir^{III} with the release of a proton and subsequently close the catalytic cycle. Hence the Ir dissolution can start before OER onset.

The structure property relationships and stability of various Ir-based catalysts like highly active perovskites, amorphous IrOx, metallic iridium, and rutile IrO_2 were examined by Geiger et al [140]. They found that the rate of dissolution depends on the structure of the catalyst. The presence of non-noble metals in the perovskites results in the amorphization and hydration of iridium oxide from its original octahedral structure after being immersed in acidic electrolyte. The amorphous structure was found to have higher corner-sharing oxygen atoms in contrast to the original structure with edge-sharing oxygen atoms that resulted in enhanced iridium dissolution (***Figure 7-5***b). The authors concluded that the involvement of lattice oxygen in the OER depends on the structure of the oxide. The overall stability of different oxides depends on two major factors; firstly, the stability of the reaction intermediates which could be higher for the rutile structure compared to

the amorphous oxides and secondly by the ratio between the edge- and corner-sharing iridium octahedra. ***Figure 7-5***c denotes the presence of interconnected hollandite-like motifs, in which oxygen is evolved through a so-called "paddle-wheel" mechanism as observed by the authors. The presence of other cations like K+ can stabilize the open hollandite structure.

7.2 Designing AST protocols for PEM electrolyzers

Accelerated stress tests (ASTs) are required to predict PEM electrolyzer system degradation throughout their expected lifetimes. Standardized AST protocols should be able to predict long term performance by considering the impact of varying field conditions and their effect on materials and system reliability. Since PEM electrolyzer systems are to be coupled with renewable energy, the intermittency of solar, wind and other sources must be considered while designing AST protocols. Moreover, for developing AST protocols collaboratively, we need to establish baselines that may be reproduced across research labs that make data comparison fair and reproducible.

The first step in designing an AST protocol is to understand the degradation mechanisms of various components such as anode IrOx catalyst, bipolar plates, Ti PTLs etc. An extensive discussion of OER mechanisms and their correlation to Ir dissolution has been done in the first part of this chapter. **Figure *7-5*** indicates the state-of-the-art understanding of OER mechanism and its link to Ir dissolution. At OER onset, Ir may transition from Ir(II) which is a stable form to Ir(III) which has been found to be unstable and soluble form. Although not all Ir is lost by solvation, but the Ir complexes have been found to redeposit at the catalyst layer, between the membrane or migrate to the cathode side. Additionally, the OER mechanisms and corresponding dissolution mechanisms can be significantly different based on type of Ir, surface oxides or method of synthesis as

discussed in the previous section. Ir catalysts from different manufacturers have varying quantities of metallic Ir, various Ir oxides and sub oxides/hydrates. Hence the stability and activity of these mixtures can be significantly different and may or may not go through a specified degradation mechanism. One way to increase the stability of Ir is to use novel catalyst support structures such as Antimony doped tin oxides (SnO_2, Sb, ATO) which have been shown by multiple studies to suppress Ir dissolution. A recent study employing operando near-ambient pressure X-ray photoelectron spectroscopy for these supported catalysts by Saveleva et. al showed reduced formation of unstable Ir(III) complexes as compared to unsupported IrOx during OER.

Along with anode catalyst degradation, the membrane and ionomer also degrade during the system lifetime. Membrane degradation can manifest as thinning which can cause crossover of hydrogen gas to the anode side resulting in a dangerous flammable mixture of hydrogen and oxygen causing fatal cell failure especially during differential pressure operation. Membrane degradation can be measured by fluorine emission rate (FRR). The FRR has been shown to increase with increasing cell temperature and decreasing current density, but the relationships are not linear making it difficult to associate this degradation mechanism to overall cell performance. The membrane can further degrade with cationic contaminants such as Fe^{+3}, Ca^{+2}, Cu^{+2} etc. in feed water. A momentary failure of water purification system can cause these cations to block proton transport sites and increase cell ohmic resistance.

The major mechanism of PTL and bipolar plate degradation comes from metal passivation by oxide layer formation at operating cell potentials and local pH. Ti passivation leads to increase in contact resistance between the PTL and the catalyst layer as well as bipolar plate. One method to mitigate passivation is by coating Ti PTLs and bipolar plates with noble metals such as Ir and Pt. However, this further increases the cost of the system. Another way is by making PTLs and bipolar

plates from stainless steel and coating with non-precious metals such as Nb. Although, this method needs more validation and flawless coatings to meet conductivity, mechanical strength, and durability requirements.

The second step in designing AST protocols is selection of stressor profile that accelerates the above mentioned degradation mechanisms. Of course, one can build short cell stacks and operate at high current density for extended amount of time with intermittent startup-shutdown to simulate systems on the field, but this approach is time consuming, requires availability of resources, automatic test stations. One of the approaches is to use square wave potential cycling as demonstrated by S. Alia et al. The square wave potential cycling was found to result in a similar Ir loss pathway as renewable power load profiles. Based on thorough literature review and understanding of OER pathways on IrOx, we developed a square wave AST protocol similar to S. Alia et al as shown **Figure *7-6***. The cell is cycled between 1.4-2.0V (vs. cathode as ref.) with each step hold for 30 sec for 20k cycles.

Accelerated stress test (AST) protocol for PEM electrolyzer with IrOx based catalyst. Flow rates can vary on the active area										
	Tcell °C	Applied current A/cm²	Applied potential V	Water	H_2	Flow (A) mlpm	Flow (C) mlpm	Comments	Cycles	Technique
Characterization										XCT, XRF, XPS, SEM
Conditioning (break in)	60	0 0.2 1 2 1.7 2 0- 3 V, 100 mvps 0- 3 V, 20 mvps		A		15-20	free flow	Preheating for 30 min 60 min current hold 60 min current hold 30 min voltage hold 20 min voltage hold 30 min voltage hold 10 fast pol curves 10 slow pol curves		
Pol curve		0.01-6	record	A				BoL Pol curve		
EIS	60		record	A		15-20		BoL EIS (100 kHz - 1 Hz)		
Tafel slopes		record	1.3-1.65 V, 10mV step					Each step hold for 300 sec		
CV			record	A	C		50	BoL CV (0.05V-1.3V, 20-150 mV/sec)		
Voltage recovery		0.2-1	record	A				Voltage recovery after every shut down and start up. Follow steps 1-3 from conditioning protocol. Hold times can be 30 minutes or less unil voltage stabilizes. Can do 10 fast LSVs		
AST		record	1.45-2					Square wave 30 sec hold at each step	0-20k cycles, standard characterization after each 5000 cycles	
Recovery		1 record	record 2	A		15-20		Current hold 30 min Voltage hold 15 min		
EIS			record	A				EIS after every cycle (100 kHz - 1 Hz)		
Pol curve	60	0.01-6	record	A		15-20		10 cycle Pol curve		
Tafel slopes		record	1.3-1.65 V, 10mV step					Each step hold for 300 sec		
CV			record	A	C	15-20	50	CV (0.05V-1.3V, 20-150mV/sec)		
Characterization										XCT, XRF, ICP-MS, (SEM,TEM at end of life)

Figure 7-6 Developed square wave AST protocol including break-in, voltage recovery and electrochemical characterization procedures. The flow rates optimized for 1 cm^2 active area operando cell.

Various electrochemical and physical MEA characterizations are performed at the beginning of life (BoL), after every 5000 cycles till the end of life (EoL) at 20k cycles. The protocol is designed to be performed on a 1 cm^2 active area operando cell as we can track evolution of interfaces with X-ray CT with AST cycling.

7.3 Tracking evolution of catalyst and interfacial properties with AST cycling

We performed AST based on the protocol mentioned above on two operando cells with 1 mg/cm^2 and 0.5 mg/cm^2 IrOx loading respectively. The MEAs for both cells were made as half CCMs with only the anode side coated with IrOx. Baseline Ti sintered PTL was used on the anode side and cathode catalyst loading was 1 mg/cm^2 Pt/C sprayed on a carbon paper to make a GDE. This makes XRF analysis easier since cathode GDE can be peeled off during analysis to avoid Pt signal

interference in Ir mapping measurements. The active area was 1 cm^2 and membrane used for both the cells was Nafion 117 with a nominal thickness of 180 µm. The cell temperature was maintained at 60 C by using cartridge heaters and heated water was circulated at 15-20 mlpm through the cell. The cycling and electrochemical characterization was performed on the cell using a Gamry 5000 Potentiostat.

XRF analysis was conducted on pristine and cycled MEAs on a Horiba XGT 9000 XRF analyzer. The point loadings were measured with a 1.2 mm diameter capillary averaged over 4 points each exposed for 300 sec. The Ir mapping was conducted with a 10 µm diameter capillary on a 2 mm^2 region of the MEA at water inlet and outlet regions. The X-ray accelerating voltage was set at 50 kV and each pixel point on the ROI was exposed for 20 ms for two times. The cells were cycled at UCI and taken to beamtimes at Advanced Light Source in Berkeley National Laboratory for X-ray CT imaging.

The XPS measurements were conducted on a Kratos AXIS Supra XPS analyzer at 530 eV kinetic energy. Background subtraction was carried out using the Shirley method, and the asymmetric Doniach−Sunjic line shape was used for fitting of Ir 4f band. The fitting was done on parameters described by Pfeifer et al [141].

Figure ***7-7*** shows polarization curves and EIS spectra for the tested cells at different cycle numbers. The performance of high loaded cell at 1 mg/cm^2 was found to improve after the first 1k cycles and continued to improve till the end of life at 10k cycles.

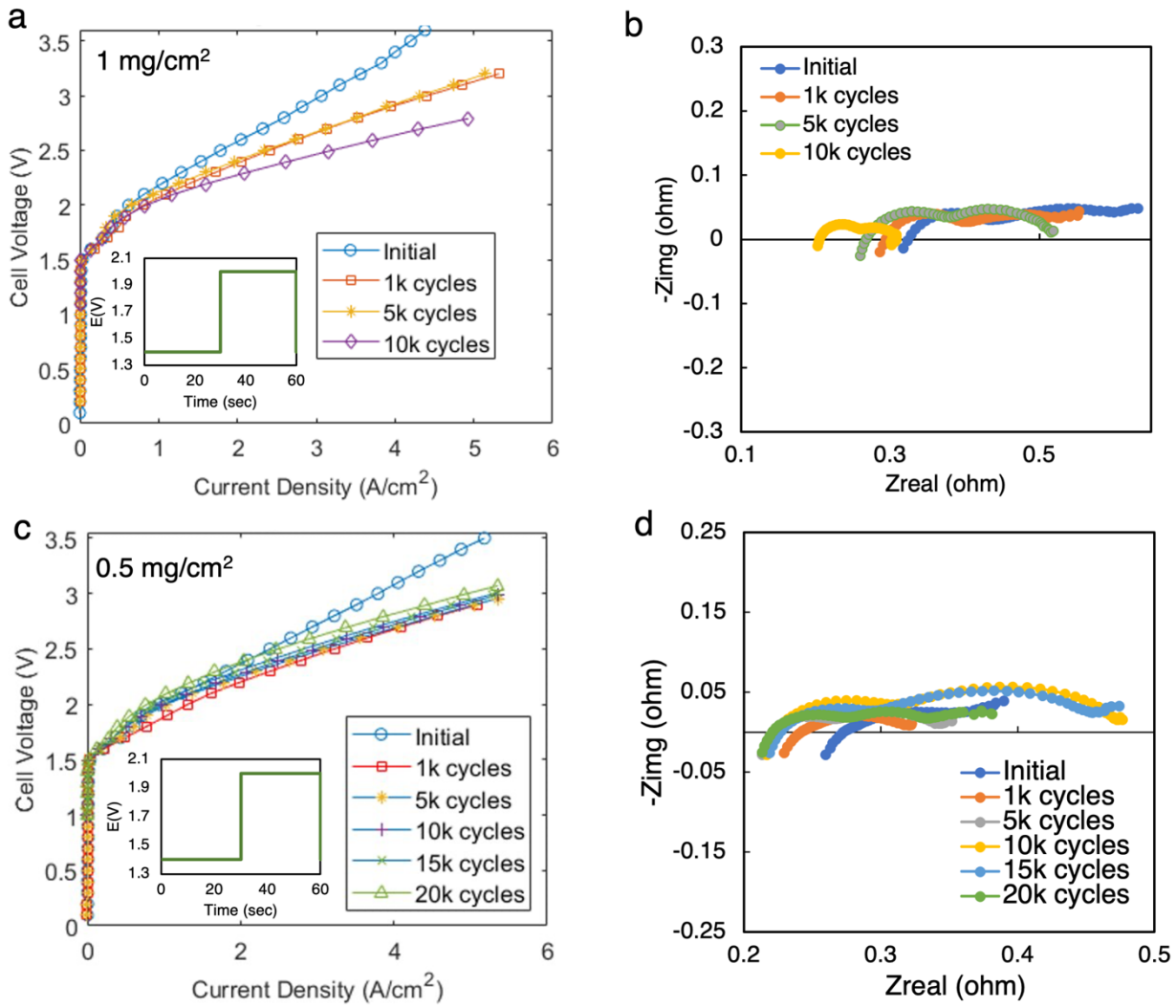

Figure 7-7 Results for cells tested with a square wave AST protocol (inset images in figures a and c) a. polarization curves for cell with 1 mg/cm^2 IrOx loading b. corresponding EIS data taken after every 5K cycles. The MEA was removed for XRF analysis after first 5K cycles and cell was reassembled. C. polarization curves for cell with 0.5 mg/cm^2 IrOx loading b. corresponding EIS data taken after every 5k cycles.

EIS spectra also shows improving HFR with cycle number indicating that there is no degradation, but in fact, the cell conditions within the first 10k AST cycles. This is typically true for high loaded MEAs since although there is Ir loss, it is small enough not to disturb the electrochemical

performance of the cell for thousands of cycles. For this reason, we selected lower loaded 0.5 mg/cm^2 cell for conducting AST. **Figure *7-7*** c and d show the polarization curves and EIS spectra of the low loaded cell at various AST cycle numbers. The cell is found to condition within the first 1000 cycles similar to the high loaded cell and has the best polarization performance. The HFR was also found to decrease within the first 1000 cycles. This indicates that ohmic losses are reduced as the membrane reaches its optimal hydration and proton transport becomes efficient. Membrane hydration also causes it to swell into the PTL and GDL further improving the contact of the catalyst layer with the PTLs. Additionally, during cell conditioning, the catalyst undergoes chemical transformation as surface chemical species evolve to OER conditions at applied potential and local pH. After 1000 cycles, however, the performance low loaded cell starts to degrade. The voltage rises to over 200 mV at 2 A/cm^2 at the EoL as compared to the conditioned cell at 1000 cycles. This accounts for voltage efficiency drop to 65% at EoL compared to 73% at the beginning of life.

We calculated the Ir loss rate by measuring the difference in loading at BoL and at 5000 cycles with XRF mapping. The color maps and loading histograms for pristine and cycled MEAs are shown in **Figure C6** in Appendix C. From XRF loading difference and normalizing to time of cell operation, we calculated the Ir loss rate at 1.30 ng/sec/cm^2 in the first 5000 cycles. This loss rate is calculated based on MEA only and does not consider catalyst that may or may not get transferred over to the PTL while cell disassembly. Although, we do not see any visible signs of catalyst transfer to the PTL. This loss rate is consistent with other reports in literature that calculate Ir loss with online ICP-MS coupled to a half cell with Ir MEA [133].

Figure 7-8 shows the Tafel slopes obtained at various AST cycle numbers for high and low loaded cells. The fitted slopes are tabulated in **Table *7-1***. For high loaded cell the Tafel slope at BoL shows the highest value possibly because the cell is not at the optimal level of conditioning. After

1000 cycles, the slope reduces slightly and maintains a stable value throughout the AST cycles. This indicates that the kinetic overpotential does not increase substantially during AST for high loaded cell.

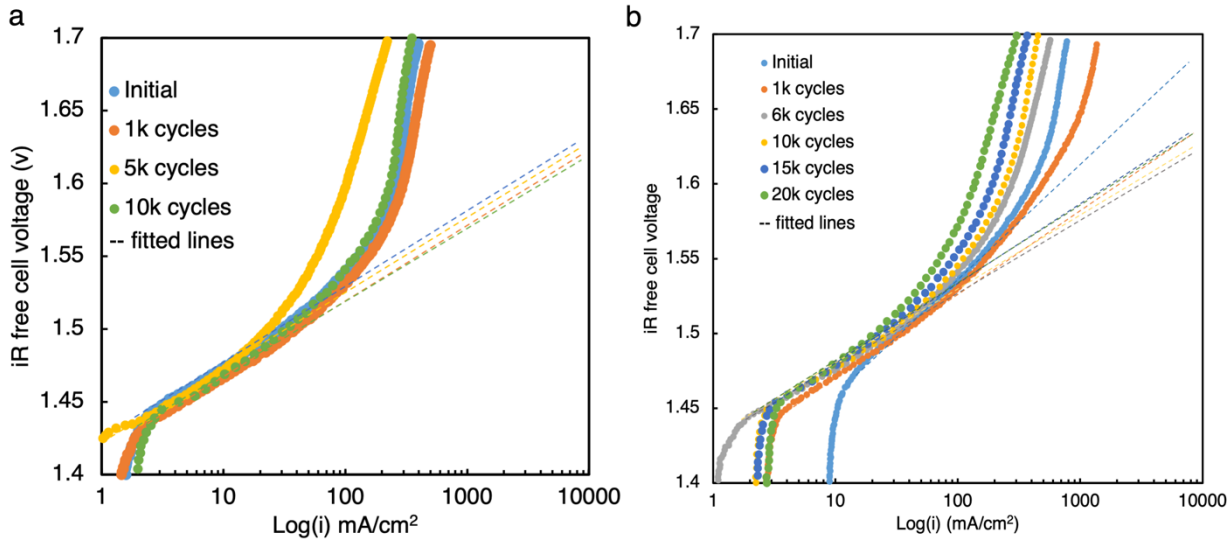

Figure 7-8 Tafel slopes for a. 1 mg/cm^2 cell b. 0.5 mg/cm^2 cell taken at different AST cycle numbers

Table 7-1 Tafel slopes at different cycle numbers

No of cycles	Tafel slopes (mV/decade)	
	1 mg/cm^2 cell	0.5 mg/cm^2 cell
Initial	61.9	80.3
1k	61.4	60.3
5k	61.3	62.2
10k	61.6	62.9
15k	-	63.9
20k	-	72.7

For low loaded cell, the Tafel slope shows the highest value at the beginning of life similar to the high loaded cell. The slope drops to the lowest value at 1000 cycles as the cell conditions. After that, the Tafel slope shows a consistent increasing trend till the EoL. As the HFR does not change

much during AST, we can conclude that most of the voltage increase comes from kinetic overpotential due to loss in Ir loading and degradation of the interface.

The change in interfacial contact (TPCA) at the BoL and EoL was studied by X-ray CT. **Figure *7-9*** shows the change in interfacial contact for both the cells. The TPCA is seen to increase slightly from 21.43% to 24.62% for high loaded cell although the measured values lie within the error limits. This increase is suggestive of reorganization of the catalyst while cycling. Although, more information is needed to corroborate this statement and we suggest identical location XRF mapping to validate movement of catalyst.

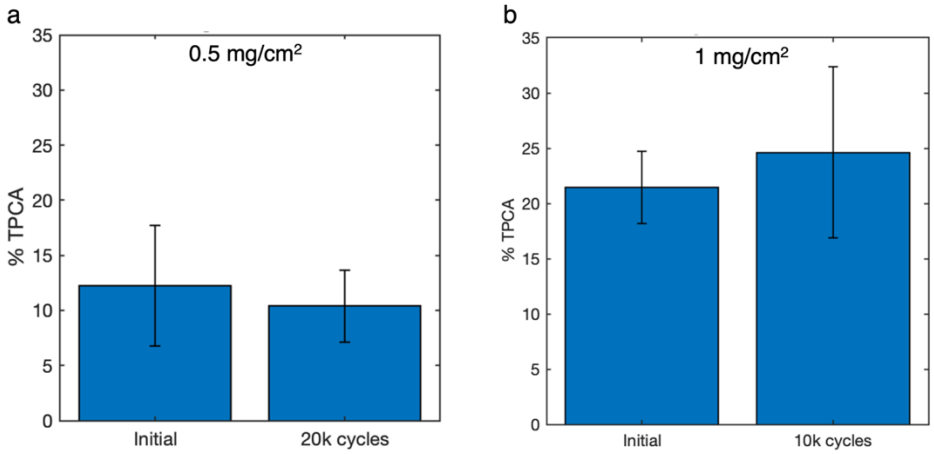

Figure 7-9 TPCA obtained from X-ray micro-CT of a. 0.5 mg/cm2 cell calculated at BoL and EoL b. 1 mg/cm^2 cell at BoL and 10K AST cycles

In contrast to the high loaded cell, the TPCA is seen to reduce slightly from 12.5% to 10.4% for the low loaded cell. The Ir loss calculated from XRF analysis reduces the TPCA which is linked to kinetic losses as discussed in chapters 3 and 4.

In order to study the surface chemistry of IrOx catalyst during cycling, we conducted XPS analysis of pristine and cycled MEA as shown in **Figure *7-10***. **Table *7-2*** shows the atomic percentages of different Ir oxidation states obtained from XPS fitting of Ir 4f band. At the BoL, the MEA contains

a mixture of metallic Ir(0), Ir(III) and Ir(IV) with the highest percentage of Ir(III). After 2500 AST cycles, the percentage of metallic Ir(0) drops from 10 % to 1.1% indicating that the surface metallic Ir gets oxidized during OER.

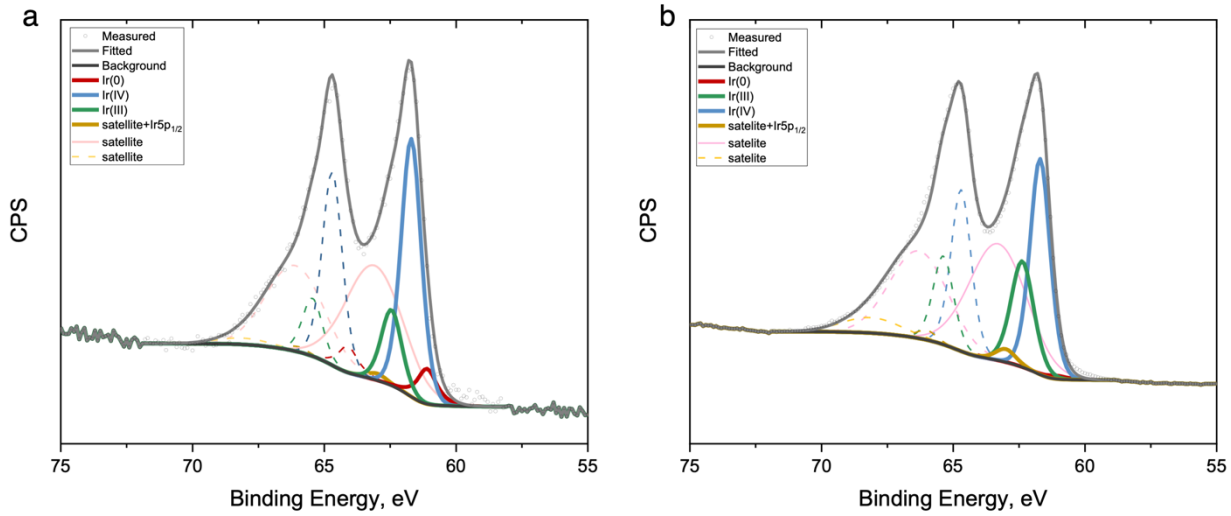

Figure 7-10 Ir 4f XP spectra of 0.5 mg/cm^2 MEA taken at beginning of life and 2500 AST cycles

Table 7-2 Atomic percentages of various Ir oxidation states obtained from XPS fitting of Ir 4f band

(Atomic %)	Pristine	2500 cycles
Ir(0)	10.0	1.1
Ir(III)	69.2	63.6
Ir(IV)	20.8	36.3
Ir(V)	0 (after subtracting the satellite and Ir5p$_{1/2}$)	

We observed a slight decrease of 5.6% of the Ir(III) state and a significant increase of Ir(IV) state by 15.5% at 2500 cycles with respect to the pristine MEA. This suggests possible transition of Ir(III)- Ir(IV) redox switch during OER at high potentials and is in accordance with the proposed paddle wheel mechanism Willinger et al. Although there is increase in the presence of higher oxidation states for the cycled MEA, Ir(III) remains the dominant oxidation state in both instances.

This is indicative of Ir oxidation to IrO_2 and subsequent formation of intermediate $HIrO_2$ complex during OER following the electrochemical oxide pathway.

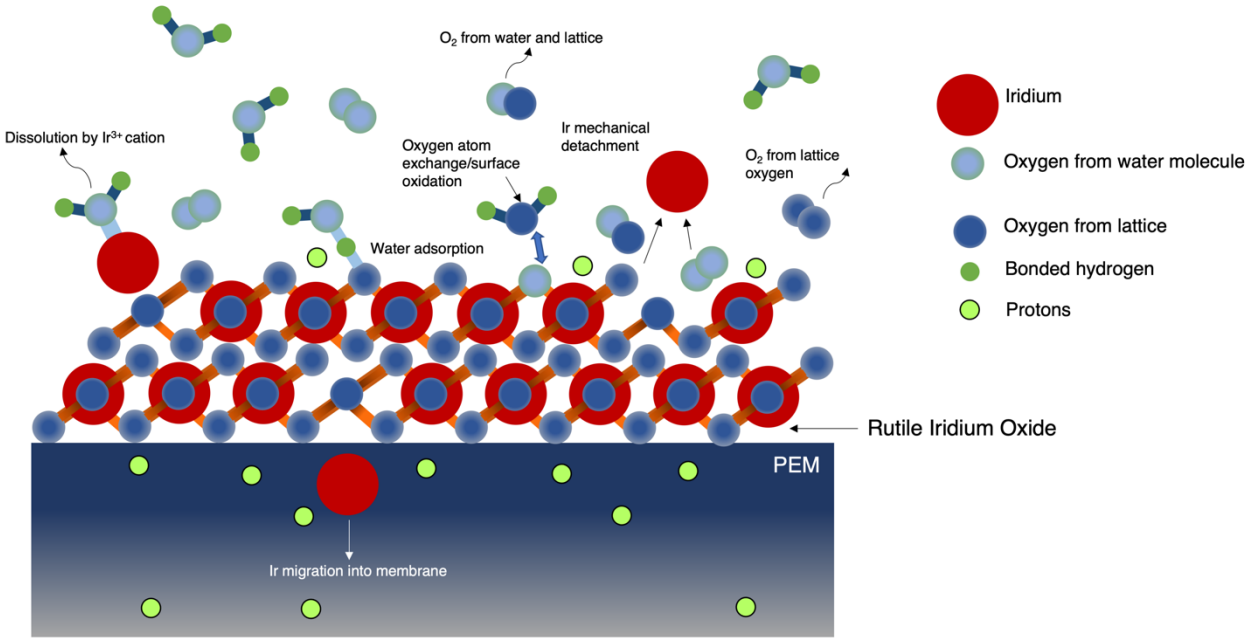

Figure 7-11 Current state of the art understanding of OER and iridium degradation mechanisms

Figure 7-11 summarizes our current state of the art understanding of OER on IrOx showing all the relevant mechanisms. Dissolution by formation of Ir^{3+} or higher oxidation number cations, Ir mechanical detachment and migration into the membrane were shown to be the dominant degradation mechanisms at or above OER potentials [133], [140], [142]–[145]. The oxygen molecules evolved can have oxygen atoms from the IrOx lattice and water, entirely from water or entirely from lattice although the relative percentages of the lattermost can be low to very low as compared to the former. Oxygen atoms from the surface can also undergo a place exchange mechanism as shown by Schweinar et al. [146]

7.4 Can use of MPLs increase catalyst utilization and durability?

The previous sections discussed PEMWE durability with catalyst dissolution mechanisms during OER and micro scale interface perspectives keeping the PTL constant. The importance of PTL morphology on catalyst utilization and durability is undeniable. PTL contact with the catalyst layer can not only influence local current density distribution over the catalyst layer and activity of the triple phase area, but also frequency of catalyst inactivation by oxygen bubble masking and mechanical detachment. The invasion patterns of oxygen in water through the PTL is dependent on PTL morphology. PTLs without MPLs have been shown to mask catalyst sites due to lateral invasion of oxygen thus reducing catalyst utilization and increasing mass transport overpotentials.

Several studies have proposed the use of MPLs for enhancement of interfacial properties but optimizing MPL microstructure and thickness are important otherwise the cell may run into mass transport and other issues. Moreover, the wettability properties of the MPLs need to be optimized for efficient water transport to the reaction sites. Chapter 6 discusses in detail the effect of MPLs on interfacial properties and how oxygen transport regimes can be changed with their addition. For a thin MPL, the flow regimes can enable better mass transport by higher utilization of transport pathways and higher pore volume utilization for oxygen transport. For thicker MPLs, although interfacial contact is enhanced, the bubble point pressure is high enough to cause mass transport issues and possible blockage of catalytic sites. Catalyst utilization is also dependent on in-plane electronic conductivity of the catalyst layer and through plane conductivity of the PTL. As the catalyst loadings are reduced, the heterogeneities in the catalyst layer have a bigger impact on the electronic percolation networks and the dependance on the PTLs for in-plane conductivity

increases. As MPLs have better interfacial contact and the contact point density is high, they can provide better point to point conductivity and reduce the dependance on catalyst layer thus enabling lower loadings. The improved contact can also be seen in the EIS spectra where the high frequency resistance for MPLs is almost 50 mΩ cm^2 lower than the baseline sintered PTL as seen in **Figure *7-12*** c. This translates to 100 mV improvement in cell potential at 2 A/cm^2. MPLs can be made more corrosion resistant and conductive with deposition of thin layers of noble metals such as Pt and Ir.

For scaling up MPL deployment, manufacturing processes need to be streamlined and quality control techniques need to be developed for fast defect detection on a roll-to-roll process. MPL uniformity is a key aspect since non uniform PTLs can cause reactant starvation and non-uniform compression ultimately leading to high overpotentials. Additionally, spare MPL pieces on the surface can cause pinholes in the membrane leading to cell failure by gas crossover or electrical shorting. Coating of MPL surfaces with noble metals pose additional challenges. Since MPL pore sizes are significantly smaller than macro porous layers, metal deposition parameters need to be set carefully in order to achieve desirable metal loading and thickness while not blocking any pores. An optimal MPL with these design parameters in consideration, they can indeed improve catalyst utilization, enable lower loadings, and improve system durability.

7.5 Characterizing electrochemical performance and 1000 hr. durability test

We conducted durability tests on the three PTL samples studied in chapter 6. The electrochemical characterization and durability tests were conducted at Nel Hydrogen in Wallingford, CT on their proprietary test stations. The cells had an active area of 28 cm^2. An IrOx loading of 2 mg/cm^2 was

used on the anode and Pt/C loading of 2 mg/cm^2 was used on the cathode with an I/C ratio of 0.2. The cells were operated at 50 ^{0}C and hydrogen differential pressure of 400 psi and were held at a constant current density of 1.8 A/cm^2 for 1000 hrs. Polarization curves were obtained at various points during the steady state holds and at the end of life. Since the tests were done on high loaded MEAs, steady state voltage responses at high current density were of interest to gauge PTL performance. Hence, the cells were operated at a fixed current density for 1000 hrs instead of voltage cycling AST.

The electrochemical characterization and durability tests of the three PTLs are shown in **Figure *7-12***. The beginning of life polarization curves and EIS data were measured on operando cells since polarization curves were collected on Nel cells at different times into the steady state holds and impedance measurements were not available. However, the end-of-life polarization curves from Nel cells are reported in **Figure *7-12*** b and the voltage responses during the 1000 hr. chronopotentiometric hold of 1.8 A/cm^2 are reported in **Figure *7-12*** d.

From the BoL polarization curves, the best performing was MPL 1 followed by baseline PTL and MPL 2 was the worst performing with seemingly high mass transport limitations. From the EIS data, the high frequency resistance (HFR) was lowest for MPL 1 at 0.13 Ω cm^2, followed by MPL 2 at 0.16 Ω cm^2 and baseline at 0.18 Ω cm^2. Hence MPLs improve HFR by over 50 mΩ cm^2 as compared to baseline because of better contact with the catalyst layer.

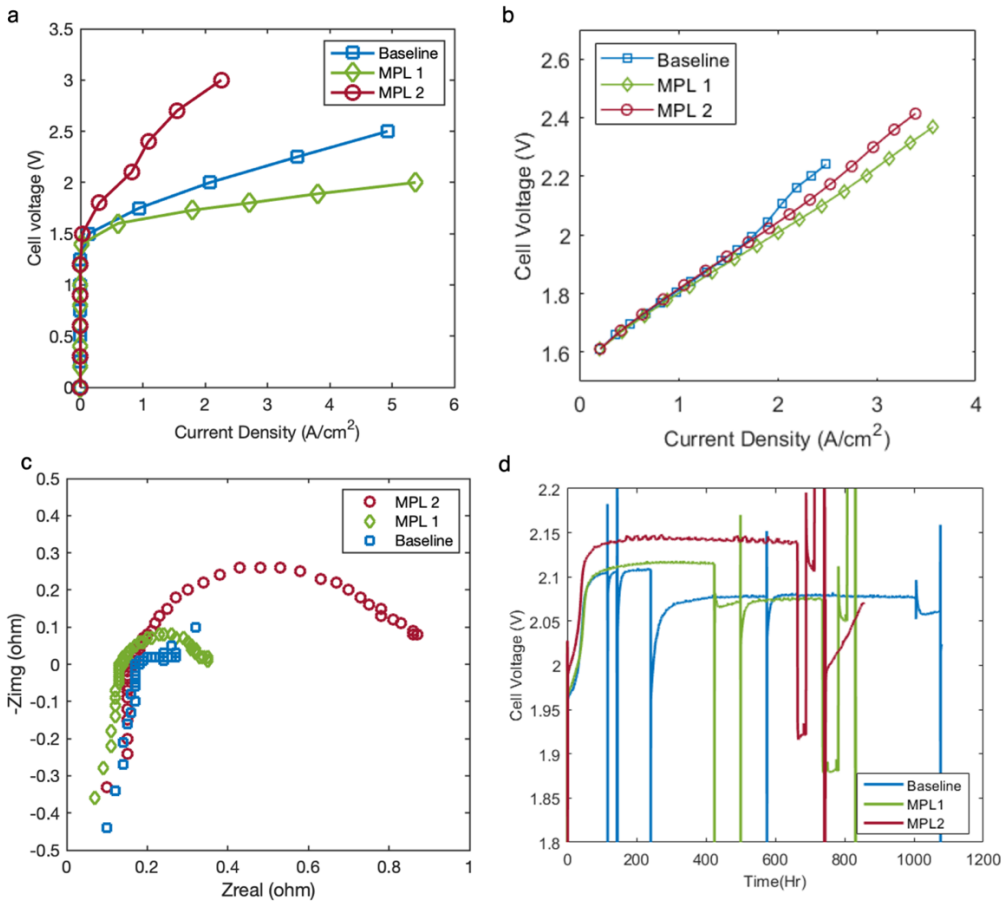

Figure 7-12 Electrochemical data obtained from operando cells and durability data obtained from Nel Hydrogen for 1000 hr durability test. The durability tests were conducted on 50 cm^2 active area MEAs with hydrogen draw pressure of 400 psi and 50 ^0C temperature. The catalyst loading was 2 mg/cm^2 IrOx on anode and 2 mg/cm^2 Pt/C on cathode. The cells were held at a constant current density of 1.8 A/cm^2 and voltage response was recorded. For the operando cells, the active area was 1 cm^2 and an IrOx loading of 1 mg/cm^2 and Pt/C loading of 1 mg/cm^2 was used on the cathode and anode respectively. a. represents polarization curves obtained from the operando cells at the beginning of life. b. represents end of life polarization curves after the 1000 hr test obtained from Nel Hydrogen. c. EIS Nyquist curves obtained from operando cells d. voltage responses of the cells during 1000 hr durability test. The dips in the voltages represent instances where pol curves were taken or there was an unexpected system shutdown.

This is consistent with the TPCA analysis that shows a much better contact for MPLs than the baseline PTL. One can also notice the charge transfer loops in the EIS data where MPL 2 has the biggest one indicating limitations to proton or electronic transport due to higher MPL and overall thickness. This is most likely the reason behind polarization curve showing mass transport limitations which were also shown by De Angelis et.al in their recent PTL thickness study [147]. MPL 1 is found to be the best performing at BoL as well as EoL among all three samples. The increased TPCA along with efficient gas transport in the PTL due to increased pore volume utilization result in reduced overpotentials and minimal overall degradation rate of 26.5 μV/hr. The baseline PTL had an average degradation rate of 82 μV/hr and MPL 2 had an average degradation rate of 89 μV/hr (115-230 hr interval after which the cell degradation rate does not change). The higher degradation rate for baseline PTL could be because of the following reasons

1. Heterogeneous interface contact: Since adjacent PTL contact points occur at intervals of ~13 μm (surface pore diameter), the interfacial non-contact areas are comparatively larger than MPLs (~4 μm contact interval based on surface pore diameter) thus reducing the overall TPCA activity leading to underutilization of catalyst layer and subsequent catalyst degradation
2. Mechanical degradation: Oxygen bubble nucleation occurs over the interfacial non-contact areas. As bubble detachment occurs when oxygen occupies maximum pore volume, its detachment frequency is slower, and size is larger. Bigger bubbles may impart higher momentum transfer to neighboring catalyst particle making its mechanical detachment more likely

7.6 Conclusions and summary

In this study, we gave a detailed overview of the state-of-the-art understanding of OER on IrOx catalyst and its link to Ir dissolution mechanisms. OER is a complex 4 electron transfer reaction and imparts significant overpotential to the system. While modeling approaches like Tafel analysis can give primary insights into the reaction mechanisms and rate determining steps, more sophisticated in-situ, and operando studies give a better mechanistic insight into catalyst activity. Studies on model systems like thermally prepared Ir or thin films over the decades has pushed our understanding towards OER catalysis but the transfer of this knowledge to non-model systems needs more investigation. OER being a complex process depends on the nature of Ir surface and reaction mechanisms and intermediates are greatly influenced by these structural properties. Even with these complexities, catalyst optimization can be performed based on semi-rational structure-activity-stability relations. Catalyst optimization for OER can be done on single oxide system like Ir and Ru oxide if their chemical properties and surface state are carefully tuned within the synthesis.

Based on this understanding, we developed accelerated stress testing protocols and tested operando cells with high and low catalyst loadings. The electrochemical tests revealed that it is difficult to degrade high loaded cells and AST protocols should be applied to low loaded MEAs in order to cause accelerated degradation and to study underlying driving factors. The voltage degradation in low loaded cells is associated mostly to kinetic overpotentials driven by catalyst dissolution. We calculated the catalyst loss in the cell by XRF analysis and found Ir loss rate at 1.30 ng/sec/cm^2 during the first 5000 AST cycles. Ir loss is also observed with a decreased TPCA at the end of life. The slight increase in TPCA for high loaded cell suggests reorganization of catalyst on the surface and we recommend conducting identical location XRF studies to understand possible Ir migration.

To study the dissolution and OER pathway, we conducted XPS analysis of pristine and cycled MEAs. The results showed that most of the metallic Ir(0) gets oxidized during OER and reaction proceeds through the electrochemical oxide pathway with Ir(III)-Ir(IV) redox switch during AST cycling.

To study the effect of MPLs on durability, we conducted 1000 hr. durability tests on three PTL samples with varying MPL thicknesses with differential pressure and intermittent startup-shutdown operating conditions to mimic real systems. The beginning of life polarization curves show that MPL 1 is the best performing among all three samples and MPL 2 ran into mass transport limitations likely because of increased MPL thickness. The end-of-life polarization curves show MPL 1 with a lowest voltage degradation rate of 26.5 μV/hr followed by baseline PTL with 82 μV/hr and MPL 2 with 89 μV/hr degradation rate. With these results, we identified major design factors for MPL design to maximize catalyst utilization and minimize degradation.

8.Contributions and Recommendations for future work

8.1 Contributions

8.1.1 Operando Cell design and development for X-ray CT

In this work, we presented the roadmap for the *operando* cells designed in our group for imaging water in fuel cells with x-ray CT and x-ray radiography. The *operando* cells presented here enable the visualization of water in fuel cells at micro scales as well as oxygen in electrolyzer mode. The micro x-ray CT fuel cell/electrolyzer underwent five generations of design iterations to optimize electrical conductivity, mechanical stability, thermal management and compression. This cell has been used to image fuel cells and electrolyzers with various catalyst layers with the aim to visualize water/oxygen. Water segmentation for operando fuel cells was achieved by subtracting an OCV

background scan from the data measured at constant current density to reduce number of image phases from three (water, carbon and pore) to just two (water and pore/carbon). Further, the development of a novel *operando* nano CT fuel cell is detailed in further sections of reference [3] including lessons learned and the challenges in x-ray imaging on this scale. The main challenge of beam damage is difficult to overcome due to the low energy < 10 keV that many of the beamlines use. We showed that this can be overcome by using beamlines that rely on Kirkpatrick-Baez (KB) mirrors (at ESRF) instead of Fresnel zone plates (APS, NSLS II) for beam focusing, as KB x-ray optics can enable imaging at nanoscale at higher energies (such as 17.5 keV at ESRF). Despite the challenges, the nano- x-ray CT sample holder design enables multiscale 3D imaging.

8.1.2 Analyzing nature of interfaces

The electrochemical and X-ray imaging methods for analyzing nature of interfaces are summarized in detail. The experimental sample set for operando X-ray CT experiments is identified based on research objectives. The electrochemical methods to measure polarization curves, Electrochemical Impedance Spectroscopy, Double layer capacity and Tafel slopes are discussed in detail. From X-ray CT imaging, the method to calculate the Triple Phase Contact Area (TPCA) is formulated.

8.1.3 Influence of PTL morphology and electrode configurations on interfacial contact and cell performance

A systematic matrix of twelve PEMWE configurations with two different types of PTLs, two types of electrode configurations namely CCM and GDE and three levels of catalyst loadings were characterized using x-ray micro-CT to quantify the interfaces and elucidate its effect on electrochemical performance and gas transport in flow-field channels. Moreover, steady-state

durability testing of all the samples was conducted and a Lattice Boltzmann Method model was constructed based on the tomography results to simulate gas transport in the two types of PTLs for varied catalyst loadings. From the tomography images, it was clear that the catalyst agglomeration and clustering increases with loadings for the CCMs and the catalyst conforms to the PTL surface during coating for the GDEs. The calculated TPCA was correlated with the double layer capacities obtained by electrochemical testing. In general, the TPCA increases with increase in catalyst loadings and C_{dl} scales proportionally. The conjunction of the TPCA along with C_{dl} gives us a measure of the electrochemically active surface area. The PTL surface morphology plays a vital role in affecting the TPCA. High loaded sintered CCM showed the highest TPCA and concomitantly highest C_{dl} among all other samples.

The general order of C_{dl} vs TPCA on the parameter space for CCMs is sintered CCM 0.5 mg cm^{-2} < fiber CCM 0.5 mg cm^{-2} < fiber CCM 1 mg cm^{-2} < sintered CCM 1 mg cm^{-2} < fiber CCM 2 mg cm^{-2} < sintered CCM 2 mg cm^{-2}. This directly relates to the BOL potential measured at 1.5 A cm^{-2}, where the cell overpotentials follow the same exact trend. Similarly, the general order of C_{dl} vs TPCA on the parameter space for GDEs is sintered GDE 0.65 $mgcm^{-2}$ < fiber GDE 0.65 $mgcm^{-2}$ < fiber GDE 1.1 $mgcm^{-2}$ < sintered GDE 1.1 $mgcm^{-2}$ < fiber GDE 1.75 $mgcm^{-2}$ < sintered GDE 1.75 $mgcm^{-2}$. This trend relates directly with the measured improvement in overpotential until medium loadings, but high loaded fiber GDE shows a ~ 30 mV rise than sintered GDE. The discrepancies associated with such performance loss especially in GDEs is attributed to influence of undesirable overpotentials that affect the kinetics as shown by the Tafel analysis. The Tafel analysis shows that on average GDE configurations had higher Tafel slopes compared to CCM configurations, indicating that there are some other non-kinetic losses are present. Low loaded GDEs show the most performance loss after steady state current density holds possibly due to

mechanical degradation of the catalyst. The investigation of oxygen content in the channels sheds light on the mass transport overpotentials. We determine 80 % oxygen in the channel to be the maximum to avoid water depletion in the catalyst layer. CCM configurations showed increase in oxygen content in the channel with increase in current density, as at higher current density more oxygen is produced and removed in the channel. The 3-D modeling suggests that for low-loaded catalyst layers the pathways for oxygen transport through the PTLs are limited, as oxygen is transported through a few preferential pathways. Fiber PTL has larger pores and more inhomogeneous pore size distribution leading to preferential oxygen transport pathways even at high catalyst loading. Sintered PTLs have more uniform and smaller pores, resulting in more uniform oxygen distribution in the PTL.

These findings add in-depth experimental and modeling insight into the nature of the PTL-catalyst layer interface and contribute to the understanding of impact of PTL bulk properties on gas and water transport

8.1.4 Investigating 2-phase flow through PTLs

In this study, X-ray CT and CFD were used to investigate oxygen transport in the PTLs of PEMWEs. This study aimed to explain the preferential pathways of oxygen transport through the PTL. X-ray CT was performed using the in-house designed electrolyzer at different water feed rates (1-3 mlpm) and current densities (1 - 4 A/cm^2). Here, an acid-treated Freudenberg GDL was used as a model PTL on the anode because its pore size distribution most closely resembles conventional Ti-based sintered or fiber PTLs. Weka machine learning incorporated with the Z project method was able to quantify oxygen content throughout the PTLs via post-processing of *operando* X-ray CT scans.

8.1.5 Elucidating use of MPLs for interfacial contact enhancement and effect on oxygen distribution

In this study, for the first time, we demonstrated the use of stained water to quantify time averaged oxygen saturation in sintered PTLs without MPL and with MPLs of varying thicknesses using X-ray microtomography. The first sample was a baseline sintered PTL with no MPL, the second sample was MPL 1 with a thin MPL of 20 μm and the third sample studied was MPL 2 with a thicker MPL of 58 μm. We quantified the effect of MPLs on triple phase contact at the interface and found that MPLs result in over 20 % higher TPCA and increase the PTL contact point density by twice as compared to sintered PTLs with no MPL. We developed novel image processing techniques to segment oxygen from total pore volume and calculated pore volume utilization. Baseline sintered PTLs were found to have lower average pore volume utilization than MPL samples. MPL samples were found to have over 20 % higher pore volume utilization at any given current density. Higher pore volume utilization in PTL was also found to proportionately increase oxygen content in channels implying improved oxygen removal efficiencies. Our bubble point measurements showed increased bubble point pressures for increasing MPL thicknesses. Hence bubble points show direct relation to MPL thickness and inverse relation to mass transport overpotentials.

Based on the 3D data as well as calculations of *Ca* and *M*, baseline sintered PTL was found to have capillary fingering as the dominant transport regime. Capillary fingering occurs when capillary forces dominate in a porous media and oxygen takes preferential pathways of removal

based on following pore-to pore transition following pathways of least capillary pressure. MPLs are seen to suppress capillary fingering and transition oxygen flow to viscous fingering which is a very important result.

8.1.6 Engineering interfaces for durability

In this study, we gave a detailed overview of the state-of-the-art understanding of OER on IrOx catalyst and its link to Ir dissolution mechanisms. OER is a complex 4 electron transfer reaction and imparts significant overpotential to the system. While modeling approaches like Tafel analysis can give primary insights into the reaction mechanisms and rate determining steps, more sophisticated in-situ, and operando studies give a better mechanistic insight into catalyst activity. Studies on model systems like thermally prepared Ir or thin films over the decades has pushed our understanding towards OER catalysis but the transfer of this knowledge to non-model systems needs more investigation. OER being a complex process depends on the nature of Ir surface and reaction mechanisms and intermediates are greatly influenced by these structural properties. Even with these complexities, catalyst optimization can be performed based on semi-rational structure-activity-stability relations. Catalyst optimization for OER can be done on single oxide system like Ir and Ru oxide if their chemical properties and surface state are carefully tuned within the synthesis.

Based on this understanding, we developed accelerated stress testing protocols and tested operando cells with high and low catalyst loadings. The electrochemical tests revealed that it is difficult to degrade high loaded cells and AST protocols should be applied to low loaded MEAs in order to cause accelerated degradation and to study underlying driving factors. The voltage degradation in low loaded cells is associated mostly to kinetic overpotentials driven by catalyst dissolution. We

calculated the catalyst loss in the cell by XRF analysis and found Ir loss rate at 1.30 ng/sec/cm^2 during the first 5000 AST cycles. Ir loss is also observed with a decreased TPCA at the end of life. The slight increase in TPCA for high loaded cell suggests reorganization of catalyst on the surface and we recommend conducting identical location XRF studies to understand possible Ir migration. To study the dissolution and OER pathway, we conducted XPS analysis of pristine and cycled MEAs. The results showed that most of the metallic Ir(0) gets oxidized during OER and reaction proceeds through the electrochemical oxide pathway with Ir(III)-Ir(IV) redox switch during AST cycling.

8.2 Recommendations for future work

8.2.1 Operando Cell design and development for X-ray CT

1. Design modifications to the current operando cell can be made in terms of modularity to make assembly and disassembly quick during beamtimes. The design changes can include quick release clamps and dowels for part alignment. We recommend next generation operando cell designs to be inspired by Baltic hardware currently used for fuel cell testing.
2. The copper current collectors can be replaced with custom made gold plated current collectors for better corrosion resistance and high electrical conductivity.
3. Operando cells can be made multi-functional by design changes made to accommodate various sensors. Acoustic sensors can be installed to measure oxygen saturation in channels while operating out of the beamline. Pressure sensors can be installed to measure cell compression. Additional cartridge heaters can be installed for high temperature operation.

4. For high pressure operation, PEEK inserts can be made and graphite plates with rubber gasketing can be installed within them to operate cells at differential pressures while maintaining X-ray transparency over the active area.

8.2.2 Analyzing nature of interfaces

1. The triple phase contact area procedure was developed to estimate the electrochemically active surface area of the electrodes. Coupling that with C_{dl} measurements on a parameter space gives a reasonable estimate of cell performance and catalyst utilization. However, the TPCA formulation does not consider the form factor of the PTL, just absolute porosity. A more comprehensive formulation can include form factor of the PTL surface and its effect on interfacial characteristics.
2. Although X-ray micro-CT is able to resolve oxygen transport in PTL and channels, a higher resolution and faster scanning is required to observe micro scale bubble formation at the interface. We recommend synchrotron operando high resolution TEM to observe these effects. Imaging can be done at beamline 32-ID-C at Advanced Photon Source at Argonne National Lab. Although challenging, an operando half-cell can be constructed with an active area of <0.1 cm^2 to observe nanoscale nucleation and detachment bubbles. The experimental results can be validated with results by S.R German et al.
3. Along with X-ray CT, electrochemical methods must be explored to estimate the ECSA of PEMWE electrodes. Although techniques such as mercury underpotential deposition have been studied in half cells, experiments should be done to validate its potential use in full cells. Identifying gases that can reversibly adsorb on Ir surface with applied potential (like CO stripping in PEM fuel cells) can help estimate ECSA with cyclic voltammograms.

8.2.3 Influence of PTL morphology and electrode configurations on interfacial contact and cell performance

1. We found experimental evidence of bottlenecks in proton and electronic conductivity between different electrode configurations. However, formulation of a holistic model that can predict proton and electron transport resistances based on the experimental data will be an important addition that will help predict PEMWE performance.
2. The idea of TPCA activity was proposed in this chapter. In order to understand how TPCA activity varies with different forms of interfacial contact, a model can be formulated based on experimental C_{dl} and TPCA that can predict variability in TPCA activity based on catalyst utilization. Additionally, experiments could be designed to measure catalyst utilization with PTLs of similar porosity and pore sizes, but different form factors (ex. fiber vs sintered) and using low loaded CCMs.
3. The use of segmented cells to measure current density distribution as a function of various PTL morphologies and bipolar plate channel geometries can be an interesting field of study
4. The degradation rate of catalyst under the interfacial contact and non-contact areas with high resolution XRF analysis and SEM will help shed light on how different interfacial contact areas affect catalyst durability. This can help us identify interfacial areas that degrade the least in turn paving the way to engineering interfaces that maximize the identified areas of least degradation along with possible tradeoffs with reactant and gas transport.

5. From results of above-mentioned studies, a 2-D model for decoupling polarization curves can be formulated that can predict catalyst utilization from PTL geometry and catalyst distribution as additional inputs.

8.2.4 Investigating 2-phase flow through PTLs

1. The current LBM CFD model assumes 100% inlet of oxygen from high catalyst loadings, 75% inlet from medium loadings and 50% inlet from low catalyst loadings. Although this assumption gives reasonable prediction of oxygen transport pathways, the actual TPCA distribution can be used to model oxygen flow and get results close to non-model systems.
2. It has been found that adding deterministic structures to PTLs such as laser ablated through pores, itched lines on PTL surface etc. can help reduce mass transport overpotentials, but oxygen transport pathways with the presence of these deterministic structures have not been validated yet and is a good area of research. Using CFD models, it would be possible to optimize design deterministic structures on PTLs based on catalyst loadings and catalyst layer uniformity.
3. Change in oxygen transport pathways with varying inlet water flow rates and temperatures would be an interesting study. Additionally, modeling oxygen invasion patterns with varying Eotvos (Eo) number can help in the design of stack orientation.
4. Finally, exploring machine learning and data driven approach to optimizing micro and macro scale interfaces can be proposed.

8.2.5 Elucidating use of MPLs for interfacial contact enhancement and effect on oxygen distribution

1. The current study is based on understanding oxygen distribution in PTLs with varying MPL thicknesses. Further studies should be done by varying MPL morphology such a porosity, pore sizes and particle thicknesses. Additionally, varying surface wettability and its effect on reactant and gas transport would be an interesting topic of study.
2. Better image processing pipelines should be developed to streamline data processing. Machine learning approaches to oxygen phase segmentation should be implemented to automate these processes and minimize human error.
3. Developing correlation charts between various PTL morphological properties and cell overpotentials can help downsize PTL selection matrix for experiments.
4. Studying oxygen distributions at various cell temperatures and its effect on durability

8.2.6 Engineering interfaces for durability

1. Several studies have pushed our understanding of OER pathways on IrOx and its interrelation to different degradation mechanisms. However, the scientific community still has differences in opinions on topics such as the extent to which lattice oxygen participates in OER, the Ir redox states at high potential and their sensitivity to dissolution, and migration of Ir on the surface during potential cycling. Reaching a consensus on these mechanistic insights is essential to establish a standardized AST protocol for PEMWEs. We propose the scientific community to conduct systematic set of advanced techniques such as operando near ambient pressure (NAP) XPS to elucidate Ir redox transitions on catalyst samples sourced from same manufacturer and processing batch, operando nano X-

ray CT and SEM/TEM to probe morphological changes to the surface during OER conditions etc. to standardize baselines.

2. Understanding activity-stability relationships among IrOx catalysts synthesized with different techniques and optimizing ink formulations for homogeneous catalyst layer at low loadings.
3. Synthesizing novel catalyst supports such as antimony doped tin oxide (ATO) and its effect on durability.
4. Developing technique of identical location XRF mapping on pristine and cycled MEA to probe possible migration and redistribution of IrOx during AST cycling.
5. Understanding the effect of precious metal coatings on durability with the aim of optimizing metal loadings and coating thicknesses without negatively affecting the durability.

References

[1] D. Kulkarni *et al.*, “Elucidating effects of catalyst loadings and porous transport layer morphologies on operation of proton exchange membrane water electrolyzers,” *Appl. Catal. B Environ.*, vol. 308, no. February, p. 121213, 2022, doi: 10.1016/j.apcatb.2022.121213.

[2] P. Satjaritanun *et al.*, “iScience Observation of Preferential Pathways for Oxygen Removal through Porous Transport Layers of Polymer Electrolyte Water Electrolyzers Observation of Preferential Pathways for Oxygen Removal through Porous Transport Layers of Polymer Electrolyte Wate,” *ISCIENCE*, vol. 23, no. 12, p. 101783, 2020, doi: 10.1016/j.isci.2020.101783.

[3] D. Kulkarni, S. J. Normile, L. G. Connolly, and I. V Zenyuk, “ Development of low temperature fuel cell holders for Operando x-ray micro and nano computed tomography to visualize water distribution ,” *J. Phys. Energy*, vol. 2, no. 4, p. 044005, 2020, doi: 10.1088/2515-7655/abb783.

[4] UNFCCC, “Nationally determined contributions under the Paris Agreement: Synthesis report by the secretariat,” *English*, no. September, pp. 1–42, 2021.

[5] A. Saeedmanesh, M. A. Mac Kinnon, and J. Brouwer, “Hydrogen is essential for sustainability,” *Curr. Opin. Electrochem.*, vol. 12, pp. 166–181, 2018, doi: 10.1016/j.coelec.2018.11.009.

[6] G. H. Rau, H. D. Willauer, and Z. J. Ren, “The global potential for converting renewable electricity to negative-CO2-emissions hydrogen,” *Nat. Clim. Chang.*, vol. 8, no. 7, pp. 621–625, 2018, doi: 10.1038/s41558-018-0203-0.

[7] M. Ali, J. Ekström, and M. Lehtonen, “Sizing hydrogen energy storage in consideration of demand response in highly renewable generation power systems,” *Energies*, vol. 11, no. 5, 2018, doi: 10.3390/en11051113.

[8] K. Ayers, N. Danilovic, R. Ouimet, M. Carmo, B. Pivovar, and M. Bornstein, “Perspectives on Low-Temperature Electrolysis and Potential for Renewable Hydrogen at Scale,” *Annu. Rev. Chem. Biomol. Eng.*, vol. 10, no. 1, pp. 219–239, 2019, doi: 10.1146/annurev-chembioeng-060718-030241.

[9] P. Patel and K. Ayers, *Electrolysis for hydrogen production*, vol. 44, no. 9. 2019.

[10] B. Pivovar, N. Rustagi, and S. Satyapal, “Hydrogen at Scale (H2@Scale) Key to a Clean, Economic, and Sustainable Energy System by,” *\The Electrochem. Soc. Interface*, vol. 27, pp. 47–52, 2018.

[11] T. Van de Graaf, I. Overland, D. Scholten, and K. Westphal, “The new oil? The geopolitics and international governance of hydrogen,” *Energy Res. Soc. Sci.*, vol. 70, p. 101667, 2020, doi: https://doi.org/10.1016/j.erss.2020.101667.

[12] DOE, “Fuel Cell Technologies Program Multi-Year Research, Development, and Demonstration Plan.” US Department Of Energy Washington, DC, 2007.

[13] T. Reier, H. N. Nong, D. Teschner, R. Schlögl, and P. Strasser, “Electrocatalytic Oxygen Evolution Reaction in Acidic Environments – Reaction Mechanisms and Catalysts,” *Adv. Energy Mater.*, vol. 7, no. 1, 2017, doi: 10.1002/aenm.201601275.

[14] M. Carmo, D. L. Fritz, J. Mergel, and D. Stolten, “A comprehensive review on PEM water

electrolysis," *Int. J. Hydrogen Energy*, vol. 38, no. 12, pp. 4901–4934, 2013, doi: 10.1016/j.ijhydene.2013.01.151.
[15] K. E. Ayers *et al.*, "Pathways to ultra-low platinum group metal catalyst loading in proton exchange membrane electrolyzers," *Catal. Today*, vol. 262, pp. 121–132, 2016, doi: 10.1016/j.cattod.2015.10.019.
[16] Z. Taie *et al.*, "Pathway to Complete Energy Sector Decarbonization with Available Iridium Resources using Ultralow Loaded Water Electrolyzers," *ACS Appl. Mater. Interfaces*, 2020, doi: 10.1021/acsami.0c15687.
[17] U. Babic, M. Suermann, F. N. Büchi, L. Gubler, and T. J. Schmidt, "Critical Review—Identifying Critical Gaps for Polymer Electrolyte Water Electrolysis Development," *J. Electrochem. Soc.*, vol. 164, no. 4, pp. F387–F399, 2017, doi: 10.1149/2.1441704jes.
[18] M. Bernt, "Analysis of Voltage Losses and Degradation Phenomena in PEM Water Electrolyzers Maximilian Philipp Bernt," 2019.
[19] S. Siracusano *et al.*, "Electrochemical characterization of single cell and short stack PEM electrolyzers based on a nanosized IrO2 anode electrocatalyst," *Int. J. Hydrogen Energy*, vol. 35, no. 11, pp. 5558–5568, 2010, doi: https://doi.org/10.1016/j.ijhydene.2010.03.102.
[20] B. S. Lee *et al.*, "Development of electrodeposited IrO2 electrodes as anodes in polymer electrolyte membrane water electrolysis," *Appl. Catal. B Environ.*, vol. 179, pp. 285–291, 2015, doi: 10.1016/j.apcatb.2015.05.027.
[21] B. S. Lee *et al.*, "Polarization characteristics of a low catalyst loading PEM water electrolyzer operating at elevated temperature," *J. Power Sources*, vol. 309, pp. 127–134, 2016, doi: 10.1016/j.jpowsour.2015.12.139.
[22] H. Su, B. J. Bladergroen, V. Linkov, S. Pasupathi, and S. Ji, "Study of catalyst sprayed membrane under irradiation method to prepare high performance membrane electrode assemblies for solid polymer electrolyte water electrolysis," *Int. J. Hydrogen Energy*, vol. 36, no. 23, pp. 15081–15088, 2011, doi: 10.1016/j.ijhydene.2011.08.057.
[23] L. Ma, S. Sui, and Y. Zhai, "Investigations on high performance proton exchange membrane water electrolyzer," *Int. J. Hydrogen Energy*, vol. 34, no. 2, pp. 678–684, 2009, doi: 10.1016/j.ijhydene.2008.11.022.
[24] W. Xu and K. Scott, "The effects of ionomer content on PEM water electrolyser membrane electrode assembly performance," *Int. J. Hydrogen Energy*, vol. 35, no. 21, pp. 12029–12037, 2010, doi: 10.1016/j.ijhydene.2010.08.055.
[25] E. Slavcheva, I. Radev, S. Bliznakov, G. Topalov, P. Andreev, and E. Budevski, "Sputtered iridium oxide films as electrocatalysts for water splitting via PEM electrolysis," *Electrochim. Acta*, vol. 52, no. 12, pp. 3889–3894, 2007, doi: 10.1016/j.electacta.2006.11.005.
[26] H. Su, V. Linkov, and B. J. Bladergroen, "Membrane electrode assemblies with low noble metal loadings for hydrogen production from solid polymer electrolyte water electrolysis," *Int. J. Hydrogen Energy*, vol. 38, no. 23, pp. 9601–9608, 2013, doi: https://doi.org/10.1016/j.ijhydene.2013.05.099.
[27] M. Bernt, A. Siebel, and H. A. Gasteiger, "Analysis of Voltage Losses in PEM Water Electrolyzers with Low Platinum Group Metal Loadings," *J. Electrochem. Soc.*, vol. 165, no. 5, pp. F305–F314, 2018, doi: 10.1149/2.0641805jes.
[28] M. Bernt and H. A. Gasteiger, "Influence of Ionomer Content in IrO 2 /TiO 2 Electrodes on PEM Water Electrolyzer Performance," *J. Electrochem. Soc.*, vol. 163, no. 11, pp. F3179–F3189, 2016, doi: 10.1149/2.0231611jes.

[29] K. A. Lewinski, D. van der Vliet, and S. M. Luopa, “NSTF Advances for PEM Electrolysis - the Effect of Alloying on Activity of NSTF Electrolyzer Catalysts and Performance of NSTF Based PEM Electrolyzers,” *ECS Trans.*, vol. 69, no. 17, pp. 893–917, 2015, doi: 10.1149/06917.0893ecst.
[30] J. E. Park *et al.*, “Ultra-low loading of IrO2 with an inverse-opal structure in a polymer-exchange membrane water electrolysis,” *Nano Energy*, vol. 58, no. January, pp. 158–166, 2019, doi: 10.1016/j.nanoen.2019.01.043.
[31] F. M. Sapountzi, S. C. Divane, E. I. Papaioannou, S. Souentie, and C. G. Vayenas, “The role of Nafion content in sputtered IrO2 based anodes for low temperature PEM water electrolysis,” *J. Electroanal. Chem.*, vol. 662, no. 1, pp. 116–122, 2011, doi: 10.1016/j.jelechem.2011.04.005.
[32] C. Rozain, E. Mayousse, N. Guillet, and P. Millet, “Influence of iridium oxide loadings on the performance of PEM water electrolysis cells: Part I–Pure IrO2-based anodes,” *Appl. Catal. B Environ.*, vol. 182, pp. 153–160, 2016, doi: https://doi.org/10.1016/j.apcatb.2015.09.013.
[33] F. Hegge *et al.*, “water electrolysis made possible by nanofiber interlayers Efficient and stable low iridium-loaded anodes for PEM water electrolysis made possible by nanofiber interlayers,” 2020, doi: 10.1021/acsaem.0c00735.
[34] Z. Taie *et al.*, “Pathway to Complete Energy Sector Decarbonization with Available Iridium Resources using Ultralow Loaded Water Electrolyzers,” *ACS Appl. Mater. Interfaces*, 2020, doi: 10.1021/acsami.0c15687.
[35] S. Siracusano, V. Baglio, N. Van Dijk, L. Merlo, and A. S. Aricò, “Enhanced performance and durability of low catalyst loading PEM water electrolyser based on a short-side chain perfluorosulfonic ionomer,” *Appl. Energy*, vol. 192, pp. 477–489, 2017, doi: 10.1016/j.apenergy.2016.09.011.
[36] P. Mazúr, J. Polonský, M. Paidar, and K. Bouzek, “Non-conductive TiO2 as the anode catalyst support for PEM water electrolysis,” *Int. J. Hydrogen Energy*, vol. 37, no. 17, pp. 12081–12088, 2012, doi: https://doi.org/10.1016/j.ijhydene.2012.05.129.
[37] L. Du, L. Xing, G. Zhang, M. Dubois, and S. Sun, “Strategies for Engineering High-Performance PGM-Free Catalysts toward Oxygen Reduction and Evolution Reactions,” *Small Methods*, vol. 4, no. 6, pp. 1–28, 2020, doi: 10.1002/smtd.202000016.
[38] J. Mo *et al.*, “Thin liquid/gas diffusion layers for high-efficiency hydrogen production from water splitting,” *Appl. Energy*, vol. 177, pp. 817–822, 2016, doi: https://doi.org/10.1016/j.apenergy.2016.05.154.
[39] E. Leonard *et al.*, “Interfacial analysis of a PEM electrolyzer using X-ray computed tomography,” *Sustain. Energy Fuels*, pp. 921–931, 2020, doi: 10.1039/c9se00364a.
[40] J. J. Caparrós Mancera, F. Segura Manzano, J. M. Andújar, F. J. Vivas, and A. J. Calderón, “An Optimized Balance of Plant for a Medium-Size PEM Electrolyzer: Design, Control and Physical Implementation,” *Electronics*, vol. 9, no. 5, 2020, doi: 10.3390/electronics9050871.
[41] K. Ayers, N. Danilovic, K. Harrison, and X. Hui, “a Forerunner for Clean Hydrogen,” *J. Electrochem. Soc.*, vol. Interface, no. 30, p. 67, 2021.
[42] A. Mayyas *et al.*, “Manufacturing Cost Analysis for Proton Exchange Membrane Water Electrolyzers,” *Natl. Renew. Energy Lab.*, no. August, p. 65, 2019, [Online]. Available: https://www.nrel.gov/docs/fy10osti/72740.pdf.%0Ahttps://www.nrel.gov/docs/fy10osti/72740.pdf.

[43] S. R. Stock, “X-ray microtomography of materials,” *Int. Mater. Rev.*, vol. 44, no. 4, pp. 141–164, 1999, doi: 10.1179/095066099101528261.
[44] J. H. Kinney and M. C. Nichols, “X-ray tomographic microscopy (XTM) using synchrotron radiation,” *Annu. Rev. Mater. Sci.*, vol. 22, no. 1, pp. 121–152, Aug. 1992, doi: 10.1146/annurev.ms.22.080192.001005.
[45] D. J. Smith, “Progress and perspectives for atomic-resolution electron microscopy,” *Ultramicroscopy*, vol. 108, no. 3, pp. 159–166, 2008, doi: 10.1016/j.ultramic.2007.08.015.
[46] J. Orloff, L. W. Swanson, and M. Utlaut, “Fundamental limits to imaging resolution for focused ion beams,” *J. Vac. Sci. Technol. B Microelectron. Nanom. Struct.*, vol. 14, no. 6, pp. 3759–3763, 1996, doi: 10.1116/1.588663.
[47] P. J. Withers, “X-ray nanotomography,” *Mater. Today*, vol. 10, no. 12, pp. 26–34, 2007, doi: 10.1016/S1369-7021(07)70305-X.
[48] M. A. Hoeh *et al.*, “In-Operando Neutron Radiography Studies of Polymer Electrolyte Membrane Water Electrolyzers,” *ECS Trans.*, vol. 69, no. 17, pp. 1135–1140, 2015, doi: 10.1149/06917.1135ecst.
[49] J. Seweryn, J. Biesdorf, T. J. Schmidt, and P. Boillat, “Communication - Neutron radiography of the water/gas distribution in the porous layers of an operating electrolyser,” *J. Electrochem. Soc.*, vol. 163, no. 11, pp. F3009–F3011, 2016, doi: 10.1149/2.0641607jes.
[50] O. F. Selamet, U. Pasaogullari, D. Spernjak, D. S. Hussey, D. L. Jacobson, and M. D. Mat, “Two-phase flow in a proton exchange membrane electrolyzer visualized in situ by simultaneous neutron radiography and optical imaging,” *Int. J. Hydrogen Energy*, vol. 38, no. 14, pp. 5823–5835, 2013, doi: 10.1016/j.ijhydene.2013.02.087.
[51] S. J. Normile and I. V Zenyuk, “Imaging ionomer in fuel cell catalyst layers with synchrotron nano transmission x-ray microscopy,” *Solid State Ionics*, vol. 335, pp. 38–46, 2019, doi: https://doi.org/10.1016/j.ssi.2019.02.017.
[52] W. M. Harris *et al.*, “Three-Dimensional Microstructural Imaging of Sulfur Poisoning-Induced Degradation in a Ni-YSZ Anode of Solid Oxide Fuel Cells,” *Sci. Rep.*, vol. 4, no. 1, p. 5246, 2014, doi: 10.1038/srep05246.
[53] D. S. Eastwood *et al.*, “Three-dimensional characterization of electrodeposited lithium microstructures using synchrotron X-ray phase contrast imaging,” *Chem. Commun.*, vol. 51, no. 2, pp. 266–268, 2015, doi: 10.1039/C4CC03187C.
[54] J. Villanova *et al.*, “Fast in situ 3D nanoimaging: a new tool for dynamic characterization in materials science,” *Mater. Today*, vol. 20, no. 7, pp. 354–359, 2017, doi: https://doi.org/10.1016/j.mattod.2017.06.001.
[55] J. Gelb, D. P. Finegan, D. J. L. Brett, and P. R. Shearing, “Multi-scale 3D investigations of a commercial 18650 Li-ion battery with correlative electron- and X-ray microscopy,” *J. Power Sources*, vol. 357, pp. 77–86, 2017, doi: https://doi.org/10.1016/j.jpowsour.2017.04.102.
[56] Q. Meyer *et al.*, “Multi-Scale Imaging of Polymer Electrolyte Fuel Cells using X-ray Micro- and Nano-Computed Tomography, Transmission Electron Microscopy and Helium-Ion Microscopy,” *Fuel Cells*, vol. 19, no. 1, pp. 35–42, 2019, doi: 10.1002/fuce.201800047.
[57] A. D. Shum, D. Y. Parkinson, X. Xiao, A. Z. Weber, O. S. Burheim, and I. V. Zenyuk, “Investigating Phase-Change-Induced Flow in Gas Diffusion Layers in Fuel Cells with X-ray Computed Tomography,” *Electrochim. Acta*, vol. 256, pp. 279–290, 2017, doi:

10.1016/j.electacta.2017.10.012.
[58] D. Spernjak *et al.*, “Enhanced Water Management of Polymer Electrolyte Fuel Cells with Additive-Containing Microporous Layers,” *ACS Appl. Energy Mater.*, vol. 1, no. 11, pp. 6006–6017, Nov. 2018, doi: 10.1021/acsaem.8b01059.
[59] I. V Zenyuk and A. Z. Weber, “Understanding Liquid-Water Management in PEFCs Using X-Ray Computed Tomography and Modeling,” *ECS Meet. Abstr.*, vol. MA2015-02, no. 37, pp. 1536–1536, 2015, doi: 10.1149/ma2015-02/37/1536.
[60] M. Mandal *et al.*, “The Importance of Water Transport in High Conductivity and High-Power Alkaline Fuel Cells,” *J. Electrochem. Soc.*, vol. 167, no. 5, p. 54501, Oct. 2019, doi: 10.1149/2.0022005jes.
[61] P. Satjaritanun, S. Hirano, I. V Zenyuk, J. W. Weidner, N. Tippayawong, and S. Shimpalee, “Numerical Study of Electrochemical Kinetics and Mass Transport inside Nano-Structural Catalyst Layer of {PEMFC} Using Lattice Boltzmann Agglomeration Method,” *J. Electrochem. Soc.*, vol. 167, no. 1, p. 13516, Oct. 2019, doi: 10.1149/2.0162001jes.
[62] I. V Zenyuk, “Bridging X-ray computed tomography and computational modeling for electrochemical energy-conversion and –storage,” *Curr. Opin. Electrochem.*, vol. 13, pp. 78–85, 2019, doi: https://doi.org/10.1016/j.coelec.2018.10.016.
[63] I. Manke *et al.*, “Investigation of water evolution and transport in fuel cells with high resolution synchrotron x-ray radiography,” *Appl. Phys. Lett.*, vol. 90, no. 17, 2007, doi: 10.1063/1.2731440.
[64] A. Schneider, C. Wieser, J. Roth, and L. Helfen, “Impact of synchrotron radiation on fuel cell operation in imaging experiments,” *J. Power Sources*, vol. 195, no. 19, pp. 6349–6355, 2010, doi: 10.1016/j.jpowsour.2010.04.032.
[65] Y. Nagai *et al.*, “Improving water management in fuel cells through microporous layer modifications: Fast operando tomographic imaging of liquid water,” *J. Power Sources*, vol. 435, p. 226809, 2019, doi: https://doi.org/10.1016/j.jpowsour.2019.226809.
[66] R. T. White *et al.*, “3D Printed Flow Field and Fixture for Visualization of Water Distribution in Fuel Cells by X-ray Computed Tomography,” *J. Electrochem. Soc.*, vol. 163, no. 13, pp. F1337–F1343, 2016, doi: 10.1149/2.0461613jes.
[67] X. Yang *et al.*, “Low-dose x-ray tomography through a deep convolutional neural network,” *Sci. Rep.*, vol. 8, no. 1, p. 2575, 2018, doi: 10.1038/s41598-018-19426-7.
[68] A. Z. Weber and J. Newman, “Coupled Thermal and Water Management in Polymer Electrolyte Fuel Cells,” *J. Electrochem. Soc.*, vol. 153, no. 12, p. A2205, 2006, doi: 10.1149/1.2352039.
[69] S. J. Normile *et al.*, “Direct observations of liquid water formation at nano- and micro-scale in platinum group metal-free electrodes by operando X-ray computed tomography,” *Mater. Today Energy*, vol. 9, pp. 187–197, 2018, doi: https://doi.org/10.1016/j.mtener.2018.05.011.
[70] X. Peng *et al.*, “Using operando techniques to understand and design high performance and stable alkaline membrane fuel cells,” *Nat. Commun.*, vol. 11, no. 1, 2020, doi: 10.1038/s41467-020-17370-7.
[71] T. Schuler, R. De Bruycker, T. J. Schmidt, and F. N. Buchi, “Polymer electrolytewater electrolysis: Correlating porous transport layer structural properties and performance: Part i. tomographic analysis of morphology and topology,” *J. Electrochem. Soc.*, vol. 166, no. 4, pp. F270–F281, 2019, doi: 10.1149/2.0561904jes.

[72] T. Schuler, T. J. Schmidt, and F. N. Büchi, “Polymer Electrolyte Water Electrolysis: Correlating Performance and Porous Transport Layer Structure: Part II. Electrochemical Performance Analysis,” *J. Electrochem. Soc.*, vol. 166, no. 10, pp. F555–F565, 2019, doi: 10.1149/2.1241908jes.
[73] J. Lopata, Z. Kang, J. Young, G. Bender, J. W. Weidner, and S. Shimpalee, “Effects of the Transport/Catalyst Layer Interface and Catalyst Loading on Mass and Charge Transport Phenomena in Polymer Electrolyte Membrane Water Electrolysis Devices,” *J. Electrochem. Soc.*, vol. 167, no. 6, p. 064507, 2020, doi: 10.1149/1945-7111/ab7f87.
[74] J. K. Lee *et al.*, “Accelerating bubble detachment in porous transport layers with patterned through pores,” *ACS Appl. Energy Mater.*, 2020, doi: 10.1021/acsaem.0c01239.
[75] A. J. Bard, L. R. Faulkner, and H. S. White, *Electrochemical methods: fundamentals and applications*. John Wiley & Sons, 2022.
[76] S. Siracusano, S. Trocino, N. Briguglio, V. Baglio, and A. S. Aricò, “Electrochemical impedance spectroscopy as a diagnostic tool in polymer electrolyte membrane electrolysis,” *Materials (Basel).*, vol. 11, no. 8, 2018, doi: 10.3390/ma11081368.
[77] J. van der Merwe, K. Uren, G. van Schoor, and D. Bessarabov, “Characterisation tools development for PEM electrolysers,” *Int. J. Hydrogen Energy*, vol. 39, no. 26, pp. 14212–14221, 2014, doi: https://doi.org/10.1016/j.ijhydene.2014.02.096.
[78] D. Gürsoy, F. De Carlo, X. Xiao, and C. Jacobsen, “TomoPy: a framework for the analysis of synchrotron~tomographic data,” *J. Synchrotron Radiat.*, vol. 21, no. 5, pp. 1188–1193, Sep. 2014, doi: 10.1107/S1600577514013939.
[79] A. Serov *et al.*, “Nano-structured platinum group metal-free catalysts and their integration in fuel cell electrode architectures,” *Appl. Catal. B Environ.*, vol. 237, no. May 2017, pp. 1139–1147, 2018, doi: 10.1016/j.apcatb.2017.08.067.
[80] S. M. Alia, K. S. Reeves, J. S. Baxter, and D. A. Cullen, “The Impact of Ink and Spray Variables on Catalyst Layer Properties, Electrolyzer Performance, and Electrolyzer Durability,” *J. Electrochem. Soc.*, vol. 167, no. 14, p. 144512, 2020, doi: 10.1149/1945-7111/abc746.
[81] J. Mo *et al.*, “Discovery of true electrochemical reactions for ultrahigh catalyst mass activity in water splitting,” *Sci. Adv.*, vol. 2, no. 11, 2016, doi: 10.1126/sciadv.1600690.
[82] T. Schuler, T. Kimura, T. J. Schmidt, and F. N. Büchi, “Towards a generic understanding of oxygen evolution reaction kinetics in polymer electrolyte water electrolysis,” *Energy Environ. Sci.*, vol. 13, no. 7, pp. 2153–2166, 2020, doi: 10.1039/d0ee00673d.
[83] T. Schuler *et al.*, “Hierarchically Structured Porous Transport Layers for Polymer Electrolyte Water Electrolysis,” *Adv. Energy Mater.*, vol. 1903216, pp. 1903216–1903228, 2019, doi: 10.1002/aenm.201903216.
[84] N. M. Marković, B. N. Grgur, and P. N. Ross, “Temperature-Dependent Hydrogen Electrochemistry on Platinum Low-Index Single-Crystal Surfaces in Acid Solutions,” *J. Phys. Chem. B*, vol. 101, no. 27, pp. 5405–5413, Jul. 1997, doi: 10.1021/jp970930d.
[85] G. Jerkiewicz, “Electrochemical Hydrogen Adsorption and Absorption. Part 1: Under-potential Deposition of Hydrogen,” *Electrocatalysis*, vol. 1, no. 4, pp. 179–199, 2010, doi: 10.1007/s12678-010-0022-1.
[86] S. M. Alia, K. E. Hurst, S. S. Kocha, and B. S. Pivovar, “Mercury Underpotential Deposition to Determine Iridium and Iridium Oxide Electrochemical Surface Areas,” *J. Electrochem. Soc.*, vol. 163, no. 11, pp. F3051–F3056, 2016, doi: 10.1149/2.0071611jes.
[87] S. Zhao *et al.*, “Calculating the Electrochemically Active Surface Area of Iridium Oxide

in Operating Proton Exchange Membrane Electrolyzers," *J. Electrochem. Soc.*, vol. 162, no. 12, pp. F1292–F1298, 2015, doi: 10.1149/2.0211512jes.
[88] M. Suermann, T. J. Schmidt, and F. N. Büchi, "Cell Performance Determining Parameters in High Pressure Water Electrolysis," *Electrochim. Acta*, vol. 211, pp. 989–997, 2016, doi: https://doi.org/10.1016/j.electacta.2016.06.120.
[89] M. Kroschel, A. Bonakdarpour, J. T. H. Kwan, P. Strasser, and D. P. Wilkinson, "Analysis of oxygen evolving catalyst coated membranes with different current collectors using a new modified rotating disk electrode technique," *Electrochim. Acta*, vol. 317, pp. 722–736, 2019, doi: https://doi.org/10.1016/j.electacta.2019.05.011.
[90] T. Shinagawa, A. T. Garcia-Esparza, and K. Takanabe, "Insight on Tafel slopes from a microkinetic analysis of aqueous electrocatalysis for energy conversion," *Sci. Rep.*, vol. 5, no. May, pp. 1–21, 2015, doi: 10.1038/srep13801.
[91] "H2-Transport Limitations in the Hydrogen Electrode in PEM Water Electrolysis," *ECS Meet. Abstr.*, 2017, doi: 10.1149/ma2017-01/31/1513.
[92] R. Iwata *et al.*, "Bubble growth and departure modes on wettable/non-wettable porous foams in alkaline water splitting," *Joule*, vol. 5, no. 4, pp. 887–900, 2021, doi: 10.1016/j.joule.2021.02.015.
[93] T. Kadyk, D. Bruce, and M. Eikerling, "How to Enhance Gas Removal from Porous Electrodes?," *Sci. Rep.*, vol. 6, no. December, pp. 1–14, 2016, doi: 10.1038/srep38780.
[94] X. Peng *et al.*, "Insights into Interfacial and Bulk Transport Phenomena Affecting Proton Exchange Membrane Water Electrolyzer Performance at Ultra-Low Iridium Loadings," *Adv. Sci.*, vol. 8, no. 21, pp. 1–9, 2021, doi: 10.1002/advs.202102950.
[95] S. M. Alia, S. Stariha, and R. L. Borup, "Electrolyzer Durability at Low Catalyst Loading and with Dynamic Operation," *J. Electrochem. Soc.*, vol. 166, no. 15, pp. F1164–F1172, Oct. 2019, doi: 10.1149/2.0231915jes.
[96] P. Aßmann, A. S. Gago, P. Gazdzicki, K. A. Friedrich, and M. Wark, "Toward developing accelerated stress tests for proton exchange membrane electrolyzers," *Curr. Opin. Electrochem.*, vol. 21, no. March, pp. 225–233, 2020, doi: 10.1016/j.coelec.2020.02.024.
[97] Z. Abdin, C. J. Webb, and E. M. Gray, "Modelling and simulation of a proton exchange membrane (PEM) electrolyser cell," *Int. J. Hydrogen Energy*, vol. 40, no. 39, pp. 13243–13257, 2015, doi: https://doi.org/10.1016/j.ijhydene.2015.07.129.
[98] J. O. Majasan, J. I. S. Cho, I. Dedigama, D. Tsaoulidis, P. Shearing, and D. J. L. Brett, "Two-phase flow behaviour and performance of polymer electrolyte membrane electrolysers: Electrochemical and optical characterisation," *Int. J. Hydrogen Energy*, vol. 43, no. 33, pp. 15659–15672, 2018, doi: 10.1016/j.ijhydene.2018.07.003.
[99] R. García-Valverde, N. Espinosa, and A. Urbina, "Simple PEM water electrolyser model and experimental validation," *Int. J. Hydrogen Energy*, vol. 37, no. 2, pp. 1927–1938, 2012, doi: https://doi.org/10.1016/j.ijhydene.2011.09.027.
[100] E. Leonard *et al.*, "Operando X-ray tomography and sub-second radiography for characterizing transport in polymer electrolyte membrane electrolyzer," *Electrochim. Acta*, vol. 276, pp. 424–433, 2018, doi: 10.1016/j.electacta.2018.04.144.
[101] C. H. Lee *et al.*, "Influence of limiting throat and flow regime on oxygen bubble saturation of polymer electrolyte membrane electrolyzer porous transport layers," *Int. J. Hydrogen Energy*, vol. 42, no. 5, pp. 2724–2735, 2017, doi: 10.1016/j.ijhydene.2016.09.114.
[102] C. H. Lee, J. K. Lee, B. Zhao, K. F. Fahy, and A. Bazylak, "Transient Gas Distribution in

Porous Transport Layers of Polymer Electrolyte Membrane Electrolyzers," *J. Electrochem. Soc.*, vol. 167, no. 2, p. 24508, Jan. 2020, doi: 10.1149/1945-7111/ab68c8.
[103] M. Zlobinski, T. Schuler, F. N. Büchi, T. J. Schmidt, and P. Boillat, "Transient and Steady State Two-Phase Flow in Anodic Porous Transport Layer of Proton Exchange Membrane Water Electrolyzer," *J. Electrochem. Soc.*, vol. 167, no. 8, p. 84509, May 2020, doi: 10.1149/1945-7111/ab8c89.
[104] J. C. Fornaciari *et al.*, "The Role of Water in Vapor-fed Proton-Exchange-Membrane Electrolysis," *J. Electrochem. Soc.*, vol. 167, no. 10, p. 104508, 2020, doi: 10.1149/1945-7111/ab9b09.
[105] E. Sattari, S. P. Zanous, M. Farhadi, and A. Mohamad, "Numerical investigation of the vapor bubble's scenarios passing through aerophobic/aerophilic porous structures using lattice Boltzmann method," *J. Power Sources*, vol. 454, p. 227929, 2020, doi: https://doi.org/10.1016/j.jpowsour.2020.227929.
[106] S. De Angelis, T. Schuler, M. A. Charalambous, F. Marone, T. J. Schmidt, and F. N. Büchi, "Unraveling two-phase transport in porous transport layer materials for polymer electrolyte water electrolysis," *J. Mater. Chem. A*, vol. 9, no. 38, pp. 22102–22113, 2021, doi: 10.1039/d1ta03379d.
[107] P. Lettenmeier *et al.*, "Comprehensive investigation of novel pore-graded gas diffusion layers for high-performance and cost-effective proton exchange membrane electrolyzers," *Energy Environ. Sci.*, vol. 10, no. 12, pp. 2521–2533, 2017, doi: 10.1039/c7ee01240c.
[108] J. Garcia-Navarro, M. Schulze, and K. A. Friedrich, "Understanding the Role of Water Flow and the Porous Transport Layer on the Performance of Proton Exchange Membrane Water Electrolyzers," *ACS Sustain. Chem. Eng.*, vol. 7, no. 1, pp. 1600–1610, 2019, doi: 10.1021/acssuschemeng.8b05369.
[109] S. Paliwal, D. Panda, S. Bhaskaran, N. Vorhauer-Huget, E. Tsotsas, and V. K. Surasani, "Lattice Boltzmann method to study the water-oxygen distributions in porous transport layer (PTL) of polymer electrolyte membrane (PEM) electrolyser," *Int. J. Hydrogen Energy*, vol. 46, no. 44, pp. 22747–22762, 2021, doi: https://doi.org/10.1016/j.ijhydene.2021.04.112.
[110] P. Lettenmeier, S. Kolb, F. Burggraf, A. S. Gago, and K. A. Friedrich, "Towards developing a backing layer for proton exchange membrane electrolyzers," *J. Power Sources*, vol. 311, pp. 153–158, 2016, doi: https://doi.org/10.1016/j.jpowsour.2016.01.100.
[111] J. K. Lee *et al.*, "Spatially graded porous transport layers for gas evolving electrochemical energy conversion: High performance polymer electrolyte membrane electrolyzers," *Energy Convers. Manag.*, vol. 226, p. 113545, 2020, doi: https://doi.org/10.1016/j.enconman.2020.113545.
[112] T. Schuler, R. De Bruycker, T. J. Schmidt, and F. N. Büchi, "Polymer Electrolyte Water Electrolysis: Correlating Porous Transport Layer Structural Properties and Performance: Part I. Tomographic Analysis of Morphology and Topology," *J. Electrochem. Soc.*, vol. 166, no. 4, pp. F270–F281, 2019, doi: 10.1149/2.0561904jes.
[113] I. V. Zenyuk, D. Y. Parkinson, G. Hwang, and A. Z. Weber, "Probing water distribution in compressed fuel-cell gas-diffusion layers using X-ray computed tomography," *Electrochem. commun.*, vol. 53, pp. 24–28, 2015, doi: 10.1016/j.elecom.2015.02.005.
[114] R. Lenormand, E. Touboul, and C. Zarcone, "Numerical models and experiments on immiscible displacements in porous media," *J. Fluid Mech.*, vol. 189, pp. 165–187, 1988,

doi: 10.1017/S0022112088000953.
[115] C. Engineering, “Viscous Fingering in,” vol. M, no. 1987, pp. 271–311, 1987.
[116] N. B. Lu, C. A. Browne, D. B. Amchin, J. K. Nunes, and S. S. Datta, “Controlling capillary fingering using pore size gradients in disordered media,” *Phys. Rev. Fluids*, vol. 4, no. 8, pp. 1–21, 2019, doi: 10.1103/PhysRevFluids.4.084303.
[117] J. Nie and Y. Chen, “Numerical modeling of three-dimensional two-phase gas–liquid flow in the flow field plate of a PEM electrolysis cell,” *Int. J. Hydrogen Energy*, vol. 35, no. 8, pp. 3183–3197, 2010, doi: https://doi.org/10.1016/j.ijhydene.2010.01.050.
[118] M. Ferer, C. Ji, G. S. Bromhal, J. Cook, G. Ahmadi, and D. H. Smith, “Crossover from capillary fingering to viscous fingering for immiscible unstable flow:Experiment and modeling,” *Phys. Rev. E - Stat. Physics, Plasmas, Fluids, Relat. Interdiscip. Top.*, vol. 70, no. 1, p. 7, 2004, doi: 10.1103/PhysRevE.70.016303.
[119] S. An, H. Erfani, O. E. Godinez-Brizuela, and V. Niasar, “Transition From Viscous Fingering to Capillary Fingering: Application of GPU-Based Fully Implicit Dynamic Pore Network Modeling,” *Water Resour. Res.*, vol. 56, no. 12, pp. 1–18, 2020, doi: 10.1029/2020WR028149.
[120] J. K. Lee and A. Bazylak, “Optimizing Porous Transport Layer Design Parameters via Stochastic Pore Network Modelling: Reactant Transport and Interfacial Contact Considerations,” *J. Electrochem. Soc.*, vol. 167, no. 1, p. 13541, Jan. 2020, doi: 10.1149/1945-7111/ab6557.
[121] J. K. Lee and A. Bazylak, “Balancing Reactant Transport and {PTL}-{CL} Contact in {PEM} Electrolyzers by Optimizing {PTL} Design Parameters via Stochastic Pore Network Modeling,” *{ECS} Trans.*, vol. 92, no. 8, pp. 801–820, Jul. 2019, doi: 10.1149/09208.0801ecst.
[122] N. T. Suen, S. F. Hung, Q. Quan, N. Zhang, Y. J. Xu, and H. M. Chen, “Electrocatalysis for the oxygen evolution reaction: Recent development and future perspectives,” *Chem. Soc. Rev.*, vol. 46, no. 2, pp. 337–365, 2017, doi: 10.1039/c6cs00328a.
[123] Y. Matsumoto and E. Sato, “Electrocatalytic properties of transition metal oxides for oxygen evolution reaction,” *Mater. Chem. Phys.*, vol. 14, no. 5, pp. 397–426, 1986, doi: https://doi.org/10.1016/0254-0584(86)90045-3.
[124] J. K. Nørskov *et al.*, “Origin of the overpotential for oxygen reduction at a fuel-cell cathode,” *J. Phys. Chem. B*, vol. 108, no. 46, pp. 17886–17892, 2004, doi: 10.1021/jp047349j.
[125] Z. W. She, J. Kibsgaard, C. F. Dickens, I. Chorkendorff, J. K. Nørskov, and T. F. Jaramillo, “Combining theory and experiment in electrocatalysis: Insights into materials design,” *Science (80-.).*, vol. 355, no. 6321, 2017, doi: 10.1126/science.aad4998.
[126] Y. Lee, J. Suntivich, K. J. May, E. E. Perry, and Y. Shao-Horn, “Synthesis and activities of rutile IrO 2 and RuO 2 nanoparticles for oxygen evolution in acid and alkaline solutions,” *J. Phys. Chem. Lett.*, vol. 3, no. 3, pp. 399–404, 2012, doi: 10.1021/jz2016507.
[127] W. Schmickler and E. Santos, *Interfacial Electrochemistry*. 2010.
[128] J. O. M. Bockris and A. K. N. Reddy, “Modern Aspects of Electrochemistry, Vol. 2.” Springer, 1970.
[129] A. Damjanovic, A. Dey, and J. Bockris, “Electrode kinetics of oxygen evolution and dissolution on Rh, Ir, and Pt-Rh alloy electrodes,” *J. Electrochem. Soc.*, vol. 113, no. 7, p. 739, 1966.
[130] A. Grimaud, W. T. Hong, Y. Shao-Horn, and J. M. Tarascon, “Anionic Redox Processes

for Enhanced Battery and Water Splitting Devices," *Nat. Mater*, vol. 15, no. 2, pp. 121–126, 2016.
[131] J. J. Velasco-Vélez *et al.*, "Electrochemically active Ir NPs on graphene for OER in acidic aqueous electrolyte investigated by in situ and ex situ spectroscopies," *Surf. Sci.*, vol. 681, no. September 2018, pp. 1–8, 2019, doi: 10.1016/j.susc.2018.10.021.
[132] S. Fierro, T. Nagel, H. Baltruschat, and C. Comninellis, "Investigation of the oxygen evolution reaction on Ti/IrO2 electrodes using isotope labelling and on-line mass spectrometry," *Electrochem. commun.*, vol. 9, no. 8, pp. 1969–1974, 2007, doi: https://doi.org/10.1016/j.elecom.2007.05.008.
[133] S. Cherevko, S. Geiger, O. Kasian, A. Mingers, and K. J. J. Mayrhofer, "Oxygen evolution activity and stability of iridium in acidic media. Part 2. - Electrochemically grown hydrous iridium oxide," *J. Electroanal. Chem.*, vol. 774, pp. 102–110, 2016, doi: 10.1016/j.jelechem.2016.05.015.
[134] N. Sivasankar, W. W. Weare, and H. Frei, "Direct Observation of a Hydroperoxide Surface Intermediate upon Visible Light-Driven Water Oxidation at an Ir Oxide Nanocluster Catalyst by Rapid-Scan FT-IR Spectroscopy," *J. Am. Chem. Soc.*, vol. 133, no. 33, pp. 12976–12979, Aug. 2011, doi: 10.1021/ja205300a.
[135] A. Grimaud, W. T. Hong, Y. Shao-Horn, and J. M. Tarascon, "Anionic redox processes for electrochemical devices," *Nat. Mater.*, vol. 15, no. 2, pp. 121–126, 2016, doi: 10.1038/nmat4551.
[136] S. Cherevko, S. Geiger, O. Kasian, A. Mingers, and K. J. J. Mayrhofer, "Oxygen evolution activity and stability of iridium in acidic media. Part 1. - Metallic iridium," *J. Electroanal. Chem.*, vol. 773, pp. 69–78, 2016, doi: 10.1016/j.jelechem.2016.04.033.
[137] O. Kasian, J. P. Grote, S. Geiger, S. Cherevko, and K. J. J. Mayrhofer, "The Common Intermediates of Oxygen Evolution and Dissolution Reactions during Water Electrolysis on Iridium," *Angew. Chemie - Int. Ed.*, vol. 57, no. 9, pp. 2488–2491, 2018, doi: 10.1002/anie.201709652.
[138] S. Geiger *et al.*, "The stability number as a metric for electrocatalyst stability benchmarking," *Nat. Catal.*, vol. 1, no. 7, pp. 508–515, 2018, doi: 10.1038/s41929-018-0085-6.
[139] E. Willinger, C. Massué, R. Schlögl, and M. G. Willinger, "Identifying Key Structural Features of IrOx Water Splitting Catalysts," *J. Am. Chem. Soc.*, vol. 139, no. 34, pp. 12093–12101, 2017, doi: 10.1021/jacs.7b07079.
[140] S. Geiger, O. Kasian, B. R. Shrestha, A. M. Mingers, K. J. J. Mayrhofer, and S. Cherevko, "Activity and Stability of Electrochemically and Thermally Treated Iridium for the Oxygen Evolution Reaction," *J. Electrochem. Soc.*, vol. 163, no. 11, pp. F3132–F3138, 2016, doi: 10.1149/2.0181611jes.
[141] V. Pfeifer *et al.*, "The electronic structure of iridium oxide electrodes active in water splitting," *Phys. Chem. Chem. Phys.*, vol. 18, no. 4, pp. 2292–2296, 2016, doi: 10.1039/c5cp06997a.
[142] F. Claudel *et al.*, "Degradation Mechanisms of Oxygen Evolution Reaction Electrocatalysts: A Combined Identical-Location Transmission Electron Microscopy and X-ray Photoelectron Spectroscopy Study," *ACS Catal.*, vol. 9, no. 5, pp. 4688–4698, 2019, doi: 10.1021/acscatal.9b00280.
[143] H. Yu, L. Bonville, J. Jankovic, and R. Maric, "Microscopic insights on the degradation of a PEM water electrolyzer with ultra-low catalyst loading," *Appl. Catal. B Environ.*, 2020,

doi: 10.1016/j.apcatb.2019.118194.
[144] J.-P. B. Haraldsted *et al.*, “Trace anodic migration of iridium and titanium ions and subsequent cathodic selectivity degradation in acid electrolysis systems,” *Mater. Today Energy*, vol. 14, p. 100352, 2019, doi: https://doi.org/10.1016/j.mtener.2019.100352.
[145] A. Lončar, D. Escalera-López, S. Cherevko, and N. Hodnik, “Inter-relationships between Oxygen Evolution and Iridium Dissolution Mechanisms,” *Angew. Chemie - Int. Ed.*, vol. 61, no. 14, 2022, doi: 10.1002/anie.202114437.
[146] K. Schweinar, B. Gault, I. Mouton, and O. Kasian, “Lattice Oxygen Exchange in Rutile IrO2 during the Oxygen Evolution Reaction,” *J. Phys. Chem. Lett.*, vol. 11, no. 13, pp. 5008–5014, Jul. 2020, doi: 10.1021/acs.jpclett.0c01258.
[147] C. C. Weber, T. Schuler, R. De Bruycker, L. Gubler, F. N. Büchi, and S. De Angelis, “On the role of porous transport layer thickness in polymer electrolyte water electrolysis,” *J. Power Sources Adv.*, vol. 15, no. March, p. 100095, 2022, doi: 10.1016/j.powera.2022.100095.

Appendix A

a)

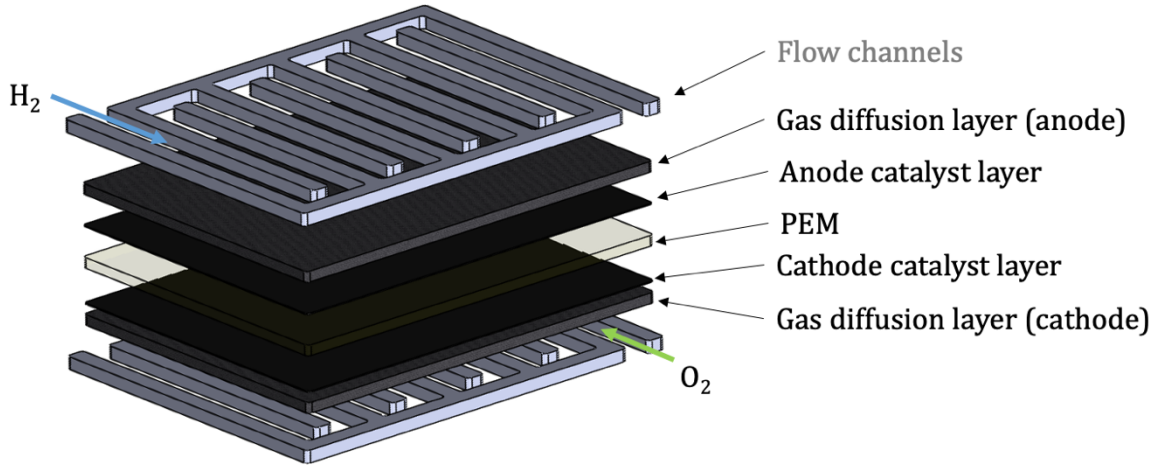

b)

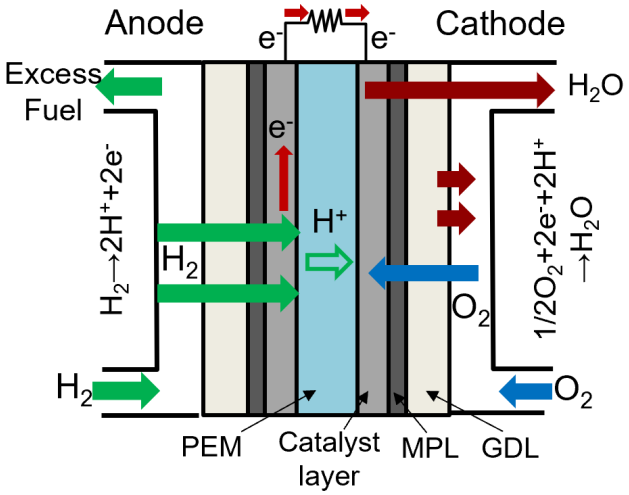

Figure A1. a) Schematic of a PEM fuel cell with flow-field and b) detailed description of PEM fuel cell reactions and transport processes.

Table A- 1 Parameters for material selection for micro x-ray CT operando fuel cell.

	¼" 6061-T6 Aluminum	300 nm Gold Sputtered on ¼" PEEK	¼" Fuel Cell Grade Graphite
I/I_0 at 22 keV	0.014	0.47	0.80
Electrical resistance of 1cm X 4cm X thickness cuboid	2.5E-5 Ω	> 0.77 Ω	0.60 Ω
Thermal Conductivity	167 W/mK	0.273 W/mK	275 W/mK in plane 5.0 W/mK thru plane
Max displacement of 1cm X 4cm X ¼" cuboid under 6 kN of force	0.27 mm	4.8 mm	1.9 mm
Durability	Excellent	Gold sputtering is prone to being scraped off	Brittle – will break if dropped or over compressed
Machinability	Most Difficult	Medium difficulty	Easily machined with desktop CNC router

Table A- 2 More details on fuel cell grade graphite physical properties.

Plate Physical Properties	
Plate Grade	Fuel Cell Grade (FU 4369)
Bulk Density	1.90 g/cm
Hardness	> 100 (Rockwell (HRB 10/40))
Compressive Strength	> 50MPa or 7250 psi
Flexural Strength	> 40 MPa or 6090 psi
Young's Modulus – Flexural	10GPa or 1.45 x 10^6
Young's Modulus – Dynamic	24GPa or 3.48 x 10^6

Plate Electrical Properties	
Specific Electrical Conductivity - XY (In-Plane)	110 S/cm
Specific Electrical Conductivity - Z (Through-Plane)	20 S/cm
Specific Electrical Resistance - XY (In-Plane)	90 micro ohms/M
Specific Electrical Resistance - Z (Through-Plane)	190 micro ohms/M (DIN 51 911) and 500 micro ohms/M(Internal Specification)
Long Term Stability	
Various Acids at 85C and 180C (185F and 356F)	2000 h
Mineral Oil at 85C and 185C (185F and 356F)	2000 h
Methanol at 90C (194F)	3000 h
Other Plate Properties	
Thermal Conductivity	55 w/mK

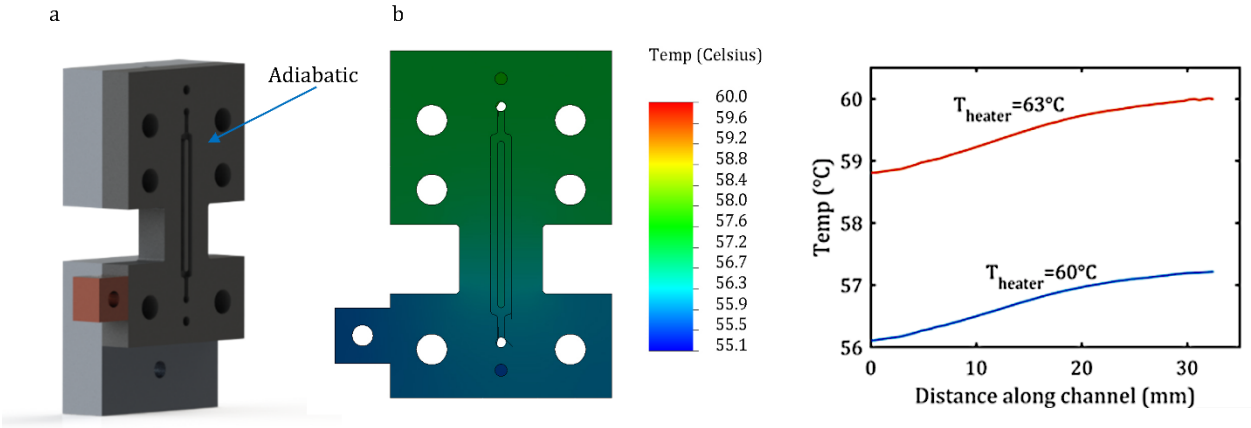

Figure A2. a) Model for thermal analysis – the channel face is modeled as adiabatic, all other faces are modeled as having a convective heat transfer coefficient of 7.3 $Wm^{-2}K^{-1}$ b) Temperature distribution along graphite plate c) Temperature distribution along the graphite

plate, where 0 mm is the bottom inlet of the channel. The simulation was repeated with the heater set to 60ºC and 63ºC respectively.

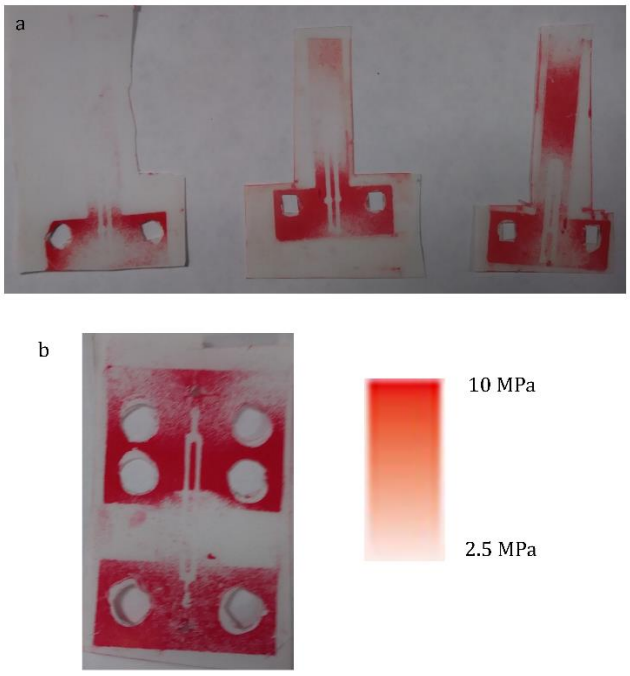

Figure A3. a) Compression pattern of cell a) Gen 3 micro CT cell b) Gen 5 micro x-ray CT cell

Thermal analysis of the gen 5 micro CT cell: The operating temperature of most fuel cells is between 60 and 80 °C. In the case of this cell, the operating temperature was 60 °C. This was accomplished with a 0.75 W cartridge heater inserted into the aluminum plate on both sides of the cell as shown in Figure 3c. Each side also had a thermocouple inserted between the aluminum plate and the graphite plate which enabled feedback control. An Arduino Uno microcontroller running a proportional-integral-derivative (PID) loop controlled a pair of transistors which provided a 5V pulse width modulation (PWM) signal to the heaters. The proportional, integral, and derivative gains of the PID controller were 1, 10, and 3 respectively. Modeling the cell as a 5

cm 60 °C vertical plate in quiescent 20 °C air gives a heat transfer coefficient due to natural convection of 7.3 $Wm^{-2}K^{-1}$ by equation S.1 Figure S3 shows the step response of the heater system.

$$Nu = 0.680 + \frac{0.670 * Ra^{\frac{1}{4}}}{[1 + (0.429/Pr)^{9/16}]^{4/9}} \quad \text{S.1}$$

$$Ra_L = Gr_L Pr = \frac{g\beta(T_s - T_\infty)L^3}{\upsilon^2} Pr \quad \text{S.2}$$

$$Nu = \frac{hL}{k} \quad \text{S.3}$$

Where h is heat transfer coefficient, k is thermal conductivity of the fluid, Nu is Nusselt number, Ra is Rayleigh number, Pr is Prandtl number, L is length of the plate, g is acceleration due to gravity, ß is volumetric thermal expansion coefficient, T_s is surface temperature, T_∞ is bulk temperature, ν is kinematic viscosity.

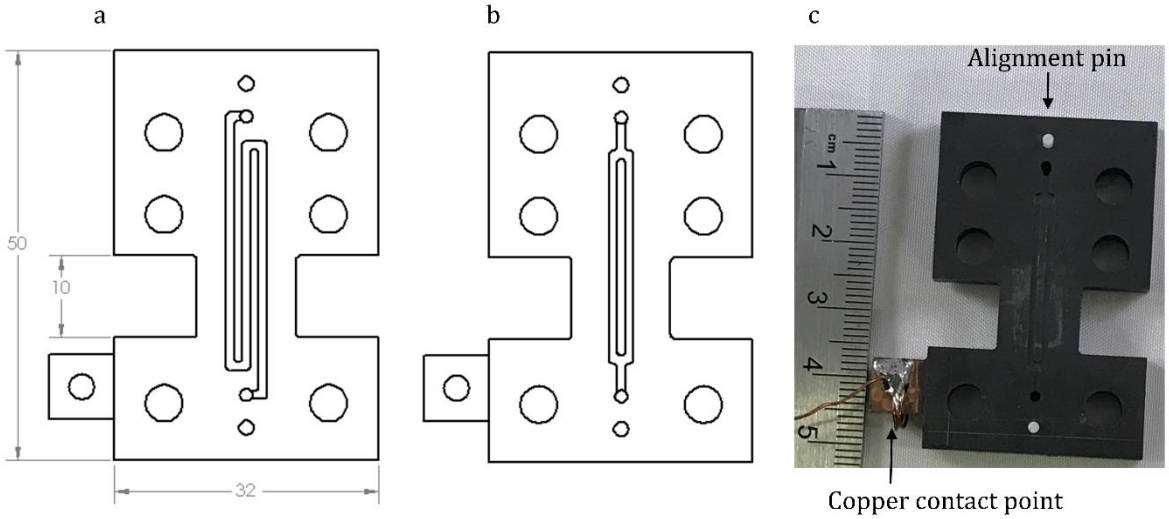

Figure A4. Fuel Cell and electrolyzer flow channel designs. Marked dimensions are in millimeters and all channels are 1mm wide x 1mm deep with 1mm land. a) Fuel cell serpentine

channel design, b) electrolyzer parallel channel design, c) photo of flow field with parallel channels. The white alignment pins at the top and bottom of the channel to ensures that the anode and cathode channels are in precise alignment. The copper electrical contact point reduces contact resistance between the plate and the wire.

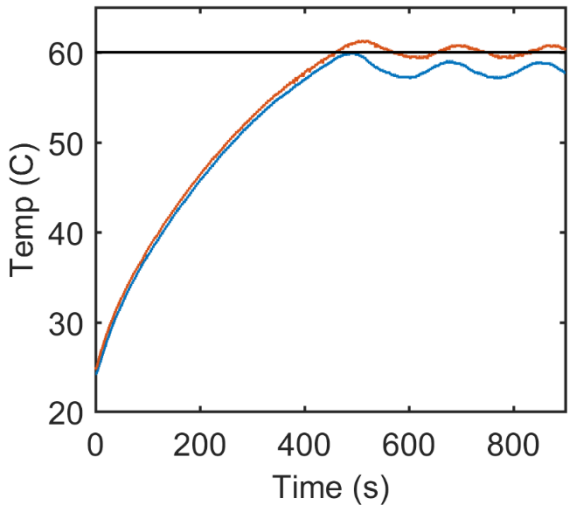

Figure A5. Step response of anode heater (blue) and cathode heater (red).

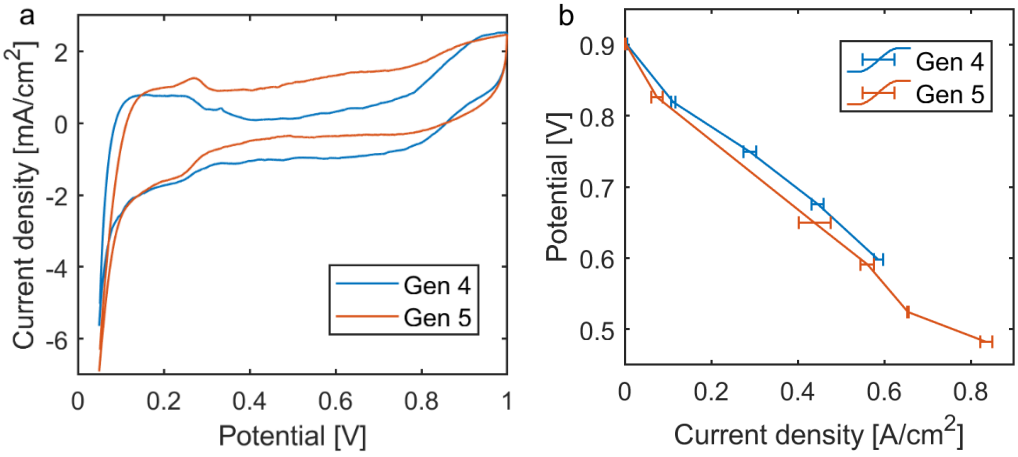

Figure A6. Comparison of electrochemical test conditions for Gen 4 and Gen 5 cells. a) Cyclic voltammetry in H_2/N_2 with 50 mV/s sweep rate. b) Polarization curves (iR-corrected) in H_2/air,

where constant current holds were used, where each point is averaged over 3 min hold and error bars indicated that average. The gas flow-rates were 0.25/0.25 slpm on anode and cathode, 60°C, ambient gas pressure.

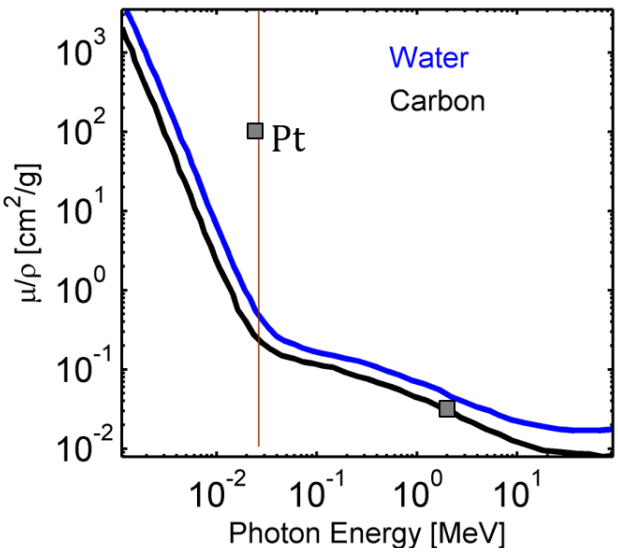

Figure A7. Linear attenuation coefficients of water and carbon as a function of incident x-ray energy. The typical micro x-ray CT energy is shown by a vertical line.

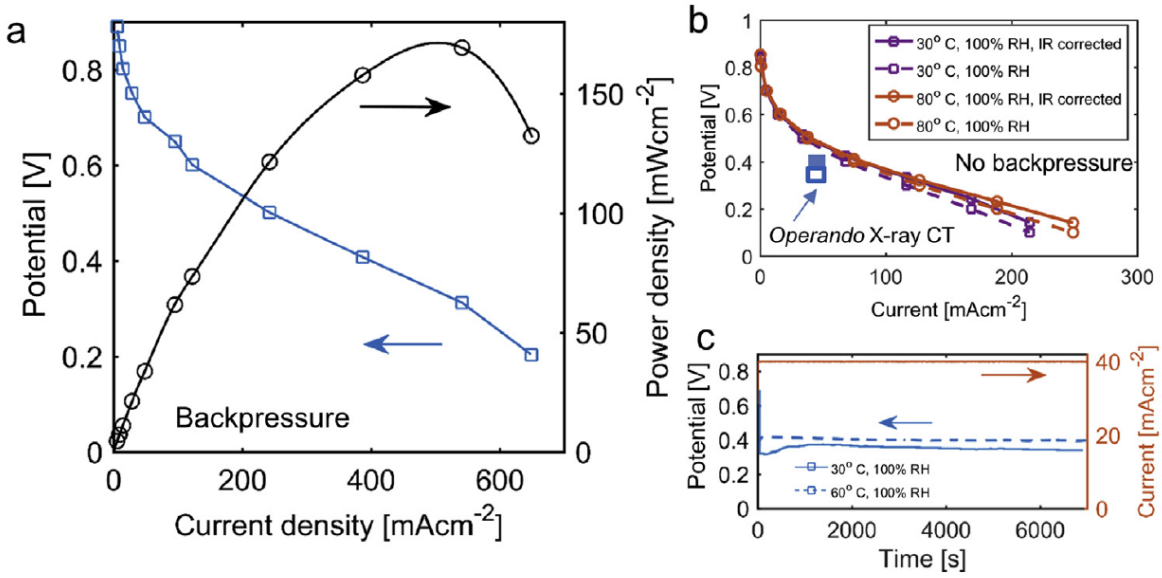

Figure A8. a) Polarization curve with the standard hardware and 5 cm^2 MEA with PGM-free cathode catalyst, tested at conditions: T_{cell} 80 °C, RH 100 %, H_2 backpressure 30 psig, air backpressure 30 psig. b) Polarization curve for the operando 1 cm^2 MEA for T_{cell} 80 °C and 30°C, tested at 100 % RH with no backpressure, where the operando cell's performance is shown too, c) operando chronopotentiometric hold at 30 °C, with no backpressure with potential profile of the cell recorded as well. Reproduced from Ref. [3] with permission from Elsevier.

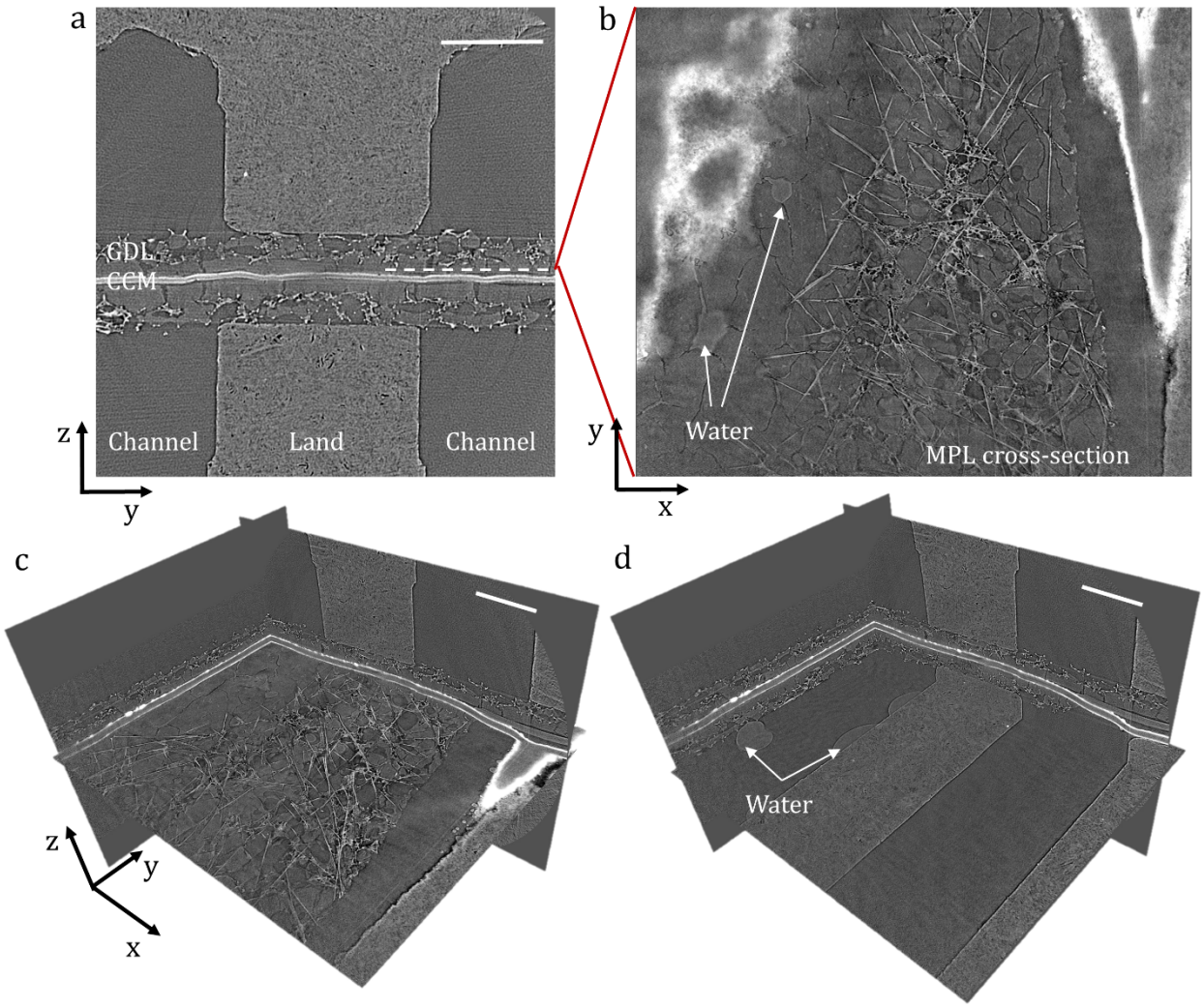

Figure A9. X-ray CT imaging of Gen 5 cell, where a) shows cross-section tomograph, b) zoom-in view of water within the MPL, c) a 3D plane showing water in the MPL, and d) water in the channels of the cell. Data collected at beamline 8.3.2 at ALS.

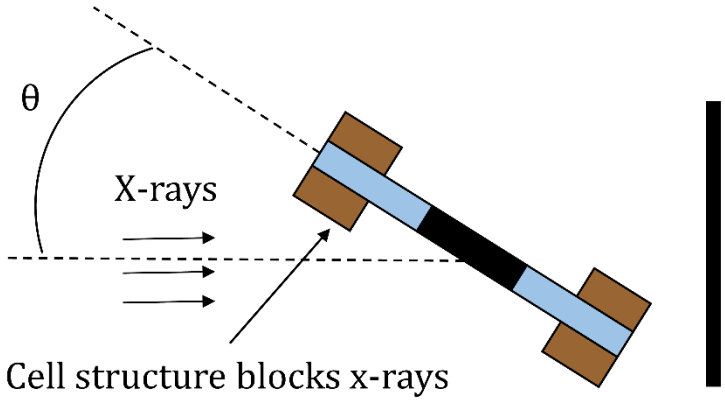

Figure A10. Top view of nano CT cell where θ is the angle of the cell relative to the beam. The cell structure blocks x-rays from reaching the collector when θ < 16°

Synchrotron Beamlines

Micro-CT

8.3.2 ALS

The source of Beamline 8.3.2 is the 4.7 Tesla magnetic field in a superconducting dipole (peak field = 6.0 Tesla) at the Advanced Light Source (ALS), a third-generation synchrotron at Lawrence Berkeley National Laboratory. As the synchrotron's electron beam passes through the magnet, a wide range of wavelengths of light are emitted and travel down beamline 8.3.2 towards the hutch. A monochromator is used to select a specific x-ray wavelength. The angle of the monochromator's diffractive elements is set to allow only the chosen wavelength to pass, although white light can also be passed by removing the monochromator elements. The x-ray energy operating range is 6 keV -46 keV. Motion control of the stage is achieved by an air bearing rotation stage which allows

360 to 1800 projections in one rotation. The detection system has a minimum 2D resolution of 1.5 μm.

Sample can be mounted on the stage with the help of a kinematic mount that is, in turn, attached to the top of the rotation stage by a magnetic plate.

For this study, energy of 25 keV was selected, the 5x optical zoom was used to generate image with 1.3 μm resolution and 3.3 mm FOV. PCO.Edge camera was used with 300 ms exposure time and 1025 number of images collected per scan.

2-BM APS

The 2-BM bending magnet beamline at Argonne national laboratory is fully dedicated to microtomography with capability to perform large field of view (20x2 mm^2) fast 2D phase contrast imaging for slow dynamic phenomena studies (0.1m/s). The beamline uses a multilayer monochromator with the x ray energy operating range of 11-35 keV. High resolution tomography of spatial resolution varying between 1 μm- 11 μm within 5 minutes - 30 minutes can be obtained. Fast imaging system provides sub second tomography. Specially designed furnaces and load cell for in situ experiments are available.

For this study, images were acquired with 20 μm LuAG scintillator, 5× lenses, and a sCMOS PCO.Edge camera. Images resulted in 1.33 μm cubic voxels and a horizontal field-of-view (FOV) of 3.3 mm. The vertical FOV depends on the selected energy. A double-multilayer monochromator was used to select a beam energy of 27.5 keV. A rotation range of 180°, 1500 projections, and an exposure time of 50 ms were selected, resulting in a total scan time of 3 min.

Nano-CT

32-ID APS

32-ID supports three main techniques: monochromatic full-field imaging, white beam full-field imaging and transmission x-ray microscopy. There are two experimental stations, 32-ID-B at 37 m from the source and 32-ID-C at 70 m from the source. Both stations are capable of white or monochromatic beams. The TXM and the monochromatic full-field imaging is housed in 32-ID-C while the white beam full-field imaging is housed in 32-ID-B. Phase and/or absorption contrast is available for all techniques. Beamline optics consists of a Kohzu double-crystal monochromator (Si (111)) in the FOE and a 3 stripe (Si, Rh, Cr) double mirror in the B station that can be moved in/out of the monochromatic beam. 32-ID has two undulators: a U33 for general broad-band spectrum usage; and a U18 providing a quasi-single line spectrum at 24.5 keV for (ultrafast) imaging and diffraction work. The x-ray energy operating range is 7-40 keV.

Monochromatic X-rays illuminate the beam shaping condenser, pass through the sample, a Fresnel zone plate (FZ), and are collected by an imaging detector. FZ plates with grating of 60 nm were used to achieve a resolution of 60 nm. The FOV was 75 μm × 75 μm, and the scan-time was approximately 20 min with 1 s per projection with 1500 projections recorded. Zernike phase contrast was used to detect low-atomic-mass elements such as carbon. Image phase retrieval and reconstructions were performed using TomoPy (an open-source software package developed by ANL). ASTRA toolbox was used for the tomographic reconstructions

18-ID NSLS II

18-ID at NSLS II is a full field x-ray imaging beamline that offers advanced capabilities for studying the morphology and oxidation states of dynamic systems in 2-D and 3-D with 30 nm resolution. The beamline source is the 100 mm-period damping wiggler (DW100). The beamline optics consists of a collimating mirror, Si (111) double-crystal-monochromator and a toroidal mirror, which serves to focus the beam onto a secondary source aperture located in the end station. The mirrors are bendable in the longitudinal direction to achieve the proper collimation and focus. The collimating mirror has 3 stripes – Si, Cr and Rh –, which, at the 4.4 mrad nominal incidence angle, leads to cut-off energies of ~ 7 keV, 12 keV and 15 keV respectively. The images can be taken in absorption contrast mode with 20-40-micron FOV. It is also capable of 2D XANES and 3D XANES tomography with a 30nm resolution.

For this study nano X-ray CT was collected at beamline at 8 keV selected energy, 30 nm spatial resolution with 40 um FOV. The scan-time was less than one minute in absorption-contrast mode.

ESRF ID16B

The ID16B beamline at the European Synchrotron Radiation Facility is a Nano analysis beamline which provides hard x-ray nanobeams optimized mainly for spectroscopic applications, including the combination of x-ray fluorescence, x-ray diffraction, x-ray Excited Optical Luminescence, x-ray absorption spectroscopy, as well as Nano tomography. The primary beamline optics includes double white beam mirror (DWM) and double-crystal monochromator (DCM) are placed as close to the source as possible (30 m and 35 m, respectively) to preserve the coherence of the beam and to minimize beam instabilities. The KB mirror nanofocusing optics at 165 m are located very close

to the sample (0.1 m) to obtain a high degree of demagnification. The beamline provides an x-ray energy range from 17 keV to 30 keV with a beam size of 50x50 nm in pink or monochromatic mode and from 80 to 100 nm in monochromatic mode. The beamline offers images to be taken in absorption contrast mode.

For this study images were collected at 17.5 keV in phase-contrast mode.

SSRL 6-2

Beamline 6-2c is a wiggler end-station dedicated to hard x-ray transmission x-ray microscopy. It houses a transmission x-ray microscope with 2D and 3D full field imaging and spectroscopic capabilities, with an instrument resolution down to 30 nm. It has specific capabilities for in-situ tomographic studies of catalytic processes including x-ray absorption spectroscopy. The x-ray energy can be selected between 2.36 keV -17.5 keV. The primary beamline optics include bent flat single-crystal Rh coated silicon mirror, a bent cylindrical single-crystal silicon mirror and a bent flat Zerodur Ni coated mirror. Beamline 6-2b is a station dedicated to High Resolution Hard x-ray Spectroscopy. The end station combines three multicrystal Johann spectrometers that enable x-ray Emission Spectroscopy (XES), Resonant Inelastic x-ray Scattering (RIXS), High-Energy Resolution Fluorescence Detected x-ray Absorption Spectroscopy (HERFD-XAS) and x-ray Raman Spectroscopy (XRS) techniques. The ambient pressure operation of the end-station provides high flexibility in implementing various sample environments (in-situ, cryogenic, He-atmosphere, furnaces, liquids, high pressurized cells, etc.)

Here for each scan, the sample was exposed 180 times for 1 s each as the sample was stationary in the radiography mode. The selected energy was 11.5 keV.

Appendix B

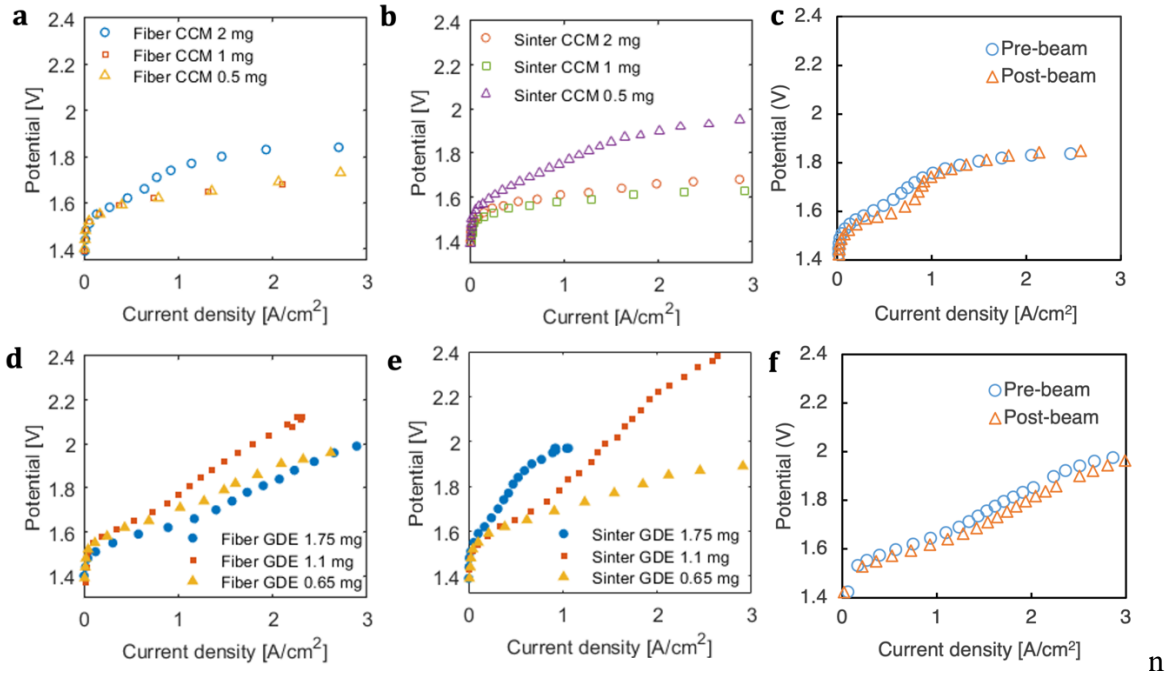

n

Figure B1 iR-free polarization curves for operando cells tested at beamlines. All cells were preconditioned at 60 °C and constant current hold of 1 A cm^{-2} for 30 minutes before obtaining polarization curves. The water flow rate at the anode was kept constant at 3 mlpm for all tests and no back pressure on the cathode was applied. c represents pre and post beam polarization curves for Fiber CCM 2 mg cell. f represents pre and post beam polarization curves for Fiber GDE 1.75 mg cell. The pre and post polarization curves of each cell are the same indicating no beam damage.

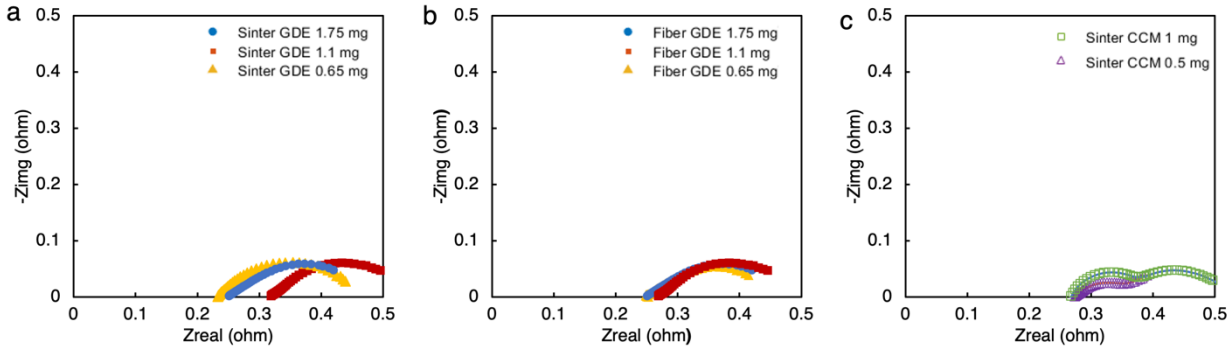

Figure B2 EIS spectra of operando cells obtained after conditioning. The data was collected at a DC voltage of 1.7 V vs ref and an AC perturbation of 10 mV from 1 MHz to 1 Hz frequency.

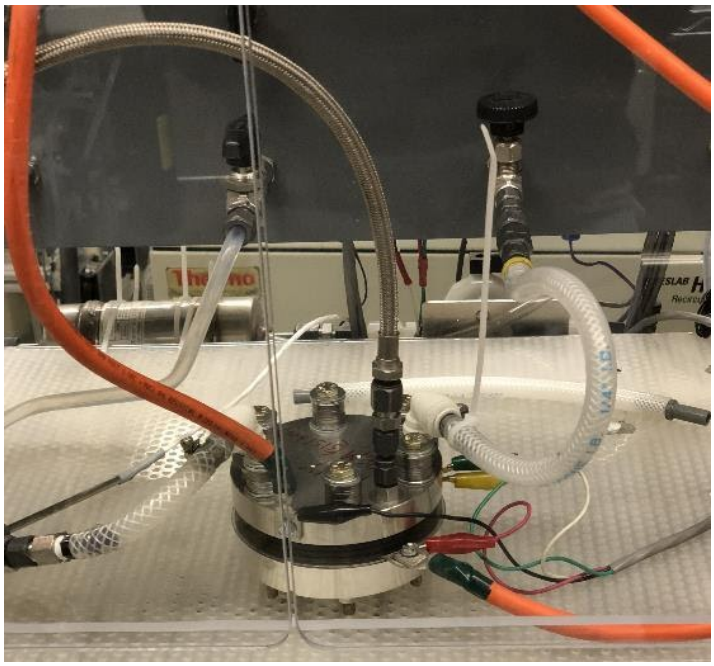

Figure B3 Image of 28 cm^2 cell stack installed on test stand at Nel Hydrogen

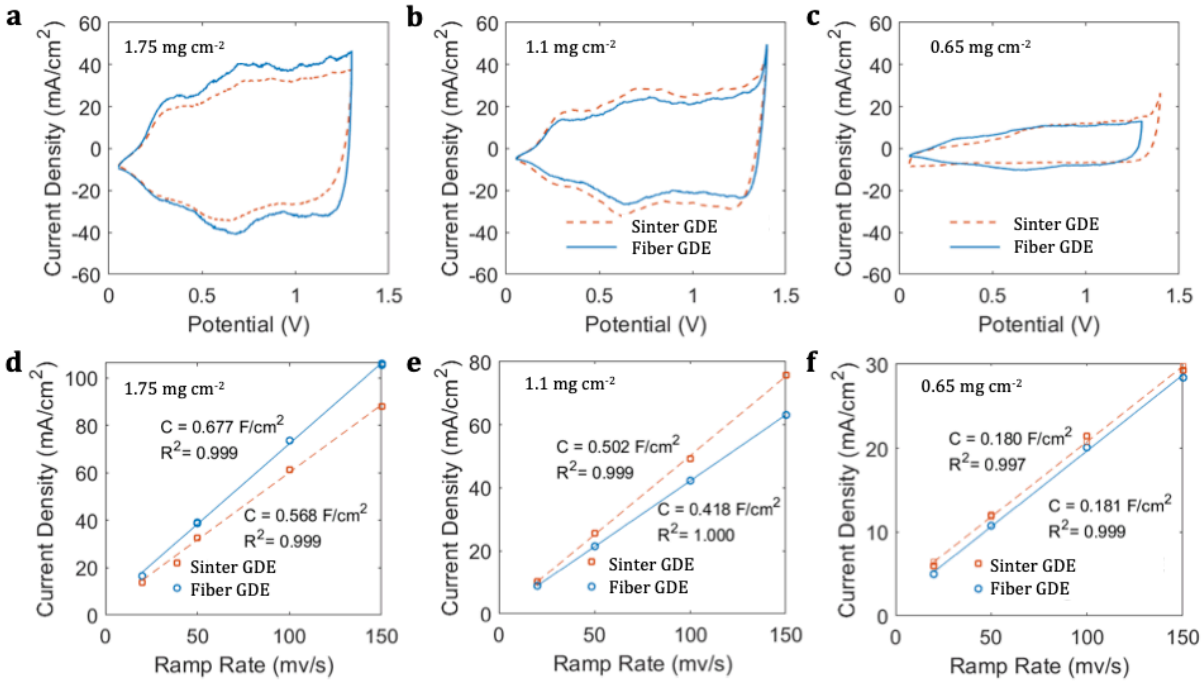

Figure B4 Cyclic voltammetry (CV) scans for fiber and sinter GDEs for double layer capacity calculations a-c) CV scans obtained at 50 mV sec^{-1} juxtaposed for fiber GDE (solid lines) and sinter GDE (dotted lines) at various loadings d-f) scan rates plotted against measured current

density within a potential range of 0.9 V -1.1 V for various loadings. The slope of the scan rate against the current density gives the double layer capacitance.

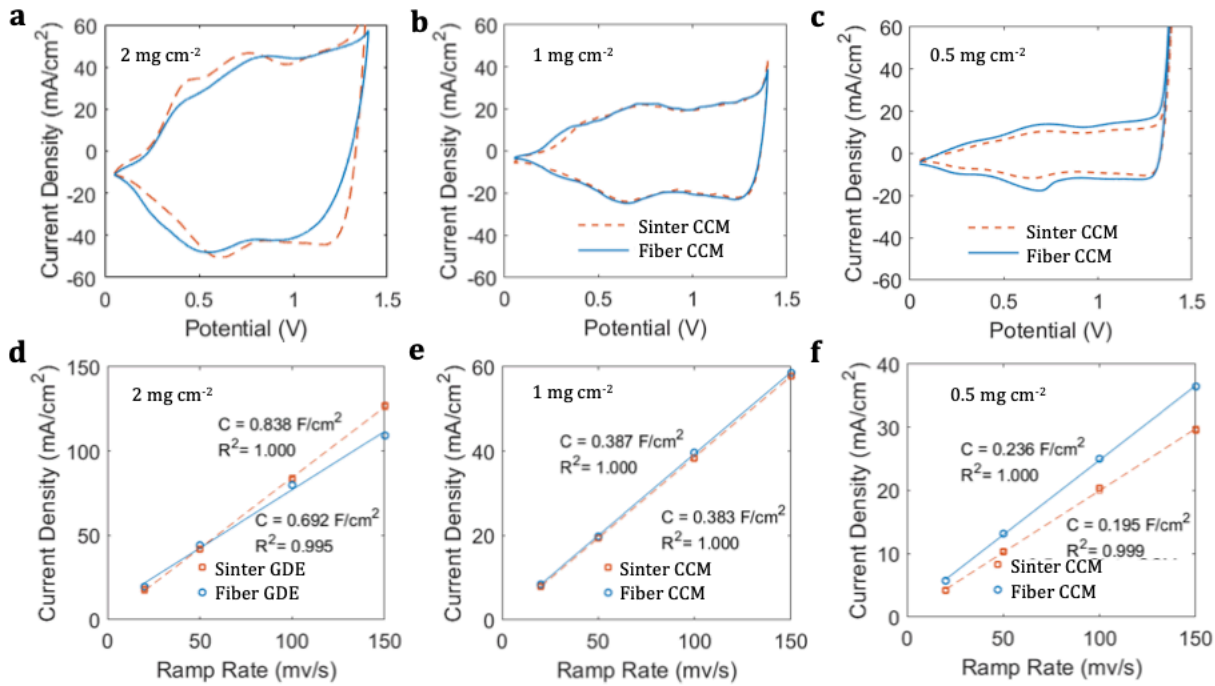

Figure B 5 Cyclic voltammetry (CV) scans for fiber and sinter CCMs for double layer capacity calculations a-c) CV scans obtained at 50 mV sec^{-1} juxtaposed for fiber CCM (solid lines) and sinter CCM (dotted lines) at various loadings d-f) scan rates plotted against measured current density within a potential range of 0.9 V -1.1 V for various loadings. The slope of the scan rate against the current density gives the double layer capacitance.

0-D model fitting of BoL polarization curves:

Table B 1 0-D model fitting parameters

Fitting constants					
Parameters					
Idea gas constant	R	8.314	J/mol.K		
Porosity		0.48			
Temperature	T	50	C	323.15	K
Exchange current, OER	i_0,OER	215	A/m^2	0.0215	A/cm^2
Reference potential	E_0	1.4	V		
Proton conductivity	κH^+	9.749066625	s/m	0.09749067	s/cm

Membrane thickness		0.017	cm		
Faraday constant	F	96485	c/mol		
Membrane concentration	CH^+	1000	mol m^{-3}		
Diffusivity of hydrogen ion in membrane	DH^+	6.00E-09	m^2/s	*Fit parameters	
Membrane conductivity		20.79010	s/m	0.1356	s/cm
Tafel slope	b	Experimental	V/dec		
TPCA		Experimental			

$$E_{cell} = E_{rev} + \eta_{kin} + \eta_{\Omega} + \eta_{MT}$$

$$E_{rev} = 1.2291 - 0.000845 \cdot (T - 298.15)$$

$$\eta_{\Omega} = i \times HFR = \frac{i \cdot t_{memb}}{\kappa}$$

$$\sigma_{memb} = \frac{F^2 C_{H+} D_{H+}}{RT}$$

$$\eta_{Kin} = b.log\left(\frac{i}{i_0.TPCA}\right)$$

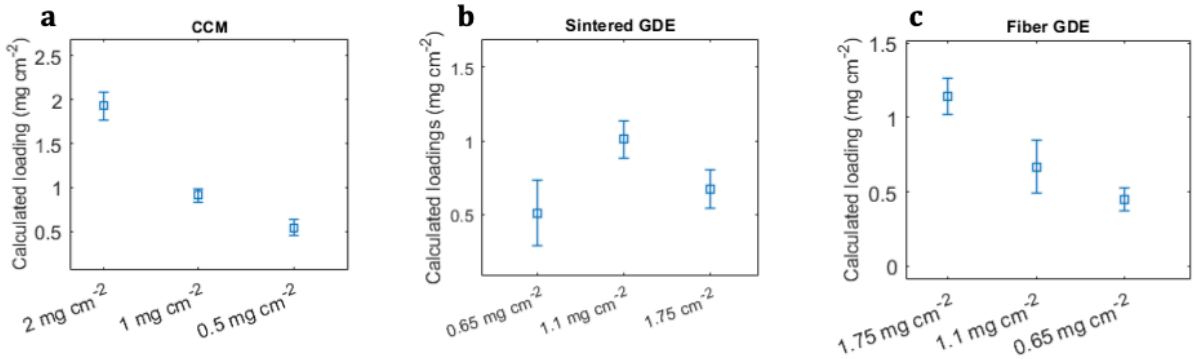

Figure B 6 Calculated catalyst loadings form X-ray tomography images a) represents both fiber and sintered CCMs b) sintered GDE c) fiber GDE.

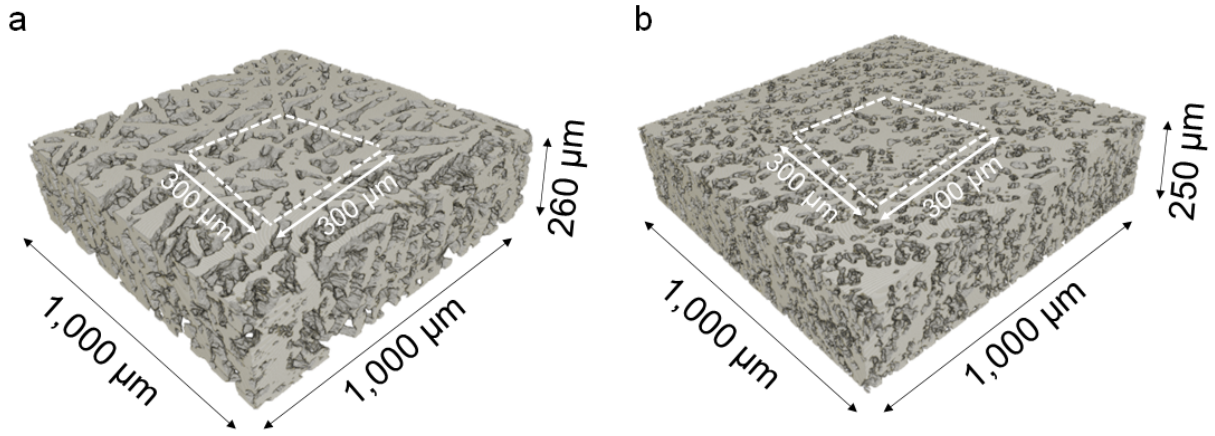

Figure B 7 Computational domain for LBM simulation of oxygen transport inside the PTL of a) Fiber PTL, and b) Sinter PTL. The computational domain has a size of 300x300x260 μm^3.

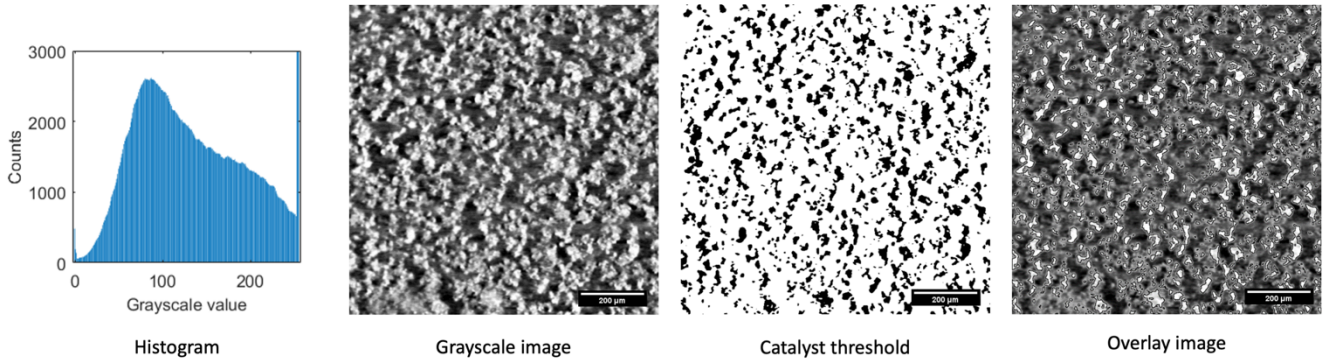

Figure B 8 Histogram, grayscale image, segmented image, and overlayed image of catalyst from Figure 1. The images are sintered GDE 1.75 mg cm^{-2}

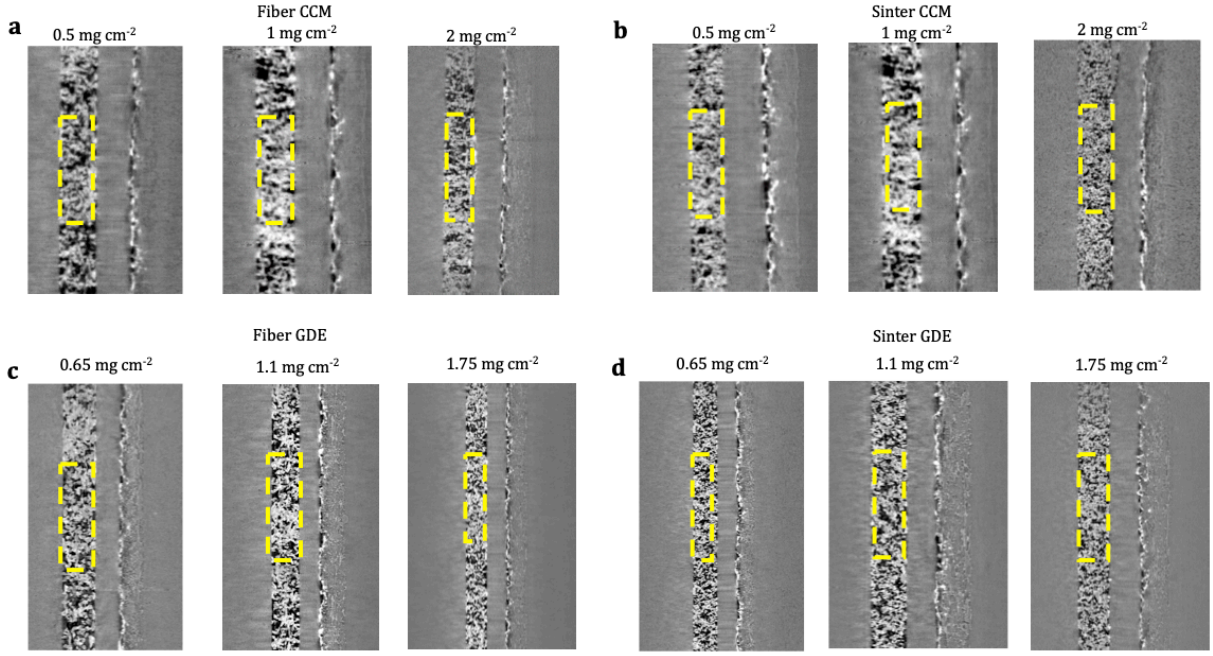

Figure B 9 In-plane X-ray tomography images of low, medium and high loaded CCMs and GDEs. The dotted areas indicate the region of interest as viewed from the x-y plane for a) fiber CCM b) sinter CCM c) fiber GDE d) sinter GDE. The water flow in the channels is from the bottom to the top. The selected ROI is in the middle of the inlet and outlet channel.

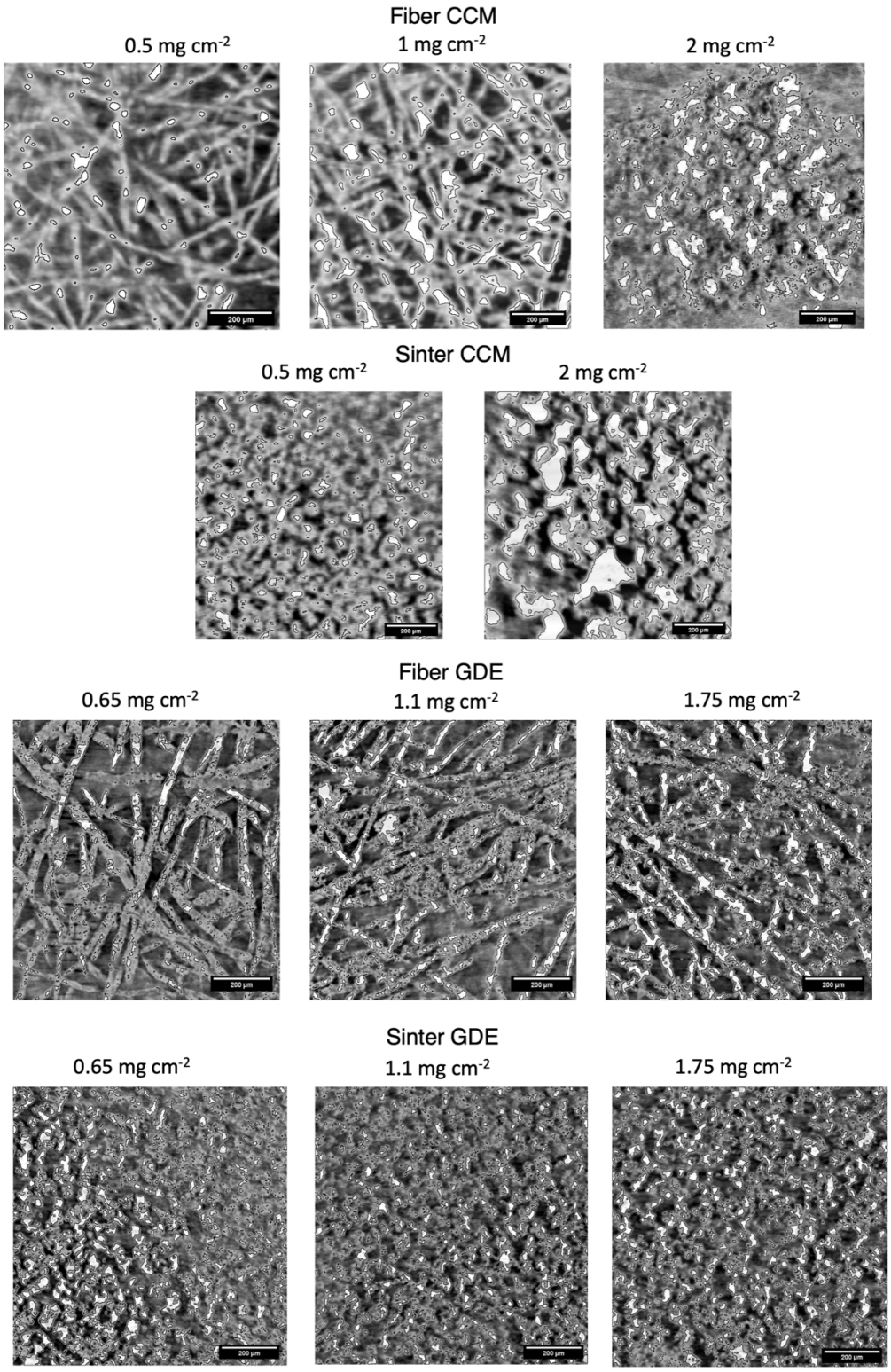

Figure B 10 Original grayscale images overlayed with catalyst outline for all electrodes

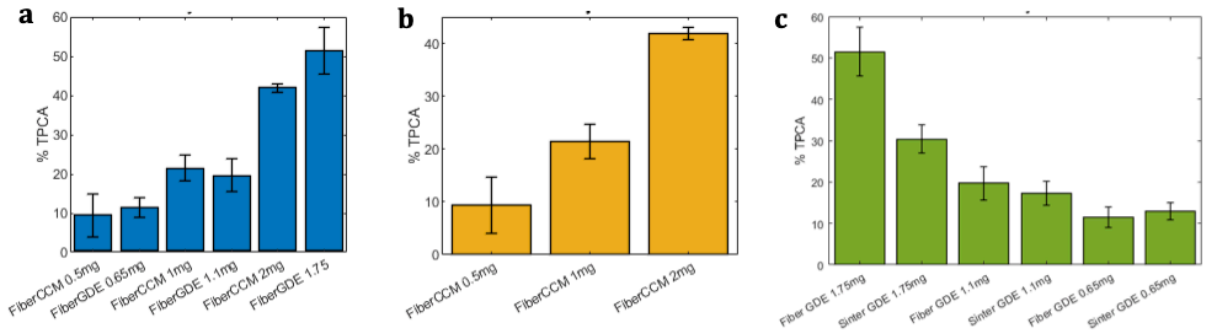

Figure B 11 Calculated triple phase contact area (TPCA) values for all the samples a) comparing similar loaded CCMs and GDEs b) comparing various loadings for CCMs c) comparing various loadings for GDEs

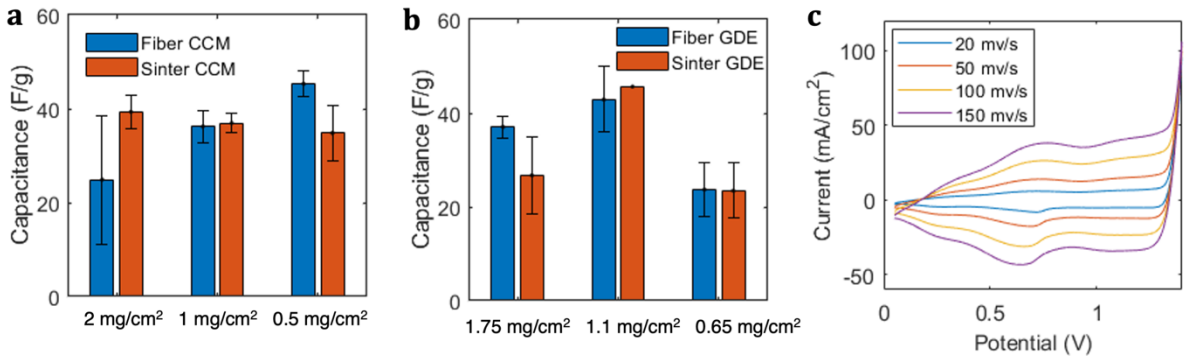

Figure B 12 a) Mass normalized double layer capacities of fiber and sintered CCMs for high, medium, and low loadings, b) Mass normalized double layer capacities of fiber and sintered GDEs for high, medium, and low loadings c) Example of CVs with different scan rates used for calculating double layer capacities. The CVs were performed on the cell Fiber CCM 0.5 mg cm^{-2}

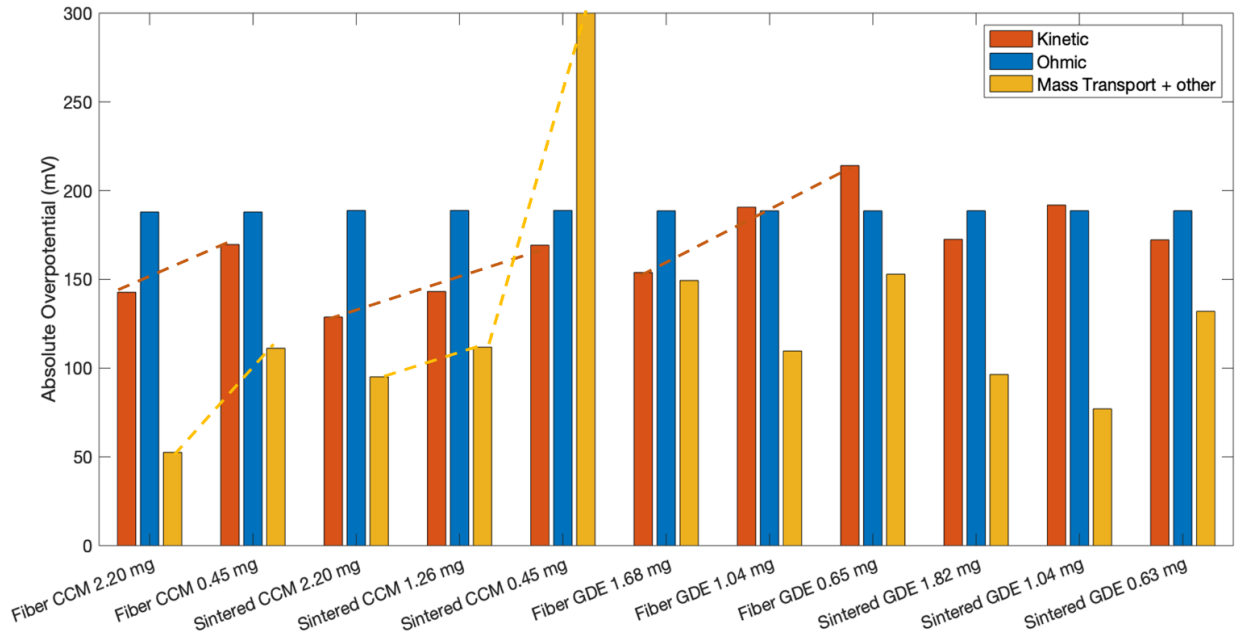

Figure B 13 Overpotential breakdown of all cell configurations at 1.5 A cm^{-2} calculated from 0-D model.

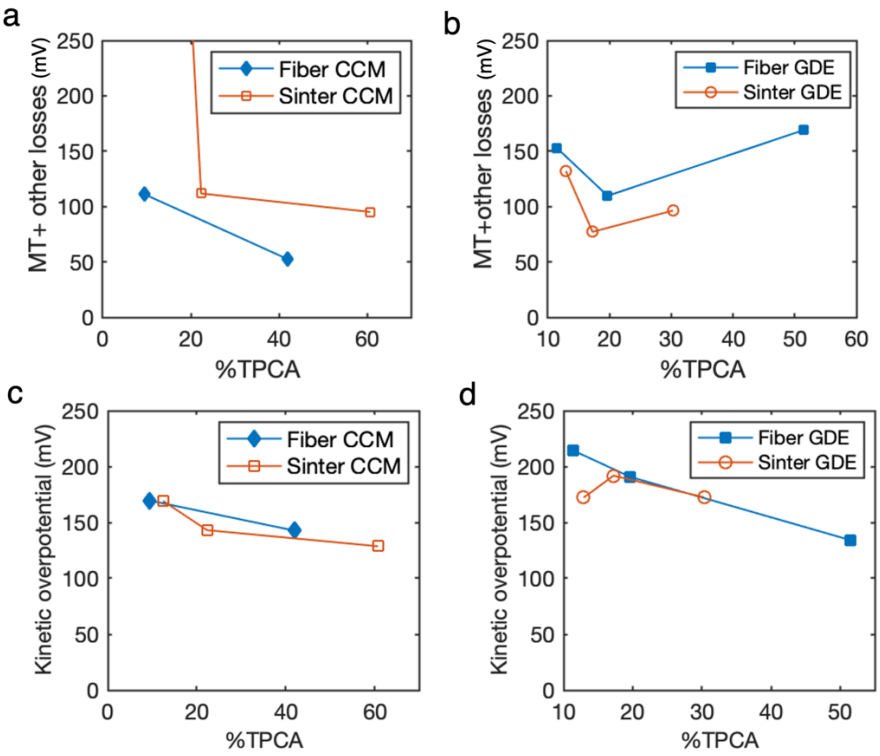

Figure B 14 Mass transport and kinetic overpotentials as a function of %TPCA for a, c) CCMs b, d) GDEs.

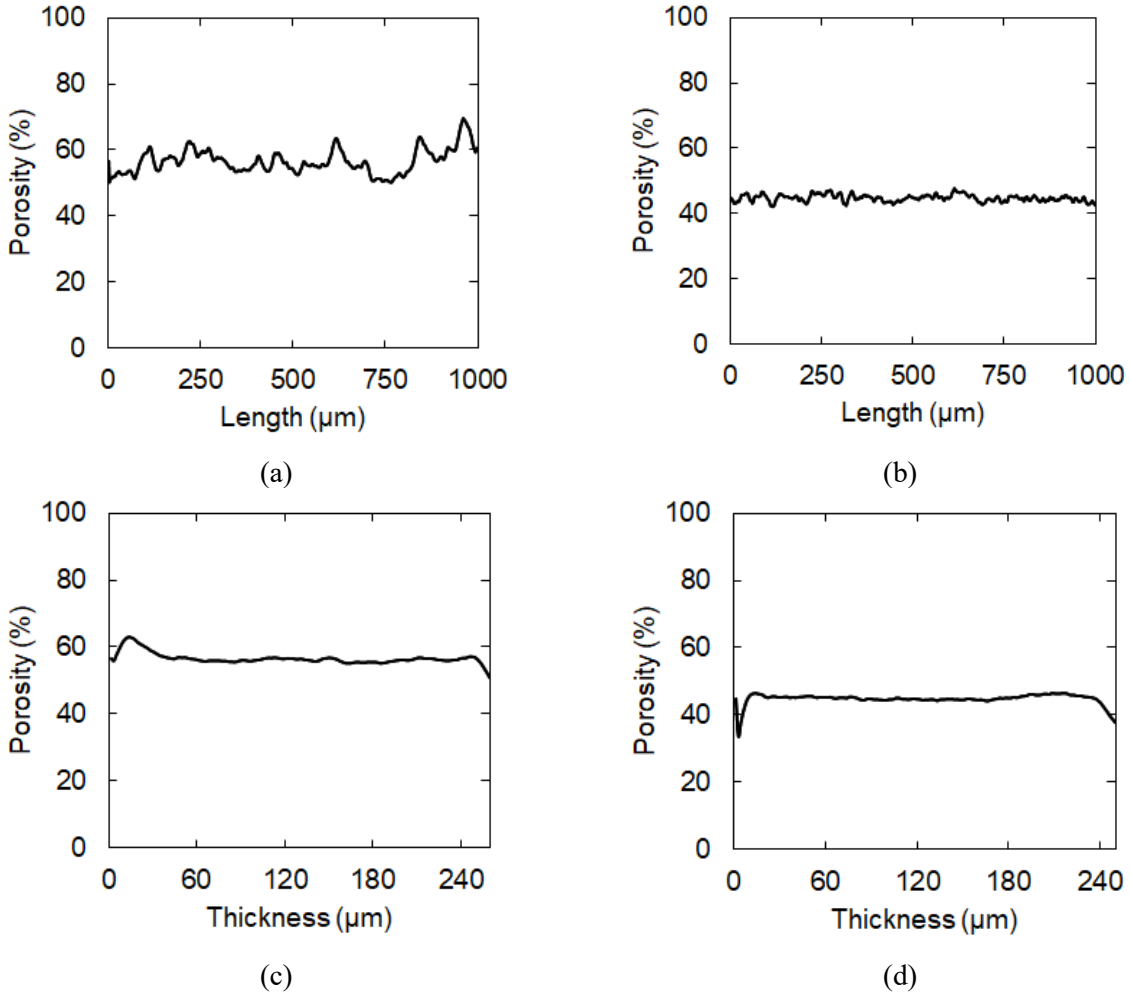

Figure B 15 a) In-plane porosity profile of fiber PTL, b) in-plane porosity profile of sinter PTL, c) through-plane porosity profile of fiber PTL, and d) through-plane porosity profile of sinter PTL. The fiber PTL has the average porosity of 56.5% and sinter PTL has the average porosity of 44.7%.

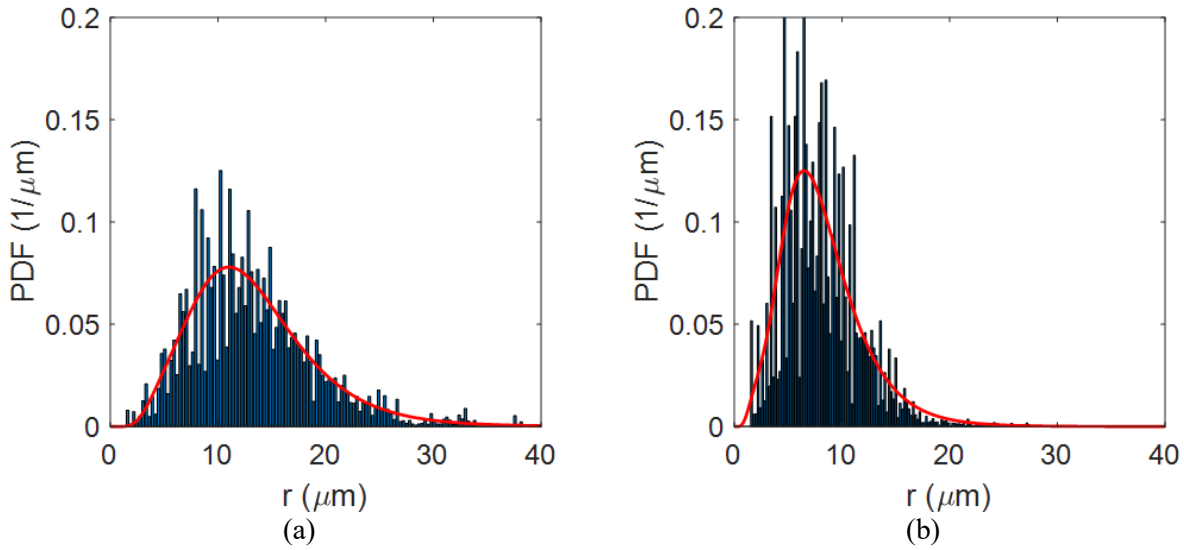

Figure B 16 a) Pore-size distribution of fiber PTL and b) pore-size distribution of sinter PTL. The fiber PTL has the mean pore radius of 13.31 µm with the maximum pore radius of 38.43 µm. The sinter PTL has the mean pore radius of 8.07 µm with the maximum pore radius of 27.57 µm.

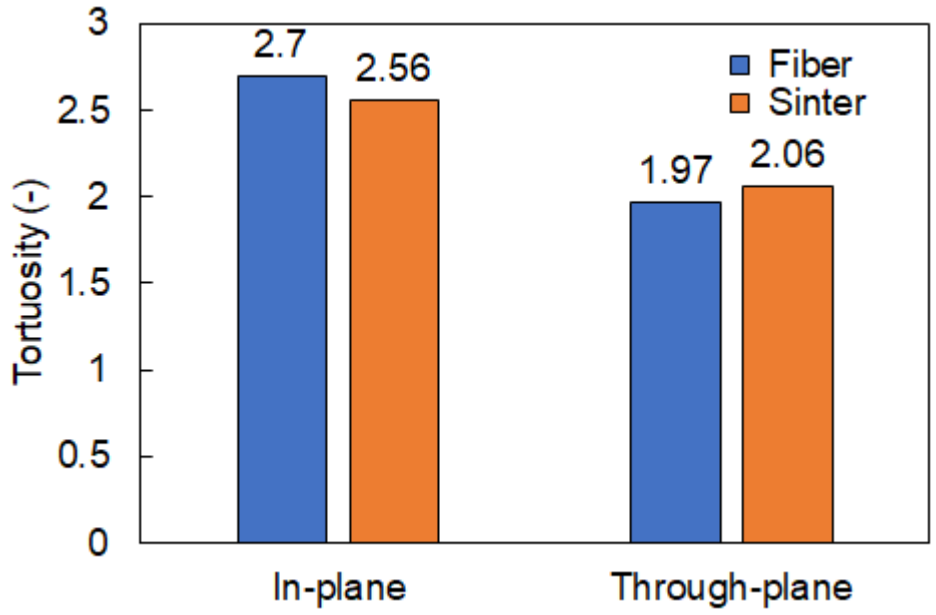

Figure B 17 In-plane and through-plane tortuosity factors for fiber and sintered PTL.

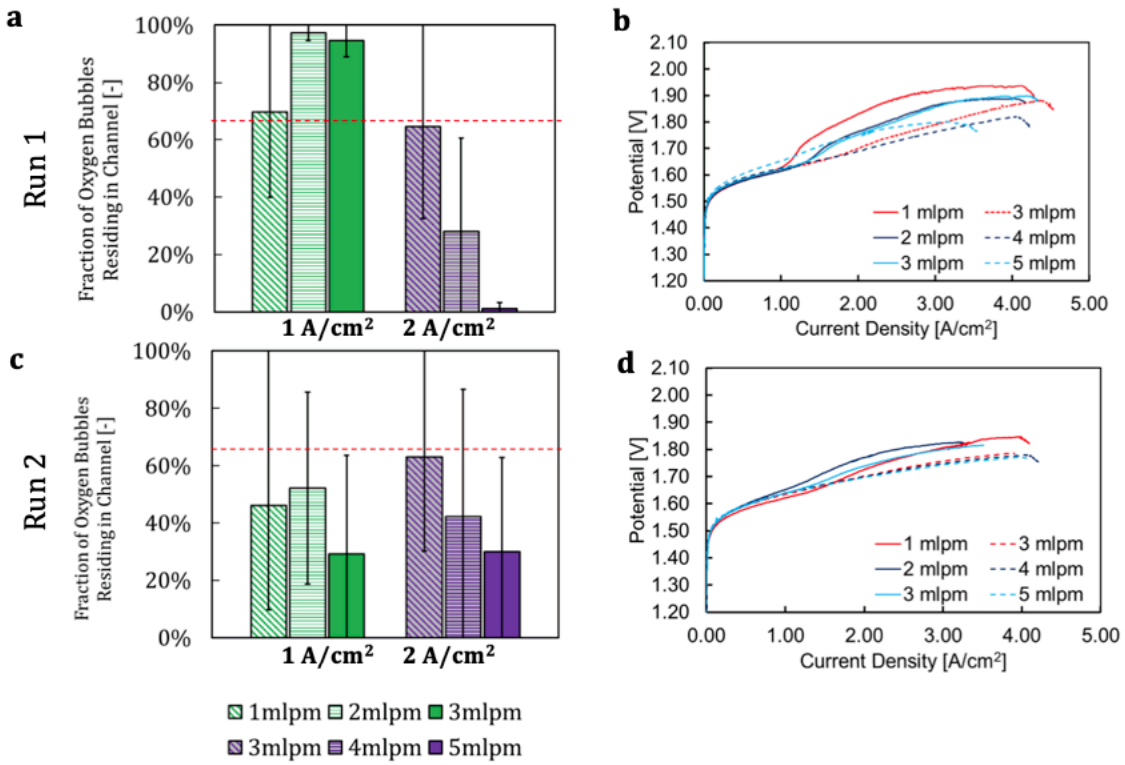

Figure B 18 Effect of flow rate on oxygen residence in the anode channel and effect on cell performance.

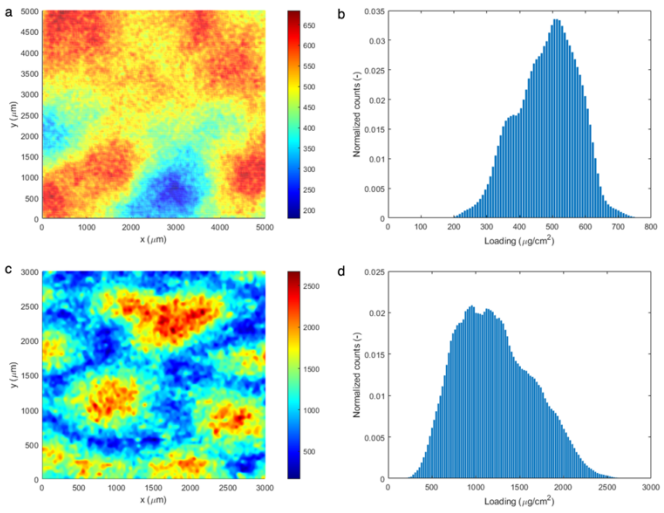

Figure B 19 XRF mapping of pristine CCMs for Ir loading of 1 mg cm^{-2} (a, b) and 0.5 mg cm^{-2} (c, d)

Table B 2 Eotvos number calculation parameters

Parameters	Value	Unit	Note
ρ_{water}	998	kg/m^3	Water density at 20 °C
ρ_{oxygen}	1.429	kg/m^3	Oxygen density at 20 °C
G	-9.81	m/s^2	Gravity
σ	0.0072	N/m	Surface tension of water at 20 °C
B	1.03E-05	m	Average pore radius
Eo	0.000136		Eotvos number

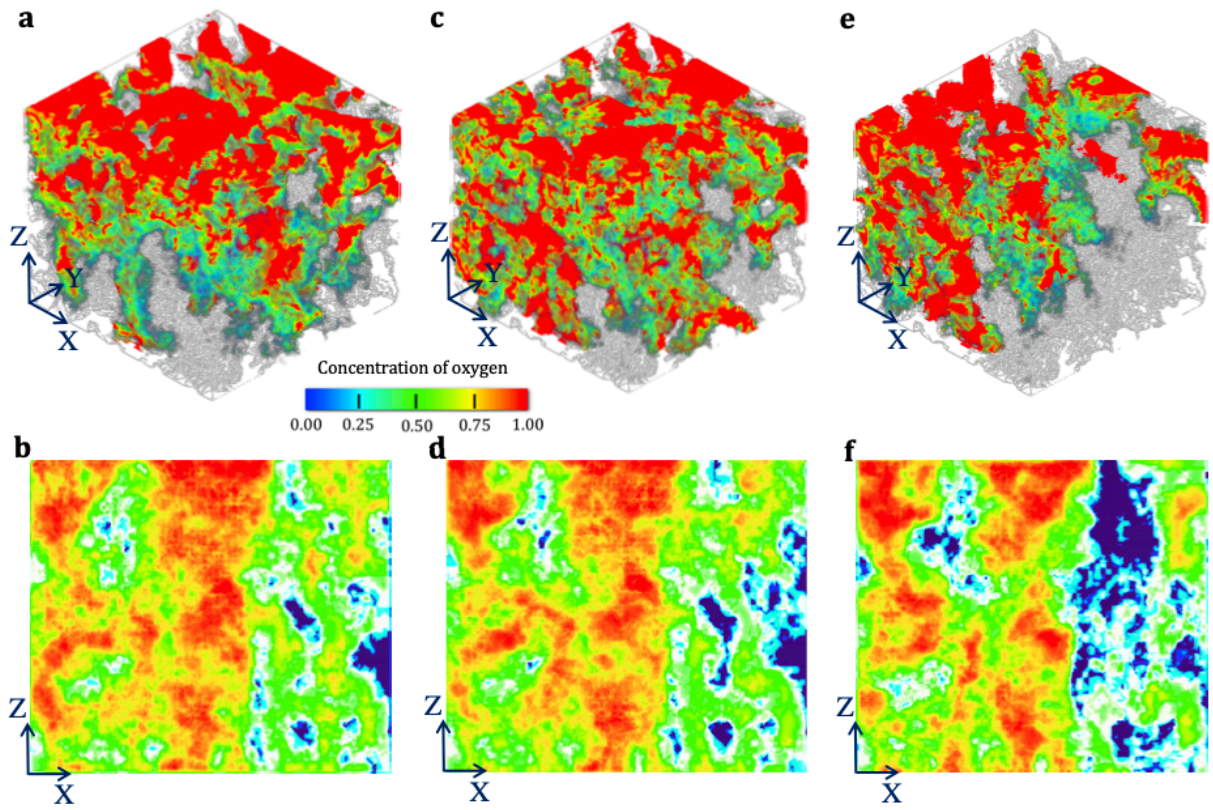

Figure B 20 Model prediction of oxygen gas transport in the anodic fiber PTL with the different catalyst homogeneous coating (a-b) Uniform catalyst coating, (c-d) Nearly uniform coating, and (e-f) non-uniform coating. Uniform catalyst coating simulates high loaded samples, nearly uniform coating simulates medium loaded samples and non-uniform coating simulates low loaded samples.

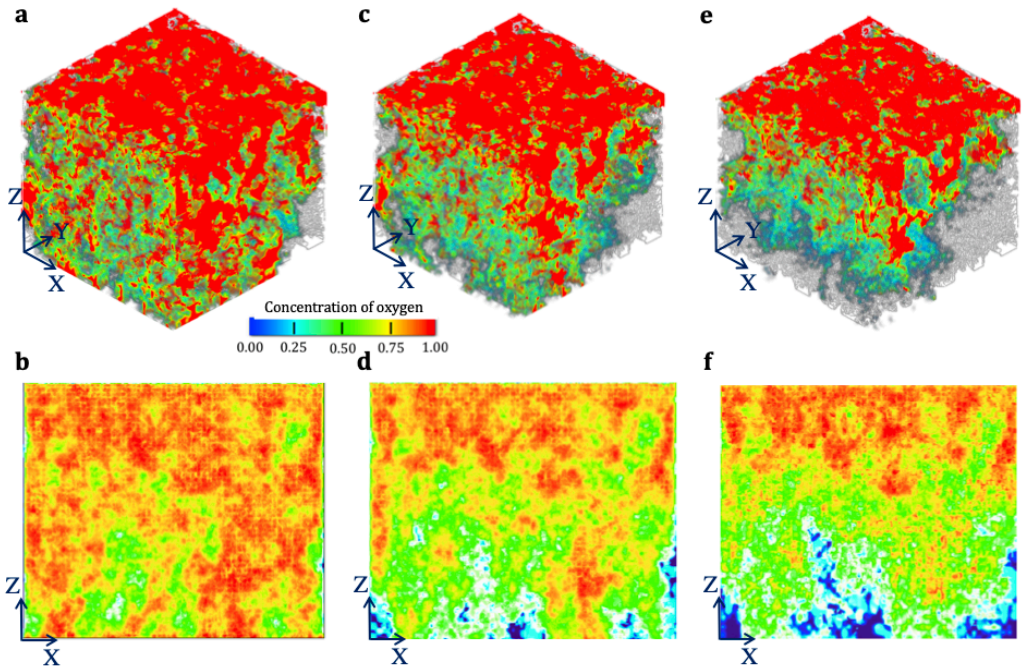

Figure B 21 Model prediction of oxygen gas transport in the anodic sinter PTL with the different catalyst homogeneous coating (a-b) Uniform catalyst coating, (c-d) Nearly uniform coating, and (e-f) Non-uniform coating. Uniform catalyst coating simulates high loaded samples, nearly uniform coating simulates medium loaded samples and non-uniform coating simulates low loaded samples.

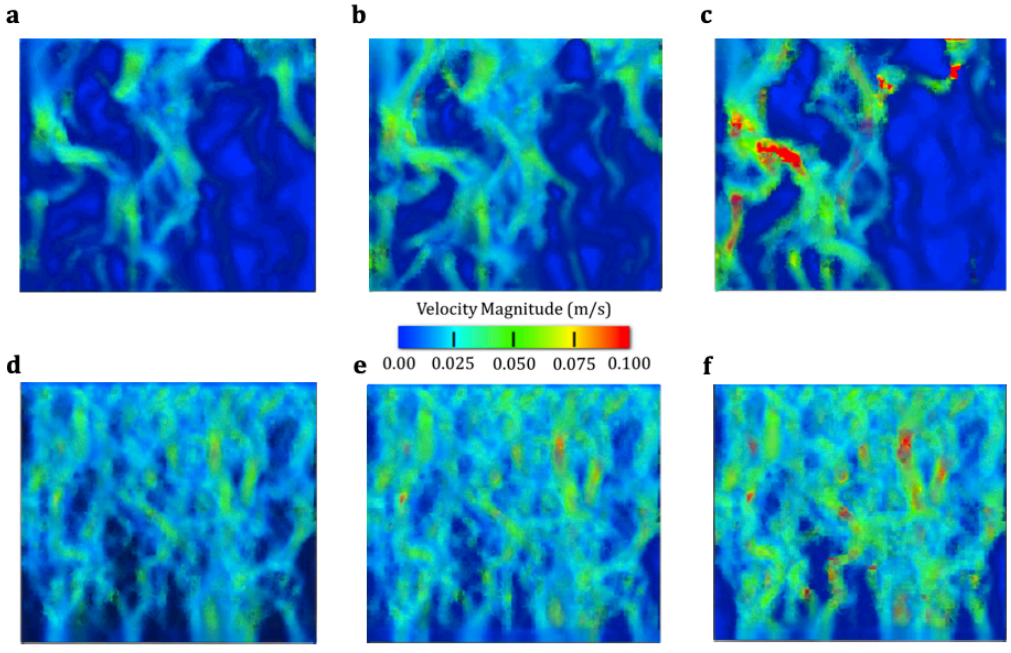

Figure B 22 Oxygen gas velocity profiles in the anodic PTL, (a-c) Fiber PTL with the uniform, nearly uniform, and non-uniform catalyst coating, respectively, (d-f) Sinter PTL with the uniform, nearly uniform, and non-uniform catalyst coating, respectively.

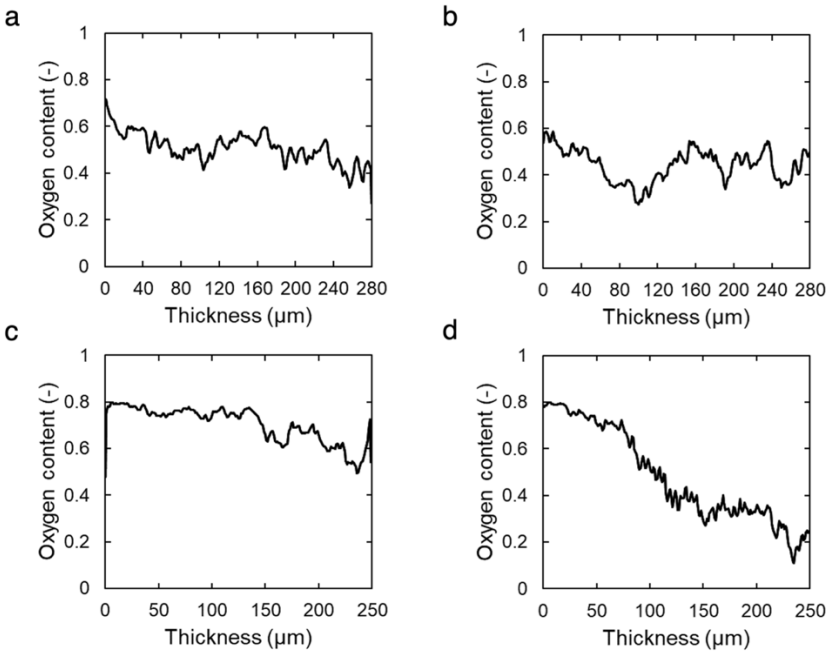

Figure B 23 Oxygen content along the thickness of PTL in a) High loaded fiber PTL, b) low loaded fiber PTL, c) high loaded sintered PTL, and d) low loaded sintered PTL.

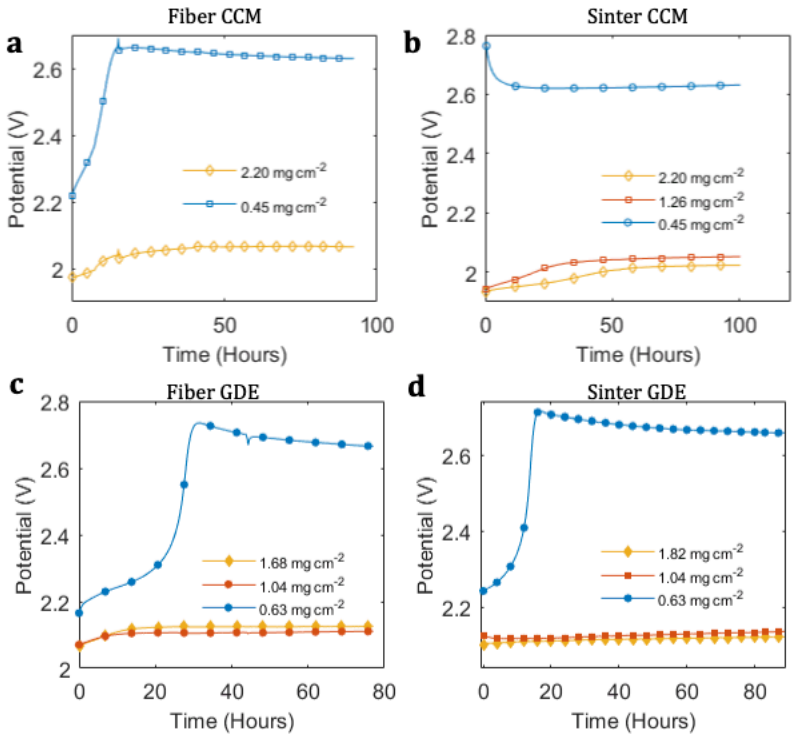

Figure B 24 Steady state chronopotentiometric holds for all samples. The cells were held at 1.8 A cm^{-2} for 90 hours at 50 ºC, constant water flow rate and balance pressure of 1 atm.

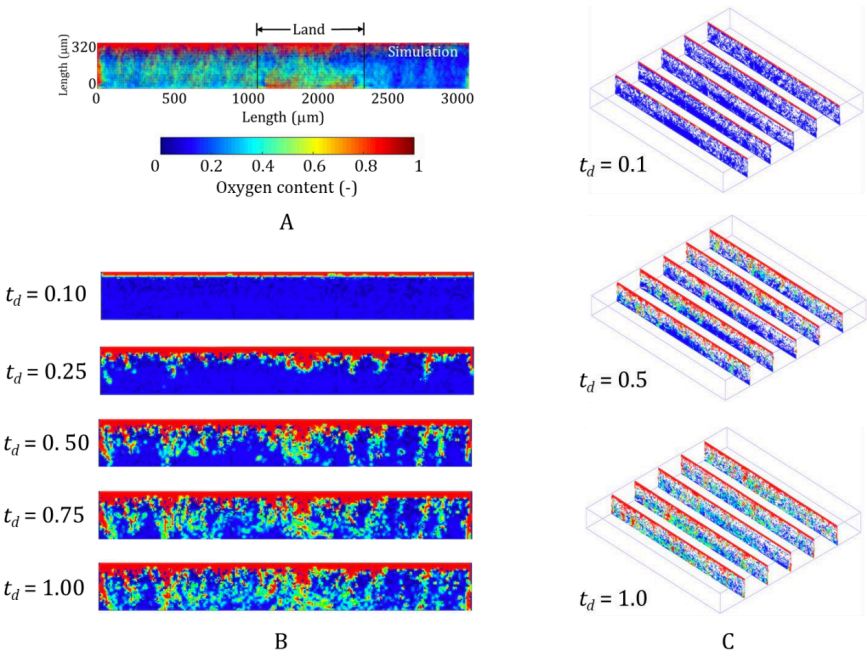

Figure B 25 CFD simulation with the uniform flux of oxygen on the top of PTL at 1 A/cm^2 with the flow rate of 2 mlpm

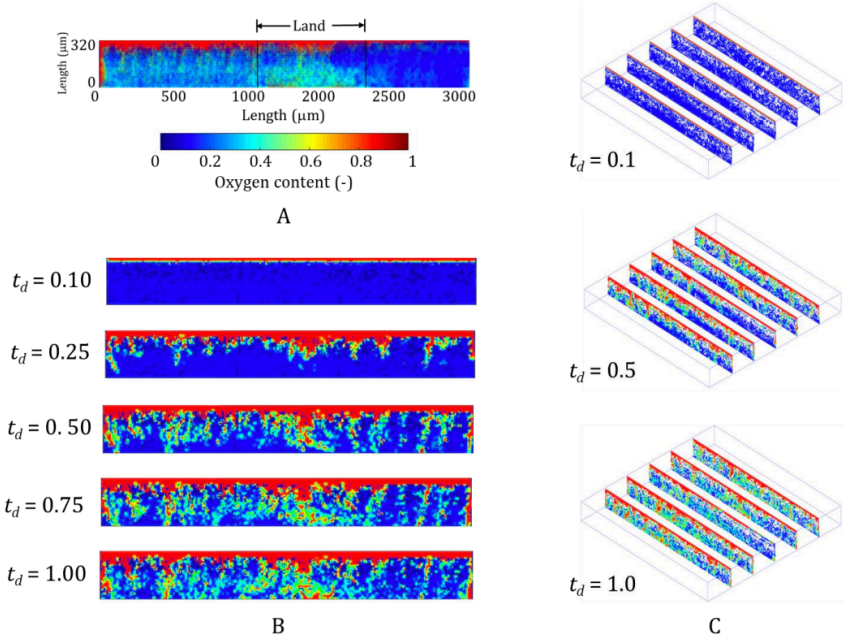

Figure B 26 CFD simulation with the uniform flux of oxygen on the top of PTL at 4 A/cm^2 with the flow rate of 2 mlpm

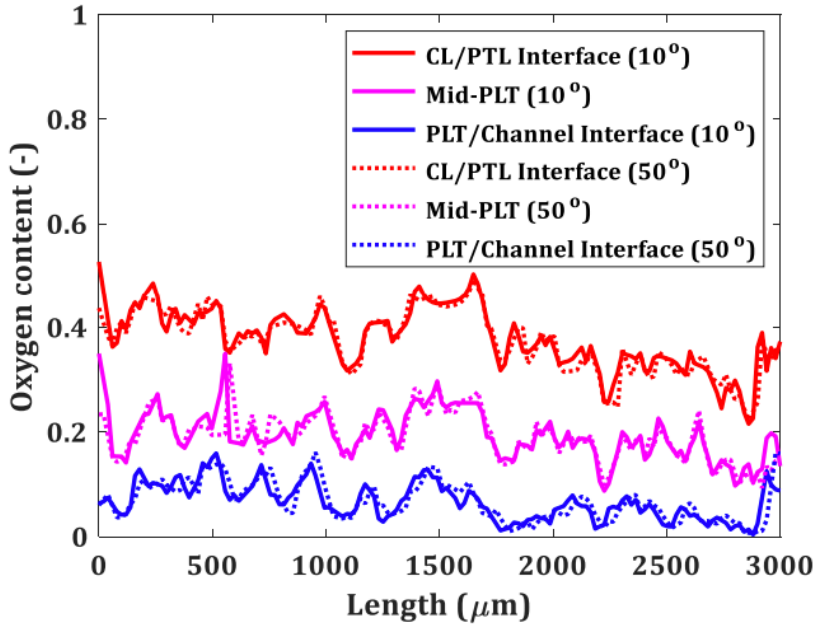

Figure B 27 The effect of wettability on oxygen content comparison between 10 and 50 degree of PTL contact angle

Appendix C

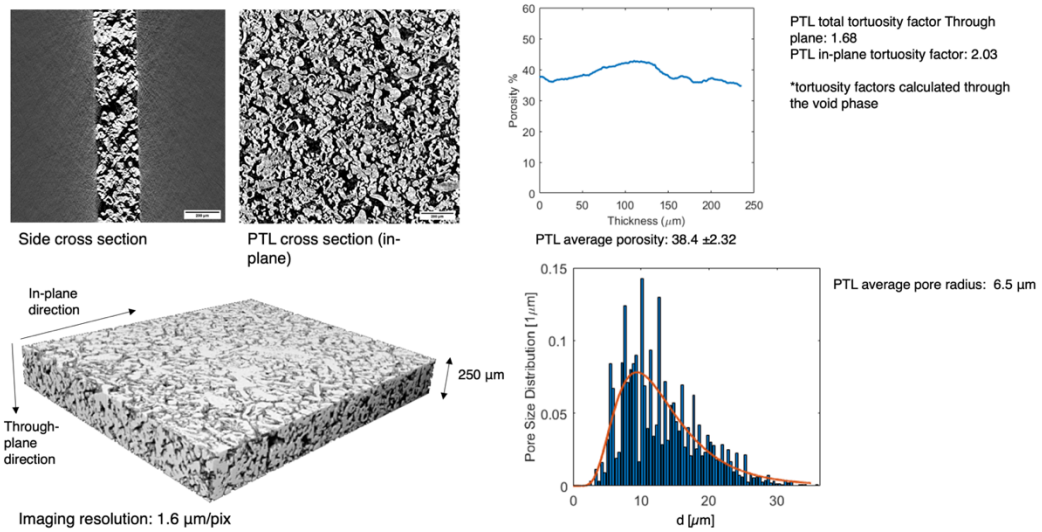

Figure C1 Morphological analysis of Single layer PTL

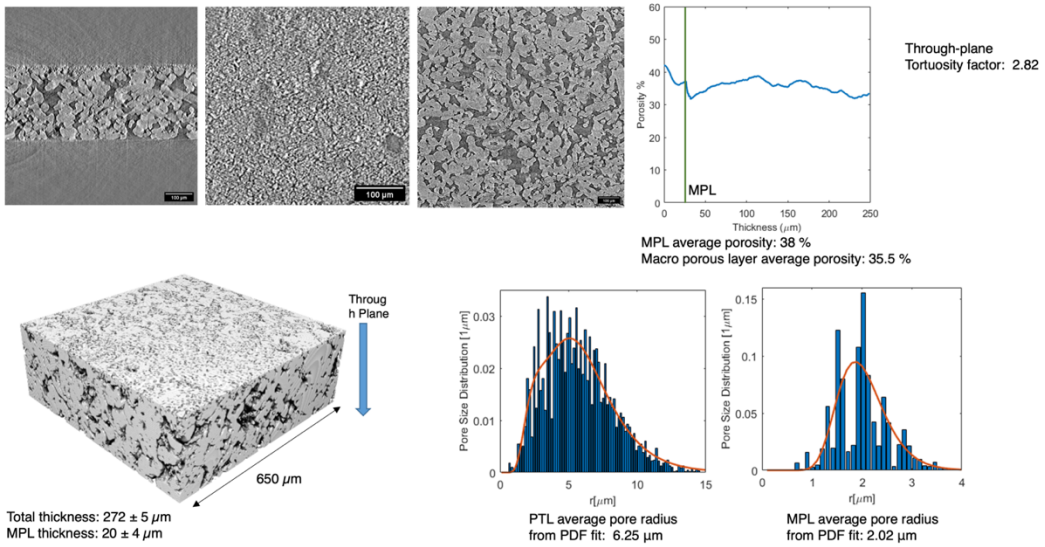

Figure C2 Morphological analysis of MPL 1

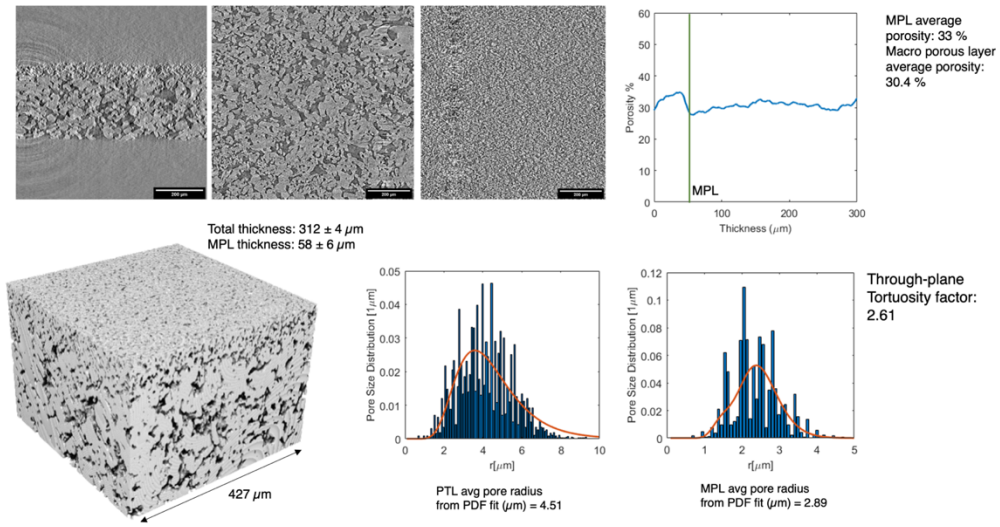

Figure C3 Morphological analysis of MPL 2

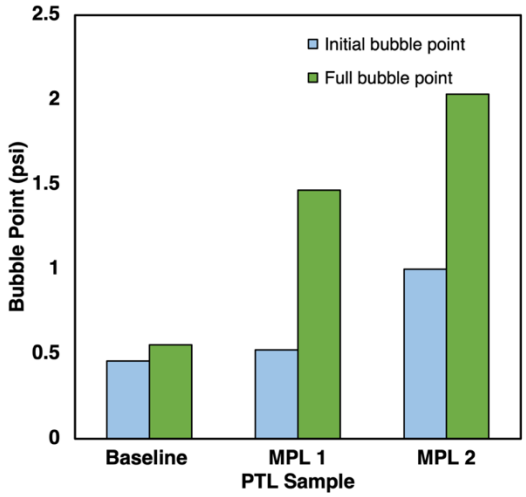

Figure C4 Initial and full bubble point measurements baseline sintered PTL, MPL 1 and MPL 2

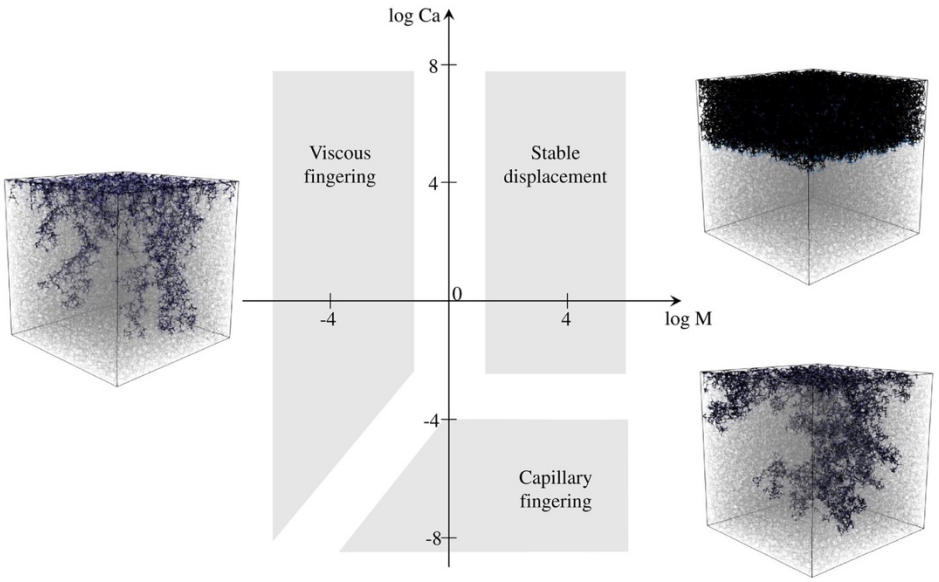

Figure C5 Immiscible two-phase flow pattern phase diagram: stable displacement at large viscosity ratio and large flow rates, viscous fingering at unfavorable viscosity ratio and large flow rates, and capillary fingering at capillary-dominated flow. Reproduced from An et. Al [119]

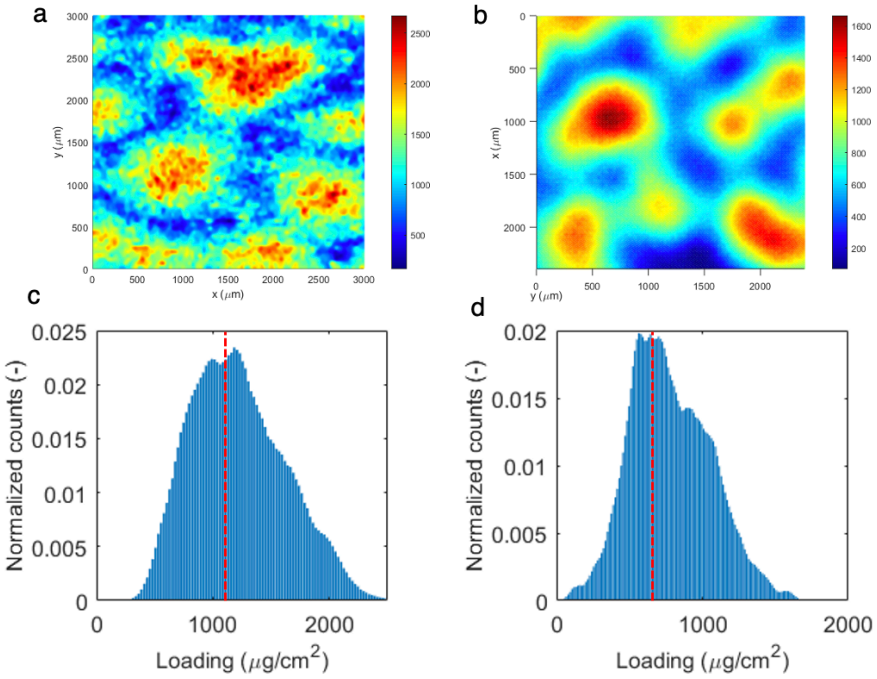

Figure C6XRF maps and loading histograms of 1 mg_{Ir}/cm^2 loaded CCM a.c. Pristine CCM, and b,d. CCM at 10000 cycles.